TUM School of Computation, Information and Technology
Technische Universität München

Efficient Model-based Reconstruction for Three-dimensional Optoacoustic Tomography

Lu Ding

Vollständiger Abdruck der von der TUM School of Computation, Information and Technology der Technischen Universität München zur Erlangung des akademischen Grades einer

Doktorin der Ingenieurwissenschaften (Dr.-Ing.)

genehmigten Dissertation.

Vorsitz:

Prof. Dr.-Ing. Werner Hemmert

Prüfer der Dissertation:

1. Prof. Dr. Vasilis Ntziachristos
2. Prof. Dr.-Ing. Chrisitan Jirauschek
3. Prof. Dr. Daniel Razansky

Die Dissertation wurde am 27.09.2022 bei der Technischen Universität München eingereicht und durch die TUM School of Computation, Information and Technology am 05.07.2023 angenommen.

Abstract

Optoacoustic tomography (OAT) combines the benefits of optical imaging and ultrasound imaging and has evolved in recent years as one of the most promising biomedical imaging modalities. OAT uses short-pulsed laser light as exciting energy and captures ultrasound waves generated by photon absorption and thermal expansion. The strength of OAT, compared to optical imaging, comes from the fact that the images are reconstructed from ultrasound waves instead of light. Since ultrasound has considerably less scattering and attenuation in tissue, OAT can achieve higher penetration depth. On the other hand, unlike ultrasonic imaging where the contrast is purely based on mechanical properties of the tissue, the contrast for OAT is provided by light absorption. A wide range of endogenous and exogenous contrast agents exist that can generate OAT signals. The range of applications can be further extended by generating multispectral images, i.e., by taking several images corresponding to different wavelengths of the laser pulse. Multi-spectral images can be unmixed to separate agents featuring distinctive absorption spectra, thus enabling unique functional and molecular imaging applications.

There are different state-of-the-art methods to reconstruct the map of absorbed light energy from the captured ultrasound signals. The most commonly used methods are the back-projection algorithms and the model-based (iterative) algorithms. The back-projection algorithm is a reconstruction method derived from the analytical solution of the wave equation. It has relatively low computational complexity and is thus widely used in high data throughput and real-time applications. The major drawback of the back-projection algorithm is that it cannot take general acquisition geometries into account, for example those used for hand-held devices. This leads to more reconstruction artifacts and poor image quality in those limited-view scenarios. Model-based reconstruction algorithms, on the other hand, are iterative reconstruction algorithms based on the inversion of a mathematical forward model of the wave propagation. Model-based algorithms can handle arbitrary acquisition geometries, but have a higher computational complexity.

In this work, novel algorithms are presented that improve upon the state-of-the-art on two main criteria: the computational complexity and the image quality. The complexity of the model-based reconstruction algorithm is reduced by introducing a novel discretization method and which leads to an efficient approach for on-the-fly calculation of the model matrix. The new algorithm can be easily parallelized on the graphics processing unit (GPU), which makes the model-based reconstruction algorithm applicable to three-dimensional imaging setups. It is demonstrated that the complexity can be further reduced by considering a rotationally symmetric interpolation kernel and factoring the model matrix into a maximally sparse matrix and a separate convolution with the impulse response. With these simplifications, which have only marginal impact on the image quality, the complexity per iteration is similar to that of the back-projection algorithm, i.e., it is able to reconstruct three-dimensional, high-resolution images in real time. Based on this efficient reconstruction method, performance is further enhanced by reducing artifacts in the reconstructed images. It is demonstrated that smearing artifacts can be significantly reduced by modeling the transducer shape using a small number of points. Finally, a projected conjugate gradient algorithm is developed for efficient non-negative constrained model-based reconstruction. That is, an algorithm that allows to reconstruct images without any physically implausible negative values. Further investigations are also conducted on how to apply the non-negative constraint reconstruction method in the multispectral imaging scenario.

Publication Record

This thesis is a publication-based dissertation, which is based on the following publications.

1. **Lu Ding**, X. Luis Deán-Ben, and Daniel Razansky. Real-time model-based inversion in cross-sectional optoacoustic tomography. *IEEE Transactions on Medical Imaging*, 35(8):1883–1891, Aug 2016

2. **Lu Ding**, X Luis Dean Ben, and Daniel Razansky. Efficient three-dimensional model-based reconstruction scheme for arbitrary optoacoustic acquisition geometries. *IEEE Transactions on Medical Imaging*, 2017

3. **Lu Ding**, Daniel Razansky, and Xosé Luís Deán-Ben. Model-based reconstruction of large three-dimensional optoacoustic datasets. *IEEE Transactions on Medical Imaging*, 39(9):2931–2940, 2020

4. Yiyong Han, **Lu Ding**, Xosé Luis Deán Ben, Daniel Razansky, Jaya Prakash, and Vasilis Ntziachristos. Three-dimensional optoacoustic reconstruction using fast sparse representation. *Optics Letters*, 42(5):979–982, 2017

5. **Lu Ding**, X Luís Deán-Ben, Christian Lutzweiler, Daniel Razansky, and Vasilis Ntziachristos. Efficient non-negative constrained model-based inversion in optoacoustic tomography. *Physics in medicine and biology*, 60(17):6733, 2015

6. **Lu Ding**, Xose Luis Dean Ben, Neal C Burton, Robert W Sobol, Vasilis Ntziachristos, and Daniel Razansky. Constrained inversion and spectral unmixing in multispectral optoacoustic tomography. *IEEE Transactions on Medical Imaging*, 2017

7. X Luís Deán-Ben, **Lu Ding**, and Daniel Razansky. Dynamic particle enhancement in limited-view optoacoustic tomography. *Optics Letters*, 42(4):827–830, 2017

8. Ghayathri Balasundaram, **Lu Ding**, Xiuting Li, Amalina Binte Ebrahim Attia, Xose Luis Dean-Ben, Chris Jun Hui Ho, Prashant Chandrasekharan, Hui Chien Tay, Hann Qian Lim, Chee Bing Ong, Ralph P. Mason, Daniel Razansky, and Malini Olivo. Noninvasive anatomical and functional imaging of orthotopic glioblastoma development and therapy using multispectral optoacoustic tomography. *Translational Oncology*, 11(5):1251–1258, 2018

Contents

Part I

Introduction and Background

Chapter 1

Introduction

1.1 Biomedical Imaging

Biomedical imaging is an invaluable tool for both disease diagnostics and biological/medical research. So it is unsurprising that the last decades saw a growing number of biomedical imaging modalities.

Some imaging modalities such as X-ray imaging are mainly used to gather *structural* (anatomical) information. However, most image modalities also gather *functional* (physiological) information, often with the help of contrast agents. For example, in computed tomography (CT) perfusion imaging, a contrast agent can be used to assess the flow through blood vessels [67]. Certain imaging modalities are even capable of imaging at the *molecular* level. In optical imaging, for example, fluorescent and bioluminescent proteins are used to track specific molecular targets [36].

When comparing imaging modalities, the following key performance characteristics are often considered.

- *Spatial resolution* indicates the ability to differentiate two close objects. It can range from tens of nanometers with some optical imaging methods to centimeters for whole body scans.

- *Penetration depth* refers to the maximum depth in biological tissue from which reliable information can still be collected. For most imaging modalities, there is a roughly inverse proportional relation between the spatial resolution and the penetration depth. That is, modalities with a high resolution, such as microscopy, are only capable of superficial imaging, while modalities with lower resolution, such as CT, are able to perform whole body scans.

- *Contrast* refers to the ability to differentiate different substances in

tissue. For example, magnetic resonance imaging (MRI) offers much better soft tissue contrast than CT.

- *Sensitivity* denotes the minimum concentration of a target substance that can still be detected by the imaging modality.
- *Temporal resolution* refers to the frequency in which consecutive images can be taken. Obtaining a sequence of images is mainly interesting for functional imaging and the required temporal resolution depends on the time behavior of the process or effect under observation.

Of course, there are other characteristics which play an important role in practice, such as the health hazard and the cost.

In the following, a short overview of the most important imaging modalities is provided.

Radiography

Radiography uses X-rays or similar ionizing radiation that travels through the tissue in straight lines to generate images of the internal structure. The contrast is created by difference in attenuation/absorption of the radiation for different substances. As a consequence, there is a very clear contrast between the soft tissue and the higher density bones, but a poor contrast between different soft tissues. Radiography includes the classical two-dimensional projection radiography, but also the more recent three-dimensional CT imaging.

Magnetic Resonance Imaging

Magnetic resonance imaging (MRI) uses magnetic fields to excite hydrogen atoms (in water and other molecules) in the tissue which will then generate a detectable, spatially encoded signal. This enables reconstruction of anatomical images of water and fat, yielding an excellent soft-tissue contrast (as opposed to CT). The main drawbacks of MRI are the relatively low spatial and temporal resolution, low sensitivity to contrast agents, as well as the cost.

Ultrasonic Imaging

In ultrasonic imaging, short narrow-band sound wave pulses are transmitted into the tissue and the reflection is captured to reconstruct a structural image of the tissue. Ultrasonic imaging has good spatial and temporal resolution, but relatively poor soft-tissue contrast, since reflections only happen between

acoustically mismatched areas. Doppler shifts in the received signals can be used to detect flow and motion. Due to its low cost, portability, and real-time nature, ultrasonic imaging is a ubiquitous imaging technology.

Nuclear Imaging

In nuclear imaging, a radioactive tracer is taken internally and the emitted radiation is captured by external sensors to form an image of the tracer location in the tissue. Nuclear imaging offers high sensitivity for functional imaging, but sees limited use due to low resolution, high cost and the use of ionizing radiation.

Optical Imaging

Optical imaging uses visible light to create high resolution images. Modalities range from cameras and microscopy to more sophisticated techniques like optical coherence tomography. Different contrast agents like fluorescent dyes and nano-particles can be used with optical imaging. The main limitation is the low penetration depth of a few tens of micrometers. In principle, imaging with higher penetration depth is possible but with severe impact on the possible resolution.

Optoacoustic Tomography

Optoacoustic tomography (OAT), which this thesis focuses on, is a biomedical imaging modality that has gained a lot of popularity in recent years. OAT is based on the photophonic effect [61], which describes the energy conversion mechanism from optical to acoustic energy when a light-absorbing sample is illuminated with amplitude-modulated light. Specifically, biomedical OAT is based on tissue excitation with a short laser pulse with typical durations of a few nanoseconds. The light energy is absorbed by tissue chromophores (light absorbing substances), which leads to thermal expansion of the tissue. The pressure (ultrasound) waves generated by the thermal expansion are then captured by ultrasonic transducers. Finally, a signal processing algorithm is applied to reconstruct the light absorption map from the measured ultrasonic signals.

Since the image is reconstructed from pressure waves, it is not required that the light to travel in straight paths to achieve good resolution. Thus, much higher imaging depth can be achieved compared to purely optical imaging methods such as confocal microscopy, two-photon microscopy, or optical coherence tomography. On the other hand, contrary to ultrasonic imaging,

the contrast is provided by light absorption as opposed to contrast purely based on mechanical properties of the tissue. The primary contrast comes from optical absorption from tissue components such as oxygenated and deoxygenated hemoglobin, melanin, bilirubin, lipids and water [56]. The strong absorption of the oxygenated and deoxygenated hemoglobin allows visualization of blood vessels with sub-millimeter resolution at centimeter-scale depth in highly scattering tissue [41, 35]. Furthermore, OAT can detect the same fluorescent agents used in optical fluorescence imaging. These fluorescent dyes, and an additional wide range of other exogenous substances, significantly enhance the contrast of OAT images. The range of applications can be further extended by generating multispectral images, i.e., by taking several images corresponding to different wavelengths of the laser pulse. Multispectral images can be unmixed to separate agents featuring distinctive absorption spectra, thus enabling unique functional and molecular imaging applications [49, 17, 7, 19]. For example, multispectral optoacoustic tomography (MSOT) can detect the oxygen saturation and concentration of hemoglobin by separating oxygenated and deoxygenated hemoglobin.

In summary, OAT capitalizes on the combination of optics and ultrasound to obtain non-invasive, high-resolution, anatomical, functional and molecular, images of biological tissues, while not being affected by the depth-limitation of classical optical imaging. Basically, OAT combines best from both worlds: the high spatial resolution and penetration depth from ultrasound imaging and the high contrast and rich information from optical imaging [64, 48].

While the promising properties of OAT have fostered a growing use in biomedical research, there are nevertheless several challenges concerning the signal-processing and reconstruction of the light absorption images or images of absorber concentrations. Arguably, the major challenge of OAT is to obtain accurate (quantitative) reconstruction with reasonable computational complexity and memory overhead. There are two types of widely used reconstruction methods, namely back-projection [69] and model-based (iterative) algorithms [37, 53, 52, 60, 43]. The back-projection method is derived from the analytical solution of the wave equation. It has relatively low complexity but cannot take general acquisition geometries into account, for example those used for hand-held devices, and leads to limited-view artifacts in the reconstructed images. Nevertheless, it is widely used due to its fast computational time. Model-based reconstruction, on the other hand, uses iterative algorithms that invert the forward propagation model. Model-based algorithms can handle arbitrary acquisition geometries but have a high computational complexity, which hinders their application to large-scale, three-dimensional imaging scenarios or real-time imaging, especially for multispectral scenarios.

1.2 Objective and Outline

There are two major objectives of this thesis. The first is to reduce the complexity of the model-based method by introducing some approximations and simplifications without deteriorating the image quality. The target is to design algorithms with complexity similar to the back-projection method.

The second objective is to remove some of the artifacts that still remain when using model-based reconstruction. This thesis focuses on handling negative values and finite transducer shapes. Of course, the goal is to remove/reduce the artifacts without a significant increase in complexity.

The thesis is structured as follows: Chapter 2 describes in detail the practical and theoretical background of OAT and introduces the state-of-the-art reconstruction methods. The second part of the thesis (Part II) gives a summary of each work published by the author and concludes the thesis with Chapter 11. The reprints of the respective work are included in the appendix with permission from the publishers.

Chapter 2

Fundamentals of Optoacoustic Tomography

In this chapter, the theoretical and practical fundamentals of OAT are presented. As explained in Chapter 1, OAT relies on the photophonic effect. The process of creating an image can be divided into three steps

- Excitation of the tissue with a short laser pulse (this is sometimes referred to as *time-domain OAT*). The light travels through the tissue and is absorbed by chromophores. The absorbed energy increases the temperature of the tissue and leads to thermal expansion.

- Acquisition of pressure waves triggered by the thermal expansion of the tissue.

- Reconstruction of the map of absorbed light energy from the acquired ultrasonic signals. Further, if it is possible to predict how the light travels through the tissue, the distribution of the absorption coefficients can be inferred. In case of multispectral imaging, this allows to reconstruct an image of the concentrations of absorbing substances (for example oxygenated and deoxygenated hemoglobin).

Fig. 2.1 shows a simple sketch of a two-dimensional OAT setup and depicts the two stages of the acquisition process.

In the next section, the theoretical background and the mathematical model for both stages of the acquisition process are explained. This system model is the foundation for the image reconstruction algorithms described subsequently. The final part of this chapter gives a short description of the different imaging systems and the experimental methods used for this thesis, as well as an overview of the different applications of OAT.

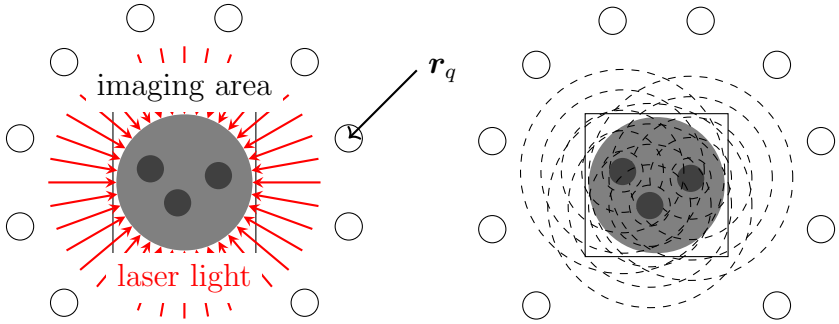

Figure 2.1: Sketch of a two-dimensional imaging setup with an incomplete ring of transducers (at positions $\boldsymbol{r}_q$) around a quadratic imaging area. On the left is the first stage of the acquisition process, namely illuminating the tissue with laser light. On the right are the resulting acoustic waves captured by the ultrasonic transducers.

2.1 Mathematical System Model

The foundation for image reconstruction in OAT is a mathematical description, a *forward model*, of the generation of pressure waves from absorbed light in the tissue. Once such a model is built, it can be inverted analytically or numerically to reconstruct a map of absorbed light energy or the actual concentration of light absorbing substances in the tissue.

In principle, both steps of the signal acquisition process need to be modeled. First, a model is required for the propagation of the laser light in the tissue (the light fluence) to know how much light energy arrives at each location. Secondly, a model is required for the propagation of pressure waves resulting from the absorbed light. The first step (modeling the light fluence) is the more complicated one and, in practice, simplifying assumptions are often used.

The light fluence at location $\boldsymbol{r}$ and time t is denoted as $\Phi(\boldsymbol{r}, t)$. It is assumed that the fluence can be separated into $\Phi(\boldsymbol{r}, t) = \phi(\boldsymbol{r})g(t)$, where $\phi(\boldsymbol{r})$ describes the instantaneous light fluence and $g(t)$ describes the shape of the laser pulse. The light fluence in the tissue $\phi(\boldsymbol{r})$ depends on the absorption coefficients $\mu_a(\boldsymbol{r})$ and scattering coefficients $\mu_s(\boldsymbol{r})$. If those coefficients are known for all locations (as well as the intensity of the incident laser light), the fluence can be calculated using numerical methods, for example with a Monte-Carlo simulation. The challenge is that those coefficients are unknown and, in fact, the map of absorption coefficients $\mu_a(\boldsymbol{r})$ is exactly what needs to be reconstructed in the end.

The absorbed energy is given by

$$H(\boldsymbol{r},t) = \Phi(\boldsymbol{r},t)\mu_a(\boldsymbol{r}) = \phi(\boldsymbol{r})\mu_a(\boldsymbol{r})g(t) = h(\boldsymbol{r})g(t). \tag{2.1}$$

This absorbed energy leads to a temperature increase and a resulting pressure wave that can be detected by ultrasonic transducers.

A lot of work in OAT focuses on the reconstruction of the absorbed energy $h(\boldsymbol{r})$ and does not consider the absorption coefficients $\mu_a(\boldsymbol{r})$ or the underlying concentration of the light absorbing substances. However, when doing multispectral imaging, it is essential to get the absorption coefficients, which are a linear combination of the concentrations $c_s(\boldsymbol{r})$, $s = 1, \ldots, S$ of chromophores in the tissue [9, 1]. That is,

$$\mu_a(\boldsymbol{r}) = \sum_{s=1}^{S} c_s(\boldsymbol{r})\alpha_s, \tag{2.2}$$

where α_s is the molar absorption coefficient of chromophore s for the given laser wavelength. To reconstruct the concentrations $c_s(\boldsymbol{r})$, data is acquired for multiple wavelengths since the absorption coefficients are wavelength dependent. More details on the reconstruction are given in the next section.

In the following derivation, the tissue is assumed to be acoustically homogeneous and isotropic, i.e., the properties determining the propagation of acoustic waves (such as the speed of sound) are the same everywhere and independent of direction. Additionally, thermal diffusion is ignored in the tissue, since the time scale for thermal relaxation is typically much larger than the time it takes for the pressure waves to propagate through the imaging region. In other words, it is assumed that *thermal confinement* holds. Under thermal confinement, the change in temperature $T(\boldsymbol{r},t)$ at location $\boldsymbol{r}$ and time t is directly proportional to the absorbed energy $H(\boldsymbol{r},t)$, i.e.,

$$\rho C_{\mathrm{V}} \frac{\partial}{\partial t} T(\boldsymbol{r},t) = H(\boldsymbol{r},t), \tag{2.3}$$

where ρ is the density of the tissue and C_V is the specific heat capacity at constant volume.

The wave equation that relates the pressure waves to the change in temperature can be derived by combining the linearized equations for the conservation laws of mass and momentum as well as some identities known from thermodynamics. The equations given here are already simplified by dropping terms that are negligible in the typical OAT scenario because of the low amplitude of the pressure wave. For more details see [63, 61].

The conservation of mass in the tissue is described approximately by

$$\frac{\partial}{\partial t}\rho(\boldsymbol{r},t) = -\rho(\boldsymbol{r},0)\nabla^{\mathrm{T}}\boldsymbol{u}(\boldsymbol{r},t), \tag{2.4}$$

where $\boldsymbol{u}(\boldsymbol{r},t)$ denotes the particle velocity and $\rho(\boldsymbol{r},t)$ denotes the density of the tissue. The baseline density at time zero can be used on the right hand side because of the small amplitude of the pressure wave.

The conservation of momentum (implied by Newton's laws of motion) in the tissue is described approximately by

$$\rho(\boldsymbol{r},0)\frac{\partial}{\partial t}\boldsymbol{u}(\boldsymbol{r},t) = -\nabla p(\boldsymbol{r},t), \tag{2.5}$$

where $p(\boldsymbol{r},t)$ denotes the pressure fluctuation in the medium. The force acting on the tissue is the negative gradient of the pressure.

Taking the time derivative of (2.4) and incorporating (2.5) leads to

$$\frac{\partial^2}{\partial t^2}\rho(\boldsymbol{r},t) = \rho(\boldsymbol{r},0)\nabla^{\mathrm{T}}\frac{\nabla p(\boldsymbol{r},t)}{\rho(\boldsymbol{r},0)}. \tag{2.6}$$

The fluctuation of the density can be expressed with the thermodynamic relation

$$\frac{\partial}{\partial t}\rho(\boldsymbol{r},t) = \rho(\boldsymbol{r},0)\kappa\frac{\partial}{\partial t}p(\boldsymbol{r},t) - \rho(\boldsymbol{r},0)\beta\frac{\partial}{\partial t}T(\boldsymbol{r},t), \tag{2.7}$$

where $T(\boldsymbol{r},t)$ denotes the temperature in the tissue and the coefficients κ and β denote the isothermal compressibility and the thermal coefficient of volume expansion, respectively. Incorporating (2.7) into (2.6) yields the wave equation

$$\rho(\boldsymbol{r},0)\kappa\frac{\partial^2}{\partial t^2}p(\boldsymbol{r},t) - \rho(\boldsymbol{r},0)\nabla^{\mathrm{T}}\frac{\nabla p(\boldsymbol{r},t)}{\rho(\boldsymbol{r},0)} = \rho(\boldsymbol{r},0)\beta\frac{\partial^2}{\partial t^2}T(\boldsymbol{r},t). \tag{2.8}$$

Assuming a uniform density ρ, this simplifies to

$$\rho\kappa\frac{\partial^2}{\partial t^2}p(\boldsymbol{r},t) - \nabla^2 p(\boldsymbol{r},t) = \rho\beta\frac{\partial^2}{\partial t^2}T(\boldsymbol{r},t). \tag{2.9}$$

Finally, with thermal confinement, incorporating (2.3) leads to

$$\frac{\partial^2}{\partial t^2}p(\boldsymbol{r},t) - c^2\nabla^2 p(\boldsymbol{r},t) = \Gamma\frac{\partial}{\partial t}H(\boldsymbol{r},t), \tag{2.10}$$

where the dimensionless Grüneisen parameter

$$\Gamma = \frac{\beta}{\rho\kappa C_V}$$

describes the efficiency of the conversion of absorbed energy to pressure.

Analogously to thermal confinement, it is also assumed that *stress confinement* holds. That is, it is assumed that the duration of the laser pulse is much shorter than the travel time of acoustic waves through the imaging volume. Thus, the short term laser pulse can be approximated by a Dirac delta $g(t) = \delta(t)$ and consequently $H(\boldsymbol{r}, t) = h(\boldsymbol{r})\delta(t)$, which leads to the initial value problem

$$\frac{\partial^2}{\partial t^2} p(\boldsymbol{r}, t) - c^2 \nabla^2 p(\boldsymbol{r}, t) = 0 \tag{2.11}$$

with initial values

$$p(\boldsymbol{r}, 0) = \Gamma h(\boldsymbol{r}) \quad \text{and} \quad \frac{\partial}{\partial t} p(\boldsymbol{r}, t)|_{t=0} = 0. \tag{2.12}$$

The forward solution of this initial value problem is given by the Poisson-type integral [12]

$$p(\boldsymbol{r}, t) = \frac{\Gamma}{4\pi c} \frac{d}{dt} \frac{1}{ct} \int_{S(\boldsymbol{r}, ct)} h(\boldsymbol{r}') d\boldsymbol{r}' \tag{2.13}$$

where $S(\boldsymbol{r}, d)$ denotes the spherical surface with center $\boldsymbol{r}$ and radius d.

In the case of an ideal transducer q that samples pressure at a single point in space, the (discrete) received signal is simply given by

$$u_q[k] = p(\boldsymbol{r}_q, t_k) \tag{2.14}$$

where $\boldsymbol{r}_q$ is the position of transducer q and t_k, $k = 1, \ldots, T$ denote the sampling instances. In certain scenarios, the transducer shape should be modeled to obtain accurate results [52, 47, 39]. The signal $u_q[k]$ received by a finite-size transducer q can be expressed as

$$u_q[k] = \int_{\Phi_q} p(\boldsymbol{r}, t_k) d\boldsymbol{r} \tag{2.15}$$

where Φ_q denotes the surface of the transducer. Note that (2.15) is still an approximation of the actually measured signal since the wave propagation effects inside the transducer are not taken into account.

The goal of a reconstruction algorithm is then to find the distribution of absorbed energy $h(\boldsymbol{r})$ (or equivalently, the initial pressure distribution $p(\boldsymbol{r}, 0)$) from the received signals $u_q[k]$. If the fluence $\phi(\boldsymbol{r})$ can be approximated, the absorption map can be obtained by $\mu_a(\boldsymbol{r}) = h(\boldsymbol{r})/\phi(\boldsymbol{r})$. This correction, which is often neglected, is nevertheless essential to get quantitative images. The state-of-the-art of reconstruction algorithms is described in the next section.

2.2 Reconstruction Methods

Early approaches for image reconstruction in OAT, such as the back-projection algorithms, are based directly on the continuous model [69]. Back-projection formulas assume a continuous, closed detection surface, which allows to invert the continuous model in (2.13) analytically. The time-domain solution is given by

$$p(\boldsymbol{r}, 0) = \int_{\Omega_0} b(\boldsymbol{r}_0, \|\boldsymbol{r} - \boldsymbol{r}_0\|/cd)\Omega_0(\boldsymbol{r})/\Omega_0 \tag{2.16}$$

where Ω_0 is a solid angle of the whole detection surface S_0 and $d\Omega_0(\boldsymbol{r})/\Omega_0$ is the solid angle of a detection element dS_0 with respect to the point $\boldsymbol{r}$. The back-projection term is given by

$$b(\boldsymbol{r}, t) = 2p(\boldsymbol{r}, t) - 2t\frac{\partial}{\partial t}p(\boldsymbol{r}, t). \tag{2.17}$$

In practice, it is only possible to capture discrete samples in space and time of the pressure waves. Thus, the integral (2.16) needs to be discretized and the derivative in (2.17) needs to be numerically approximated.

The main problem with the back-projection algorithms is the assumption of a closed detection surface, which often is not available in practice. For example, hand-held devices intended to be used for clinical applications often only have a limited field-of-view. For such geometries, the back-projection algorithms produces smearing artifacts in the reconstructed absorption maps, i.e., the shapes of absorbing objects become distorted. In this case, reconstruction methods that make no assumption regarding the detection geometry, such as the model-based approaches, yield better results.

Model-based methods approximate the linear, continuous to discrete model ((2.13) and (2.15)) by a linear, discrete to discrete forward model

$$\boldsymbol{u} = \boldsymbol{A}\boldsymbol{h}, \tag{2.18}$$

where the model matrix $\boldsymbol{A}$ maps the discretized absorption map $\boldsymbol{h}$ onto the time-sampled received signals $\boldsymbol{u}$ ($\boldsymbol{u}$ is formed simply by stacking all the received signals $u_q[k]$ into a single vector).

Some methods for model-based reconstruction generate the model matrix $\boldsymbol{A}$ offline (since it is static for a fixed acquisition geometry) and use the stored matrix when actually running image reconstruction (e.g. [14]). This approach can be problematic for three-dimensional setups, where, even though $\boldsymbol{A}$ is a sparse matrix, the memory overhead might be too large to run the reconstruction on the GPU.

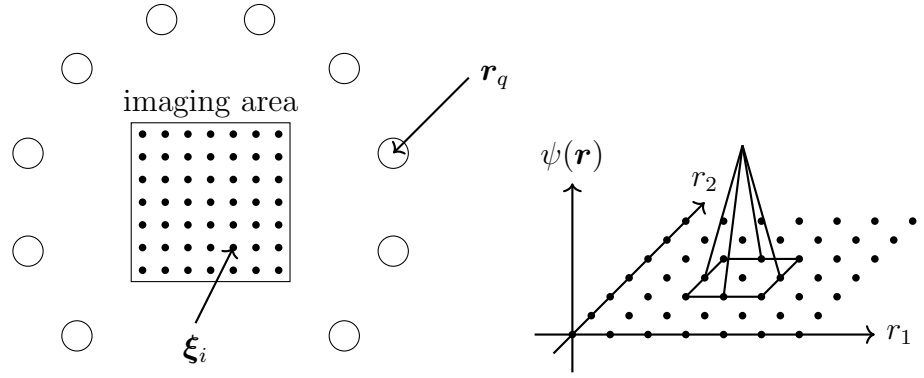

Figure 2.2: Illustration of the discretization of the imaging area (with pixel positions $\boldsymbol{\xi}_i$) on the left and bilinear interpolation kernel on the right. The bilinear interpolation kernel is the equivalen of the trilinear interpolation kernel given in (2.20) for a two-dimensional setup.

Another approach is to calculate the elements of the model matrix on-the-fly [58]. To form a discrete-to-discrete model for these *matrix free* approaches, the absorption map $h(\boldsymbol{r})$ is typically approximated by [58, 59]

$$h(\boldsymbol{r}) \approx \sum_{i=1}^{M} \psi(\boldsymbol{r} - \boldsymbol{\xi}_i)[\boldsymbol{h}]_i \tag{2.19}$$

where $\boldsymbol{\xi}_i \in \mathbb{R}^3$ enumerates the points of the three-dimensional Cartesian grid that covers the imaging area and M is the total number of pixels used for reconstruction. For example, to reconstruct an image with resolution of $100 \times 100 \times 100$ voxels, $M = 10^6$. The function $\psi(\boldsymbol{r})$ is an interpolation kernel (sometimes also called extension function). For example, the trilinear interpolation kernel is given by

$$\psi_{\text{tri}}(\boldsymbol{r}) = \begin{cases} (1 - |r_1|/d_{\text{grid}})(1 - |r_2|/d_{\text{grid}})(1 - |r_3|/d_{\text{grid}}) & \text{for } \|\boldsymbol{r}\|_\infty \leq d_{\text{grid}} \\ 0 & \text{else} \end{cases}, \tag{2.20}$$

where d_{grid} is the distance between neighboring grid points. Another example would be the simple sphere

$$\psi_{\text{sph}}(\boldsymbol{r}) = \begin{cases} 1 & \text{for } \|\boldsymbol{r}\|_2 \leq a \\ 0 & \text{else} \end{cases} \tag{2.21}$$

where a is the sphere radius (which should be picked based on the grid spacing d_{grid}). Fig. 2.2 illustrates the discretization of the imaging area and the bilinear interpolation kernel used for the simplified two-dimensional setup.

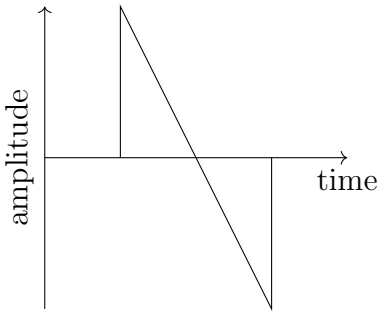

Figure 2.3: Acoustic impulse response of an excited sphere.

The approximation of the continuous absorption map in (2.19) can be plugged into the continuous model (2.13) to get a linear, discrete-to-discrete model. The entries of the model matrix $\boldsymbol{A}$ are then the time-sampled impulse responses for each pixel transducer pair. For example, if a sphere (cf. (2.21)) is placed at each pixel position, the impulse response has the typical N-shape [63] depicted in Fig. 2.3.

While this basic approach (of using interpolation kernels for the discretization) can be found in several algorithms in literature, there are differences in which kernels are used and in how the coefficients of the model matrix are actually computed on-the-fly for those specific kernels [58, 59, 14]. One contribution of this thesis is to present a novel approach for the coefficient calculation that works for any bounded interpolation kernel and allows for very efficient implementation of iterative reconstruction methods.

Once the discrete linear model is formulated, an estimate $\hat{\boldsymbol{h}}$ of the discrete absorption vector $\boldsymbol{h}$ can be calculated from a measured pressure signal $\boldsymbol{p}$ with a simple least squares approach

$$\hat{\boldsymbol{h}} = \underset{\boldsymbol{h}}{\operatorname{argmin}} \|\boldsymbol{A}\boldsymbol{h} - \boldsymbol{p}\|^2. \tag{2.22}$$

The well-known solution to the least squares problem is given by

$$\hat{\boldsymbol{h}} = \boldsymbol{A}^{\dagger}\boldsymbol{p} \tag{2.23}$$

where $\boldsymbol{A}^{\dagger}$ denotes the Moore-Penrose pseudo-inverse of $\boldsymbol{A}$. Since the model matrix is huge, even for two-dimensional geometries, calculating the solution directly via the pseudo-inverse is usually not feasible. Instead, iterative methods, e.g. the Krylov-subspace method LSQR [42], can be used. The LSQR method converges super-linearly towards the optimal solution and only requires the evaluation of one matrix vector product involving $\boldsymbol{A}$ and one matrix vector product involving $\boldsymbol{A}^{\mathrm{T}}$ in each iteration. These matrix-vector products dominate the complexity of our model-based reconstruction.

Model-based reconstruction also allows to add regularization terms and constraints in a straightforward matter. For example, the standard Tikhonov regularization can be added to the cost function in (2.22). The algorithm can also be adopted to enforce certain sparsity property in the resulting images [25, 51]. Non-negative constraints enforcing physically meaningful positive values in the reconstructed absorption distribution have also been shown to be very useful [21].

State-of-the-art model-based inversion requires a significantly higher computational complexity and memory overhead compared to back-projection methods. Our novel approaches, which are included in Part II, help to close that gap.

2.3 Multispectral Unmixing

For multispectral unmixing, data are acquired using different laser wavelengths in rapid succession [9, 1]. That is, multiple absorption maps $\boldsymbol{h}_\ell$, $\ell = 1, \ldots, L$ can be reconstructed with

$$\boldsymbol{h}_\ell = \boldsymbol{\phi}_\ell \odot \boldsymbol{\mu}_\ell, \tag{2.24}$$

where $\odot$ denotes element-wise multiplication and

$$\boldsymbol{\mu}_\ell = \sum_{s=1}^{S} \boldsymbol{c}_s \alpha_{s\ell}. \tag{2.25}$$

Each index ℓ corresponds to a distinct wavelength λ_ℓ. Analogously to how $\boldsymbol{h}$ is the discretization of $h(\boldsymbol{r})$, the vectors $\boldsymbol{\mu}$ and $\boldsymbol{c}_s$ are the discretizations of the continuous spatial distribution of the absorption coefficient $\mu_a(\boldsymbol{r})$ and the concentrations of the chromophores $\boldsymbol{c}_s(\boldsymbol{r})$, respectively (cf. (2.2)).

Defining the matrices

$$\boldsymbol{H} = [\boldsymbol{h}_1, \ldots, \boldsymbol{h}_L], \quad \boldsymbol{C} = [\boldsymbol{c}_1, \ldots, \boldsymbol{c}_S], \quad \boldsymbol{\Phi} = [\boldsymbol{\phi}_1, \ldots, \boldsymbol{\phi}_L] \tag{2.26}$$

and the matrix $\boldsymbol{M} \in \mathbb{R}^{S \times L}$ with

$$[\boldsymbol{M}]_{s\ell} = \alpha_{s\ell}, \tag{2.27}$$

(2.24) can be reformulated as

$$\boldsymbol{H} = \boldsymbol{\Phi} \odot (\boldsymbol{C}\boldsymbol{M}). \tag{2.28}$$

To reconstruct $\boldsymbol{C}$ from $\boldsymbol{H}$, the linear least-squares problem

$$\min_{\boldsymbol{C}} \|\boldsymbol{H} - \boldsymbol{\Phi} \odot (\boldsymbol{C}\boldsymbol{M})\|^2 \tag{2.29}$$

should be solved. The optimizer is given by

$$\widehat{\boldsymbol{C}} = (\boldsymbol{H} \oslash \boldsymbol{\Phi})\boldsymbol{M}^{+} \tag{2.30}$$

where $\oslash$ denotes element-wise division. Since $\boldsymbol{M}$ is typically a small matrix, $\widehat{\boldsymbol{C}}$ can be calculated directly.

The typical approach is to separate the estimation of the absorption maps $\boldsymbol{h}_\ell$ from the unmixing to get the concentrations $\boldsymbol{c}_s$ (see for example [9]). One contribution of this thesis is looking into ways to combine those steps, especially for the case where non-negative constraints are imposed on the concentrations and the absorption maps.

For multispectral unmixing, it is especially important to take the fluence into account, because the penetration depth of the laser light is different at different wavelengths. If the difference in light fluence is ignored, estimates of the chromophore concentrations become inaccurate. This effect is called *spectral coloring*.

2.4 Chromophores and Contrast Agents

The detection of multiple chromophores is enabled by the multispectral imaging approach described in the previous section. The excitation wavelengths should be selected based on the spectra of the target chromophores. As mentioned before, OAT can detect the same fluorescent agents as the ones used in optical fluorescence imaging. But several intrinsically present chromophores are also of interest.

Examples for relevant intrinsic chromophores include oxygenated and deoxygenated hemoglobin, lipid, fat, water and melanin [74]. Optoacoustic imaging based on intrinsic contrast chromophores enables many biomedical applications. For example, from the concentrations of oxygenated and deoxygenated hemoglobin, the oxygen saturation can be calculated. In general, many diseases cause changes in tissue composition, which can be detected and quantified with MSOT.

Externally administered imaging agents can further enhance the contrast of optoacoustic imaging. Common exogenous agents that have been approved for human use include fluorescent dyes such as indocyanine green (ICG) [65], methylene blue [54], and Evans blue [72]. Other fluorescent dyes have been evaluated in animal models, e.g., IRDye800CW [34] and AlexaFluor750 [3].

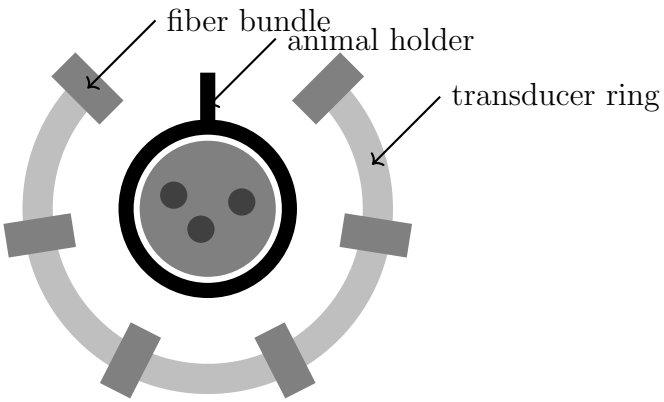

Figure 2.4: Sketch of the MSOT system. It consists of a ring of transducers around an animal holder with a field-of-view of 270 degrees. Fiber bundles provide laser illumination of a tissue cross-section from different directions. The setup allows to capture two-dimensional multispectral images.

These fluorescent dyes are not targeting any specific molecular processes, but can be functionalized through combination with other targeting probes [71] Another class of externally administered contrast agents is nanoparticles, such as gold nanoparticles or carbon nanotubes. A detailed overview of available exogenous contrast agents can be found in [74].

Cells can also be genetically engineered to produce proteins with fluorescent tags such as the green fluorescent protein (GFP). The peak absorption of GFP is at a wavelength of 488 nm, at which light has a limited penetration depth in tissue. Nowadays, there are many derivatives of GFP and other fluorescent proteins with peak absorption at higher wavelengts, which might are more suitable for OAT [50, 30].

2.5 Hardware Setups and Methodology

For preclinical studies, MSOT is particularly interesting because of the wide range of applications that are enabled by its ability to separate chromophores with different absorption spectra. There are several commercially available systems for MSOT imaging of small animals [68].

For the evaluation of reconstruction algorithms with a two-dimensional setup and spectral unmixing approaches in this thesis, the MSOT256-TF system [49] from iThera is used. Fig. 2.4 shows an illustration of the system. It has a planar acquisition geometry and acquires cross-sectional images. The illumination source is a tunable (680-960nm) short-pulsed ($<$ 10ns) laser. The

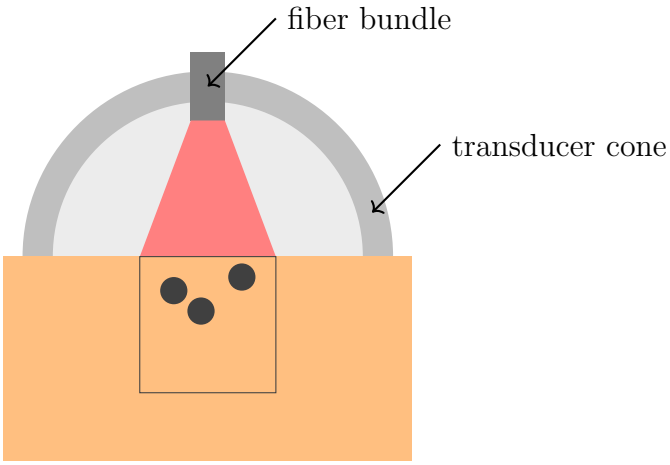

Figure 2.5: Sketch of the handheld CUP system. The transducers are arranged on the inner surface of a half-sphere, leading to a partial field-of-view of the imaging area. With this setup, three-dimensional images of the optical absorption can be reconstructed.

laser beam is guided with 10 fiber bundles to form a ring-shaped illumination on the surface of the imaging sample. An array of 256 cylindrically focused transducers covering 270 degree field-of-view is placed around the sample to capture the generated optoacoustic responses of the imaged cross-section.

The improved reconstruction methods discussed in this thesis are even more relevant for handheld devices used for preclinical and clinical studies. Fig. 2.5 illustrates the typical geometry of the handheld system. An array of adjacent piezoelectric elements is densely distributed on a spherical surface. The illumination source is guided via a fiber bundle through a cylindrical cavity in the transducer array. In this work, several handheld devices are used, which differ in number of transducer elements, central frequency of the transducers and the solid angular coverage. A detailed description of these setups is given in [16].

Since these devices only offer a limited field-of-view, artifacts appear when using the back projection method to reconstruct the light absorption images. However, since it is desirable to have real-time images for a handheld device, state-of-the-art model-based reconstruction is often prohibitively complex.

Many other hardware setups with different trade-offs for imaging depth and resolution can be found in the literature (see e.g. [62] for an overview). Special hardware setups are also needed for specific clinical applications, e.g. breast cancer detection [26, 32], optoacoustic endoscopy [70], and optoacoustic ocular imaging [10].

To evaluate reconstruction algorithms, experiments with tissue mimicking phantoms are often performed. Phantoms are created by molding 1.3% of agar powder (by weight) and 1% intralipid (by volume) to mimic tissue background absorption and scattering properties [28]. For example, for some work presented in this thesis phantoms with embedded micro-spheres were used. By embedding absorbing micro-spheres in a phantom, artifacts in the reconstructed images can be clearly recognized, which makes it convenient to compare the quality between different reconstruction methods.

2.6 Applications

Due to the flexibility of OAT, there are many pre-clinical and clinical applications. OAT provides structural as well as functional/molecular information. As mentioned above, for functional and molecular imaging, it benefits from capturing images at multiple wavelengths to differentiate chromophores. Due to the short acquisition time, OAT can also be used to observe dynamic processes. In the following, several examples for the different types of applications are presented.

For structural images, contrast is provided mostly by hemoglobin in blood vessels. This allows rendering volumetric images of whole mice [15, 49, 4], but also blood vessels in the human body [15, 35] down to single capillaries [38] and cells [57].

With MSOT, oxygenated and deoxygenated hemoglobin can be differentiated, as well as exogenous markers and fluorescent proteins. Thus, the technique can observe blood oxygenation [33], gene expression [50, 30], and tumors targeted by markers [11, 5, 27].

It can observe dynamic processes, such as organ perfusion [6, 18] hemodynamic changes and glucose response of the brain [66, 73, 31], gastric emptying [40], cardiovascular dynamics [18], tumor growth [30, 8], uptake and clearance of exogenous markers [8], as well as neural dynamics [16].

There are many translational studies that try to bring OAT into different clinical applications. There is work on optoacoustic endoscopy [70], imaging of sentinel lymph nodes [55], ocular imaging [10], lipid detection in atherosclerosis plaques [29], guided biopsy [44], and detection of breast cancer [26, 32].

Part II

Publications

Overview

This part of the thesis includes summaries of the relevant work published by the author, where each summary also highlights the contributions of the author.

The publications are not listed in chronological order, but sorted by topic. Firstly, work is presented that relates to fast model-based reconstruction, followed by work on reconstruction with non-negative constraints and quantitative imaging, and finally work highlighting applications of these refined reconstruction approaches. The full publications are included in the appendix (with permission from the publishers).

In the end, the whole thesis is concluded with an outlook to potential future work.

Chapter 3

Real-time Model-based Inversion in Cross-sectional Optoacoustic Tomography

3.1 Summary

In [23], a novel discretization method is introduced for a two-dimensional imaging setup. The discretization is based on the interpolation kernel approach mentioned in Section 2.2. Using the discretized absorption map (2.19) in the continuous forward solution (2.13) leads to a circular integral for a 2D setup, which needs to be solved for each pixel-transducer pair and time instance. The result of these integrals yields the discrete impulse responses for the pixel-transducer pairs.

The integral can be simplified by using a far-field assumption, i.e., it is assumed that the pixel size (the support of the interpolation kernel) is small compared to the distance between pixel and transducer, which is usually the case. This enables calculating prototypes for the pixel to transducer impulse responses, which only depend on the angle of the transducer as seen from the pixel and not on the distance. These impulse-response prototypes are stored in a 2D look-up table (with time and angle dimensions), which is then use for on-the-fly calculation of matrix-vector products involving the model matrix on the GPU.

In this work, the image quality achieved using the proposed approach is compared to state-of-the art model based reconstruction methods. The convergence behavior is also analyzed when the new model is combined with the iterative LSQR algorithm to reconstruct the images. The novel discretization method is evaluated with two different interpolation kernels. The conic ker-

nel is less accurate, but has the advantage that is is rotationally symmetric, i.e., the impulse-response prototype is the same for all angles. Thus, only a one-dimensional look-up table is needed for the on-the-fly calculation of the model matrix.

For the experiments, a small animal optoacoustic tomography system (MSOT256-TF, iThera Medical GmbH, Munich, Germany) is used, which consists of a 256-element arc-shaped array of cylindrically-focused transducers covering 270° around the imaged object. The results showed that for both, the bilinear and the conic interpolation kernel, the image quality is comparable to state-of-the-art methods.

Further investigations indicated that acceptable reconstruction performance can be achieved by running five iterations of the LSQR algorithm. This results in rendering 6 frames per second with the bilinear interpolation kernel and 13 frames per second with the conic interpolation kernel on a AMD Radeon HD 7900 series GPU. Since the model matrix is calculated on the fly, the complexity can be further reduced by reconstructing multiple frames at once. In this case, there is a trade-off between frame-rate and delay. If a delay of one second can be tolerated, the frame-rate increases to 20 frames per second and 27 frames per second for the bilinear and conic interpolation methods, respectively.

The raw acquisition data from the experiments were provided by a colleague. The algorithms were derived by the author of the thesis. The reconstruction with the different methods and the analysis was also done by the author.

3.2 Publication

Lu Ding, X. Luis Deán-Ben, and Daniel Razansky. Real-time model-based inversion in cross-sectional optoacoustic tomography. *IEEE Transactions on Medical Imaging*, 35(8):1883–1891, Aug 2016

Chapter 4

Efficient Three-dimensional Model-based Reconstruction Scheme for Arbitrary Optoacoustic Acquisition Geometries

4.1 Summary

In [20], the results from [23] are extended to a three-dimensional setup. A trilinear interpolation kernel is used for the discretization and an equivalent method for image reconstruction on the GPU is applied.

For a three dimensional setup, on-the-fly calculation of the model matrix is crucial to enable model-based reconstruction. While it is still possible to keep the sparse model matrix in (GPU) memory for two-dimensional reconstruction, the space requirements of up to 300 GB for three dimensions exceed current hardware capabilities.

The impact of modeling of the transducer shape on the image quality is investigated. The circular transducer area is approximated by 24 weighted grid points. Of course, this increases computational cost by a factor of 24 compared to the point-transducer model.

The first results were obtained by numerical simulation. An imaging volume containing several small light-absorbing micro-spheres was simulated. It can be observed that modeling the transducer shape reduces distortion in the shape of the reconstructed micro-spheres, especially for micro-spheres located away from the center of the imaging volume.

These results were confirmed with experiments on a tissue mimicking phantom with embedded absorbing micro-spheres, where artifacts for micro-spheres located near the edge of the imaging volume.

Further experiments imaging blood vessels in a finger, demonstrated the improved image quality of the model-based reconstruction compared to the state-of-the-art back-projection method.

For this work, the algorithms, and analysis were provided by the author of this thesis. Some of the experiments were conducted in collaboration with the co-authors of the paper.

4.2 Publication

Lu Ding, X Luis Dean Ben, and Daniel Razansky. Efficient three-dimensional model-based reconstruction scheme for arbitrary optoacoustic acquisition geometries. *IEEE Transactions on Medical Imaging*, 2017

Chapter 5

Model-based Reconstruction of Large Three-dimensional Optoacoustic Datasets

5.1 Summary

Three-dimensional optoacoustic datasets are in general huge since OAT is able to achieve a high spatial and temporal resolution. Even with the improvement from the previous work in [20], three-dimensional model-based reconstruction for this kind of large-scale datasets requires a long reconstruction time. Therefore, in [24], a rotational-symmetric interpolation kernel is used to further accelerate the reconstruction. In [20], the model matrix is constructed by calculating its non-zero elements using a look-up table. This still requires several calculation steps and look-ups per voxel-transducer pair. In [24], the look-up table is removed by splitting the model-matrix into a cyclic convolution and a maximally sparse matrix, which contains only one non-zero element per pixel-transducer pair.

Furthermore, an alternative reconstruction method is proposed, which simply multiplies the transpose of the model matrix with the acquired signals. That is, a matched filter is applied using the impulse responses for each pixel-transducer pair, which can also be interpreted as an improved discrete back-projection method. In fact, the widely used back-projection method [cf. (2.16)] is essentially a matched filter with an idealized impulse response, that does not take into account the discrete nature of the captured signals or the reconstructed image.

The reconstruction using the proposed algorithms are compared with the previous model-based algorithm and the widely used back-projection algo-

rithm. The results are evaluated in terms of reconstruction quality and speed with three *in vivo* experiments: human finger vasculature scan, mouse whole-body imaging and mouse brain ICG-perfusion.

It is shown that the accelerated model-based reconstruction is able to obtain the same imaging quality with a reconstruction speed up of approximately an order of magnitude. The proposed alternative reconstruction method is slightly inferior in image quality, but it is well-suited for processing of extremely large datasets or real-time imaging.

For this work, the algorithms, and analysis were provided by the author of the thesis. Some of the experiments were conducted in collaboration with the co-authors.

5.2 Publication

Lu Ding, Daniel Razansky, and Xosé Luís Deán-Ben. Model-based reconstruction of large three-dimensional optoacoustic datasets. *IEEE Transactions on Medical Imaging*, 39(9):2931–2940, 2020

Chapter 6

Three-dimensional Optoacoustic Reconstruction Using Fast Sparse Representation

6.1 Summary

In [25], our previous work from [20] was extended by adding sparsity inducing regularization terms. That is, an L1 penalty term is added to the cost function in (2.22). The L1 penalty is not applied directly to the image but a representation of the image in a different basis. This basis transform should lead to a sparse representation for typical images and should require a low computational complexity. A popular choice is the wavelet transform, which was also used in this work.

Results obtained using the back-projection algorithm, the model-based algorithm with L2 regularization and two model-based algorithm with L1 regularization are compared with simulation data and *in vivo* human palmar arch vessel scans. It is demonstrated that using the L1 regularization leads to reduced artifacts and higher SNR in incomplete or insufficient data acquisition scenarios.

The author of this thesis provided the model-based reconstruction framework that made this work possible and provided assistance with the analysis and visual representation of the results.

6.2 Publication

Yiyong Han, **Lu Ding**, Xosé Luis Deán Ben, Daniel Razansky, Jaya Prakash, and Vasilis Ntziachristos. Three-dimensional optoacoustic reconstruction using fast sparse representation. *Optics Letters*, 42(5):979–982, 2017

Chapter 7

Efficient Non-negative Constrained Model-based Inversion in Optoacoustic Tomography

7.1 Summary

Negative absorption values are common artifacts in optoacoustic image reconstruction. They appear, since the forward model cannot perfectly match the experimental measurements for various reasons, such as band-width limited transducers, limited acquisition view, model mismatch in wave propagation, etc.

In [22], the problem is addressed by solving large least-squares problems with non-negative constraints. Six state-of-the-art algorithms for solving non-negative constrained least-squares problems are investigated and an accelerated projected conjugate gradient method is proposed, which is especially suited for the kind of large, ill-conditioned problems that are encountered in model-based reconstruction.

Several experiments are performed to analyze the reconstruction results and compare the convergence behavior of the different algorithms. Firstly, in a phantom experiment, results with and without the non-negative constraints are compared. The non-negative constraint leads to a noticeable improvement in image quality. When comparing the convergence speed of the non-negative algorithms, the proposed algorithm converged more than twice as fast as the second best algorithm.

A quantitative evaluation was further performed with a second phantom

experiment. Different concentration of ink were injected into a tubing in the phantom. It is shown that with a non-negative constrained algorithm, the reading of the absorption value in the reconstructed image is proportional to the actual concentration, while this is not the case without the constraints.

In a third experiment, *in vivo* mice were imaged in the spleen and kidney regions using a cross-sectional MSOT setup. Images reconstructed 1) without non-negative constraints, 2) thresholding negative values to zero and 3) with non-negative constraints were compared. Imposing the non-negative constraints was shown to be beneficial since it can remove background artifacts while retaining useful information deep inside the tissue.

The first two experiments were performed by the author of this thesis and one co-author. The data from the third experiment was provided by a colleague. The algorithms were derived by the author. The reconstruction with the different methods and the analysis were also done by the author.

7.2 Publication

Lu Ding, X Luís Deán-Ben, Christian Lutzweiler, Daniel Razansky, and Vasilis Ntziachristos. Efficient non-negative constrained model-based inversion in optoacoustic tomography. *Physics in medicine and biology*, 60(17):6733, 2015

Chapter 8

Constrained Inversion and Spectral Unmixing in Multispectral Optoacoustic Tomography

8.1 Summary

In MSOT, the concentration maps of spectrally distinct absorbers are usually obtained through a two-step procedure. Firstly, the light absorption maps are reconstructed separately for each excitation wavelength. Secondly, spectral unmixing is used to reconstruct the concentration maps from the multispectral absorption maps (cf. Section 2.3).

Since both steps are linear transformations in the forward model, they can combined to directly reconstruct the concentrations from the measured pressure signals. Without additional constraints, the solution to the combined problem is the same as for the two step approach. However, as demonstrated in previous work [22], Imposing non-negative constraints can improve image quality significantly.

In [21], the work in [22] is extended to MSOT. Several methods are investigated by imposing the non-negative constraints in different steps in the inversion procedure in either separate or combined manners.

Several experiments were designed to evaluate the performance of the different methods. Firstly, a phantom experiment was conducted. Different concentrations of AF750 were flushed into two polyethylene tubings inside the phantom. The quantitative reading of the concentration of AF750 inside the tubing was evaluated for the different reconstruction methods.

Secondly, a ring-shaped polyethylene tubing was inserted in the the rectum of a mouse. Different concentrations of AF750 and gold-nanorods were flushed into the tubing. The same quantitative analysis was performed as in the first experiment. Additionally, a cross-talk analysis was done on 10 cross-sections in the intestinal/leg region for both contrast agents.

The first two quantitative experiments showed consistent results that most of the methods, except for one, delivered good results.

In the third experiment, an *in vivo* mouse was imaged with an iRFP target tumor. In the fourth experiment, the accumulation of IRdye800CW was imaged in the kidney region during renal clearance in an *in vivo* healthy mouse. For these two experiments, the different methods were qualitatively evaluated based on the theoretical distribution of the contrast agents.

The first two experiments were performed by the author and one co-author. The data of the third and fourth experiments were provided by a colleague. The algorithms were derived by the author. The reconstruction with the different methods and the analysis were also done by the author.

8.2 Publication

Lu Ding, Xose Luis Dean Ben, Neal C Burton, Robert W Sobol, Vasilis Ntziachristos, and Daniel Razansky. Constrained inversion and spectral unmixing in multispectral optoacoustic tomography. *IEEE Transactions on Medical Imaging*, 2017

Chapter 9

Dynamic Particle Enhancement in Limited-view Optoacoustic Tomography

9.1 Summary

In [13], the artifacts in limited-view optoacoustic setups was tackled. It is assumed that small particles are flowing with high-speed through the area of interest. With OAT, a sequence of images of the flowing particles can be captured. Adding up the sequence of reconstructed images yields an image of the path (e.g. blood vessels), along which the particles flow.

Since each of the individual images only contains a small set of particles, it is possible to obtain a fairly accurate reconstruction despite the limited view. However, by simply adding up the images, the negative artifacts in the individual images accumulate, leading to significant impairments in the combined image. But the non-negative reconstruction approach previously published by the author, is able to remove most of the artifacts in the individual images and thus yields a clean picture of the combined structure by adding these non-negative images, effectively eliminating the limited-view problem.

Results are shown for a numerical simulation and a tubing experiment as proof of concept. In the latter experiment, India ink was flushed into a ring-shaped tubing. Images were taken at 100 frames per second with a hand-held device with an angular coverage of 90 degrees. The reconstructed images showed that the proposed approach significantly enhanced the contrast of the tubing boundaries perpendicular to the transducer.

The author provided the reconstructed images shown in the paper, by ap-

plying the non-negative constrained reconstruction method to the measured pressure signals.

9.2 Publication

X Luís Deán-Ben, **Lu Ding**, and Daniel Razansky. Dynamic particle enhancement in limited-view optoacoustic tomography. *Optics Letters*, 42(4):827–830, 2017

Chapter 10

Noninvasive Anatomical and Functional Imaging of Orthotopic Glioblastoma Development and Therapy using Multispectral Optoacoustic Tomography

10.1 Summary

In [2], the potential of MSOT to track changes in the oxygenation in orthotopic glioblastoma and the surrounding brain tissues is analyzed when a vascular disruptive agent (VDA) is administered. To this end, *in vivo* experiments were performed on mice injected with tumor cells. The oxygenation level upon administration of VDA was monitored up to 15 days.

To generate the oxygenation images from the MSOT data, the newly introduced approach from [21] was used for non-negative image reconstruction and unmixing.

It is shown that with this advanced reconstruction approach, MSOT is able to monitor tumor growth and assess hemodynamic changes upon administration of VDAs.

For this work, the author provided guidance on suitable methods for image reconstruction. The author further processed the data from the experiments and generated the oxygenation maps.

10.2 Publication

Ghayathri Balasundaram, **Lu Ding**, Xiuting Li, Amalina Binte Ebrahim Attia, Xose Luis Dean-Ben, Chris Jun Hui Ho, Prashant Chandrasekharan, Hui Chien Tay, Hann Qian Lim, Chee Bing Ong, Ralph P. Mason, Daniel Razansky, and Malini Olivo. Noninvasive anatomical and functional imaging of orthotopic glioblastoma development and therapy using multispectral optoacoustic tomography. *Translational Oncology*, 11(5):1251–1258, 2018

Chapter 11

Discussion and Outlook

In this thesis, novel algorithms are presented for the reconstruction of light-absorption maps from ultrasonic signals. The aim is to improve upon existing algorithms on the two main criteria: the computational complexity and the image quality. Of course, there is often a trade-off between the two aspects. By investing more complexity, better image quality can be achieved and vice versa.

But as seen in the presented work, sometimes it is possible to yield substantial improvements in computational complexity and memory overhead with negligible impact on image quality and, on the other hand, some artifacts in the reconstructed images can be removed without much impact on the complexity.

Specifically, this work has the following major contributions:

- A novel method is introduced for discretization and on-the-fly calculation of the model matrix (in 2D and 3D scenarios), which exploits a far-field assumption to calculate the impulse responses for all voxel-transducer pairs. Prototypes for the impulse-responses are stored in a small look-up table which is used to calculate matrix-vector products with the model matrix. This new method can run efficiently on a GPU with minimal memory overhead.

- The complexity of the model-based reconstruction is further reduced by using a rotationally symmetric interpolation kernel and factoring the model matrix into a maximally sparse part (with one entry per voxel-transducer pair) and a separate convolution with the impulse response. Since the convolution can be calculate using an FFT, this reduces the complexity by an order of magnitude, leading to a complexity per iteration similar to that of the back-projection algorithm.

It is also shown that this simplification does not have a visible impact on the reconstructed images.

- It is demonstrated how to model the transducer shape using a small number of points. This increases the complexity proportional to the number of points used, but can significantly reduce smearing artifacts at the edges of the imaging region.

- A projected conjugate gradient algorithm is developed that runs non-negative constrained model-based reconstruction with similar complexity as the unconstrained version. It is further investigated how to apply the constrained reconstruction in the multispectral case, where it is possible to either run the unmixing step separately or directly combine it with the model-based reconstruction.

The new efficient model-based reconstruction algorithms can improve imaging quality in three-dimensional setups, where previously only back-projection algorithms were feasible. But they are also beneficial for other less challenging setups when real-time reconstruction is required.

The proposed methods are especially important for MSOT applications, which need high quality and quantitative image reconstruction for multiple wavelengths. In order to obtain an accurate distribution of different chromophores with spectral unmixing, the reconstruction quality of the single wavelength images needs to be guaranteed. Images reconstructed using the back-projection algorithm are known to contain negative values, which cannot be removed in a clean way and thus makes it challenging to use back-projection for multispectral imaging. Instead, a non-negative constrained model-based algorithm should be used to obtain meaningful results. For the large five-dimensional datasets (three spatial dimensions, one dimension for time, and one for the wavelength) generated by MSOT systems, state-of-the-art model-based methods are often prohibitively complex, but our method for non-negative reconstruction combined with our efficient GPU implementation can be used even in the most challenging scenarios.

As demonstrated, the new models and techniques for image reconstruction can be readily combined with ideas from other signal-processing fields such as compressed sensing [46, 45, 25]. It might be interesting to further investigate the combination of different low-complexity, iterative compressed-sensing algorithms with the proposed linear models.

Even with the proposed refinements to the modeling and reconstruction method, imaging artifacts are still present due to reflections, non-linearities and other model mismatches. One major open challenge is to find a way to incorporate light fluence in the reconstruction method without increasing

complexity too much. Right now, machine learning is very popular in various image processing applications. Calculating the light fluence from the absorption map (which, in general, is a very difficult non-linear problem) could be done approximately via machine learning. There might also be other options to combine machine learning with the presented model-based methods to enhance reconstruction quality and further reduce artifacts in the reconstructed images.

The most convenient way to get ground truth data for a machine learning approach would be to have an accurate and realistic enough simulation of the system that produces the artifacts. Thus, some work should look into more accurate simulation for light and acoustic wave propagation.

Despite the remaining challenges, OAT is a promising imaging modality with many applications (cf. Section 2.5). Hopefully, the contributions in this thesis help to open up new applications, especially for clinical studies that use limited-view hand-held devices, which, up to now, typically used the less accurate back-projection reconstruction to handle the large three-dimensional datasets in real-time.

Acknowledgements

This thesis would not have been possible without the help and support of a number of people.

First, I would like to thank my supervisors Prof. Vasilis Ntziachristos and Prof. Daniel Razansky for accepting me into their institute and research group and for providing an open, and well-equipped research environment where I was able to freely pursue my research interests.

Special thanks go to Dr. Xose Luis Deán-Ben, who mentored and guided all my research efforts. He helped me with both, the theoretical and practical aspects of my research. He was always available for a friendly discussion and patiently answered all my questions.

I thank all my colleagues for friendly conversations and companionship during my years at the institute. They helped me get through the more difficult phases of my studies.

I also thank my co-authors from other institutes for their friendly collaboration in our joint research efforts.

Last but not least, I thank my family and friends for their encouragement and especially my husband David for his continuous love and support.

Bibliography

[1] Guillaume Bal and Kui Ren. On multi-spectral quantitative photoacoustic tomography in diffusive regime. *Inverse Problems*, 28:025010, 01 2012.

[2] Ghayathri Balasundaram, **Lu Ding**, Xiuting Li, Amalina Binte Ebrahim Attia, Xose Luis Dean-Ben, Chris Jun Hui Ho, Prashant Chandrasekharan, Hui Chien Tay, Hann Qian Lim, Chee Bing Ong, Ralph P. Mason, Daniel Razansky, and Malini Olivo. Noninvasive anatomical and functional imaging of orthotopic glioblastoma development and therapy using multispectral optoacoustic tomography. *Translational Oncology*, 11(5):1251–1258, 2018.

[3] Sibaprasad Bhattacharyya, Shuyan Wang, Daniel Reinecke, William Kiser Jr, Robert A Kruger, and Timothy R DeGrado. Synthesis and evaluation of near-infrared (nir) dye- herceptin conjugates as photoacoustic computed tomography (pct) probes for her2 expression in breast cancer. *Bioconjugate chemistry*, 19(6):1186–1193, 2008.

[4] Hans-Peter Brecht, Richard Su, Matthew Fronheiser, Sergey A Ermilov, Andre Conjusteau, and Alexander A Oraevsky. Whole-body three-dimensional optoacoustic tomography system for small animals. *Journal of biomedical optics*, 14(6):064007–064007, 2009.

[5] Andreas Buehler, Eva Herzog, Angelica Ale, Bradley D Smith, Vasilis Ntziachristos, and Daniel Razansky. High resolution tumor targeting in living mice by means of multispectral optoacoustic tomography. *EJNMMI research*, 2(1):1–6, 2012.

[6] Andreas Buehler, Eva Herzog, Daniel Razansky, and Vasilis Ntziachristos. Video rate optoacoustic tomography of mouse kidney perfusion. *Optics letters*, 35(14):2475–2477, 2010.

[7] Andreas Buehler, Marcin Kacprowicz, Adrian Taruttis, and Vasilis Ntziachristos. Real-time handheld multispectral optoacoustic imaging. *Optics letters*, 38(9):1404–1406, 2013.

[8] Neal C Burton, Manishkumar Patel, Stefan Morscher, Wouter HP Driessen, Jing Claussen, Nicolas Beziere, Thomas Jetzfellner, Adrian Taruttis, Daniel Razansky, Bohumil Bednar, et al. Multispectral opto-acoustic tomography (msot) of the brain and glioblastoma characterization. *Neuroimage*, 65:522–528, 2013.

[9] Benjamin T. Cox, Jan G. Laufer, Paul C. Beard, and Simon R. Arridge. Quantitative spectroscopic photoacoustic imaging: a review. *Journal of Biomedical Optics*, 17(6):1 – 23, 2012.

[10] Adam de La Zerda, Yannis M Paulus, Robert Teed, Sunil Bodapati, Yosh Dollberg, Butrus T Khuri-Yakub, Mark S Blumenkranz, Darius M Moshfeghi, and Sanjiv Sam Gambhir. Photoacoustic ocular imaging. *Optics letters*, 35(3):270–272, 2010.

[11] Adam De La Zerda, Cristina Zavaleta, Shay Keren, Srikant Vaithilingam, Sunil Bodapati, Zhuang Liu, Jelena Levi, Bryan R Smith, Te-Jen Ma, Omer Oralkan, et al. Carbon nanotubes as photoacoustic molecular imaging agents in living mice. *Nature nanotechnology*, 3(9):557–562, 2008.

[12] X Luís Dean-Ben, Andreas Buehler, Vasilis Ntziachristos, and Daniel Razansky. Accurate model-based reconstruction algorithm for three-dimensional optoacoustic tomography. *IEEE Transactions on Medical Imaging*, 31(10):1922–1928, 2012.

[13] X Luís Deán-Ben, **Lu Ding**, and Daniel Razansky. Dynamic particle enhancement in limited-view optoacoustic tomography. *Optics Letters*, 42(4):827–830, 2017.

[14] X Luís Dean-Ben, Vasilis Ntziachristos, and Daniel Razansky. Acceleration of optoacoustic model-based reconstruction using angular image discretization. *IEEE Transactions on medical imaging*, 31(5):1154–1162, 2012.

[15] X Luis Dean-Ben, Ali Ozbek, and Daniel Razansky. Volumetric real-time tracking of peripheral human vasculature with gpu-accelerated three-dimensional optoacoustic tomography. *IEEE transactions on medical imaging*, 32(11):2050–2055, 2013.

[16] X Luís Deán-Ben, Gali Sela, Antonella Lauri, Moritz Kneipp, Vasilis Ntziachristos, Gil G Westmeyer, Shy Shoham, and Daniel Razansky. Functional optoacoustic neuro-tomography for scalable whole-brain monitoring of calcium indicators. *Light: Science & Applications*, 5(12):e16201–e16201, 2016.

[17] Xosé Luís Deán-Ben, Erwin Bay, and Daniel Razansky. Functional optoacoustic imaging of moving objects using microsecond-delay acquisition of multispectral three-dimensional tomographic data. *Scientific reports*, 4, 2014.

[18] Xosé Luís Deán-Ben, Steven James Ford, and Daniel Razansky. High-frame rate four dimensional optoacoustic tomography enables visualization of cardiovascular dynamics and mouse heart perfusion. *Scientific reports*, 5(1):1–9, 2015.

[19] Alexander Dima, Neal C Burton, and Vasilis Ntziachristos. Multispectral optoacoustic tomography at 64, 128, and 256 channels. *Journal of biomedical optics*, 19(3):036021–036021, 2014.

[20] **Lu Ding**, X Luis Dean Ben, and Daniel Razansky. Efficient three-dimensional model-based reconstruction scheme for arbitrary optoacoustic acquisition geometries. *IEEE Transactions on Medical Imaging*, 2017.

[21] **Lu Ding**, Xose Luis Dean Ben, Neal C Burton, Robert W Sobol, Vasilis Ntziachristos, and Daniel Razansky. Constrained inversion and spectral unmixing in multispectral optoacoustic tomography. *IEEE Transactions on Medical Imaging*, 2017.

[22] **Lu Ding**, X Luís Deán-Ben, Christian Lutzweiler, Daniel Razansky, and Vasilis Ntziachristos. Efficient non-negative constrained model-based inversion in optoacoustic tomography. *Physics in medicine and biology*, 60(17):6733, 2015.

[23] **Lu Ding**, X. Luis Deán-Ben, and Daniel Razansky. Real-time model-based inversion in cross-sectional optoacoustic tomography. *IEEE Transactions on Medical Imaging*, 35(8):1883–1891, Aug 2016.

[24] **Lu Ding**, Daniel Razansky, and Xosé Luís Deán-Ben. Model-based reconstruction of large three-dimensional optoacoustic datasets. *IEEE Transactions on Medical Imaging*, 39(9):2931–2940, 2020.

[25] Yiyong Han, **Lu Ding**, Xosé Luis Deán Ben, Daniel Razansky, Jaya Prakash, and Vasilis Ntziachristos. Three-dimensional optoacoustic reconstruction using fast sparse representation. *Optics Letters*, 42(5):979–982, 2017.

[26] M Heijblom, D Piras, W Xia, JCG Van Hespen, JM Klaase, FM Van den Engh, TG Van Leeuwen, W Steenbergen, and S Manohar. Visualizing breast cancer using the twente photoacoustic mammoscope: what do we learn from twelve new patient measurements? *Optics express*, 20(11):11582–11597, 2012.

[27] Eva Herzog, Adrian Taruttis, Nicolas Beziere, Andrey A Lutich, Daniel Razansky, and Vasilis Ntziachristos. Optical imaging of cancer heterogeneity with multispectral optoacoustic tomography. *Radiology*, 263(2):461–468, 2012.

[28] Steven L Jacques. Optical properties of biological tissues: a review. *Physics in Medicine & Biology*, 58(11):R37, 2013.

[29] Krista Jansen, Min Wu, Antonius FW van der Steen, and Gijs van Soest. Photoacoustic imaging of human coronary atherosclerosis in two spectral bands. *Photoacoustics*, 2(1):12–20, 2014.

[30] Amit P Jathoul, Jan Laufer, Olumide Ogunlade, Bradley Treeby, Ben Cox, Edward Zhang, Peter Johnson, Arnold R Pizzey, Brian Philip, Teresa Marafioti, et al. Deep in vivo photoacoustic imaging of mammalian tissues using a tyrosinase-based genetic reporter. *Nature Photonics*, 9(4):239–246, 2015.

[31] Moritz Kneipp, Jake Turner, Sebastian Hambauer, Sandro M Krieg, Jens Lehmberg, Ute Lindauer, and Daniel Razansky. Functional real-time optoacoustic imaging of middle cerebral artery occlusion in mice. *PloS one*, 9(4):e96118, 2014.

[32] Robert A Kruger, Cherie M Kuzmiak, Richard B Lam, Daniel R Reinecke, Stephen P Del Rio, and Doreen Steed. Dedicated 3d photoacoustic breast imaging. *Medical physics*, 40(11):113301, 2013.

[33] Jan Laufer, Clare Elwell, Dave Delpy, and Paul Beard. In vitro measurements of absolute blood oxygen saturation using pulsed near-infrared photoacoustic spectroscopy: accuracy and resolution. *Physics in Medicine & Biology*, 50(18):4409, 2005.

[34] Meng-Lin Li, Jung-Taek Oh, Xueyi Xie, Geng Ku, Wei Wang, Chun Li, Gina Lungu, George Stoica, and Lihong V Wang. Simultaneous molecular and hypoxia imaging of brain tumors in vivo using spectroscopic photoacoustic tomography. *Proceedings of the IEEE*, 96(3):481–489, 2008.

[35] Xosé Luís Deán-Ben and Daniel Razansky. Adding fifth dimension to optoacoustic imaging: volumetric time-resolved spectrally enriched tomography. *Light: Science & Applications*, 3(1):e137–e137, 2014.

[36] Gary D Luker and Kathryn E Luker. Optical imaging: current applications and future directions. *Journal of Nuclear Medicine*, 49(1):1–4, 2008.

[37] Christian Lutzweiler and Daniel Razansky. Optoacoustic imaging and tomography: reconstruction approaches and outstanding challenges in image performance and quantification. *Sensors*, 13(6):7345–7384, 2013.

[38] Konstantin Maslov, Hao F Zhang, Song Hu, and Lihong V Wang. Optical-resolution photoacoustic microscopy for in vivo imaging of single capillaries. *Optics letters*, 33(9):929–931, 2008.

[39] Kenji Mitsuhashi, Kun Wang, and Mark A Anastasio. Investigation of the far-field approximation for modeling a transducer's spatial impulse response in photoacoustic computed tomography. *Photoacoustics*, 2(1):21–32, 2014.

[40] Stefan Morscher, Wouter HP Driessen, Jing Claussen, and Neal C Burton. Semi-quantitative multispectral optoacoustic tomography (msot) for volumetric pk imaging of gastric emptying. *Photoacoustics*, 2(3):103–110, 2014.

[41] Vasilis Ntziachristos and Daniel Razansky. Molecular imaging by means of multispectral optoacoustic tomography (msot). *Chemical Reviews*, 110(5):2783–2794, 2010.

[42] Christopher C Paige and Michael A Saunders. Lsqr: An algorithm for sparse linear equations and sparse least squares. *ACM transactions on Mathematical Software*, 8(1):43–71, 1982.

[43] G Paltauf, JA Viator, SA Prahl, and SL Jacques. Iterative reconstruction algorithm for optoacoustic imaging. *The Journal of the Acoustical Society of America*, 112(4):1536–1544, 2002.

[44] Daniele Piras, Chiel Grijsen, Peter Schutte, Wiendelt Steenbergen, and Srirang Manohar. Photoacoustic needle: minimally invasive guidance to biopsy. *Journal of biomedical optics*, 18(7):070502, 2013.

[45] Jaya Prakash, Aditi Subramani Raju, Calvin B Shaw, Manojit Pramanik, and Phaneendra K Yalavarthy. Basis pursuit deconvolution for improving model-based reconstructed images in photoacoustic tomography. *Biomedical optics express*, 5(5):1363–1377, 2014.

[46] Jean Provost and Frédéric Lesage. The application of compressed sensing for photo-acoustic tomography. *IEEE transactions on medical imaging*, 28(4):585–594, 2009.

[47] Daniel Queirós, Xosé Luís Déan-Ben, Andreas Buehler, Daniel Razansky, Amir Rosenthal, and Vasilis Ntziachristos. Modeling the shape of cylindrically focused transducers in three-dimensional optoacoustic tomography. *Journal of biomedical optics*, 18(7):076014–076014, 2013.

[48] Daniel Razansky. Multispectral optoacoustic tomography—volumetric color hearing in real time. *IEEE Journal of Selected Topics in Quantum Electronics*, 18(3):1234–1243, 2012.

[49] Daniel Razansky, Andreas Buehler, and Vasilis Ntziachristos. Volumetric real-time multispectral optoacoustic tomography of biomarkers. *Nature protocols*, 6(8):1121–1129, 2011.

[50] Daniel Razansky, Martin Distel, Claudio Vinegoni, Rui Ma, Norbert Perrimon, Reinhard W Köster, and Vasilis Ntziachristos. Multispectral opto-acoustic tomography of deep-seated fluorescent proteins in vivo. *Nature photonics*, 3(7):412–417, 2009.

[51] Amir Rosenthal, Thomas Jetzfellner, Daniel Razansky, and Vasilis Ntziachristos. Efficient framework for model-based tomographic image reconstruction using wavelet packets. *Medical Imaging, IEEE Transactions on*, 31(7):1346–1357, 2012.

[52] Amir Rosenthal, Vasilis Ntziachristos, and Daniel Razansky. Model-based optoacoustic inversion with arbitrary-shape detectors. *Medical physics*, 38(7):4285–4295, 2011.

[53] Amir Rosenthal, Vasilis Ntziachristos, and Daniel Razansky. Acoustic inversion in optoacoustic tomography: A review. *Current medical imaging reviews*, 9(4):318, 2013.

[54] Kwang Hyun Song, Erich W Stein, Julie A Margenthaler, and Lihong V Wang. Noninvasive photoacoustic identification of sentinel lymph nodes containing methylene blue in vivo in a rat model. *Journal of biomedical optics*, 13(5):054033, 2008.

[55] Liang Song, Chulhong Kim, Konstantin Maslov, K Kirk Shung, and Lihong V Wang. High-speed dynamic 3d photoacoustic imaging of sentinel lymph node in a murine model using an ultrasound array. *Medical physics*, 36(8):3724–3729, 2009.

[56] Subhadra Srinivasan, Brian W Pogue, Shudong Jiang, Hamid Dehghani, Christine Kogel, Sandra Soho, Jennifer J Gibson, Tor D Tosteson, Steven P Poplack, and Keith D Paulsen. Interpreting hemoglobin and water concentration, oxygen saturation, and scattering measured in vivo by near-infrared breast tomography. *Proceedings of the National Academy of Sciences*, 100(21):12349–12354, 2003.

[57] Eric M Strohm, Elizabeth SL Berndl, and Michael C Kolios. High frequency label-free photoacoustic microscopy of single cells. *Photoacoustics*, 1(3-4):49–53, 2013.

[58] Kun Wang, Chao Huang, Yu-Jiun Kao, Cheng-Ying Chou, Alexander A Oraevsky, and Mark A Anastasio. Accelerating image reconstruction in three-dimensional optoacoustic tomography on graphics processing units. *Medical physics*, 40(2), 2013.

[59] Kun Wang, Robert W. Schoonover, Richard Su, Alexander Oraevsky, and Mark A. Anastasio. Discrete imaging models for three-dimensional optoacoustic tomography using radially symmetric expansion functions. *IEEE Transactions on Medical Imaging*, 33(5):1180–1193, 2014.

[60] Kun Wang, Richard Su, Alexander A Oraevsky, and Mark A Anastasio. Investigation of iterative image reconstruction in three-dimensional optoacoustic tomography. *Physics in medicine and biology*, 57(17):5399, 2012.

[61] Lihong V Wang. *Photoacoustic imaging and spectroscopy*. CRC press, 2009.

[62] Lihong V Wang and Song Hu. Photoacoustic tomography: in vivo imaging from organelles to organs. *Science*, 335(6075):1458–1462, 2012.

[63] Lihong V Wang and Hsin-I Wu. *Photoacoustic Tomography*, chapter 12, pages 283–321. John Wiley & Sons, Ltd, 2009.

[64] Lihong V Wang and Junjie Yao. A practical guide to photoacoustic tomography in the life sciences. *nature methods*, 13(8):627–638, 2016.

[65] Xueding Wang, Geng Ku, Malgorzata A Wegiel, Darryl J Bornhop, George Stoica, and Lihong V Wang. Noninvasive photoacoustic angiography of animal brains in vivo with near-infrared light and an optical contrast agent. *Optics letters*, 29(7):730–732, 2004.

[66] Xueding Wang, Yongjiang Pang, Geng Ku, Xueyi Xie, George Stoica, and Lihong V Wang. Noninvasive laser-induced photoacoustic tomography for structural and functional in vivo imaging of the brain. *Nature biotechnology*, 21(7):803–806, 2003.

[67] H-J Wittsack, Afra M Wohlschläger, Eva K Ritzl, Raimund Kleiser, Mathias Cohnen, Rüdiger J Seitz, and Ulrich Mödder. Ct-perfusion imaging of the human brain: advanced deconvolution analysis using circulant singular value decomposition. *Computerized Medical Imaging and Graphics*, 32(1):67–77, 2008.

[68] Jun Xia and Lihong V. Wang. Small-animal whole-body photoacoustic tomography: A review. *IEEE Transactions on Biomedical Engineering*, 61(5):1380–1389, 2014.

[69] Minghua Xu and Lihong V Wang. Universal back-projection algorithm for photoacoustic computed tomography. *Physical Review E*, 71(1):016706, 2005.

[70] Joon-Mo Yang, Konstantin Maslov, Hao-Chung Yang, Qifa Zhou, K Kirk Shung, and Lihong V Wang. Photoacoustic endoscopy. *Optics letters*, 34(10):1591–1593, 2009.

[71] Qiuhong Yang, Shuang Cai, M Laird Forrest, Huizhong Cui, and Xinmai Yang. In vivo photoacoustic imaging of chemotherapy-induced apoptosis in squamous cell carcinoma using a near-infrared caspase-9 probe. *Journal of Biomedical Optics*, 16(11):116026, 2011.

[72] Junjie Yao, Konstantin I Maslov, Song Hu, and Lihong V Wang. Evans blue dye-enhanced capillary-resolution photoacoustic microscopy in vivo. *Journal of biomedical optics*, 14(5):054049, 2009.

[73] Junjie Yao, Jun Xia, Konstantin I Maslov, Mohammadreza Nasiriavanaki, Vassiliy Tsytsarev, Alexei V Demchenko, and Lihong V Wang. Noninvasive photoacoustic computed tomography of mouse brain metabolism in vivo. *Neuroimage*, 64:257–266, 2013.

[74] Sophia Zackrisson, SMWY Van De Ven, and SS Gambhir. Light in and sound out: Emerging translational strategies for photoacoustic imagingtranslational strategies for photoacoustic imaging. *Cancer research*, 74(4):979–1004, 2014.

Appendix A

Publication: Real-time Model-based Inversion in Cross-sectional Optoacoustic Tomography

Real-Time Model-Based Inversion in Cross-Sectional Optoacoustic Tomography

Lu Ding, Xosé Luís Deán-Ben, and Daniel Razansky*

***Abstract*—Analytical (closed-form) inversion schemes have been the standard approach for image reconstruction in optoacoustic tomography due to their fast reconstruction abilities and low memory requirements. Yet, the need for quantitative imaging and artifact reduction has led to the development of more accurate inversion approaches, which rely on accurate forward modeling of the optoacoustic wave generation and propagation. In this way, multiple experimental factors can be incorporated, such as the exact detection geometry, spatio-temporal response of the transducers, and acoustic heterogeneities. The model-based inversion commonly results in very large sparse matrix formulations that require computationally extensive and memory demanding regularization schemes for image reconstruction, hindering their effective implementation in real-time imaging applications. Herein, we introduce a new discretization procedure for efficient model-based reconstructions in two-dimensional optoacoustic tomography that allows for parallel implementation on a graphics processing unit (GPU) with a relatively low numerical complexity. By on-the-fly calculation of the model matrix in each iteration of the inversion procedure, the new approach results in imaging frame rates exceeding 10 Hz, thus enabling real-time image rendering using the model-based approach.**

***Index Terms*—Model-based reconstruction, optoacoustic tomography, photoacoustic tomography, real-time imaging.**

I. Introduction

MUCH like other tomographic imaging modalities, optoacoustic tomography (OAT) relies upon a mathematical reconstruction procedure to render images of biological samples. The algorithm employed strongly influences the imaging performance, affecting a number of parameters, which include image contrast, spatial and temporal resolution, severeness of image artifacts, and overall image quantification abilities.

Several approaches have been suggested for tomographic image reconstruction in OAT [1]–[12]. The reconstruction performance may vary in each case depending on the exact tomographic configuration employed as well as on acoustic properties of the imaged volume [8]–[11], [13]–[15]. Although analytical (closed-form) inversion algorithms, such as filtered back-projection [2], may generally result in fast and memory-efficient reconstructions, model-based approaches based on numerical (or semi-analytical) inversion of an optoacoustic forward model provide extra flexibility in terms of their applicability to different types of imaging systems and samples [10], [11]. In this way, one could for instance account for specific experimental and modeling imperfections, such as spatially-dependent response of the ultrasound transducers [9], [16], [17] or acoustic heterogeneities and attenuation in the sample and the surrounding medium [18]–[20].

Model-based reconstruction methods based on the time-domain optoacoustic wave equation are typically associated to large sparse matrix formulations. The main operations in the iterative inversion procedure are the multiplication of vectors with the model matrix and its transpose. Even though the model matrix is sparse, the large dimensionality of the problem leads to a significant computational complexity and memory overhead. Several approaches have been introduced to reduce both the computational operations and the memory requirements of model-based inversions. For example, it has been shown that the forward model can be significantly simplified in a cross-sectional acquisition geometry by assuming that the optoacoustic sources lie in a plane [21]. Thereby, the resulting two-dimensional model matrix can readily be stored in memory, in a way that fast inversion can be achieved with standard inversion algorithms. A discrete wavelet packet decomposition can be used to further speed up the computations, since the inversion is decoupled into smaller subproblems [22], although memory requirements are not significantly reduced. Both the computational complexity and memory overhead can be reduced by decreasing the number of measurements (projections) and applying appropriate regularization for sparse recovery [23]. On the other hand, inherent symmetries of the acquisition setup can be exploited to reduce the necessary memory [24]–[26]. Alternatively, the memory requirements can be drastically reduced by on-the-fly calculating the matrix vector products without explicitly storing the model matrix [27]. Efficient parallel implementation of this approach on a graphics processing units (GPU) is then feasible, so that the reconstruction time can be substantially accelerated in the same way as in other reconstruction methods [28]. Recently, other reconstruction approaches based on efficient sparse decomposition of the sequence of acquired signals have also been shown to significantly accelerate model-based reconstructions when handling multi-frame data [29], [30]. However, real-time visualization implies image reconstruction between the subsequent laser pulses, which cannot be achieved if multiple frames need to be accumulated prior to image rendering.

Manuscript received November 14, 2015; revised January 29, 2016; accepted February 07, 2016. Date of publication March 02, 2016; date of current version July 29, 2016. D. R. acknowledges support from the European Research Council under Grant ERC-2010-StG-260991. *Asterisk indicates corresponding author.*

L. Ding and X. L. Deán-Ben are with the Institute for Biological and Medical Imaging, Technical University of Munich and Helmholtz Center Munich, 85764 Neuherberg, Germany.

*D. Razansky is with the Institute for Biological and Medical Imaging, Technical University of Munich and Helmholtz Center Munich, 85764 Neuherberg, Germany (e-mail: dr@tum.de).

Color versions of one or more of the figures in this paper are available online at http://ieeexplore.ieee.org.

Digital Object Identifier 10.1109/TMI.2016.2536779

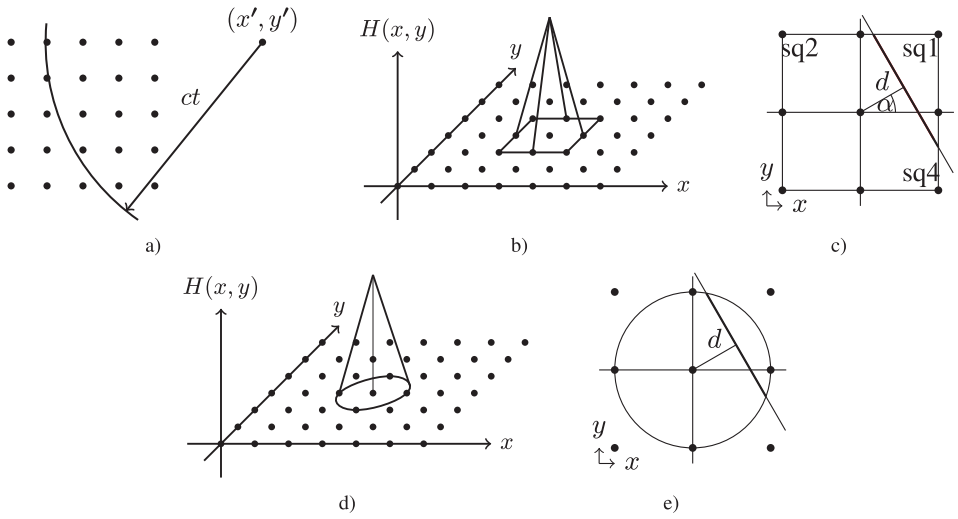

Fig. 1. Illustration of the discretization procedure for the cross-sectional (two-dimensional) optoacoustic imaging problem. a) Discretization of the forward model on a Cartesian grid using b) c) bilinear interpolation and d) e) circular interpolation.

The proposed method drastically reduces the computational complexity of on-the-fly calculations of the matrix-vector products by storing a small table of precalculated values. The new approach then results in imaging frame rates exceeding 10 Hz, thus enabling real-time image rendering using a model-based inversion method. Note that the term real time is usually employed in optoacoustics to refer to the capability to reconstruct images with no significant delay between data acquisition and image display, even for acquisition times larger than 1 s [31], [32]. Additionally, 10 Hz represents the optimal frame rate for attaining the best signal-to-noise performance while staying below the maximum permissible laser exposure limits, namely 20 $\mathrm{mJ/cm^2}$ energy density per pulse and 200 $\mathrm{mW/cm^2}$ average power density. For pulse repetition rates higher than 10 Hz, the energy per pulse must then be reduced, leading to a suboptimal signal-to-noise performance [33].

II. Methods

A. The Forward Model

For short-pulsed laser illumination fulfilling the so-called thermal confinement conditions [34], a Dirac's delta function can be assumed to closely resemble the temporal profile of the light intensity, in which case the optoacoustically-generated pressure wave follows the following equation [35], [36]

$$\frac{\partial^2 p(\boldsymbol{r},t)}{\partial t^2} - c^2\nabla^2 p(\boldsymbol{r},t) = \Gamma H(\boldsymbol{r})\frac{\partial \delta(t)}{\partial t}, \tag{1}$$

being Γ the dimensionless Grüneisen parameter, c the speed of sound in the medium and $H(\boldsymbol{r})$ the amount of energy absorbed in the tissue per unit volume. An exact analytical solution of (1) is subsequently given by the Poisson-type integral as [35], [37]

$$p(\boldsymbol{r}',t) = \frac{\Gamma}{4\pi c}\frac{\partial}{\partial t}\int_S \frac{H(\boldsymbol{r})}{|\boldsymbol{r}'-\boldsymbol{r}|}dS(t), \tag{2}$$

where the integral is performed along a spherical surface $S(t)$ defined as $|\boldsymbol{r}'-\boldsymbol{r}| = ct$. In cross-sectional tomography, the optoacoustic sources are assumed to lie in the same plane as the measurement points, in which case (2) is reduced into a two dimensional formulation [21], i.e.,

$$p(\boldsymbol{r}',t) = \frac{\partial}{\partial t}\int_{L(t)} \frac{H(\boldsymbol{r})}{|\boldsymbol{r}'-\boldsymbol{r}|}dL(t), \tag{3}$$

where $L(t)$ denotes a circumference for which $|\boldsymbol{r}'-\boldsymbol{r}| = ct$. Note that the latter equation is expressed in arbitrary units after neglecting all the constant terms.

B. Discretization an a Cartesian Grid

In order to discretely represent the temporal profiles of the measured pressure signals, one may define a regular Cartesian grid covering all the optoacoustic sources in the imaged volume, as depicted by solid circles in Fig. 1(a). Each point in the Cartesian grid represents one single pixel of a two dimensional image corresponding to the distribution of the absorbed optical energy. According to (3), the pressure signal at the transducer location $\boldsymbol{r}' = (x', y')$ and time instant t equals to the derivative of the integral of the absorption distribution on an arc, as shown in Fig. 1(a). The absorption at an arbitrary location $\boldsymbol{r}$ within the grid can be subsequently interpolated from the known absorption values at the pixel points. Thus, (3) can be approximated via

$$\begin{aligned} p(\boldsymbol{r}',t) &= \frac{\partial}{\partial t}\int_{L(t)} \frac{\sum_i H(r_i)K(\boldsymbol{r}-\boldsymbol{r}_i)}{|\boldsymbol{r}'-\boldsymbol{r}|}dL(t) \\ &= \sum_i H(r_i)\frac{\partial}{\partial t}\left(\frac{1}{ct}\int_{L(t)} K(\boldsymbol{r}-\boldsymbol{r}_i)dL(t)\right), \end{aligned} \tag{4}$$

where $K(\boldsymbol{r}-\boldsymbol{r}_i)$ is the interpolation function, i.e., the contribution of the pixel at location $\boldsymbol{r}_i$ to the optical absorption at location $\boldsymbol{r}$. Accordingly, we define

$$p_i(\boldsymbol{r}',t) = \frac{\partial}{\partial t}\left(\frac{1}{ct}\int_{L(t)} K(\boldsymbol{r}-\boldsymbol{r}_i)dL(t)\right) \tag{5}$$

as the pressure contribution of the ith pixel to the pressure signal $p(\boldsymbol{r}', t)$, which can be further expressed as

$$p(\boldsymbol{r}', t) = \sum_i H(r_i) p_i(\boldsymbol{r}', t). \tag{6}$$

In the following subsections, we introduce two different interpolation models to calculate $p_i(\boldsymbol{r}', t)$ when the pixel size is much smaller than the distance ct travelled by the optoacoustic wave. In general, many interpolation methods are applicable within the framework of the suggested reconstruction approach, each exhibiting a different trade-off between accuracy and computational complexity. In this work, we used the standard bilinear interpolation method and a simpler approach, termed "circular interpolation", mainly in order to optimize the reconstruction runtime.

1) Bilinear Interpolation: The absorbed energy at an arbitrary location $H(\boldsymbol{r}) = H(x, y)$ can be calculated as a function of the absorption at its 4 neighboring pixels by using bilinear interpolation. In this way, pixel i only contributes to the absorption distribution in an area within the 4 neighboring grid points (Fig. 1(b)). The interpolation function is then given by

$$K(\boldsymbol{r} - \boldsymbol{r}_i) = \begin{cases} 0 & \text{for } \|\boldsymbol{r} - \boldsymbol{r}_i\|_\infty \geqslant \Delta xy \\ \widetilde{K} & \text{for } \|\boldsymbol{r} - \boldsymbol{r}_i\|_\infty < \Delta xy \end{cases}, \tag{7}$$

where

$$\widetilde{K} = \left(1 - \frac{|x - x_i|}{\Delta xy}\right)\left(1 - \frac{|y - y_i|}{\Delta xy}\right), \tag{8}$$

and Δxy is the corresponding grid width.

Let the distance between the measuring location $\boldsymbol{r}'$ and the pixel position $\boldsymbol{r}_i$ be denoted by s. Considering a grid size Δxy much smaller than s, the integral in (5) can be approximated as the integral along a straight line in the square region for which $K(\boldsymbol{r} - \boldsymbol{r}_i)$ is not zero, as illustrated in Fig. 1(c). We define d as the distance from $\boldsymbol{r}_i$ to the integration line and α as the angle with respect to the horizontal axis [cf. Fig. 1(c)]. Since $d = s - ct$, one may rewrite (5) as

$$p_i(\boldsymbol{r}', t) = -c\frac{\partial}{\partial d}\left[\left(\frac{1}{s - d}\right)\int_{L(t)} K(\boldsymbol{r} - \boldsymbol{r}_i) dL(t)\right], \tag{9}$$

or, equivalently

$$p_i(\boldsymbol{r}', t) = -\frac{c}{(s - d)^2} I(d, \alpha) - \frac{c}{s - d} dI(d, \alpha), \tag{10}$$

where

$$I(d, \alpha) = \int_{L(t)} K(\boldsymbol{r} - \boldsymbol{r}_i) dL(t), \tag{11}$$

$$dI(d, \alpha) = \frac{\partial}{\partial d}\int_{L(t)} K(\boldsymbol{r} - \boldsymbol{r}_i) dL(t). \tag{12}$$

Taking into account that $dI(d, \alpha)$ is in the order of $max\,[I(d, \alpha)]/\Delta xy$, the first term in (10) can be neglected, leading to

$$p_i(\boldsymbol{r}', t) = -\frac{c}{s - d} dI(d, \alpha), \tag{13}$$

where $dI(d, \alpha)$ does not depend on the pixel position $\boldsymbol{r}_i$ and can be thus expressed analytically (see Appendix A for a detailed derivation).

2) Circular Interpolation: The calculation of the optical absorption distribution at any point can be further simplified by interpolating in a circular neighborhood of each pixel. In this case, the interpolation function is represented instead by the cone shown in Fig. 1(d). The circular interpolation function is then given by

$$K(\boldsymbol{r} - \boldsymbol{r}_i) = \begin{cases} 0 & |\boldsymbol{r} - \boldsymbol{r}_i| \geqslant \Delta xy \\ 1 - \frac{|\boldsymbol{r} - \boldsymbol{r}_i|}{\Delta xy} & |\boldsymbol{r} - \boldsymbol{r}_i| < \Delta xy \end{cases}. \tag{14}$$

As a result, the derivative $dI(d, \alpha)$ in (9) for the circular interpolation is independent of the angle α and only depends on the distance d (Fig. 1(e)). Therefore, $p_i(\boldsymbol{r}', t)$ can be expressed as

$$p_i(\boldsymbol{r}', t) = -\frac{c}{s - d} dI(d). \tag{15}$$

See Appendix B for more details on the calculation of $dI(d)$ in (15).

C. Image Reconstruction

Optoacoustic tomographic reconstruction implies processing the pressure signals collected at a set of transducer locations $\boldsymbol{r}'_1, \ldots, \boldsymbol{r}'_L$ and time instants $t_1, \ldots, t_K$. Let

$$\boldsymbol{p}_{ij} = \begin{pmatrix} p_i(\boldsymbol{r}'_j, t_1) \\ \vdots \\ p_i(\boldsymbol{r}'_j, t_K) \end{pmatrix} \tag{16}$$

represent the theoretical pressure signal for the considered instants at position $\boldsymbol{r}'_j$ generated by a unit absorber at pixel i and

$$\boldsymbol{h} = \begin{pmatrix} H(\boldsymbol{r}_1) \\ \vdots \\ H(\boldsymbol{r}_N) \end{pmatrix} \tag{17}$$

denote a vector representing optical absorption at the pixels $1, \ldots, N$ of the reconstruction grid. By considering (6), a linear model

$$\boldsymbol{p} = \boldsymbol{A}\boldsymbol{h} \tag{18}$$

can be defined with the model matrix expressed as

$$\boldsymbol{A} = [\boldsymbol{a}_1, \ldots, \boldsymbol{a}_N], \tag{19}$$

where

$$\boldsymbol{a}_i = \begin{pmatrix} \boldsymbol{p}_{i1} \\ \vdots \\ \boldsymbol{p}_{iL} \end{pmatrix}. \tag{20}$$

Image reconstruction is then done by minimizing the least squared error between the measured signals in a vector form $\boldsymbol{p}_m$ and the corresponding signals predicted by the forward model, i.e.,

$$\hat{\boldsymbol{h}} = \arg\min_{\boldsymbol{h}} \|\boldsymbol{p}_m - \boldsymbol{A}\boldsymbol{h}\|_2. \tag{21}$$

The least squared inversion problem in (21) can be solved with iterative methods such as LSQR [38], which requires one calculation of a matrix-vector multiplication with the model matrix,

$\boldsymbol{Av}$, and one multiplication with its transpose, $\boldsymbol{A}^{\mathsf{T}}\boldsymbol{u}$, in each iteration. The vectors $\boldsymbol{v}$ and $\boldsymbol{u}$ are updated in each iteration of the LSQR algorithm using the results of the matrix-vector products.

An additional regularization term may be included in (21). However, no regularization is required in the LSQR inversion of the two dimensional model provided sufficient angular coverage is available in the cross-sectional optoacoustic tomographic imaging system [21].

D. GPU Implementation

The most computationally demanding operations in the above mentioned iterative inversion procedure are associated with the matrix-vector multiplications $\boldsymbol{Av}$ and $\boldsymbol{A}^{\mathsf{T}}\boldsymbol{u}$. Those operations can be significantly accelerated by a GPU-based implementation, which can generally be done in various ways. The most straightforward approach consists in the precalculation of the model matrix $\boldsymbol{A}$ and its subsequent storage on the GPU memory. Despite the sparsity of $\boldsymbol{A}$, this approach is hindered by the relatively small internal memory resources available on the GPUs, which may turn insufficient for storing model matrices corresponding to the required number of image pixels, simultaneously detected signals and their temporal sampling resolution. This limitation is particularly relevant for high-resolution reconstructions or three-dimensional inversions [37], [39] employing very large model matrices. For instance, the model matrix in the examples shown later in this work (i.e., with 256 channels, 732 sampling instants and 200×200 pixels) occupies around 300 MB of memory in a sparse representation. The memory needed is increased several orders of magnitude for a non-sparse representation. Standard GPUs have an internal memory of around 1–4 GB, which is enough to store the entire model-matrix for the reconstruction examples shown in this paper. However, it can be insufficient for reconstructions with a higher resolution, number of channels or sampling instants. On the other hand, the memory requirements exponentially increase for three-dimensional reconstructions, where the model matrix generally occupies many tens of GBs of memory. Another approach consists in on-the-fly calculation of the elements of the model matrix in each iteration of the inversion procedure [27]. This approach is widely applicable as no storage is required, but the required computational time is generally longer due to the need to repeat the same operations multiple times.

We propose an alternative approach based on the precalculation and storage of a small look-up table containing the derivatives $dI(d,\alpha)$ and $dI(d)$ in (13) and (15) corresponding to the different values of d and α. Such table can readily be stored in the GPU memory, and the calculation of the elements of the model matrix simply involves divisions and multiplications. As opposed to the large amount of memory that may be required for storing the entire model matrix on a GPU, the precalculated look-up tables for dI only occupy 800 Byte and 156 KB of memory for the bilinear and circular interpolation methods, respectively (for 200 different values of d and 200 different values of α). Since $\boldsymbol{A}$ is highly sparse, $\boldsymbol{Av}$ and $\boldsymbol{A}^{\mathsf{T}}\boldsymbol{u}$ can be subsequently obtained by calculating only the non-zero elements and multiplying them with the corresponding elements of the vectors $\boldsymbol{v}$ and $\boldsymbol{u}$. The matrix vector multiplications $\boldsymbol{Av}$ and $\boldsymbol{A}^{\mathsf{T}}\boldsymbol{u}$ are calculated row-wise and in parallel. In the calculation of $\boldsymbol{A}^{\mathsf{T}}\boldsymbol{u}$, each computing unit (kernel) calculates a value for each of the N pixels, namely the multiplication of non-zero elements of $\boldsymbol{a}_i$ [cf. (19)] with the corresponding elements in vector $\boldsymbol{u}$. In calculating $\boldsymbol{Av}$, each computing unit performs the operations corresponding to one transducer position and one sampling instant, i.e., the multiplication of non-zero elements of $\left[p_1(\boldsymbol{r}'_j, t_k), \ldots, p_N(\boldsymbol{r}'_j, t_k)\right]$ [cf. (13) (15)] with their corresponding elements in vector $\boldsymbol{v}$. The specific steps for the parallel implementation of these operations are illustrated in Appendix C. In a practical implementation, the symmetry of the bilinear interpolation function can be exploited to reduce the storage requirement for the lookup table (see Appendix A).

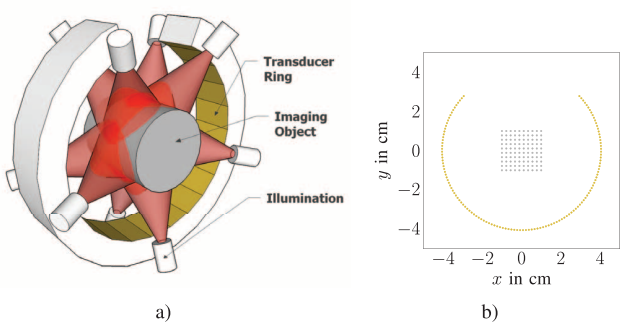

a) b)

Fig. 2. Illustration of the experimental cross-sectional optoacoustic tomography system. a) Three-dimensional representation of the actual experimental system. b) Geometrical distribution of transducer locations (gold dots) and Cartesian grid (gray dots) considered for two dimensional reconstruction.

Further acceleration of the reconstruction process is possible if multiple images are simultaneously reconstructed since the matrix elements are only calculated once for all the reconstructed images. This approach is convenient for off-line reconstructions but not appropriate for real-time imaging since, in the latter case, the reconstruction must be accomplished in between the consecutive signal acquisitions.

E. Experimental Measurements

The performance of the proposed model-based reconstruction approach was examined with experimental data acquired from mice. For this, a small animal optoacoustic tomography system (MSOT256-TF, iThera Medical GmbH, Munich, Germany) was used, which is based on signal acquisition with 256-element arc-shaped array of cylindrically-focused transducers covering 270° around the imaged object [40]. The system attains ring-type illumination on the surface of the imaged object by means of a fiber bundle. An illustration of the system is shown in Fig. 2. The acquired signals were digitized at 40 megasamples per second and band-pass filtered with cut-off frequencies 0.1 and 7 MHz.

The proposed algorithm using both interpolation methods was first compared to a reference model-based reconstruction algorithm [20]. Then, the inversion performance was evaluated as a function of various parameters, such as number of LSQR iterations, number of projections and number of sampling time instants in the acquired signal (time resolution). As a reference, we considered the image reconstructed with bilinear interpolation, 20 LSQR iterations, 256 projections and 1098 time instants. Finally, the reconstruction times of bilinear interpolation and circular interpolation were compared both

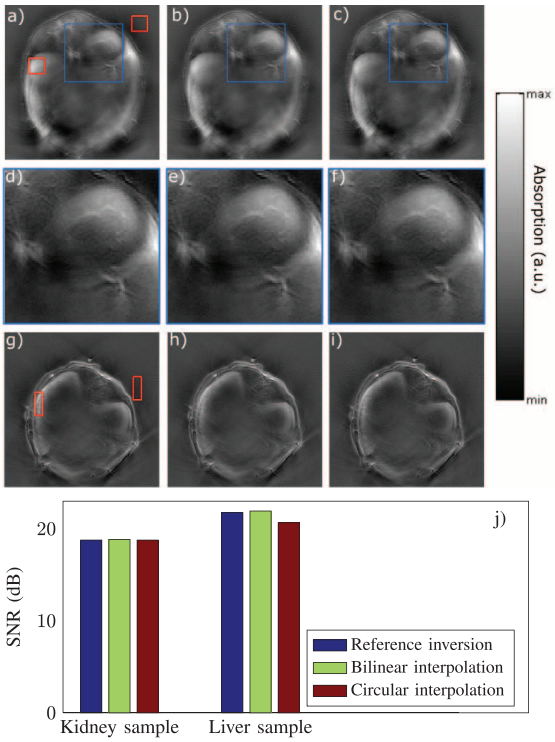

Fig. 3. Cross-sectional images acquired from a mouse in the kidney and liver regions. a) and g) are reconstructed using the standard iterative model-based inversion. Reconstructions using the proposed algorithm are shown in b) and h) for the bilinear interpolation and c) and i) for the circular interpolation respectively. d)-f) close-up images of the corresponding blue regions in a)-c). j) SNR performance of the different reconstruction schemes.

for single frame and multiple frame reconstructions using the optimum parameters. All images were reconstructed with 200 $\times$ 200 pixels.

The reconstruction was done on a AMD Radeon HD 7900 series GPU with 3 GB on-board memory and 32 computing units (2048 stream processors). The reconstruction was implemented using the OpenCL framework and executed in Matlab (MathWorks, Natick, MA) as a mex function.

III. Results

The cross-sectional images of the mice in the kidney/spleen and liver regions are shown in Fig. 3. The images in Fig. 3(a) and (g) were reconstructed with a previously introduced model-based algorithm [20]. The reconstructed images obtained by using the proposed algorithm with bilinear interpolation and circular interpolation are plotted in Fig. 3(b) (h) and (c) (i) respectively. Fig. 3(d)–(f) show close-up images of the blue rectangular regions in a)-c). No significant difference in the imaged small structures in the kidney regions can be observed in the three images. For all three approaches, the acquired pressure signals were cut and downsampled to 1098 time instants prior to reconstruction. All 256 projections were considered and the number of LSQR iterations were set to 10. Fig. 3(j) shows the signal to noise ratios (SNR) of Fig. 3(a)–(c) and (g)–(i) calculated with the absorption values in the squared regions marked in Fig. 3(a) and (g). Specifically, the SNR was calculated as the maximum reconstructed absorption in a region inside the mouse normalized to the standard deviation of the reconstructed absorption in a region outside the mouse. The obtained SNR of the kidney images a) to c) were 18.7744, 18.8475 and 18.7727 and the calculated SNR of the liver images g) to i) were 21.7461, 21.9314 and 20.6545. No essential differences between the reconstructed images using the three approaches can be observed.

For the purpose of evaluting the image quality of reconstructed images using different parameters, we used the reference image shown in Fig. 4(e), which is obtained as described in Section II-E. The relative error is calculated as the norm of the difference with the reference image normalized with the norm of the reference image. Fig. 4(a)–(d) show examples of images with increasing numbers of iterations, yielding resulting relative errors of 58.5%, 37.5%, 17.8% and 13% respectively. The differences of Fig. 4(a)–(d) with respect to the reference image are displayed in Fig. 4(f)–(i). Minor differences can be seen in h) and i), which indicates acceptable image quality is achieved for a relative error below 20%.

The relative error and the reconstruction time are shown as a function of the number of LSQR iterations in Fig. 5(a) and (b) for the bilinear interpolation and the circular interpolation approaches respectively. The corresponding normalized errors with both methods are reduced to approximately 13% and 15% after 5 LSQR iterations respectively, which was considered an acceptable performance. On the other hand, a two-fold reduction in the reconstruction time is achieved with circular interpolation as compared with the bilinear interpolation approach for the same number of iterations. The relative error and reconstruction time with respect to the number of projections (detector positions) are further presented in Fig. 5(c) and (d) for the two interpolation methods. For a given number of projections, virtual signals were obtained by interpolating between the original 256 detection channels, while the angular coverage was maintained in all cases. 5 LSQR iterations were performed in the reconstruction. Note that a decrease in the number of projection leads to a significant increase in the error. Therefore, all 256 channels should be used to optimize the image quality for the number of pixels considered [41]. The performance results for different number of time instants are shown in Fig. 5(e) and (f) for the two interpolation approaches. The reconstruction was done with 5 LSQR iterations and 256 projections. The length of the signals was fixed to 30 μs in all cases. For both interpolation approaches, no significant further improvement was achieved when increasing the number of time samples beyond 700.

The performance of the proposed algorithm is summarized in Table I. The reconstruction parameters were selected according to the results presented in Fig. 5 so that the reconstruction time is optimized without compromising image quality. Specifically, the number of LSQR iterations was set to 5, all 256 projections were taken and the signals were downsampled to 732 time instants. As shown in the table, it was possible to achieve 6 and 13 frames per second for single frame reconstruction by employing the bilinear and circular interpolation models respectively. When applying the multiple frame reconstruction

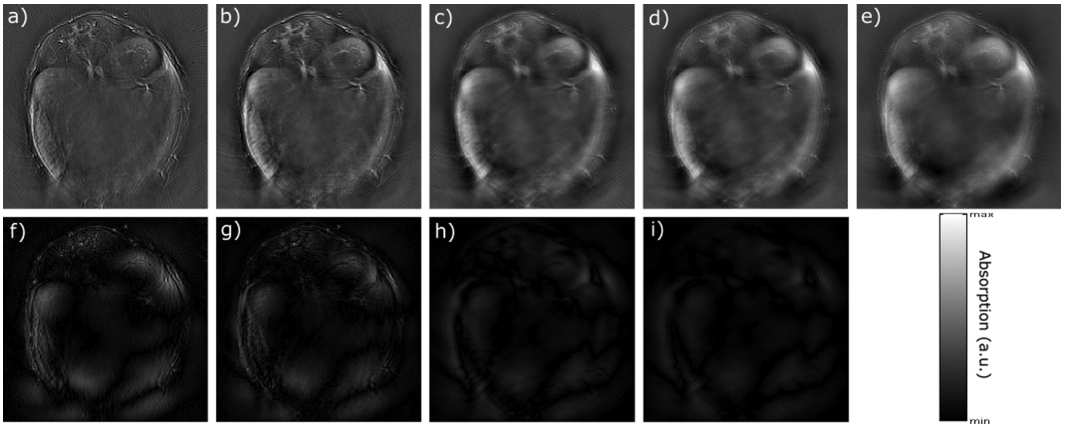

Fig. 4. Estimated relative errors. a) – d) are images reconstructed with 1, 2, 4, and 5 iterations, respectively, using the on-the-fly matrix calculation algorithm. Comparison to the reference image in e), reconstructed with the standard model-based algorithm with 20 iterations, results in estimated relative errors of 58.5%, 37.5%, 17.8%, and 13%, respectively. f) – i) Differences between the reference image and the images in a) – d).

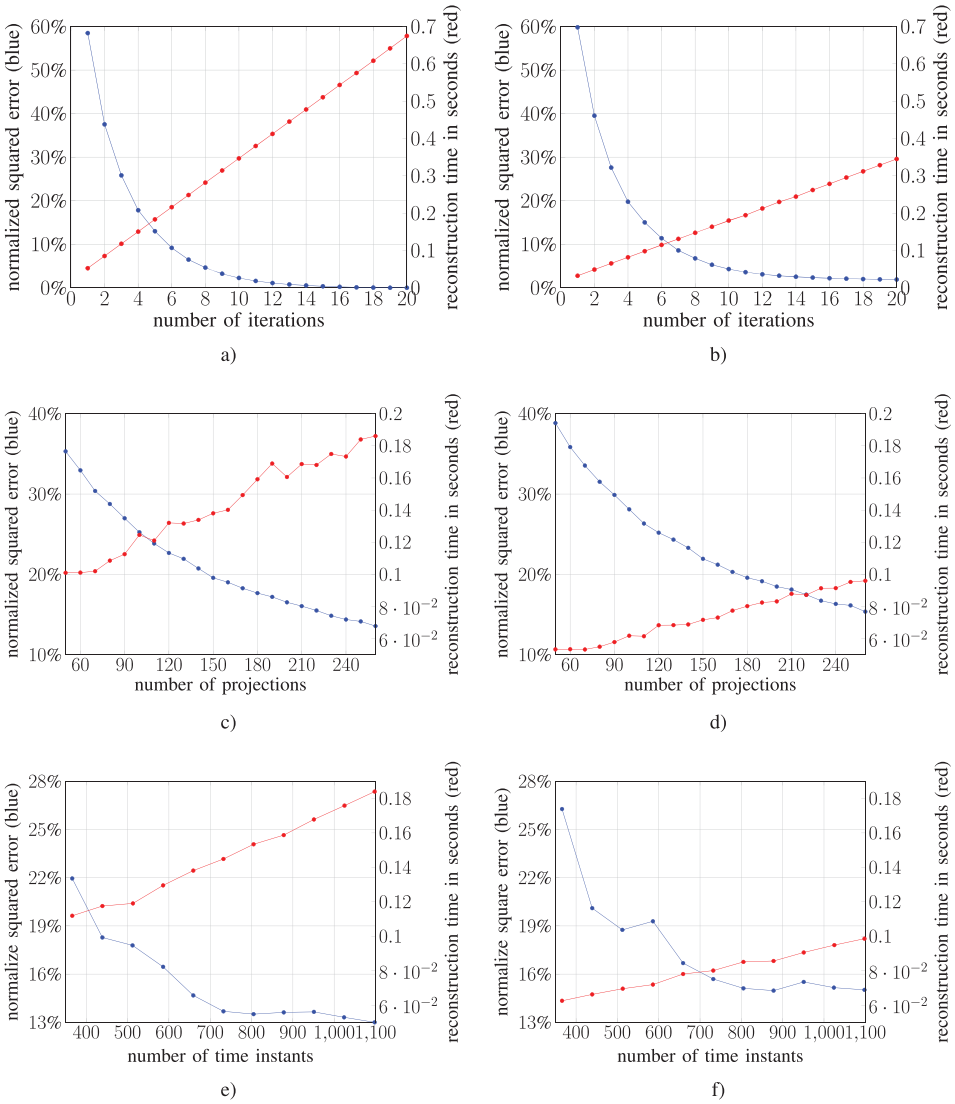

Fig. 5. Influence of different parameters on the image quality and reconstruction speed. Left and right columns show results for the bilinear and circular interpolations, respectively. We vary a)-b) the number of iterations, c)-d) the number of projections and e)-f) the number of time instants.

approach 21 and 27 frames could be reconstructed simultaneously within one second with the two interpolation approaches. As a reference, standard model-based reconstruction on the CPU using the same parameters needs around 94 s to build the

TABLE I
PERFORMANCE OF THE SINGLE- AND MULTIPLE-FRAME RECONSTRUCTIONS USING BILINEAR AND CIRCULAR INTERPOLATION APPROACHES.

	Bilinear interpolation	Circular interpolation
Single frame recon.	6 frames/s	13 frames/s
Multiple frame recon.	21 frames/s	27 frames/s

model-matrix and 0.9 s to reconstruct one frame on an Intel Core i7-4820K CPU @ 3.7 GHz.

IV. DISCUSSION AND CONCLUSIONS

Model-based reconstruction approaches are generally known to render better image quality and accuracy as compared to the approximate analytical inversion schemes [37], [39]. Yet, the analytical (closed-form) inversion schemes have been so far the dominant approach for image reconstruction in optoacoustic tomography due to their fast reconstruction abilities and low memory requirements [28]. In this work, a novel discretization procedure for model-based reconstruction in two-dimensional (cross-sectional) optoacoustic tomography has been introduced. The suggested method allows for parallel implementation on a GPU with relatively low complexity, which is achieved by on-the-fly calculation of the model matrix in each iteration of the inversion procedure. Parallelization and acceleration of the reconstruction on a GPU are equally possible with the other model-based approaches, such as those using pre-calculation of the model matrix. However, memory limitations may restrict applicability of the latter approaches, especially when handling dense image grids or large number of voxels in three-dimensional reconstructions. In contrast, applicability of our methodology does not depend on the size of the model matrix as it only requires the storage of a small look-up table on the GPU memory. Moreover, the look-up table approach significantly accelerates the on-the-fly computation of the matrix elements as only one additional multiplication and division are needed. Here two interpolation approaches were proposed and analyzed. It was demonstrated that reconstructions based on circular interpolation yield slightly reduced image quality as compared to the bilinear interpolation method, yet attain twice the reconstructed frame rates exceeding 10 frames per second for a two-dimensional grid of 200×200 pixels. The suggested reconstruction method was additionally demonstrated to reconstruct multiple frames simultaneously, in which case imaging rate exceeding 20 frames per second were achieved. This performance matches well the pulse repetition and spatial resolution parameters of some common real-time optoacoustic tomography systems for small animal imaging [33], [42]. Yet, the plea for real-time performance is of particular importance when considering clinical translation of the optoacoustic technology using hand-held probes [43], [44]. The proposed framework can further be extended to three-dimensional model-based reconstructions. In this case, the integral in the forward model is performed along a spherical surface instead of a circumference, thus the integration path in the neighborhood of each pixel can be approximated as a plane instead of a straight line. Our future work will address the three-dimensional problem with the suggested methodology in order to further demonstrate the benefits of this approach.

APPENDIX

Bilinear Interpolation:

We derive in this section the analytical expression for $dI(d,\alpha)$ for the bilinear interpolation approach. Due to the symmetry of bilinear interpolation in a square grid it is verified that

$$dI(d,\alpha) = -dI(-d,\alpha), \tag{22}$$

and

$$dI(d,\alpha) = dI(d,\alpha'), \tag{23}$$

being

$$\alpha' = \min\left(|\alpha|, |\alpha - \frac{\pi}{2}|, |\alpha - \pi|, |\alpha - \frac{3\pi}{2}|\right). \tag{24}$$

Then, we only need to derive the analytical expression for $d \geqslant 0$ and for $0 \leqslant \alpha \leqslant \pi/4$. In that case, it can be expressed as a linear combination of the derivative of the integral in the squares indicated in Fig. 1(c).

$$dI(d,\alpha) = dI_{\mathrm{sq1}}(d,\alpha) + dI_{\mathrm{sq2}}(d,\alpha) + dI_{\mathrm{sq4}}(d,\alpha). \tag{25}$$

The straight line along which the integral is calculated can be expressed as

$$x(y) = \frac{d}{\cos\alpha} - y\tan\alpha, \tag{26}$$

where $(x,y) = (0,0)$ represents the position of the pixel. With

$$\widetilde{dI}_{\mathrm{sq1}} = \frac{\partial}{\partial d}\int_{y_a}^{y_b} \frac{(\Delta xy - x(y))\,(\Delta xy - y)}{\Delta xy^2}\frac{dy}{\cos\alpha}, \tag{27}$$

we have

$$dI_{\mathrm{sq1}}(d,\alpha) = \begin{cases} \widetilde{dI}_{\mathrm{sq1}} & \text{for } 0 \leqslant d < \sqrt{2}\Delta xy\cos\left(\frac{\pi}{4} - \alpha\right) \\ 0 & \text{for } d \geqslant \sqrt{2}\Delta xy\cos\left(\frac{\pi}{4} - \alpha\right) \end{cases}. \tag{28}$$

The integration limits y_a and y_b correspond to

$$y_a = \begin{cases} \widetilde{y}_{a,\mathrm{sq1}} & \text{for } \Delta xy\cos\alpha \leqslant d < \sqrt{2}\Delta xy\cos\left(\frac{\pi}{4} - \alpha\right) \\ 0 & \text{for } \Delta xy\sin\alpha \leqslant d < \Delta xy\cos\alpha \\ 0 & \text{for } 0 \leqslant d < \Delta xy\sin\alpha \end{cases} \tag{29}$$

with

$$\widetilde{y}_{a,\mathrm{sq1}} = \frac{d}{\sin\alpha} - \tan\left(\frac{\pi}{2} - \alpha\right)\Delta xy, \tag{30}$$

and

$$y_b = \begin{cases} \Delta xy & \text{for } \Delta xy\cos\alpha \leqslant d < \sqrt{2}\Delta xy\cos\left(\frac{\pi}{4} - \alpha\right) \\ \Delta xy & \text{for } \Delta xy\sin\alpha \leqslant d < \Delta xy\cos\alpha \\ \frac{d}{\sin\alpha} & \text{for } 0 \leqslant d < \Delta xy\sin\alpha \end{cases}. \tag{31}$$

With

$$\widetilde{dI}_{\mathrm{sq2}} = \frac{\partial}{\partial d}\int_{y_a}^{y_b} \frac{(\Delta xy + x(y))\,(\Delta xy - y)}{\Delta xy^2}\frac{dy}{\cos\alpha}, \tag{32}$$

we have

$$dI_{\mathrm{sq2}}(d,\alpha) = \begin{cases} \widetilde{dI}_{\mathrm{sq2}} & \text{for } 0 \leqslant d < \Delta xy\sin\alpha \\ 0 & \text{for } d \geqslant \Delta xy\sin\alpha \end{cases}. \tag{33}$$

In this case, the integration limits y_a and y_b are given by

$$y_a = \frac{d}{\sin\alpha} \quad \text{for } 0 \leqslant d < \Delta xy\sin\alpha \tag{34}$$

and

$$y_b = \Delta xy \quad \text{for } 0 \leqslant d < \Delta xy\sin\alpha. \tag{35}$$

Finally, with

$$\widetilde{dI}_{\mathrm{sq4}} = \frac{\partial}{\partial d}\int_{y_a}^{y_b} \frac{(\Delta xy - x(y))\,(\Delta xy + y)}{\Delta xy^2}\frac{dy}{\cos\alpha}, \tag{36}$$

Algorithm 1: Implementation of kernel $\boldsymbol{A}^{\mathsf{T}}\boldsymbol{u}$

Input : $\boldsymbol{u}$: input vector
c: speed of sound
Δxy: pixel width
L: number of transducers
$\boldsymbol{r}'_1, \cdots, \boldsymbol{r}'_L$: transducer locations
$\boldsymbol{r}_i$: location of pixel i
$\boldsymbol{t}$: time instant vector
dI_{Table}: lookup table for dI values
Output: $(\boldsymbol{A}^{\mathsf{T}}\boldsymbol{u})_i$
$(\boldsymbol{A}^{\mathsf{T}}\boldsymbol{u})_i \leftarrow 0$
for $\ell = 1$ **to** L **do**
  $\boldsymbol{w} \leftarrow \boldsymbol{r}'_\ell - \boldsymbol{r}_i$
  $s \leftarrow |\boldsymbol{w}|$
  $n_1 \leftarrow \left\lceil \frac{-t_0 + \frac{s-\sqrt{2}\Delta xy}{c}}{t_1 - t_0} \right\rceil$
  $n_2 \leftarrow \left\lfloor \frac{-t_0 + \frac{s+\sqrt{2}\Delta xy}{c}}{t_1 - t_0} \right\rfloor$
  for $k = n_1$ **to** n_2 **do**
    $\alpha \leftarrow \arctan(\frac{\boldsymbol{w}_y}{\boldsymbol{w}_x})$
    $d \leftarrow s - ct_k$
    $dI \leftarrow dI_{Table}(d, \alpha)$
    $(\boldsymbol{A}^{\mathsf{T}}\boldsymbol{u})_i \leftarrow (\boldsymbol{A}^{\mathsf{T}}\boldsymbol{u})_i - [\boldsymbol{u}]_k \frac{c}{s-d} dI$

we have

$$dI_{\mathrm{sq4}}(d,\alpha) = \begin{cases} \widetilde{dI}_{\mathrm{sq4}} & \text{for } 0 \leqslant d < \Delta xy \cos\alpha \\ 0 & \text{for } d \geqslant \Delta xy \cos\alpha \end{cases}. \quad (37)$$

The integration limits y_a and y_b can be expressed as

$$y_a = \begin{cases} \widetilde{y}_{a,\mathrm{sq4}} & \text{for } \sqrt{2}\Delta xy \sin\left(\frac{\pi}{4} - \alpha\right) \leqslant d < \Delta xy \cos\alpha \\ -\Delta xy & \text{for } 0 \leqslant d < \sqrt{2}\Delta xy \sin\left(\frac{\pi}{4} - \alpha\right) \end{cases}, \quad (38)$$

with

$$\widetilde{y}_{a,\mathrm{sq4}} = \frac{d}{\sin\alpha} - \tan\left(\frac{\pi}{2} - \alpha\right)\Delta xy, \quad (39)$$

and

$$y_b = \begin{cases} 0 & \text{for } \sqrt{2}\Delta xy \sin\left(\frac{\pi}{4} - \alpha\right) \leqslant d < \Delta xy \cos\alpha \\ 0 & \text{for } 0 \leqslant d < \sqrt{2}\Delta xy \sin\left(\frac{\pi}{4} - \alpha\right) \end{cases}. \quad (40)$$

The exact analytical expressions for $dI(d,\alpha)$ are then calculated with the symbolic toolbox of Matlab and are not displayed here due to its complexity.

Circular Interpolation:

We derive in this section the analytical expression for $dI(d)$ for the circular interpolation approach. The integral along the straight line within the round neighborhood of a pixel equals the area of intersection of a vertical plane cutting the cone illustrated in Fig. 1(d). Since the cone is circularly symmetric, we consider the integral along the straight line $x = d$ without loss of generality. We assume that the distance d is normalized by the pixel size Δxy. The function value of the cone with diameter one along $x = d$ is given by

$$f(y) = \begin{cases} 1 - \sqrt{y^2 + d^2} & \text{for } |y| < \sqrt{1 - d^2} \\ 0 & \text{otherwise} \end{cases}. \quad (41)$$

Algorithm 2: Implementation of kernel $\boldsymbol{A}\boldsymbol{v}$. Note that all coordinates are with respect to the lower left corner of the reconstructed image such that the pixel in row m and column j is at position $r_x = m\Delta xy$ and $r_y = j\Delta xy$

Input : $\boldsymbol{v}$: input vector
c: speed of sound
n: width of the picture in pixels
Δxy: pixel width
$\boldsymbol{r}'_\ell$: transducer location
t: time instant
dI_{Table}: lookup table for dI values
Output: $(\boldsymbol{A}\boldsymbol{v})_\ell$
$(\boldsymbol{A}\boldsymbol{v})_\ell \leftarrow 0$
for $m = 0$ **to** $n - 1$ **do**
  For each row m calculate the intersections of the line $x = m\Delta xy$ with the rings around $\boldsymbol{r}'_\ell$ with radiuses $ct + \sqrt{2}\Delta xy$ and $ct - \sqrt{2}\Delta xy$.
  if *No intersection* **then**
    continue
  if *only the outer ring intersects at* y_1 *and* y_2 *with* $y_1 < y_2$ **then**
    $j_1 \leftarrow \lfloor y_1/\Delta xy \rfloor$
    $j_2 \leftarrow \lceil y_2/\Delta xy \rceil$
  else if *Four intersection points* $y_1 < y_2 < y_3 < y4$ **then**
    $j_1 \leftarrow \lfloor y_1/\Delta xy \rfloor$
    $j_2 \leftarrow \lceil y_2/\Delta xy \rceil$
    $j_3 \leftarrow \lfloor y_3/\Delta xy \rfloor$
    $j_4 \leftarrow \lceil y_4/\Delta xy \rceil$
  for $j = j_1, \ldots, j_2, j_3, \ldots, j_4$ *and* $0 \leq j \leq n - 1$ **do**
    $i \leftarrow$ linear index of the pixel in row m and column j
    $\boldsymbol{w} \leftarrow \boldsymbol{r}'_\ell - \boldsymbol{r}_i$
    $s \leftarrow |\boldsymbol{w}|$
    $\alpha \leftarrow \arctan(\frac{\boldsymbol{w}_y}{\boldsymbol{w}_x})$
    $d \leftarrow s - ct$
    $dI \leftarrow dI_{Table}(d, \alpha)$
    $(\boldsymbol{A}\boldsymbol{v})_\ell \leftarrow (\boldsymbol{A}\boldsymbol{v})_\ell - [\boldsymbol{v}]_i \frac{c}{s-d} dI$

The area integral is thus given by

$$2\sqrt{1-d^2} - \int_{-\sqrt{1-d^2}}^{\sqrt{1-d^2}} \sqrt{y^2 + d^2}\,dy = \sqrt{1-d^2} + \frac{1}{2}d^2\left(\log\left(1 - \sqrt{1-d^2}\right) - \log\left(1 + \sqrt{1-d^2}\right)\right). \quad (42)$$

Consequently, the derivative of integral dI can be obtained by differentiating (42) with respect to d

$$dI(d) = d\left(\log\left(1 - \sqrt{1-d^2}\right) - \log\left(1 + \sqrt{1-d^2}\right)\right). \quad (43)$$

GPU Implementation:

The detailed implementations of $\boldsymbol{A}^{\mathsf{T}}\boldsymbol{u}$ and $\boldsymbol{A}\boldsymbol{v}$ on the GPU kernel are described in Alg. 1 and Alg. 2. Note that we only demonstrate the implementation of the bilinear interpolation since the implementation of the circular interpolation is almost identical.

REFERENCES

[1] G. Paltauf, J. A. Viator, S. A. Prahl, and S. L. Jacques, "Iterative reconstruction algorithm for optoacoustic imaging," *J. Acoust. Soc. Am.*, vol. 112, no. 4, pp. 1536–1544, 2002.

[2] M. Xu and L. V. Wang, "Universal back-projection algorithm for photoacoustic computed tomography," *Phys. Rev. E*, vol. 71, p. 016706, Jan. 2005.

[3] B. E. Treeby and B. T. Cox, "k-wave: Matlab toolbox for the simulation and reconstruction of photoacoustic wave fields," *J. Biomed. Opt.*, vol. 15, no. 2, pp. 021314–021314, 2010.

[4] Y. Hristova, P. Kuchment, and L. Nguyen, "Reconstruction and time reversal in thermoacoustic tomography in acoustically homogeneous and inhomogeneous media," *Inverse Problems*, vol. 24, no. 5, p. 055006, 2008.

[5] R. Schulze *et al.*, "On the use of frequency-domain reconstruction algorithms for photoacoustic imaging," *J. Biomed. Opt.*, vol. 16, no. 8, pp. 086002–086002, 2011.

[6] P. Mohajerani, S. Kellnberger, and V. Ntziachristos, "Frequency domain optoacoustic tomography using amplitude and phase," *Photoacoustics*, vol. 2, no. 3, pp. 111–118, 2014.

[7] K. P. Köstli *et al.*, "Optoacoustic imaging using a three-dimensional reconstruction algorithm," *IEEE J. Sel. Topics Quant. Electron.*, vol. 7, no. 6, pp. 918–923, Nov./Dec. 2001.

[8] K. Wang *et al.*, "An imaging model incorporating ultrasonic transducer properties for three-dimensional optoacoustic tomography," *IEEE Trans. Med. Imag.*, vol. 30, no. 2, pp. 203–214, Feb. 2011.

[9] K. Mitsuhashi, K. Wang, and M. A. Anastasio, "Investigation of the far-field approximation for modeling a transducer's spatial impulse response in photoacoustic computed tomography," *Photoacoustics*, vol. 2, no. 1, pp. 21–32, 2014.

[10] C. Lutzweiler and D. Razansky, "Optoacoustic imaging and tomography: Reconstruction approaches and outstanding challenges in image performance and quantification," *Sensors*, vol. 13, no. 6, pp. 7345–7384, 2013.

[11] A. Rosenthal, V. Ntziachristos, and D. Razansky, "Acoustic inversion in optoacoustic tomography: A review," *Curr. Med. Imag. Rev.*, vol. 9, no. 4, p. 318, 2013.

[12] L. Ding, X. L. Deán-Ben, C. Lutzweiler, D. Razansky, and V. Ntziachristos, "Efficient non-negative constrained model-based inversion in optoacoustic tomography," *Phys. Med. Biol.*, vol. 60, no. 17, p. 6733, 2015.

[13] X. L. Deán-Ben, D. Razansky, and V. Ntziachristos, "The effects of acoustic attenuation in optoacoustic signals," *Phys. Med. Biol.*, vol. 56, no. 18, p. 6129, 2011.

[14] X. L. Deán-Ben, V. Ntziachristos, and D. Razansky, "Effects of small variations of speed of sound in optoacoustic tomographic imaging," *Med. Phys.*, vol. 41, no. 7, p. 073301, 2014.

[15] M. Kneipp *et al.*, "Effects of the murine skull in optoacoustic brain microscopy," *J. Biophoton.*, vol. 9999, 2015.

[16] A. Rosenthal, V. Ntziachristos, and D. Razansky, "Model-based optoacoustic inversion with arbitrary-shape detectors," *Med. Phys.*, vol. 38, no. 7, pp. 4285–4295, 2011.

[17] D. Queirós *et al.*, "Modeling the shape of cylindrically focused transducers in three-dimensional optoacoustic tomography," *J. Biomed. Opt.*, vol. 18, no. 7, pp. 076014–076014, 2013.

[18] X. L. Deán-Ben, R. Ma, A. Rosenthal, V. Ntziachristos, and D. Razansky, "Weighted model-based optoacoustic reconstruction in acoustic scattering media," *Phys. Med. Biol.*, vol. 58, no. 16, p. 5555, 2013.

[19] C. Huang, L. Nie, R. W. Schoonover, L. V. Wang, and M. A. Anastasio, "Photoacoustic computed tomography correcting for heterogeneity and attenuation," *J. Biomed. Opt.*, vol. 17, no. 6, pp. 0612111–0612115, 2012.

[20] X. L. Deán-Ben, V. Ntziachristos, and D. Razansky, "Acceleration of optoacoustic model-based reconstruction using angular image discretization," *IEEE Trans. Med. Imag.*, vol. 31, no. 5, pp. 1154–1162, May 2012.

[21] A. Rosenthal, D. Razansky, and V. Ntziachristos, "Fast semi-analytical model-based acoustic inversion for quantitative optoacoustic tomography," *IEEE Trans. Med. Imag.*, vol. 29, no. 6, pp. 1275–1285, Jun. 2010.

[22] A. Rosenthal, T. Jetzfellner, D. Razansky, and V. Ntziachristos, "Efficient framework for model-based tomographic image reconstruction using wavelet packets," *IEEE Trans. Med. Imag.*, vol. 31, no. 7, pp. 1346–1357, Jul. 2012.

[23] Y. Han, S. Tzoumas, A. Nunes, V. Ntziachristos, and A. Rosenthal, "Sparsity-based acoustic inversion in cross-sectional multiscale optoacoustic imaging," *Med. Phys.*, vol. 42, no. 9, pp. 5444–5452, 2015.

[24] S. Bu *et al.*, "Model-based reconstruction integrated with fluence compensation for photoacoustic tomography," *IEEE Trans. Biomed. Eng.*, vol. 59, no. 5, pp. 1354–1363, May 2012.

[25] C. Lutzweiler, X. L. Deán-Ben, and D. Razansky, "Expediting model-based optoacoustic reconstructions with tomographic symmetries," *Med. Phys.*, vol. 41, no. 1, p. 013302, 2014.

[26] M. A. A. Caballero, J. Gateau, X.-L. Déan-Ben, and V. Ntziachristos, "Model-based optoacoustic image reconstruction of large three-dimensional tomographic datasets acquired with an array of directional detectors," *IEEE Trans. Med. Imag.*, vol. 33, no. 2, pp. 433–443, Feb. 2014.

[27] K. Wang *et al.*, "Accelerating image reconstruction in three-dimensional optoacoustic tomography on graphics processing units," *Med. Phys.*, vol. 40, no. 2, p. 023301, 2013.

[28] X. L. Dean-Ben, A. Ozbek, and D. Razansky, "Volumetric real-time tracking of peripheral human vasculature with GPU-accelerated three-dimensional optoacoustic tomography," *IEEE Trans. Med. Imag.*, vol. 32, no. 11, pp. 2050–2055, Nov. 2013.

[29] K. Wang, J. Xia, C. Li, L. V. Wang, and M. A. Anastasio, "Fast spatiotemporal image reconstruction based on low-rank matrix estimation for dynamic photoacoustic computed tomography," *J. Biomed. Opt.*, vol. 19, no. 5, pp. 056007–056007, 2014.

[30] C. Lutzweiler, S. Tzoumas, A. Rosenthal, V. Ntziachristos, and D. Razansky, "High-throughput sparsity-based inversion scheme for optoacoustic tomography," *IEEE Trans. Med. Imag.*, vol. 35, no. 2, pp. 674–684, Feb. 2016.

[31] J. Xia *et al.*, "Whole-body ring-shaped confocal photoacoustic computed tomography of small animals in vivo," *J. Biomed. Opt.*, vol. 17, no. 5, pp. 0505061–0505063, 2012.

[32] L. Xiang, B. Wang, L. Ji, and H. Jiang, "4-d photoacoustic tomography," *Sci. Rep.*, vol. 3, 2013.

[33] X. L. Deán-Ben, E. Bay, and D. Razansky, "Functional optoacoustic imaging of moving objects using microsecond-delay acquisition of multispectral three-dimensional tomographic data," *Sci. Rep.*, vol. 4, 2014.

[34] V. È. Gusev, "Laser optoacoustics," *Am. Inst. Phys.*, 1993.

[35] B. T. Cox, S. Kara, S. R. Arridge, and P. C. Beard, "k-space propagation models for acoustically heterogeneous media: Application to biomedical photoacoustics," *J. Acoust. Soc. Am.*, vol. 121, no. 6, pp. 3453–3464, 2007.

[36] L. V. Wang, *Photoacoustic Imaging and Spectroscopy*. Boca Raton, FL: CRC Press, 2009.

[37] X. L. Dean-Ben, A. Buehler, V. Ntziachristos, and D. Razansky, "Accurate model-based reconstruction algorithm for three-dimensional optoacoustic tomography," *IEEE Trans. Med. Imag.*, vol. 31, no. 10, pp. 1922–1928, Oct. 2012.

[38] C. C. Paige and M. A. Saunders, "LSQR: An algorithm for sparse linear equations and sparse least squares," *ACM Trans. Math. Software*, vol. 8, no. 1, pp. 43–71, 1982.

[39] K. Wang, R. Su, A. A. Oraevsky, and M. A. Anastasio, "Investigation of iterative image reconstruction in three-dimensional optoacoustic tomography," *Phys. Med. Biol.*, vol. 57, no. 17, p. 5399, 2012.

[40] D. Razansky, A. Buehler, and V. Ntziachristos, "Volumetric real-time multispectral optoacoustic tomography of biomarkers," *Nature Protocols*, vol. 6, no. 8, pp. 1121–1129, 2011.

[41] A. Dima, N. C. Burton, and V. Ntziachristos, "Multispectral optoacoustic tomography at 64, 128, and 256 channels," *J. Biomed. Opt.*, vol. 19, no. 3, pp. 036021–036021, 2014.

[42] L. V. Wang and S. Hu, "Photoacoustic tomography: In vivo imaging from organelles to organs," *Science*, vol. 335, no. 6075, pp. 1458–1462, 2012.

[43] A. Dima and V. Ntziachristos, "Non-invasive carotid imaging using optoacoustic tomography," *Opt. Exp.*, vol. 20, no. 22, pp. 25044–25057, 2012.

[44] A. Buehler, M. Kacprowicz, A. Taruttis, and V. Ntziachristos, "Real-time handheld multispectral optoacoustic imaging," *Opt. Lett.*, vol. 38, no. 9, pp. 1404–1406, 2013.

Appendix B

Publication: Efficient Three-dimensional Model-based Reconstruction Scheme for Arbitrary Optoacoustic Acquisition Geometries

Efficient 3-D Model-Based Reconstruction Scheme for Arbitrary Optoacoustic Acquisition Geometries

Lu Ding, Xosé Luís Deán-Ben, and Daniel Razansky

***Abstract*— Optimal optoacoustic tomographic sampling is often hindered by the frequency-dependent directivity of ultrasound sensors, which can only be accounted for with an accurate 3-D model. Herein, we introduce a 3-D model-based reconstruction method applicable to optoacoustic imaging systems employing detection elements with arbitrary size and shape. The computational complexity and memory requirements are mitigated by introducing an efficient graphic processing unit (GPU)-based implementation of the iterative inversion. On-the-fly calculation of the entries of the model-matrix via a small look-up table avoids otherwise unfeasible storage of matrices typically occupying more than 300GB of memory. Superior imaging performance of the suggested method with respect to standard optoacoustic image reconstruction methods is first validated quantitatively using tissue-mimicking phantoms. Significant improvements in the spatial resolution, contrast to noise ratio and overall 3-D image quality are also reported in real tissues by imaging the finger of a healthy volunteer with a hand-held volumetric optoacoustic imaging system.**

***Index Terms*— Optoacoustic tomography, photoacoustic tomography, model-based inversion, volumetric imaging.**

I. Introduction

OPTOACOUSTIC (OA) imaging at depths beyond the transport mean free path in living biological tissues (∼1 mm) relies on the optimal arrangement of ultrasound sensors and accuracy of the acoustic inversion algorithm for rendering quantitative high-quality reconstructions [1], [2]. The accuracy in mapping light absorption within a three-dimensional (3-D) region by means of OA excitation is determined by the available tomographic coverage and detection bandwidth [3], [4]. In response, OA imaging systems are commonly based on acquisition geometries that maximize the detection angular coverage around the imaged volume [5]–[8].

Ideally, point-like detectors exhibiting infinite bandwidth would render the best quality reconstructions in optoacoustic tomography (OAT). In reality, finite-size detectors are used instead to provide sufficient sensitivity, particularly in real-time imaging applications that do not permit signal averaging [9]. The associated frequency-dependent directivity of the finite-sized sensing elements may lead to additional artifacts in the reconstructed images [10], [11]. In some cases, the transducer aperture is purposely shaped such that the dimensionality of the imaging (tomographic) problem is reduced into two dimensions or a single dimension. For example, cylindrically-focused transducers are used in cross-sectional OAT, where image reconstruction is performed in two-dimensional (2D) slices through a 3-D object [12], [13]. The resulting 2D reconstruction problem is theoretically simpler and less computationally demanding than in the 3-D imaging case, and real-time OAT reconstructions were achieved with both analytical backprojection-type inversion algorithms and more accurate model-based (MB) schemes [14]. The latter were also shown efficient in accounting for the transducer dimensions [10], [11], [15] and acoustic heterogeneities in the sample [16], [17] as well as for negative artifact removal [18]. Another imaging approach employing dimensionality reduction is acoustic-resolution OA microscopy, where a large-aperture spherically-focused transducer is raster-scanned to form images [19]. In this case, one may assume the collected signals to represent depth-profiles for each position of the transducer, so that 2D or 3-D images can be rendered by simply stacking up the individual OA waveforms. However, also in this case, a more accurate image reconstruction approach would generally account for the frequency-dependent sensitivity field of the transducer [20], [21].

It is important to take into account that dimensionality reduction readily introduces modeling errors since the actual size and shape of the transducers cannot be properly accounted for within the one or two dimensions as ultrasound propagation is inherently three dimensional. Consequently, a 3-D model is generally necessary for optimizing image reconstruction, which significantly elevates the computational complexity due to the increased number of variables. In fact, 3-D modeling is further challenged by the vast amount of memory required to store the resulting model matrices. One approach seeks to reduce the memory overhead by calculating the model-matrix

Manuscript received February 21, 2017; revised May 2, 2017; accepted May 8, 2017. Date of publication May 12, 2017; date of current version August 31, 2017. This work was supported by the European Research Council under Grant ERC-2015-CoG-682379 and Grant ERC-2015-PoC-692952 *(Corresponding author: Daniel Razansky.)*.

L. Ding is with the Helmholtz Center Munich, Institute for Biological and Medical Imaging, Oberschleißheim, Germany, and also with the Faculty of Medicine and the Faculty of Electrical Engineering, Technical University of Munich, 85764 Munich, Germany.

X. L. Deán-Ben is with the Helmholtz Center Munich, Institute for Biological and Medical Imaging, Oberschleißheim, Germany.

D. Razansky is with the Helmholtz Center Munich, Institute for Biological and Medical Imaging, Oberschleißheim, Germany, and also with the Faculty of Medicine and the Faculty of Electrical Engineering, Technical University of Munich, 85764 Munich, Germany (e-mail: dr@tum.de).

Color versions of one or more of the figures in this paper are available online at http://ieeexplore.ieee.org.

Digital Object Identifier 10.1109/TMI.2017.2704019

on-the-fly within each step of an iterative algorithm, which can be further accelerated via graphics processing unit (GPU) implementation [23]. Recently, we introduced a new discretization method to obtain a linear forward model from the continuous 2D OA wave equation [14]. This has allowed for a more efficient GPU implementation of the inversion procedure as only a few operations are required to calculate entries of the model-matrix. Hence, parallel computations can be performed with extremely low memory overhead.

The current work deals with a generalization of the efficient MB inversion framework for full 3-D OA reconstruction problems, for which the low-memory overhead becomes paramount. We further extend the methodology to explicitly account for the 3-D transducer shape. The improvement in imaging performance is demonstrated in numerical simulations and experimental measurements in phantoms and living tissues.

II. Methods

A. Discretization of the 3-D Time-Domain OA Forward Model

When the duration of the excitation laser pulse is short enough to fulfill both the acoustic and thermal confinement regimes, the pressure field emitted due to the optical excitation as a function of space $\boldsymbol{r}$ and time t can be expressed as [24]

$$p(\boldsymbol{r},t)=\frac{\Gamma}{4\pi c}\frac{\partial}{\partial t}\frac{1}{ct}\int_{S(\boldsymbol{r},t)}H(\boldsymbol{r}')d\boldsymbol{r}', \tag{1}$$

where $H(\boldsymbol{r}')$ is the absorbed energy per unit volume in the tissue, Γ is the dimensionless Grüneisen parameter and c is the speed of sound. In the following, we omit the constant term $\frac{\Gamma}{4\pi c}$ for simplicity since it does not affect model-based reconstruction. The integral is performed along a spherical surface $S(\boldsymbol{r},t)$ with radius $|\boldsymbol{r}'-\boldsymbol{r}|=ct$. The discretization of the forward model in (1) is done by considering N voxels on a Cartesian grid representing a volume enclosing all the OA sources. The location of each image voxel is represented by $\boldsymbol{r}_i$. The amount of absorbed energy at an arbitrary location in space $H(\boldsymbol{r}')$ is approximated by the weighted superposition of interpolation functions $K(\boldsymbol{r}')$ shifted to the different voxel positions $\boldsymbol{r}_i$, i.e.,

$$H(\boldsymbol{r}')\approx\sum_{i=1}^{N}h_i K(\boldsymbol{r}'-\boldsymbol{r}_i), \tag{2}$$

where h_i is the absorption at voxel i. Then, (1) can be expressed as

$$p(\boldsymbol{r},t)=\sum_{i=1}^{N}h_i\frac{\partial}{\partial t}\frac{1}{ct}\int_{S(\boldsymbol{r},t)}K(\boldsymbol{r}'-\boldsymbol{r}_i)d\boldsymbol{r}'. \tag{3}$$

By defining

$$p_i(\boldsymbol{r},t)=\frac{\partial}{\partial t}\frac{1}{ct}\int_{S(\boldsymbol{r},t)}K(\boldsymbol{r}'-\boldsymbol{r}_i)d\boldsymbol{r}', \tag{4}$$

(3) is reduced to

$$p(\boldsymbol{r},t)=\sum_{i=1}^{N}h_i\,p_i(\boldsymbol{r},t). \tag{5}$$

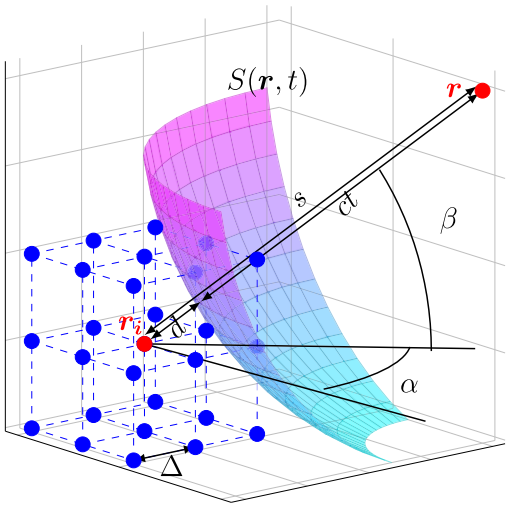

Fig. 1. 3-D discretization of the OA forward model on a Cartesian grid. Intersection of the spherical integral surface $S(\boldsymbol{r},t)$ with the Δ-neighborhood of voxel i. The positions of voxel i and the measurement location are denoted by $\boldsymbol{r}_i$ and $\boldsymbol{r}$, respectively. The distance between $\boldsymbol{r}_i$ and $\boldsymbol{r}$ is denoted by s and the distance between $\boldsymbol{r}_i$ and the spherical surface is denoted by d. The azimuth and elevation angles are denoted by α and β respectively.

$p_i(\boldsymbol{r},t)$ corresponds to the contribution of a unit absorption at voxel i to the pressure wave detected at location $\boldsymbol{r}$ and time point t.

A variety of interpolation methods can be applied for calculating $K(\boldsymbol{r}'-\boldsymbol{r}_i)$. Herein, the standard trilinear interpolation method is suggested [24]. Trilinear interpolation represents a trade-off between accuracy and computational complexity. Higher order interpolation methods may further improve image quality. However, modeling errors due to acoustic heterogeneities or the frequency response of the transducer(s) are generally the main error source. The corresponding interpolation function is given by

$$K(\boldsymbol{r})=\begin{cases}\left(1-\frac{|x|}{\Delta}\right)\left(1-\frac{|y|}{\Delta}\right)\left(1-\frac{|z|}{\Delta}\right) & \text{for } \|\boldsymbol{r}\|_\infty<\Delta\\ 0 & \text{for } \|\boldsymbol{r}\|_\infty\geqslant\Delta,\end{cases} \tag{6}$$

where Δ is the voxel size (Fig. 1) and $\boldsymbol{r}=(x,y,z)$. Non-zero values of the interpolation function only exist in the Δ-neighborhood of voxel i, i.e. h_i only contributes to $H(\boldsymbol{r}')$ when $\boldsymbol{r}'$ is less than a voxel away from voxel i. Thereby, the surface integral in (3) differs from zero only when the surface intersects the Δ-neighborhood, as illustrated in Fig. 1. Let the distance between the measuring location $\boldsymbol{r}$ and the voxel location $\boldsymbol{r}_i$ be denoted by s. Since the voxel size Δ is typically several orders of magnitude smaller than s, the spherical surface integral in the Δ neighborhood of the $\boldsymbol{r}_i$ voxel can be approximated by a planar surface integral. Errors may be produced in the near field region for optoacoustic sensing elements placed in direct contact with the region of interest [25]. The integral value depends on the distance d from its surface (denoted by S') to the voxel $\boldsymbol{r}_i$, and on the direction from $\boldsymbol{r}_i$ to $\boldsymbol{r}'$, which can be parameterized with

two angles α and β. Thus, with $ct = s - d$, (4) can be reformulated as

$$p_i(\boldsymbol{r},t) = -c\frac{\partial}{\partial d}\frac{1}{s-d}\int_{S'(\boldsymbol{r},t)} K(\boldsymbol{r}'-\boldsymbol{r}_i)d\boldsymbol{r}' = -\frac{c}{(s-d)^2}I(d,\alpha,\beta) - \frac{c}{s-d}dI(d,\alpha,\beta), \quad (7)$$

with

$$I(d,\alpha,\beta) = \int_{S'(\boldsymbol{r},t)} K(\boldsymbol{r}'-\boldsymbol{r}_i)d\boldsymbol{r}' \quad (8)$$

and

$$dI(d,\alpha,\beta) = \frac{\partial}{\partial d}\int_{S'(\boldsymbol{r},t)} K(\boldsymbol{r}'-\boldsymbol{r}_i)d\boldsymbol{r}'. \quad (9)$$

Considering that $dI(d,\alpha,\beta)$ is in the order of $\frac{\max(I(d,\alpha,\beta))}{\Delta}$, the first term in (7) can be neglected, i.e.,

$$p_i(\boldsymbol{r},t) \approx -\frac{c}{s-d}dI(d,\alpha,\beta). \quad (10)$$

A detailed description of the calculation of $dI(d,\alpha,\beta)$ is included in Appendix B.

The discrete forward model in (5) can be used to define an inverse problem for the OA reconstruction. Specifically, collecting the time-discrete pressure signals from all transducers in a vector $\boldsymbol{p}$ and the optical absorption values at pixel positions h_i in a vector $\boldsymbol{h}$, the corresponding linear model can be expressed in a matrix form as

$$\boldsymbol{p} = \boldsymbol{A}\boldsymbol{h}, \quad (11)$$

where $\boldsymbol{A}$ is the model matrix representing a particular reconstruction problem. The columns of $\boldsymbol{A}$ represent the OA signals associated to each voxel of the grid. The reconstruction problem consists in finding the absorption vector $\hat{\boldsymbol{h}}$ for which the theoretical model better matches the experimentally measured pressure signals $\boldsymbol{p}_m$. Typically, the aim is to solve a least squares problem defined as

$$\hat{\boldsymbol{h}} = \arg\min_{\boldsymbol{h}} \|\boldsymbol{A}\boldsymbol{h} - \boldsymbol{p}_m\|_2^2, \quad (12)$$

where additional regularization terms may further be needed in some cases [26], [27]. The least squares problem in (12) can be solved iteratively e.g. with the LSQR method [22].

B. Transducer Shape

Most ultrasound sensors have a finite aperture (size) which directly corresponds to their directional sensitivity. Thereby, reconstruction algorithms assuming point-like sensors would usually result in inaccurate reconstructions. In particular, the sensitivity of commonly used piezoelectric sensors scales with size, which in turn increases their directivity. The signal p_{S_T} collected by a finite-size transducer perfectly matched to water can be assumed to be proportional to the integral of the pressure on the transducer surface, i.e., it can be approximated in arbitrary units as

$$p_{S_\mathrm{T}} \approx \int_{S_\mathrm{T}} p(\boldsymbol{r},t)d\boldsymbol{r}. \quad (13)$$

The integral in (13) can be discretized by dividing the surface S_T into a finite set of surface elements with positions $\boldsymbol{r}_j$ and area $\Delta\boldsymbol{r}_j$. Thereby

$$p_{S_\mathrm{T}} \approx \sum_{j=0}^{M} p(\boldsymbol{r}_j,t)\Delta\boldsymbol{r}_j, \quad (14)$$

where M is the number of divided surface elements of one transducer. Assuming all transducers have the same shape, the linear forward model is altered as follows

$$\boldsymbol{p} \approx \sum_{j=0}^{M} \boldsymbol{A}_j\Delta\boldsymbol{r}_j\boldsymbol{h}. \quad (15)$$

That is, the model matrix is replaced by a weighted sum of M model matrices, one for each discrete surface element of the transducer.

Clearly, the computational complexity of methods involving matrix-vector products increases linearly with the number of surface elements M. On the other hand, the discretization of the transducer surface into sub-areas allows accounting for the frequency-dependent directivity.

C. GPU Implementation

In each iteration of the LSQR algorithm, the most time consuming operations are the two matrix-vector products $\boldsymbol{A}\boldsymbol{v}$ and $\boldsymbol{A}^\mathsf{T}\boldsymbol{u}$, where $\boldsymbol{v}$ and $\boldsymbol{u}$ are updated for subsequent iterations. As previously mentioned, the interpolation function $K(\boldsymbol{r}')$ only has a small support in the order of the voxel size [see (6)]. Therefore, for most voxel positions $\boldsymbol{r}_i$, the integral in (4) is zero, and hence the model-matrix is sparse. However, despite its sparsity, the size of the 3-D model-matrix is generally very large, which leads to computational inefficiency and memory overhead.

In order to accelerate the inversion process, computations can be parallelized on a GPU. However, it is not possible to store the entire model matrix on the GPU due to the large memory requirements. Instead, the matrix-vector multiplications must be calculated on-the-fly for each iteration of the inversion process. The discretization approach introduced in section II-A is particularly efficient for on-the-fly calculations since the term $dI(d,\alpha,\beta)$ in (9) is independent of the voxel position and only depends on three parameters. Due to symmetries, the values of $dI(d,\alpha,\beta)$ for $d \in [0, \sqrt{3}\Delta]$, $\alpha \in [0, \frac{\pi}{4}]$ and $\beta \in [0, \frac{\pi}{2}]$ are pre-calculated and saved in a small look-up table as suggested in [14] for the 2D case. Thus, the calculation of the entries of the model matrix $p_i(\boldsymbol{r},t)$ simply involves a small number of floating-point operations and a search in a look-up table. For reconstruction in this paper, we used a look-up table with 50 values for d, α and β respectively.

The computational complexity of the suggested approach is higher than that of the CPU implementation of the LSQR algorithm with a pre-calculated model matrix since such model matrix needs to be repetitively generated. However, the order of complexity remains the same as the complexity per iteration of the LSQR method is directly proportional to the number of non-zero entries of the model matrix. The order of complexity

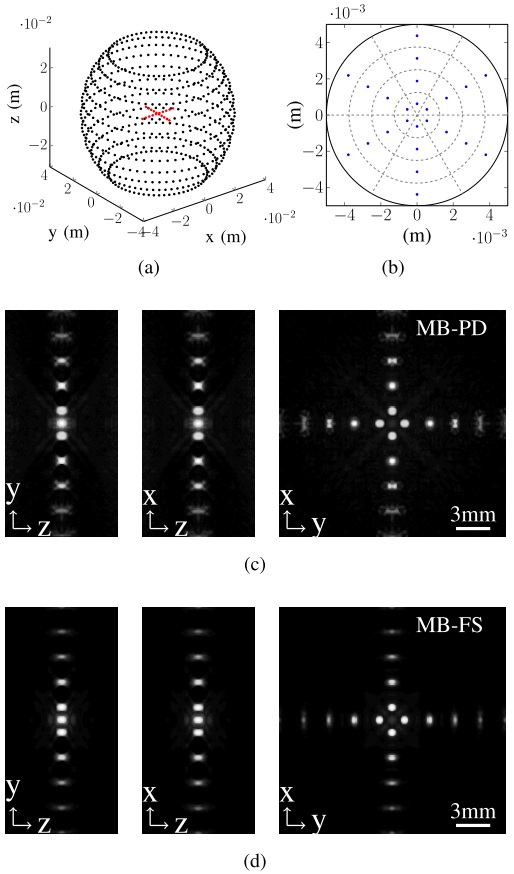

Fig. 2. The simulated scanning geometry. a) Positions of the transducers (black dots) and absorbing microspheres (red dots). b) Discretization of one transducer surface into 24 sub-areas with the corresponding central positions being indicated (blue dots). c) MIPs of the 3-D images reconstructed with the MB-PD method. d) MIPs of the 3-D images reconstructed with the MB-FS method.

is $O(gNL)$ where g is the oversampling ratio, N is the number of voxels and L is the number of transducers.

The GPU implementation of the two most important kernels corresponding to the operations $\boldsymbol{A}^{\mathsf{T}}\boldsymbol{u}$ and $\boldsymbol{A}\boldsymbol{v}$ are further described in detail in Appendix A.

D. Numerical Simulations

The performance of the suggested GPU-based MB reconstruction method was first tested in numerical simulations. Fig. 2a) depicts the simulated scanning geometry, where each black dot represents the center of a given transducer position and the red dots represent 300μm microspheres placed in the central region of the imaged volume. Specifically, an OA setup with unfocused transducers (diameter 1cm) fully surrounding the image object was simulated, where 3780 transducer scanning positions covering an angle of 360° around the imaged object and 100° in the elevational direction were considered. The pressure signals were simulated by discretizing the transducer shape into 24 surface elements (Fig. 2b), where the pressure waves at the central position of each surface element were calculated analytically [28]. MB reconstructions were performed by assuming point detectors and by considering finite-sized sensors discretized to 24 surface elements. In both cases, 2000 time instants sampled at 40 MHz were considered for each transducer position and a region of interest of $2 \times 2 \times 1\text{cm}^3$ was discretized to 4 million voxels.

E. Experimental Measurements

The MB reconstruction approach was subsequently tested experimentally. For this, a custom-made 3-D OA imaging system was used, which is described in detail elsewhere [29]. In short, it consists of an array of 512 adjacent piezoelectric elements densely distributed on a spherical surface. The spherical aperture covers an angle of 140° (solid angle of 1.316π). Each element has an approximate size of $2.5 \times 2.5\text{mm}^2$ and a central frequency of 10MHz. The illumination source consists of a short-pulsed (< 10ns) optical parametric oscillator (OPO)-based laser (Innolas Laser GmbH, Krailling, Germany). The excitation light is guided via a fiber bundle through a 5mm cylindrical cavity in the transducer array. The recorded raw optoacoustic signals from all the channels were simultaneously sampled at 40 mega samples per second by a custom-made digital acquisition system.

In the first experiment, a 50μm diameter absorbing microsphere was embedded in a light scattering phantom (phantom 1) created by molding 1.3% of agar powder (by weight) and 1% Intralipid (by volume). The phantom was first positioned so that the microsphere was located at the geometrical center of the spherical array's surface, toward which all the array elements are directed. Subsequently, the phantom was scanned with the angular-dependent sensitivity of the transducer elements playing a increasing role as the microsphere moves toward periphery. In the second experiment, a group of 50μm diameter microspheres were randomly distributed in another scattering agar-based phantom with (phantom 2). Both phantoms were imaged by setting the laser illumination wavelength to 720nm. The energy density at the sample surface was approximately 19mJ/cm^2. The recorded signals were averaged 500 times to enhance the signal-to-noise ratio (SNR).

A third experiment was done to test the performance of the suggested algorithm in real biological tissues. For this, the finger of a healthy volunteer was imaged with the same OA system by setting the laser wavelength to 800nm to ensure deeper tissue penetration. The OA system was operated in a hand-held mode, hence no signal averaging was possible due to motion.

In order to best evaluate the algorithm's performance, the images in all the experiments were reconstructed with three different methods, namely, the back-projection (BP) algorithm [9], the MB-based algorithm introduced in section II considering point detectors (MB-PD) and the same MB algorithm but accounting for the finite size and shape of the transducers (MB-FS). Since the region of interest is small compared to the distance of the transducers to the region of interest, the weighting factor in [30] marginally affects the results and was not considered. Each individual detection element of the array was split into 16 surface elements for reconstructing with the MB-FS method. Before reconstruction, the acquired signals were band-pass filtered between 0.5MHz and 15MHz.

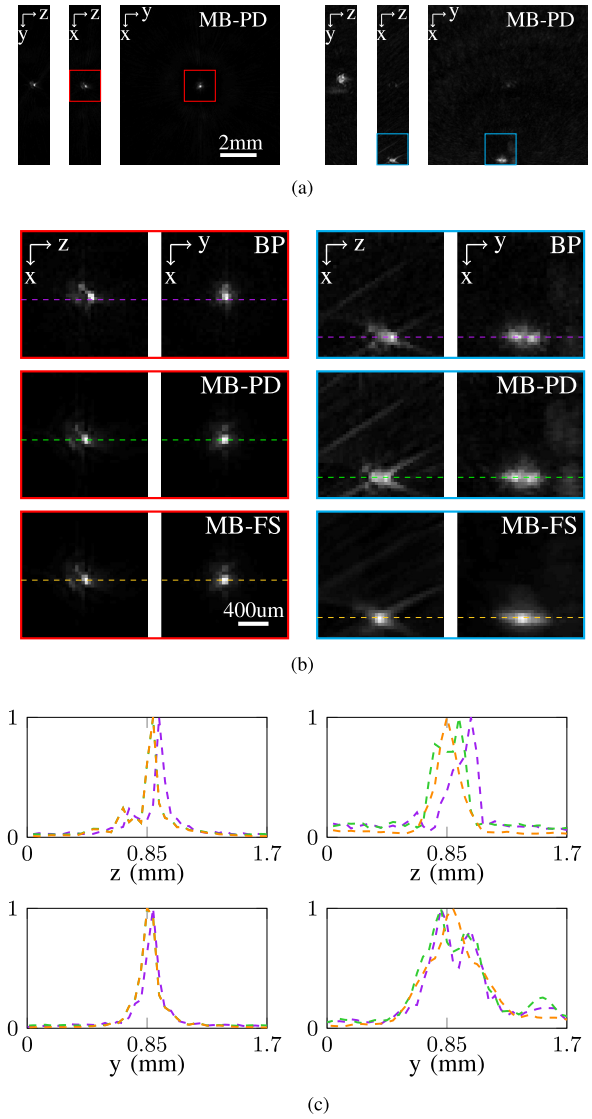

Fig. 3. Imaging results from the phantom containing a single microsphere. a) MIPs of the MB-PD-based reconstructions for the central and peripheral microsphere positions. b) Zoom-ins of the regions of interest marked in red and blue reconstructed with all three methods. c) Line profiles over the images in b). Profiles along the z (first row) and y (second row) directions are plotted for both the central (left) and peripheral (right) positions of the sphere. Yellow, green and magenta profiles correspond to images reconstructed with the BP, the MB-PD and the MB-FS methods, respectively, as indicated in b).

All experimental reconstructions were performed using an image grid of $200 \times 200 \times 200$ voxels and 5 LSQR iterations. The computations were performed on a AMD Radeon HD 7900 series GPU. The reconstruction was implemented using the OpenCL framework and executed in Matlab (MathWorks, Natick, MA) as a mex function.

III. Results

A. Simulations

Fig. 2 shows the results of the numerical simulations described in section II-D, demonstrating the benefits of

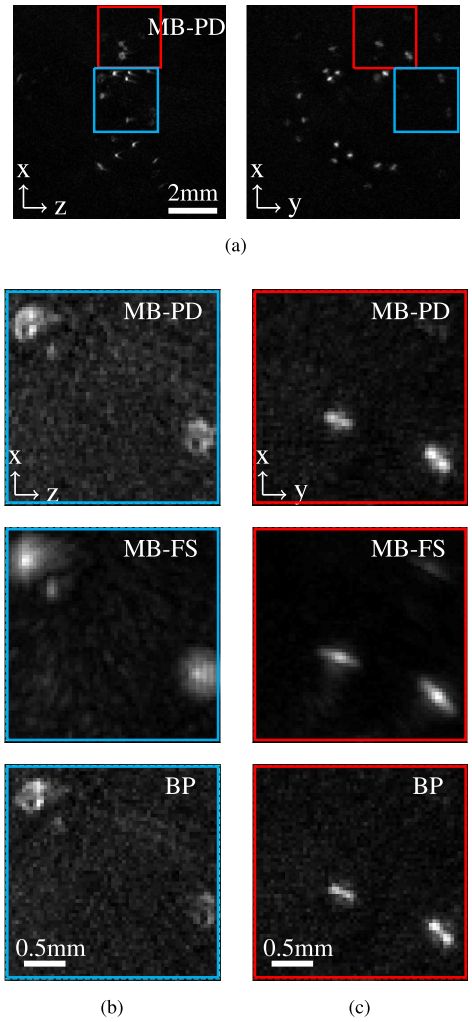

Fig. 4. Experimental results for the phantom with randomly distributed microspheres. a) MIPs of the images reconstructed with the MB-PD method. b) and c) Zoom-in images of the blue and red rectangular regions marked in a) for all three methods.

modeling the transducer shape. In particular, Fig. 2c) and d) show the maximum intensity projections (MIPs) of the 3-D images reconstructed with the MB-PD and MB-FS methods, respectively. It can be readily recognized that the shape of the reconstructed microspheres located away from the center of the field of view is distorted by the MB-PD method (Fig. 2c). Specifically, the lateral blur generated by the non-ideal spatial impulse response of the transducers is readily visible [10]. On the contrary, the shape is restored when the MB-FS is employed (Fig. 2d).

B. Experimental Measurements

Fig. 3 shows the reconstructed images of phantom 1. Fig. 3a) shows the MIPs of the 3-D images obtained with the microsphere at the center (left) and at the periphery (right) of the field of view. The images in Fig. 3a) were reconstructed with the MB-PD method. The zoomed-in images of the red and blue rectangular areas are shown in Fig. 3b) for all three

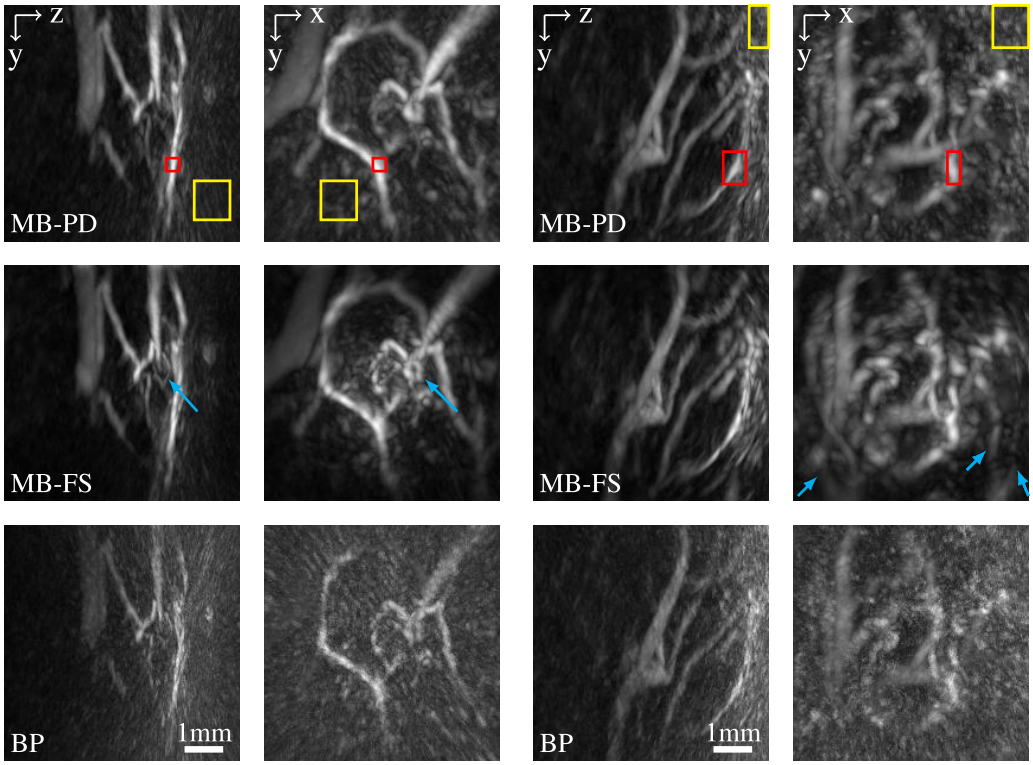

Fig. 5. Maximum intensity projections of the reconstructed images of vascular structures in the first a) and forth b) fingers of a healthy volunteer. The images reconstructed with the MB-PD, MB-FS and BP methods are shown. The red and yellow rectangular regions are used to calculate the SNR in the reconstructed images.

reconstruction methods. When the microsphere was located at the center of the field of view, no significant difference in the images reconstructed with the three methods was observed. However, the lateral blur associated with the spatial impulse response of the transducers was again evident in the BP and MB-PD images when the microsphere was located near the edge of the imaged field of view. These images can be erroneously interpreted as if two separate microspheres were present. A more accurate reconstruction is obtained with the MB-FS method. The distortion and correction effects become even more apparent when inspecting Fig. 3c), where the profiles along the lines marked in Fig. 3b) are plotted in yellow, green and magenta for the BP, MB-PD and MB-FS methods, respectively. For the microsphere located at the edge, the profile for the MB-FS method correctly shows a single peak while the profiles for the BP and the MB-PD methods have two peaks, although the Full Width at Half Maximum (FWHM) values for the different methods have no significant differences.

Fig. 4 shows the images obtained from phantom 2. The MIPs of the images reconstructed with the MB-PD method are presented in Fig. 4a). The zoom-ins of two selected off-center areas (marked in red and blue) are shown in Figs. 4b) and 4c) for the MB-PD, MB-FS and BP methods, respectively. Note that the cropped volumes in Fig. 4b) and c) do not contain all the visible particles in the MIPs of Fig. 4a). Again, the microsphere shape distortions can be readily rectified in both off-center areas using the MB-FS method.

Finally, two representative 3-D snapshots from the *in vivo* finger imaging experiment are shown in Fig. 5. Images acquired from an index finger are shown in Fig. 5a), whereas Fig. 5b) shows data from a little finger. One may note that the images reconstructed with the BP algorithm are severely affected by noise. Here strong artifacts appear in the background, hampering a clear identification of the shape of the vascular structures. On the other hand, the MB methods (MB-PD and MB-FS) are generally less sensitive to noise, yielding a significantly better image quality. The higher noise content of the images reconstructed with the back-projection algorithm is mainly attributed to the presence of streak-type artifacts [24] and the overall better performance of iterative reconstruction methods [31]. Sparsity-based reconstruction can further improve contrast and reduce image artifacts in three-dimensional optoacoustic tomography [32]. For a more quantified assessment, we calculated the signal-to-noise ratio (SNR) in the reconstructed images as the maximum signal value in selected regions of interest (red rectangles) divided by the root mean squared noise in selected background regions (yellow rectangles). The SNR values for the MB-PD, MB-FS and BP methods are 17.74, 38.55, and 10.54 for Fig. 5a) and 7.68, 25.93 and 5.61 for Fig. 5b), respectively. Evidently, the MB-FS method significantly

outperforms the other methods in terms of SNR but also in terms of the shape and overall appearance of the vascular structures (as exemplified with blue arrows). Reconstruction time for single image volumes consisting of 8 million voxels was 0.5s, 64s and 17min for the BP, MB-PD and MB-FS methods, respectively. The run time of the GPU-based method introduced herein is significantly faster than the previously-suggested CPU-based algorithm [24]. For comparison purposes, the number of voxels in the images of Fig. 5 was reduced to $100 \times 100 \times 50$, so that model-based reconstruction can be performed on the CPU. Specifically, the calculations were done on a workstation with an Intel(R) Xeon(R) CPU X5650 @2.67 GHz processor and 144 GB RAM. The CPU calculation of the model matrix for the MB-PD method took around 3.7 hours and required approximately 17.6 GB of memory for storage. Once the model matrix was stored, the CPU LSQR inversion time was 47.6s. On the other hand, GPU reconstruction for the MB-PS method with the same number of voxels took 4.6s. Note that apart from the large computational time, the conventional model-based approach is further hampered by high memory requirements that may prevent high-resolution reconstruction, particularly when using the MB-FS method.

IV. Discussion and Conclusions

In this work, we have introduced an efficient 3-D MB reconstruction procedure generally applicable to a broad range of OA imaging techniques. The developed MB reconstruction framework may not only benefit the 3-D imaging systems but also approaches based on cross-sectional or one-dimensional data acquisition. Indeed, simplifications commonly made during 2D OAT or acoustic-resolution OA microscopy reconstructions may lead to substantial image artifacts and poorly quantified information in the images, thus methods accounting for the actual 3-D shape of the transducer are generally preferable.

In practice, 3-D MB reconstructions are hampered by the large memory overhead and computational complexity, so that computer processing unit (CPU)-based implementations are usually impractical. For example, while the model-matrix for the reconstruction of the finger images showcased herein is more than 99% sparse (i.e. contains less than 1% non-zero entries), it requires nearly 300GB of memory to be stored in a sparse representation, which is too large to fit into the memory of a standard computer. Thus, reconstructions based on a-priori calculated model matrix [24] becomes unfeasible for high-resolution imaging or for a large number of simultaneously recorded signals (projections). Furthermore, due to the high computational complexity, it may take hours to days to calculate the full forward model matrix, whereas several model-matrices need to be additionally calculated in order to account for the size and shape of the transducer.

On the other hand, efficient implementation of a 3-D MB reconstruction procedure on a GPU is also not straightforward. This is because model matrices representing a full 3-D model cannot generally be saved on the internal GPU memory (typically only a few GB in size) in order to perform parallel calculations.We reduce this memory overhead by on-the-fly calculation of the matrix-vector products $\boldsymbol{Au}$ and $\boldsymbol{A}^{\mathsf{T}}\boldsymbol{v}$ without the need for calculating and storing the entire model-matrix [26]. To further reduce computational complexity, we introduced herein a new 3-D MB approach that stores a small look-up table occupying less than 500KB of memory on the GPU, from which the elements of the model-matrix can be calculated. Calculation of entries in the model-matrix only involves the subtraction, division and multiplication operations between the entries of the look-up table (cf. (7)). In this way, the reconstruction time for typical 3-D MB is reduced to tens of seconds when considering point detectors and increases linearly with the number of sub-elements when taking into account the detector shape.

The advantages of the suggested MB reconstruction algorithm were illustrated by comparing the results with those rendered with a standard back-projection algorithm. It was experimentally shown in phantoms and *in vivo* experiments that tomographic reconstructions in 3-D optoacoustic imaging systems can be substantially improved when accounting for the correct detector shape, which was evinced by the higher SNR and better visibility of vascular structures in the images, especially for off-the-center regions of the detection geometry. Generally, the capability to account for the size and shape of the transducer can be exploited in other systems e.g. based on cylindrically-focused transducers, where accurate 3-D models have shown to contribute to the improvement of spatial resolution and overall image quality in cross-sectional optoacoustic reconstructions [15]. In addition, the *in vivo* experiment performed with the 3-D hand-held imaging device, has clearly shown that the conventional back-projection inversion is more sensitive to noise, whereas the MB schemes achieved significantly higher image quality even without modeling the finite size of the transducers.

The approach to calculate the matrix-vector products suggested in this work can be directly incorporated in other inversion procedures. For example, matrix-vector multiplications also dominate the complexity of algorithms employing compressed sensing approaches [32]–[34].

In conclusion, we have introduced an efficient 3-D MB reconstruction approach that is applicable to arbitrary OA acquisition geometries employing detection elements with arbitrary size and shape. Significant improvements in the spatial resolution, contrast to noise ratio and overall image quality were accomplished when applying the newly introduced approach to 3-D data acquired from a finger of a healthy volunteer using a hand-held volumetric optoacoustic imaging system. The high computational efficiency and low memory requirements of the proposed reconstruction framework anticipate its practical applicability in realistic imaging scenarios involving large datasets, which may also contain multi-spectral and time-lapse optoacoustic data.

Appendix A

The GPU implementations of $\boldsymbol{A}^{\mathsf{T}}\boldsymbol{u}$ and $\boldsymbol{Av}$ are given in Algorithm 1 and Algorithm 2 respectively.

Algorithm 1 Implementation of Kernel $\boldsymbol{A}^{\mathsf{T}}\boldsymbol{u}$

Input : $\boldsymbol{u}$: input vector
c: speed of sound
Δ: voxel width
L: number of transducers
$\boldsymbol{r}_1, \cdots, \boldsymbol{r}_L$: transducer locations
$\boldsymbol{r}_i$: location of voxel i
$\boldsymbol{t}$: time instant vector
N_s: number of sampling instants
dI_{Table}: lookup table for dI values
Output: $(\boldsymbol{A}^{\mathsf{T}}\boldsymbol{u})_i$
$(\boldsymbol{A}^{\mathsf{T}}\boldsymbol{u})_i \leftarrow 0$
for $\ell = 1$ **to** L **do**
  $\boldsymbol{w} \leftarrow \boldsymbol{r}_\ell - \boldsymbol{r}_i$
  $s \leftarrow |\boldsymbol{w}|$
  $n_1 \leftarrow \left\lceil \frac{-t_0 + \frac{s-\sqrt{3}\Delta}{c}}{t_1 - t_0} \right\rceil$
  $n_2 \leftarrow \left\lfloor \frac{-t_0 + \frac{s+\sqrt{3}\Delta}{c}}{t_1 - t_0} \right\rfloor$
  $\alpha \leftarrow \arctan(\frac{w_y}{w_x})$
  $\beta \leftarrow \arctan(\frac{w_z}{\sqrt{w_x^2 + w_y^2}})$
  for $k = n_1$ **to** n_2 **do**
    $d \leftarrow s - ct_k$
    $dI \leftarrow dI_{Table}(d, \alpha, \beta)$
    $(\boldsymbol{A}^{\mathsf{T}}\boldsymbol{u})_i \leftarrow (\boldsymbol{A}^{\mathsf{T}}\boldsymbol{u})_i - \frac{c}{s-d} dI[\boldsymbol{u}]_{(l-1)N_s+k-1}$

Algorithm 2 Implementation of Kernel $\boldsymbol{A}\boldsymbol{v}$

Input : $\boldsymbol{v}$: input vector
c: speed of sound
Δ: voxel width
L: number of transducers
$\boldsymbol{r}_1, \cdots, \boldsymbol{r}_L$: transducer locations
$\boldsymbol{r}_i$: location of voxel i
$\boldsymbol{t}$: time instant vector
N_s: number of sampling instants
dI_{Table}: lookup table for dI values
$\boldsymbol{A}\boldsymbol{v} \leftarrow \boldsymbol{0}$
Output: $\boldsymbol{A}\boldsymbol{v}$
for $\ell = 1$ **to** L **do**
  $\boldsymbol{w} \leftarrow \boldsymbol{r}_\ell - \boldsymbol{r}_i$
  $s \leftarrow |\boldsymbol{w}|$
  $n_1 \leftarrow \left\lceil \frac{-t_0 + \frac{s-\sqrt{3}\Delta}{c}}{t_1 - t_0} \right\rceil$
  $n_2 \leftarrow \left\lfloor \frac{-t_0 + \frac{s+\sqrt{3}\Delta}{c}}{t_1 - t_0} \right\rfloor$
  $\alpha \leftarrow \arctan(\frac{w_y}{w_x})$
  $\beta \leftarrow \arctan(\frac{w_z}{\sqrt{w_x^2 + w_y^2}})$
  for $k = n_1$ **to** n_2 **do**
    $d \leftarrow s - ct_k$
    $dI \leftarrow dI_{Table}(d, \alpha, \beta)$
    Use an atomic add operation to sum up the results of parallel calculations
    $(\boldsymbol{A}\boldsymbol{v})_{(l-1)N_s+k-1} \leftarrow$
    $(\boldsymbol{A}\boldsymbol{v})_{(l-1)N_s+k-1} - \frac{c}{s-d} dI[\boldsymbol{v}]_{(l-1)N_s+k-1}$

APPENDIX B

In the following, we describe in detail how the term $I(d, \alpha, \beta)$ and $dI(d, \alpha, \beta)$ in (8) and (9) are calculated as a function of d for given values of α and β.

The calculations described herein were done using the MATLAB symbolic toolbox. Since the results are stored in a look-up table, the complexity of the calculation is not a major concern. The resulting expression for $dI(d, \alpha, \beta)$ depends on how a plane intersects a cube.

We assume that the distance d is normalized by Δ. Thus, the aim is to calculate the integral of the function

$$f(\boldsymbol{r}) = \begin{cases} (1 - |r_1|)(1 - |r_2|)(1 - |r_3|) & \text{for } \|\boldsymbol{r}\|_\infty < 1 \\ 0 & \text{for } \|\boldsymbol{r}\|_\infty \geqslant 1 \end{cases} \tag{16}$$

on the plane

$$\boldsymbol{n}^{\mathsf{T}}\boldsymbol{r} = d \tag{17}$$

where

$$\boldsymbol{n} = [\cos(\alpha)\cos(\beta), \sin(\alpha)\cos(\beta), \sin(\beta)]^{\mathsf{T}}. \tag{18}$$

We parameterize the plane as

$$\boldsymbol{g}(v, u; d) = d\boldsymbol{n}(\alpha, \beta) + v\boldsymbol{y}(\alpha, \beta) + u\boldsymbol{z}(\alpha, \beta) \tag{19}$$

where $\boldsymbol{y}$ and $\boldsymbol{z}$ are chosen such that $\boldsymbol{n}$, $\boldsymbol{y}$, and $\boldsymbol{z}$ form an orthonormal basis. Note that these vectors only depend on α and β and are constant for different values of d. The integral is then calculated as

$$I(d, \alpha, \beta) = \int_{-\infty}^{\infty}\int_{-\infty}^{\infty} f(\boldsymbol{g}(v, u; d))dudv. \tag{20}$$

Due to the piecewise definition of the function $f(\boldsymbol{r})$, the calculation of the integral in (20) is not straightforward and needs to be performed separately for each octant. The following description is for the first octant (r_1, r_2 and r_3 positive). The other parts are calculated analogously. For the first octant, $f(\boldsymbol{r})$ is given by

$$f_1(\boldsymbol{r}) = (1 - r_1)(1 - r_2)(1 - r_3). \tag{21}$$

Integration is performed over the intersection of the plane defined by $\boldsymbol{g}(v, u; d)$ with the cube $\mathcal{C} = [0, 1] \times [0, 1] \times [0, 1]$. The intersection is a convex polygon. To calculate the integral, the extreme points of the polygon are expressed in terms of the coordinates v and u. Therefore, the intersection points of the plane $\boldsymbol{g}(v, u; d)$ with the edges of the cube $\mathcal{C}$ need to be calculated (Fig. 6). Note that the intersection points vary with different values of d.

The twelve edges of the cube ($i = 1, \ldots, 12$) can be parameterized as

$$w_i\boldsymbol{e}_i + \boldsymbol{s}_i \tag{22}$$

with $w_i \in [0, 1]$. $\boldsymbol{e}_i$ is a unit vector parallel to the edge and $\boldsymbol{s}_i$ is a shift vector perpendicular to $\boldsymbol{e}_i$. The intersection with the

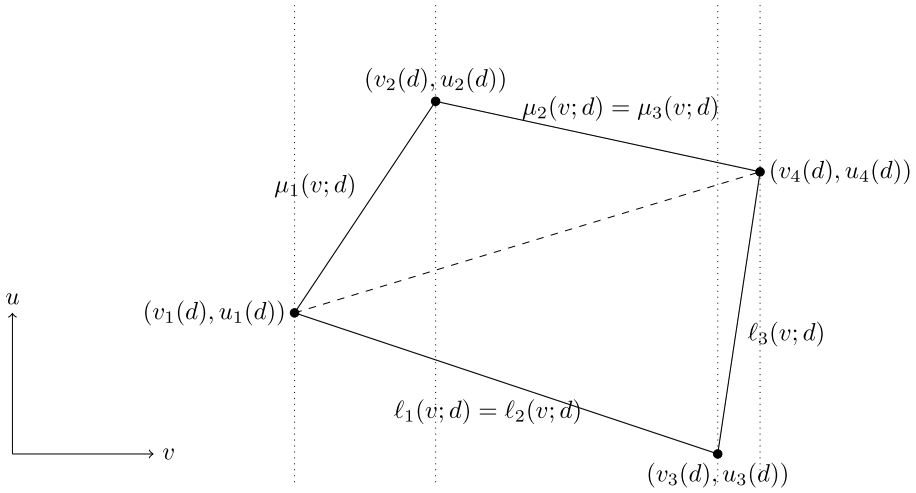

Fig. 6. Intersection points and integral limits in (v, u) coordinates.

twelve edges are characterized by the coordinates v, u and w, which can be calculated by setting (22) equals (19). The analytical expression of these coordinates as a function of d ($(v_i(d), u_i(d))$ and a corresponding $w_i(d)$) are calculated with the MATLAB symbolic toolbox. Only those points for which $w_i(d)$ lies between 0 and 1 are considered actual intersections. The number of intersecting points depends on α and β and further changes for different values of d.

For a certain value of d, we obtain several valid intersection points $(v_i(d), u_i(d))$. If the number of intersection points is less than three, the integral is zero. For $n \geq 3$ intersection points, an integral with piecewise linear limits needs to be calculated, i.e.,

$$I_1(d) = \sum_{j=1}^{n-1} \int_{v_j(d)}^{v_{j+1}(d)} \int_{\ell_j(v;d)}^{\mu_j(v;d)} f_1(\boldsymbol{g}(u, v; d)) du dv. \quad (23)$$

The upper and lower integral limits $\mu_j(v; d)$ and $\ell_j(v; d)$ are linear in v. Fig. 6 illustrates the intersection points and integral limits in the (v, u) coordinates.

We can sort the intersection points with respect to $v_i(d)$. Since the intersection is a convex polygon, all points above the line connecting $(v_1(d), u_1(d))$ with $(v_n(d), u_n(d))$ belong to the upper limit and all points below belong to the lower limit. The connecting lines $\mu_j(v; d)$ and $\ell_j(v; d)$ then define the limits of the integral.

Once the analytical expression of $I(d, \alpha, \beta)$ is calculated, $dI(d, \alpha, \beta)$ can also be easily derived.

References

[1] D. Razansky, "Multispectral optoacoustic tomography—Volumetric color hearing in real time," *IEEE J. Sel. Topics Quantum Electron.*, vol. 18, no. 3, pp. 1234–1243, May/Jun. 2012.

[2] L. V. Wang and J. Yao, "A practical guide to photoacoustic tomography in the life sciences," *Nature Methods*, vol. 13, no. 8, pp. 627–638, 2016.

[3] Y. Xu, L. V. Wang, G. Ambartsoumian, and P. Kuchment, "Reconstructions in limited-view thermoacoustic tomography," *Med. Phys.*, vol. 31, no. 4, pp. 724–733, 2004.

[4] X. L. Deán-Ben and D. Razansky, "On the link between the speckle free nature of optoacoustics and visibility of structures in limited-view tomography," *Photoacoustics*, vol. 4, no. 4, pp. 133–140, 2016.

[5] H.-P. Brecht, R. Su, M. Fronheiser, S. A. Ermilov, A. Conjusteau, and A. A. Oraevsky, "Whole-body three-dimensional optoacoustic tomography system for small animals," *J. Biomed. Opt.*, vol. 14, no. 6, p. 064007, 2009.

[6] R. A. Kruger, R. B. Lam, D. R. Reinecke, S. P. D. Rio, and R. P. Doyle, "Photoacoustic angiography of the breast," *Med. Phys.*, vol. 37, no. 11, pp. 6096–6100, 2010.

[7] R. Ellwood, O. Ogunlade, E. Zhang, P. Beard, and B. Cox, "Orthogonal Fabry-pérot sensors for photoacoustic tomography," *Proc. SPIE*, vol. 9780, p. 9708, 2016.

[8] T. F. Fehm, X. L. Deán-Ben, S. J. Ford, and D. Razansky, "*In vivo* whole-body optoacoustic scanner with real-time volumetric imaging capacity," *Optica*, vol. 3, no. 11, pp. 1153–1159, 2016.

[9] X. L. Dean-Ben, A. Ozbek, and D. Razansky, "Volumetric real-time tracking of peripheral human vasculature with GPU-accelerated three-dimensional optoacoustic tomography," *IEEE Trans. Med. Imag.*, vol. 32, no. 11, pp. 2050–2055, Nov. 2013.

[10] A. Rosenthal, V. Ntziachristos, and D. Razansky, "Model-based optoacoustic inversion with arbitrary-shape detectors," *Med. Phys.*, vol. 38, no. 7, pp. 4285–4295, 2011.

[11] K. Mitsuhashi, K. Wang, and M. A. Anastasio, "Investigation of the far-field approximation for modeling a transducer's spatial impulse response in photoacoustic computed tomography," *Photoacoustics*, vol. 2, no. 1, pp. 21–32, 2014.

[12] A. Rosenthal, D. Razansky, and V. Ntziachristos, "Fast semi-analytical model-based acoustic inversion for quantitative optoacoustic tomography," *IEEE Trans. Med. Imag.*, vol. 29, no. 6, pp. 1275–1285, Jun. 2010.

[13] X. L. Deán-Ben, V. Ntziachristos, and D. Razansky, "Acceleration of optoacoustic model-based reconstruction using angular image discretization," *IEEE Trans. Med. Imag.*, vol. 31, no. 5, pp. 1154–1162, May 2012.

[14] L. Ding, X. L. Deán-Ben, and D. Razansky, "Real-time model-based inversion in cross-sectional optoacoustic tomography," *IEEE Trans. Med. Imag.*, vol. 35, no. 8, pp. 1883–1891, Aug. 2016.

[15] D. Queirós, X. L. Déan-Ben, A. Buehler, D. Razansky, A. Rosenthal, and V. Ntziachristos, "Modeling the shape of cylindrically focused transducers in three-dimensional optoacoustic tomography," *J. Biomed. Opt.*, vol. 18, no. 7, p. 076014, 2013.

[16] X. L. Deán-Ben, R. Ma, A. Rosenthal, V. Ntziachristos, and D. Razansky, "Weighted model-based optoacoustic reconstruction in acoustic scattering media," *Phys. Med. Biol.*, vol. 58, no. 16, p. 5555, 2013.

[17] C. Huang, L. Nie, R. W. Schoonover, L. V. Wang, and M. A. Anastasio, "Photoacoustic computed tomography correcting for heterogeneity and attenuation," *J. Biomed. Opt.*, vol. 17, no. 6, pp. 0612111–0612115, 2012.

[18] L. Ding, X. L. Deán-Ben, C. Lutzweiler, D. Razansky, and V. Ntziachristos, "Efficient non-negative constrained model-based inversion in optoacoustic tomography," *Phys. Med. Biol.*, vol. 60, no. 17, p. 6733, 2015.

[19] S. Park, C. Lee, J. Kim, and C. Kim, "Acoustic resolution photoacoustic microscopy," *Biomed. Eng. Lett.*, vol. 4, no. 3, pp. 213–222, 2014.

[20] M.-L. Li, H. F. Zhang, K. Maslov, G. Stoica, and L. V. Wang, "Improved *in vivo* photoacoustic microscopy based on a virtual-detector concept," *Opt. Lett.*, vol. 31, no. 4, pp. 474–476, 2006.

[21] J. Turner, H. Estrada, M. Kneipp, and D. Razansky, "Improved optoacoustic microscopy through three-dimensional spatial impulse response synthetic aperture focusing technique," *Opt. Lett.*, vol. 39, no. 12, pp. 3390–3393, 2014.

[22] C. C. Paige and M. A. Saunders, "LSQR: An algorithm for sparse linear equations and sparse least squares," *ACM Trans. Math. Softw.*, vol. 8, no. 1, pp. 43–71, Mar. 1982.

[23] K. Wang, C. Huang, Y.-J. Kao, C.-Y. Chou, A. A. Oraevsky, and M. A. Anastasio, "Accelerating image reconstruction in three-dimensional optoacoustic tomography on graphics processing units," *Med. Phys.*, vol. 40, no. 2, p. 023301, 2013.

[24] X. L. Dean-Ben, A. Buehler, V. Ntziachristos, and D. Razansky, "Accurate model-based reconstruction algorithm for three-dimensional optoacoustic tomography," *IEEE Trans. Med. Imag.*, vol. 31, no. 10, pp. 1922–1928, Oct. 2012.

[25] A. P. Jathoul *et al.*, "Deep *in vivo* photoacoustic imaging of mammalian tissues using a tyrosinase-based genetic reporter," *Nature Photon.*, vol. 9, pp. 239–246, Jan. 2015.

[26] K. Wang, R. Su, A. A. Oraevsky, and M. A. Anastasio, "Investigation of iterative image reconstruction in three-dimensional optoacoustic tomography," *Phys. Med. Biol.*, vol. 57, no. 17, p. 5399, 2012.

[27] Y. Han, S. Tzoumas, A. Nunes, V. Ntziachristos, and A. Rosenthal, "Sparsity-based acoustic inversion in cross-sectional multiscale optoacoustic imaging," *Med. Phys.*, vol. 42, no. 9, pp. 5444–5452, 2015.

[28] L. V. Wang and H.-I. Wu, *Biomedical Optics: Principles and Imaging*. Hoboken, NJ, USA: Wiley, 2012.

[29] X. L. Deán-Ben *et al.*, "Functional optoacoustic neuro-tomography for scalable whole-brain monitoring of calcium indicators," *Light, Sci. Appl.*, vol. 5, no. 12, p. e16201, 2016.

[30] M. Xu and L. V. Wang, "Universal back-projection algorithm for photoacoustic computed tomography," *Phys. Rev. E, Stat. Phys. Plasmas Fluids Relat. Interdiscip. Top.*, vol. 71, no. 1, p. 016706, 2005.

[31] L. L. Geyer *et al.*, "State of the art: Iterative CT reconstruction techniques," *Radiology*, vol. 276, no. 2, pp. 339–357, 2015.

[32] Y. Han, L. Ding, X. L. D. Ben, D. Razansky, J. Prakash, and V. Ntziachristos, "Three-dimensional optoacoustic reconstruction using fast sparse representation," *Opt. Lett.*, vol. 42, no. 5, pp. 979–982, 2017.

[33] J. Provost and F. Lesage, "The application of compressed sensing for photo-acoustic tomography," *IEEE Trans. Med. Imag.*, vol. 28, no. 4, pp. 585–594, Apr. 2009.

[34] J. Prakash, A. S. Raju, C. B. Shaw, M. Pramanik, and P. K. Yalavarthy, "Basis pursuit deconvolution for improving model-based reconstructed images in photoacoustic tomography," *Biomed. Opt. Exp.*, vol. 5, no. 5, pp. 1363–1377, 2014.

APPENDIX B. PUBLICATION: EFFICIENT THREE-DIMENSIONAL MODEL-BASED RECONSTRUCTION SCHEME FOR ARBITRARY OPTOACOUSTIC ACQUISITION GEOMETRIES

Appendix C

Publication: Model-based Reconstruction of Large Three-dimensional Optoacoustic Datasets

This article has been accepted for publication in a future issue of this journal, but has not been fully edited. Content may change prior to final publication. Citation information: DOI 10.1109/TMI.2020.2981835, IEEE Transactions on Medical Imaging

Model-based reconstruction of large three-dimensional optoacoustic datasets

Lu Ding, Daniel Razansky, and Xosé Luís Deán-Ben

***Abstract*—Iterative model-based algorithms are known to enable more accurate and quantitative optoacoustic (photoacoustic) tomographic reconstructions than standard back-projection methods. However, three-dimensional (3D) model-based inversion is often hampered by high computational complexity and memory overhead. Parallel implementations on a graphics processing unit (GPU) have been shown to efficiently reduce the memory requirements by on-the-fly calculation of the actions of the optoacoustic model matrix, but the high complexity still makes these approaches impractical for large 3D optoacoustic datasets. Herein, we show that the computational complexity of 3D model-based iterative inversion can be significantly reduced by splitting the model matrix into two parts: one maximally sparse matrix containing only one entry per voxel-transducer pair and a second matrix corresponding to cyclic convolution. We further suggest reconstructing the images by multiplying the transpose of the model matrix calculated in this manner with the acquired signals, which is equivalent to using a very large regularization parameter in the iterative inversion method. The performance of these two approaches is compared to that of standard back-projection and a recently introduced GPU-based model-based method using datasets from *in vivo* experiments. The reconstruction time was accelerated by approximately an order of magnitude with the new iterative method, while multiplication with the transpose of the matrix is shown to be as fast as standard back-projection.**

***Index Terms*—Optoacoustic tomography, photoacoustic tomography, image reconstruction, model-based reconstruction, large datasets**

I. Introduction

MODEL-BASED reconstruction methods have been available since early developments in tomographic imaging modalities such as x-ray computed tomography (CT) or single photon emission CT (SPECT) [1], [2]. However, the high computational burden associated to the many iterations generally involved has limited their practical applicability to reconstructions from a low number of measuring points [3]. Instead, analytical approaches such as filtered back-projection have been traditionally used in spite of the fact that they are not suited to all acquisition geometries and are sometimes derived from simplifications that may lead to artefacts in the images [4]. More recently, the increase in the computational capacity of modern computers, particularly in parallel computing with graphics processing units (GPUs) [5], has fostered the developments of model-based approaches for high-resolution reconstructions from large amounts of data [6].

In optoacoustic (OA, photoacoustic) tomography, efforts have also been directed to the development of reconstruction algorithms based on the numerical inversion of a wave propagation model [7], [8], [9], [10], [11], [12], [13]. As opposed to other imaging modalities, no "standard" OA imaging system exist, and a myriad of embodiments based of different types of light delivery methods, ultrasound transducers and acquisition geometries have been tailored to specific biomedical applications [14]. Model-based image formation algorithms offer sufficient flexibility to be applicable in most of such configurations, which is unfeasible with other methods. Of particular importance is the capability of model-based reconstruction methods to account for the finite size of focused or unfocused detectors required in most systems [15], [16], [17]. Acoustic propagation effects due to acoustic mismatches or ultrasound attenuation can also be incorporated into OA models [18], [19], [20], [21], [22], [23], [24], [25]. These effects can also be considered using time-reversal reconstruction, which also represents a very flexible approach [26], [27], [28], [29], [30]. Moreover, the time reversal operator can also be incorporated into iterative methods to capitalize on the advantages of these [11]. For example, image contrast and resolution can be enhanced by including regularization terms or constrains in the inversion procedure [31], [32], [33], [34], [35]. Efforts have also been directed on the parallel implementation of iterative inversion algorithms on the time [20], [33], [36] and frequency domains [37], [38] to exploit the computational power of GPUs. However, while real-time reconstruction has been achieved for two-dimensional (2D, cross-sectional) imaging [39], iterative reconstruction of three-dimensional (3D) regions remains relatively slow. An alternative approach consists in directly inverting the model matrix e.g. via singular value decomposition (SVD) [40], [41], [42] or wavelet-packet representations [43], [44]. The implementation of these methods for large 3D datasets involving a large number of unknowns remains however challenging. Machine and deep learning methods have also found applicability for the reconstruction of OA images [45], [12], [46], [47], although a large number of datasets are required for efficient training and concerns still exist on the validity of the results obtained.

Recently, we have introduced a 3D model-based reconstruction method generally applicable in arbitrary acquisition geometries [48]. The model was derived from a discretization of the solution of the OA wave equation in the time domain. Iterative inversion was performed by on-the-fly calculation of the actions of the model matrix and its transpose from a small

Lu Ding is with the Institute for Biological and Medical Imaging (IBMI), Helmholtz Zentrum München, Daniel Razansky and Xosé Luís Deán-Ben are with Faculty of Medicine and Institute of Pharmacology and Toxicology, University of Zürich, and with Institute for Biomedical Engineering and Department of Information Technology and Electrical Engineering, ETH Zürich, e-mail: xl.deanben@pharma.uzh.ch

This article has been accepted for publication in a future issue of this journal, but has not been fully edited. Content may change prior to final publication. Citation information: DOI 10.1109/TMI.2020.2981835, IEEE Transactions on Medical Imaging

look-up table, thus avoiding the generally unfeasible memory storage of the entire matrix. Parallel implementation of the algorithm on a GPU further enabled a significant acceleration of the reconstruction time ($\sim$ 64s for 200x200x200 voxels reconstructed from 512 time-resolved signals consisting of 500 samples each). However, 3D model-based reconstruction still remains impractical for large multi-frame datasets acquired via probe scanning [49], [50], [51], [52] or time-lapse measurements [53], [54], [55]. The trade-off between imaging frame rate and field of view is clearly manifested in spiral volumetric optoacoustic tomography (SVOT), which enables adapting the temporal resolution to a specific volume of interest in order to be able to image biological processes at multiple temporal scales and scalable fields of view [56].

In this work, we introduce a simplified method for the discretization of the OA model that enables significantly reducing the complexity of the iterative inversion procedure. We further test the performance of the method in a non-iterative approach, where the reconstruction is performed with the product of the transpose of the model matrix and the acquired signals in an analogous manner as standard back-projection. This non-iterative method is preferable in cases where the iterative approach turns impractical, e.g. in large SVOT scans involving a large number of unknowns. The experimental performance of the introduced model-based (iterative and non-iterative) methodology with regard to image contrast, resolution and quantitativeness is analyzed for numerical simulations, for a sequence of images acquired with a spherical transducer array and for whole-mouse images acquired with SVOT.

II. Materials and Methods

A. Discretization of the continuous time-domain forward model

The discretization of the time-domain forward model has been described in detail in [48] and is briefly reviewed herein. For an ideal transducer at position $\mathbf{r}_q$ that acquires pressure samples at time instances $t_0 + kT$, with $k = 1, \ldots, K$, the discrete pressure samples $[\mathbf{p}_q]_k$ can be estimated with the continuous to discrete OA forward model given (in arbitrary units) by

$$[\mathbf{p}_q]_k = \frac{\partial}{\partial t}\frac{1}{ct}\int_{S(\mathbf{r}_q,ct)} h(\mathbf{r})dS(\mathbf{r}_q,ct)\Bigg|_{t=t_0+kT}, \quad (1)$$

where c denotes the speed of sound in the medium, $h(\mathbf{r})$ is the absorbed optical energy per unit volume inside the imaging volume and $S(\mathbf{r}_q, ct)$ is the spherical surface with center $\mathbf{r}_q$ and radius ct. In Eq. 1, a uniform Grüneisen parameter was assumed and the constant terms were removed for simplicity. Note that for a non-uniform Grüneisen parameter $\Gamma(\mathbf{r})$, the same model in Eq. 1 can be used to reconstruct the initial OA pressure $p_0(\mathbf{r}) = \Gamma(\mathbf{r})h(\mathbf{r})$. To form a discrete to discrete model, we approximate $h(\mathbf{r})$ as

$$h(\mathbf{r}) = \sum_{i=1}^{M} \Psi(\mathbf{r} - \mathbf{r}_i)h(\mathbf{r}_i), \quad (2)$$

where $\mathbf{r}_i$ represent each of the M points of the three-dimensional Cartesian grid that covers the imaging volume. The function $\Psi(\cdot)$ is an interpolation kernel with bounded support. In [48], we used a trilinear interpolation kernel $\Psi_{\mathrm{tri}}(\cdot)$ between the grid points $\mathbf{r}_i$, i.e.,

$$\Psi_{\mathrm{tri}}(\mathbf{r}) = \begin{cases} \prod_{j=1}^{3}(1 - |r^j|/d_{\mathrm{grid}}), & \text{if } \|\mathbf{r}\|_\infty \leq d_{\mathrm{grid}} \\ 0, & \text{otherwise} \end{cases} \quad (3)$$

where $\mathbf{r} = (r^1, r^2, r^3)$ and d_{grid} is the distance between neighboring grid points. From Eqs. (1) to (3), it is possible to express the discrete pressure vector $\mathbf{p}_q$ for all time instants as

$$\mathbf{p}_q = \mathbf{A}_q\mathbf{h}, \quad (4)$$

where $[\mathbf{h}]_i = h(\mathbf{r}_i)$ and

$$[\mathbf{A}_q]_{k,i} = \frac{\partial}{\partial t}\frac{1}{ct}\int_{S(\mathbf{r}_q,ct)} \Psi(\mathbf{r} - \mathbf{r}_i)dS(\mathbf{r}_q,ct)\Bigg|_{t=t_0+kT}. \quad (5)$$

Since the distance between the transducer position $\mathbf{r}_q$ and the voxel location $\mathbf{r}_i$ is typically much larger than d_{grid}, a far-field assumption can be made: we approximate the spherical surface $S(\mathbf{r}_q, ct)$ by the plane $\mathbf{n}_{q,i}^T(\mathbf{r} - \mathbf{r}_q) = -ct$ with the normal vector $\mathbf{n}_{q,i} = (\mathbf{r}_q - \mathbf{r}_i)/\|\mathbf{r}_q - \mathbf{r}_i\|_2$. Defining

$$g(x;\mathbf{n}) = \frac{\partial}{\partial x}\int_{\mathbf{n}^T\mathbf{r}=x} \Psi(\mathbf{r})dS_{\mathbf{n}^T\mathbf{r}=x}. \quad (6)$$

The entries of $\mathbf{A}_q$ can then be approximated as [48]

$$[\mathbf{A}_q]_{k,i} \approx -\frac{c}{d_{q,i}}g\left(d_{q,i} - c\left(t_0 + kT\right);\mathbf{n}_{q,i}\right), \quad (7)$$

with $d_{q,i} = \|\mathbf{r}_i - \mathbf{r}_q\|_2$. In [48], we have suggested to use a look-up table to store non-zero values of $g(x;\mathbf{n})$, where the normal vector $\mathbf{n}$ was parameterized by two angles.

B. Simplified model matrix

Herein, we introduce simplifications in the calculation of the model matrix to reduce both memory overhead and computational complexity. First, a rotational symmetric interpolation kernel $\Psi_{\mathrm{rot}}(\cdot)$ that discards the dependency of parameter $\mathbf{n}$ is defined as

$$\Psi_{\mathrm{rot}}(\mathbf{r}) = \begin{cases} 1 - \|\mathbf{r}\|_2/d_{\mathrm{grid}}, & \text{if } \|\mathbf{r}\|_2 \leq d_{\mathrm{grid}} \\ 0, & \text{otherwise} \end{cases} \quad (8)$$

For this interpolation kernel Eq. (6) does not depend on the unit normal vector $\mathbf{n}$ and hence $g(x;\mathbf{n})$ can be expressed as $g(x)$. Note that the function $\Psi_{\mathrm{rot}}(\cdot)$ is not strictly speaking an interpolation kernel as it does not verify $\sum_{i=1}^{M}\Psi_{\mathrm{rot}}(\mathbf{r} - \mathbf{r}_i) = 1$, and thus it leads to 'gaps' in the approximation of $h(\mathbf{r})$. Additionally, we introduce another simplification by assuming that for all $d_{q,i}$, there exists an $k_{q,i} \in \mathbb{N}$ such that

$$d_{q,i} = c\left(t_0 + k_{q,i}T\right), \quad (9)$$

In other words, it is assumed that the time of flight from each voxel to each transducer lies exactly on the grid of

This article has been accepted for publication in a future issue of this journal, but has not been fully edited. Content may change prior to final publication. Citation information: DOI 10.1109/TMI.2020.2981835, IEEE Transactions on Medical Imaging

sampling instances $t_0, \ldots, t_0 + kT$. The $k_{q,i}$ represents the grid index of the time of flight from the i-th voxel to the q-th transducer. With this assumption and defining a sequence $\overline{g}[n] = -g(-cnT)$ with $n \in \mathbb{Z}$, Eq. (7) can be reformulated into

$$[\mathbf{A}_\mathrm{q}]_{k,i} = \frac{c}{d_{q,i}} \overline{g}\,[k - k_{q,i}] = \left(\overline{g} * \frac{c}{d_{q,i}} \delta_{k,q,i} \right)[k], \qquad (10)$$

where $\delta_{k,q,i}$ is a sequence with $\delta_{k,q,i}[k] = 1$ at $k = k_{q,i}$ and zero elsewhere. Note that $\overline{g}[k] = 0$ for $|k| > k_\Delta = \lfloor \frac{\Delta}{cT} \rceil$, where $\Delta = d_\mathrm{grid}$ for the interpolation function in Eq. (8). For reasonable choices of t_0 and K, we have $k_\Delta < k_{q,i} < K - k_\Delta$. Thus we can define the vector

$$g = [\overline{g}(0), \overline{g}(1), \ldots, \overline{g}(k_\Delta), 0, \ldots, 0, \overline{g}(-k_\Delta), \ldots, \overline{g}(-1)]^T \in \mathbb{R} \qquad (11)$$

and calculate the entries of $\mathbf{A}_\mathrm{q}$ for the i-th voxel as

$$[\mathbf{A}_\mathrm{q}]_i = \frac{c}{d_{q,i}} g *_c e_{k,q,i}, \qquad (12)$$

where $*_c$ denotes a cyclic convolution and $e_{k,q,i}$ is the $k_{q,i}$-Cartesian unit vector. With the unitary discrete Fourier transform (DFT) matrix $\mathbf{F}$, the cyclic convolution of g with an arbitrary vector x of length K is given by

$$g *_c x = \mathbf{F}^H \mathrm{diag}(\mathbf{F} g) \mathbf{F} x, \qquad (13)$$

Note that the convolution operator $\mathbf{G} = \mathbf{F}^H \mathrm{diag}(\mathbf{F} g) \mathbf{F}$ does not depend on the index i of the voxel due to the rotationally symmetric interpolation function. Thus, we can write

$$\mathbf{A}_q = \mathbf{G} \mathbf{S}_q, \qquad (14)$$

where $\mathbf{S}_q$ is a sparse matrix with only one non-zero entry per column. Specifically, in column i, the non-zero entry is $c/d_{q,i}$ at position $k_{q,i}$. In practice, $k_{q,i}$ is approximated as

$$k_{q,i} = \left\lfloor \frac{d_{q,i}}{cT} - \frac{t_0}{T} \right\rceil, \qquad (15)$$

where $\lfloor \cdot \rceil$ denotes the nearest integer. The convolution operation is graphically depicted in Fig. 1. The error that is introduced by the on-grid assumption can be reduced by increasing the number of time samples, e.g., by interpolation of the measured pressure signals. The complete forward model for Q transducers is given by

$$\underbrace{\begin{pmatrix} \mathbf{p}_1 \\ \vdots \\ \mathbf{p}_Q \end{pmatrix}}_{\mathbf{p}} = \underbrace{\begin{pmatrix} \mathbf{G} & & \\ & \ddots & \\ & & \mathbf{G} \end{pmatrix} \overbrace{\begin{pmatrix} \mathbf{S}_1 \\ \vdots \\ \mathbf{S}_Q \end{pmatrix}}^{\mathbf{S}}}_{\mathbf{A}} \mathbf{h}. \qquad (16)$$

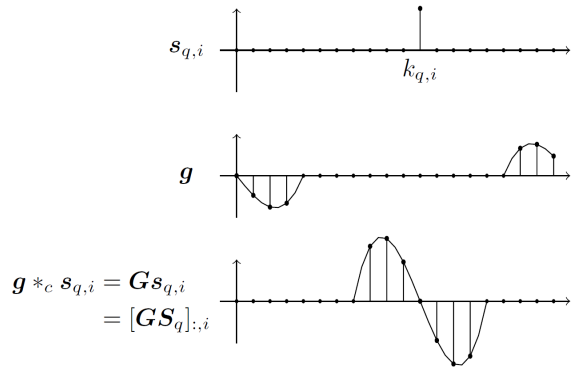

Fig. 1: Graphical representation fo the convolution operation. The scaled unit vector $s_{q,i}$ corresponding to the i-th column of $\mathbf{S}_q$ is cyclically convolved with the impulse response $\mathbf{g}$.

C. Reconstruction procedure

If the model matrix $\mathbf{A}$ is calculated, the absorption $\mathbf{h}$ can be reconstructed from a vector of measured pressure signals $\mathbf{p}_m$ by solving the least-squares problem

$$\min_\mathbf{h} \left\{ \|\mathbf{A}\mathbf{h} - \mathbf{p}_m\|_2^2 + R(h) \right\}, \qquad (17)$$

where $\|\mathbf{A}\mathbf{h} - \mathbf{p}_m\|_2$ and $R(h)$ are the so-called fidelity and regularization terms. Regularization is generally required in many practical cases, particularly in three-dimensional imaging scenarios, due to limitations in the angular coverage or in the number of measurement locations. For commonly-used Tikhonov regularization, the term $R(h)$ is given by

$$R(h) = \lambda \|\mathbf{L}\mathbf{h}\|_2^2, \qquad (18)$$

being $\mathbf{L}$ the Tikhonov matrix and λ the regularization parameter. Considering $R(h)$ given by Eq. (18) with $\mathbf{L} = \mathbf{I}$, being $\mathbf{I}$ the identity matrix, the solution $\widehat{\mathbf{h}}$ to Eq. (17) is given in closed-form as

$$\widehat{\mathbf{h}} = \left(\mathbf{A}^T \mathbf{A} + \lambda \mathbf{I} \right)^{-1} \mathbf{A}^T \mathbf{p}_m. \qquad (19)$$

In practice, the computation of the inverse of $\mathbf{A}$ is generally unfeasible and an accurate approximation of the solution to Eq. (18) is instead calculated iteratively e.g. with the LSQR algorithm [57]. The most complex computations in the iterative procedure are matrix-vector products involving the model matrix and its transpose. By using the model introduced in section II-B, these computations can be significantly simplified. Herein, we refer to this approach as the fast model-based (fMB) method.

On the other hand, in some imaging scenarios only a relatively low number of pressure signals are acquired, which is generally insufficient information to accurately reconstruct a region of interest (ROI) of millions of voxels. This is the case for volumetric hand-held scans, where only a few hundreds of transducers are integrated in the device. In such a case, λ can be chosen to be extremely large to suppress artifacts and enhance the signal to noise ratio (SNR). Then, the term $\lambda\mathbf{I}$ is

This article has been accepted for publication in a future issue of this journal, but has not been fully edited. Content may change prior to final publication. Citation information: DOI 10.1109/TMI.2020.2981835, IEEE Transactions on Medical Imaging

dominant over $\mathbf{A}^T\mathbf{A}$ in Eq. (19) and the solution (in arbitrary units) can be approximated as

$$\widehat{\mathbf{h}} = \mathbf{A}^T\mathbf{p}_m, \tag{20}$$

Note that Eq. (20) is closely related to the standard BP method. In the BP algorithm the convolution represented by matrix G is replaced by another operator that calculates the numerical derivative. Eq. (20) is expected to render better results since the discretization of the absorption map $\mathbf{h}$ is taken into account with $\mathbf{G}$. In other words, Eq. (20) can be regarded as the adaptation of the BP method to the discrete-to-discrete model. Hence, we refer to this approach as the model back-projection (MBP) method. Alternatively, Eq. (20) can be regarded as a cross-correlation with the theoretical signals generated by each voxel and the results can be interpreted in terms of matched filters [58].

D. GPU implementation

The most burdensome calculations of iterative reconstruction algorithms are the matrix-vector multiplications involving the model matrix and its transpose. In high-resolution 3D OA imaging systems, even the simplified model matrix $\mathbf{S}$ can easily occupy tens of GB and hence can generally not be stored in the internal memory of a GPU. Therefore, $\mathbf{S}$ needs to be computed on-the-fly during the matrix-vector multiplications [48]. A detailed description of the calculations of the matrix-vector products is given in Algorithms 1 and 2 (Appendix). The convolution with $\mathbf{G}$ (cf. Eq. (13)) is also calculated on the GPU using a fast Fourier transform (FFT) library.

As mentioned above, the complexity of the reconstruction with iterative algorithms such as LSQR is dominated by matrix vector products with the model matrix, namely the products $\mathbf{A}\mathbf{v}$ and $\mathbf{A}^T\mathbf{u}$. For the discretization approach introduced in this work, this involves the convolution $\mathbf{G}$ and the multiplication with $\mathbf{S}$. Since each column of $\mathbf{S}_q$ has only one entry, the complexity of matrix vector multiplications involving $\mathbf{S}$ is $\mathcal{O}(QM)$. On the other hand, the complexity in the calculation of the convolutions is $\mathcal{O}(K \log K)$. If the pressure signal $\mathbf{p}$ in Eq. (16) is initially transformed to the frequency domain, the inverse FFT in $\mathbf{G}$ can be avoided and thus discard one FFT per matrix-vector multiplication. Nevertheless, this is not significant in three-dimensional reconstructions as $K << M$. Thus, the multiplication with $\mathbf{S}$ dominates and the complexity is still $\mathcal{O}(QM)$ for typical setups. The previously introduced approach described in [48] has the same order of complexity since also a fixed number of operations are required for each pixel-transducer pair. However, the number of operations per pixel-transducer pair is significantly reduced with the method introduced herein. The complexity of least-squares reconstruction scales linearly with the number of iterations in the LSQR algorithm whereas the complexity of the MF approach, which is not iterative, is similar to that of the BP algorithm.

E. Numerical simulations

The performance of the methods introduced in this work, namely the fMB and the MBP methods described in section II-C, was first evaluated and compared to standard methods in numerical simulations. For this, two different arrangement of ultrasound sensors (measuring locations) were considered. The first arrangement (Fig. 2a) consisted of 875 positions equally distributed on a spherical surface with 40 mm radius. The second arrangement (Fig. 2b) was based one of the spherical transducer arrays described in II-F consisting of 512 positions distributed along a hemispherical surface ($140°$ angular coverage) with 40 mm radius. An optical absorption distribution consisting of 5 truncated paraboloids with radii 0.5, 0.75, 1, 1.25 and 1.5 mm randomly distributed in a ROI of $10 \times 10 \times 10$ mm^3 (blue cubes in Fig. 2a and Fig. 2b) was considered. For this type of absorbers, the OA signals can be analytically calculated [17]. Gaussian noise was added to the simulated signals (Matlab function awgn) corresponding to signal-to-noise ratio (SNR) levels of 5 and 15 dB measured as the ratio of the total signal power and total noise power. Image reconstruction was performed with the original and the noisy signals.

F. Experimental measurements

A comparison of the performance of the approach introduced in this work with standard methods was done. Specifically, the fMB and the MBP methods described in section II-C were compared with the iterative model-based (MB) approach described in [48] and the standard back-projection (BP) algorithm [59] using experimental data of biological tissues *in vivo*.

The experiments were performed using three previously introduced spherical transducer arrays. In short, each array consists of adjacent piezoelectric elements densely distributed on a spherical surface and features a central cylindrical cavity for light delivery. The illumination source was a short-pulsed (< 10 ns) optical parametric oscillator (OPO)-based laser (Innolas Laser GmbH, Krailling, Germany) with per-pulse wavelength tuning capability between 700 and 900 nm at pulse repetition frequencies up to 100 Hz. The light beam was guided via a fiber bundle through a cylindrical cavity in the transducer array. Parallel acquisition of the pressure signals for all array elements was performed at 40 megasamples per second with a custom-made data acquisition system (DAQ, Falkenstein Microsysteme GmbH, Taufkirchen, Germany) and transmitted to a PC via Ethernet.

In the first experiment, the finger of a healthy volunteer was imaged at 800 nm with a spherical array arranged for hand-held operation mode. The array consists of 512 transducer elements with approximate size of 2.5×2.5 mm^2 and a central frequency of 10 MHz [60]. The spherical aperture covers an angle of $140°$. The second experiment was performed with SVOT, which is based on a spherical array comprising 256 elements with 4 MHz central frequency and $90°$ solid angular coverage [61]. The array was fixed on a rotational-translation platform to perform a whole-body scan of a living mouse following a spiral trajectory [56]. The front and back side of the mouse were separately reconstructed. Each dataset included 735 scanning positions and was reconstructed only using the BP and MBP methods. The long computational

This article has been accepted for publication in a future issue of this journal, but has not been fully edited. Content may change prior to final publication. Citation information: DOI 10.1109/TMI.2020.2981835, IEEE Transactions on Medical Imaging

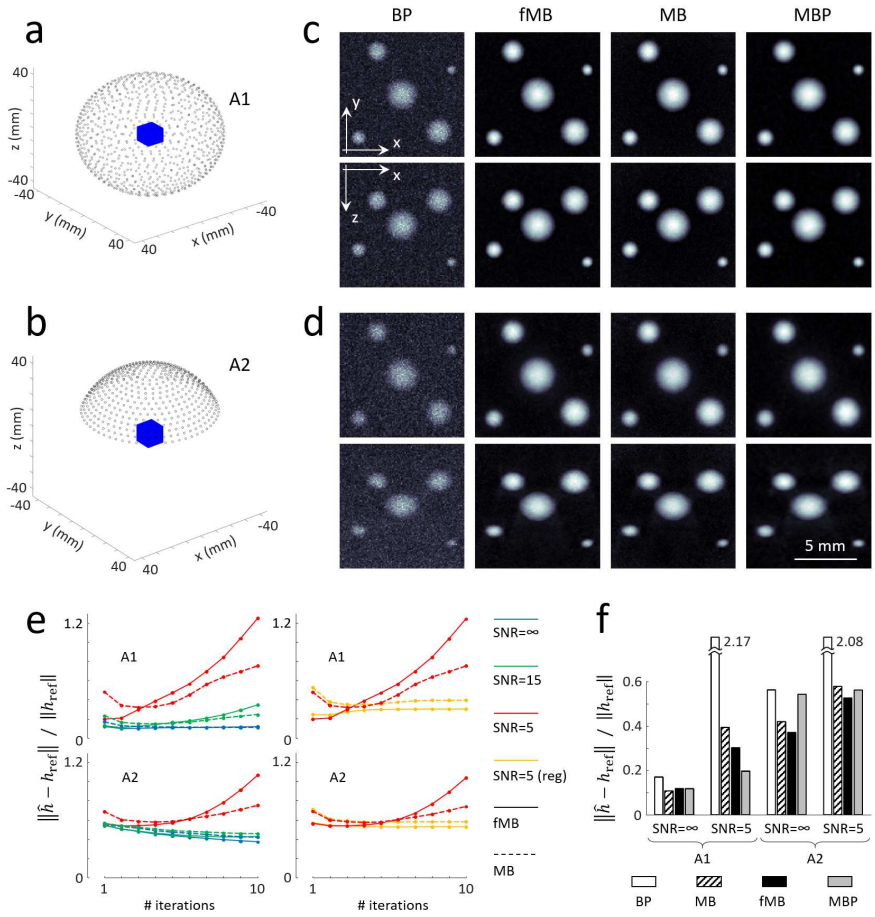

Fig. 2: Numerical simulation results. (a) First arrangement of ultrasound sensors (A1) corresponding to uniformly distributed positions on a spherical surface. (b) Second arrangement of ultrasound sensors (A2) corresponding to a spherical array of transducers used in the experiments. The blue cubes in (a) and (b) indicates the region of interest (ROI). (c) Maximum intensity projections (MIPs) of 3D images for the configuration A1 reconstructed with the 4 algorithms considered (BP, MB, fMB and MBP) for simulated signals with SNR=5. Optimal Tikhonov regularization was considered for MB and fMB. (d) Equivalent images for the configuration A2. (e) Relative errors of the images rendered with iterative methods (MB and fMB) for the configurations A1 and A2 as a function of the number of iterations, noise level and the incorporation of a regularization term. (f) Relative errors of the images rendered with all reconstruction algorithms for the configurations A1 and A2 with and without noise in the simulated signals. 10 iterations and an optimal regularization parameter were considered for the iterative methods.

time of the MB and fMB methods makes them impractical for such extremely large datasets. In the third experiment, a spherical array consisting of 512 elements with 5 MHz central frequency and 140° angular coverage was used in a stationary position [62]. The brain region of a nude mouse (15 weeks) was imaged during the injection of 30 μl (1.5 g/L concentration) of indocyanine green (ICG). Perfusion of this agent into the brain vasculature was monitored in real time by setting the laser wavelength to 800 nm and the pulse repetition frequency to 50 Hz. No signal averaging was performed. Animal experiments were performed in full compliance with the institutional guidelines of the Helmholtz Center Munich and with approval from the Government District of Upper Bavaria.

III. Results

The numerical simulation results are displayed in Fig. 2. Fig. 2c and Fig. 2d show the reconstructed images obtained with the 4 algorithms considered when taking the simulated signals with SNR $=$ 5 dB for the acquisition geometries in Fig. 2a (A1) and Fig. 2b (A2), respectively. Specifically, maximum intensity projections (MIPs, top and side views) are shown. It appears that the images rendered with BP reconstruction have significantly higher noise levels than those obtained with the model-based algorithms. A more quantitative comparison of the images rendered with different methods is provided in Fig. 2e and Fig. 2f. The relative error of the image was calculated as the mean square difference of the reconstructed image with respect to the theoretical image

This article has been accepted for publication in a future issue of this journal, but has not been fully edited. Content may change prior to final publication. Citation information: DOI 10.1109/TMI.2020.2981835, IEEE Transactions on Medical Imaging

normalized with the norm of the theoretical image. Fig. 2e displays the relative errors rendered the iterative methods (MB and fMB) as a function of the number of iterations. Both iterative methods converge without including a regularization term when there is no noise in the signals (blue lines). However, they diverge for noisy signals (green and red lines), where the MB method (dashed lines) appears to be slightly more robust to noise than the fMB method (continuous lines). Note that higher errors are generally produced for the configuration A2 than for A1 arguably due to distortion associated to limited-view effects [63]. The divergence of iterative methods when noise is present could be corrected by adding a Tikhonov regularization term (orange lines), where the optimal regularization parameter that minimizes the relative error after 10 iterations was considered. Fig. 2f displays the relative errors for all reconstruction methods with and without noise in the signals for the two configurations of sensors. For the iterative methods, 10 iterations and the optimal regularization parameter were considered. When no noise is present in the signals, a higher errors is produced with BP reconstruction for the configuration A1. This is arguably due to streak-type artefacts in the images, which are more prominent for BP algorithms [64]. A relatively high error is also produced for the MBP method for the A2 configuration. We ascribe this to a lower performance under limited-view scenarios. Indeed, the absorbers appear to be more elongated for MBP than for MB and fMB in Fig. 2d. On the other hand, MBP appears to perform better with noisy signals, in which case the largest errors are by far produced with BP.

Fig. 3 depicts the finger imaging results. The first and second columns display MIPs (top and side views) of the 3D images obtained using the BP, MBP, MB and fMB methods, respectively. The third column displays the cross-sections of the reconstructed 3D images in the x-z plane for the position marked as a blue dotted line in the top left image. Overall, the images reconstructed with the BP algorithm have more artifacts and a higher background noise than the other images. MBP yields slightly higher image quality than BP (see white arrows). On the other hand, the images reconstructed with MB and fMB have less artifacts and the vascular structures are better defined as compared to the images rendered with BP and MBP. Iterative reconstruction methods hence appear to render more accurate results, although this comes at the expense of a much higher complexity and computational time.

Fig. 4 shows the results of the SVOT whole-body scan of the mouse. Fig. 4a illustrates the scanning geometry. Fig. 4b shows the front-side MIPs of the 3D images of the mouse obtained using the BP (left) and MBP (right) methods. It is shown that the artifacts pointed by yellow arrows outside the mouse in the image rendered with BP are significantly reduced with the MBP method. Fig. 4c shows the back-side MIP images rendered with the BP (left) and MBP (right) methods. Zoom-in images of two selected regions in Fig. 4c are displayed in Fig. 4d. It is shown that vascular structures are also more clearly resolved in the MBP (right) images than in the BP (left) images (yellow arrows).

Fig. 5 presents the results of the ICG perfusion monitoring experiment. Fig. 5a exhibits the MBP images (MIPs along

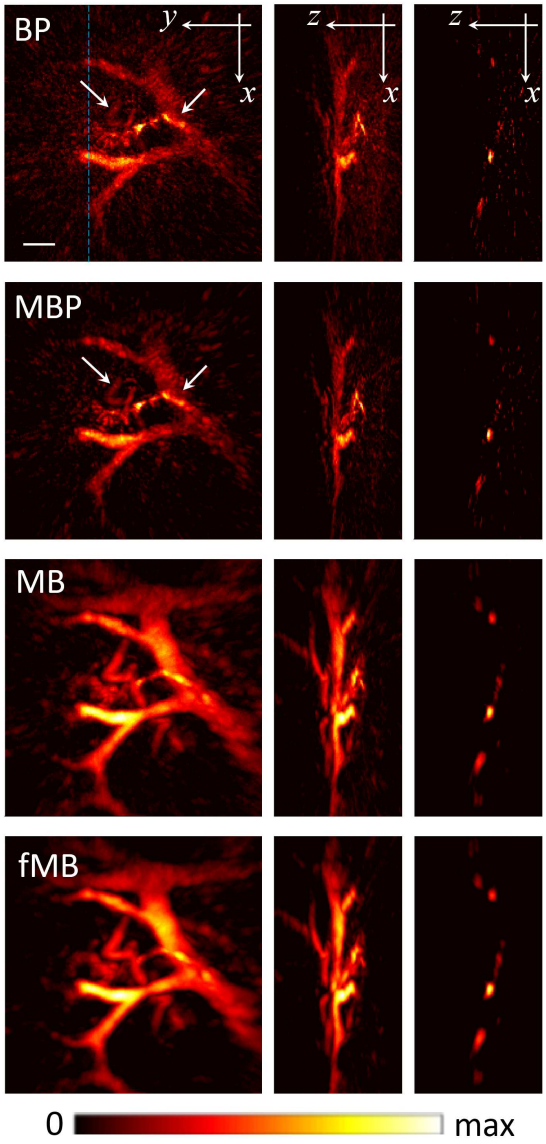

Fig. 3: Images of the finger vasculature of a healthy volunteer. Maximum intensity projections (MIPs) along the z and y directions are shown in the first and second columns, respectively. The third column displays the x-z cross-sectional images at the y position marked by the dotted blue line in the top-left image. Scalebar – 1mm.

This article has been accepted for publication in a future issue of this journal, but has not been fully edited. Content may change prior to final publication. Citation information: DOI 10.1109/TMI.2020.2981835, IEEE Transactions on Medical Imaging

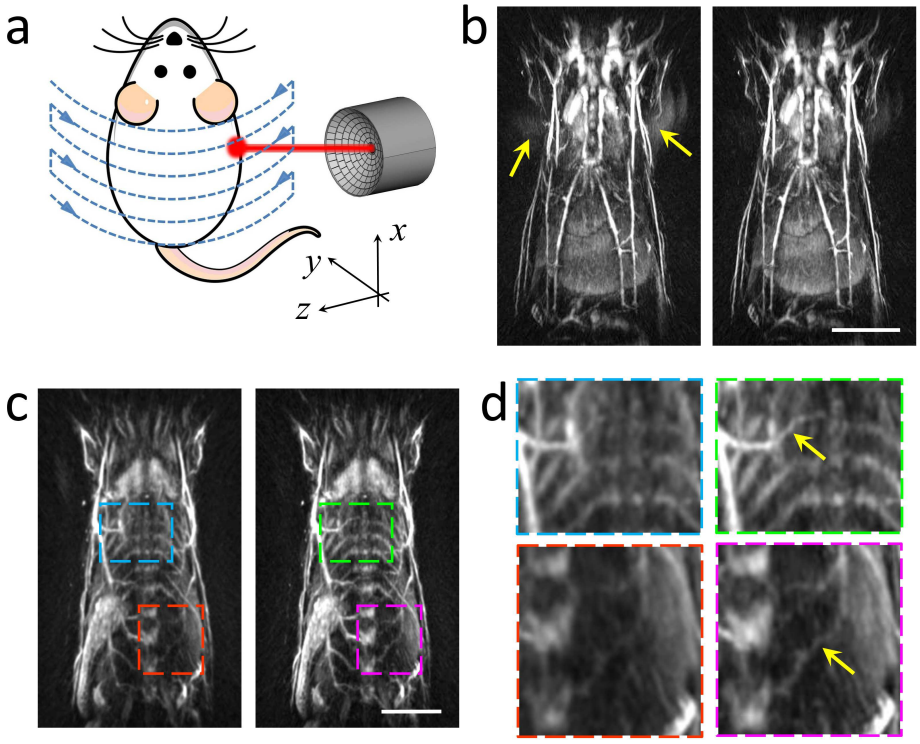

Fig. 4: *In vivo* whole-body SVOT scan of a mouse. a) Scanning geometry. b) Maximum intensity projections (MIPs) of the front part of the mouse using the BP (left) and MBP (right) methods. c) MIPs of the back part of the mouse using the BP (left) and MBP (right) methods. d) Zoom-in images of selected rectangular areas in c) with BP images in the left column and MBP images on the right column. Scalebars – 10mm.

the z and x directions) at four different time instants before and after the injection of ICG. The increase in signal due to the bolus appearance of the agent can be clearly seen in different vascular structures of the brain. The time profiles of the OA signal intensity for two different ROIs indicated in Fig. 5a are plotted in Fig. 5b. They were extracted from the images reconstructed with the BP, MB, fMB and MBP methods, respectively. The injection time interval and the time instants corresponding to the four images displayed in Fig. 5a are indicated with red and gray dashed lines, respectively. The profiles corresponding to ROI2 show lower intensity and slower decay than those corresponding to ROI1. It is shown that the temporal OA signals for all model-based methods (MB, fMB and MBP) almost perfectly match and barely change for the BP method. Specifically, the relative increase and subsequent decay of the signals are the same with all methods. Thereby, no quantitative errors have been produced due to the simplifications introduced in this work. Model-based reconstruction is however significantly accelerated. In this example, the MBP method can even render 30 reconstructed frames per second. The good trade-off between image quality and reconstruction speed makes the MBP method practical for real-time imaging scenarios. Table 1 lists the reconstruction times per frame of the different model-based algorithms for the experiments performed, considering 10 iterations for the iterative methods.

IV. Discussion and Conclusions

The model-based OA reconstruction approach introduced herein has been shown to have sufficiently low complexity for becoming practically applicable in large-scale datasets while yielding equivalent results as those obtained with previously introduced implementations. Large-scale can refer to large amounts of data, large number of unknowns or both. In both cases, standard model-based inversion is impractical due to the long computational times generally required. Acquisition and processing of large datasets is often needed in many applications, and accurate reconstruction is essential for proper interpretation of the results. For example, a large number of signals are needed for the reconstruction of large volumes such as the female breast [50], [52] or a whole mouse [49], [65]. The algorithm employed affects the resolution, contrast and overall quality of the images. A large number of signals are also required for the reconstruction of a sequence of images. This is essential for the visualization of dynamic events at multiple time scales, such as brain activity [55], [66], [67], cardiovascular dynamics [68], [69], pharmacokinetics of agents [70], [71] and many others.

The newly introduced discretization method has enabled accelerating iterative reconstructions by an order of magnitude

This article has been accepted for publication in a future issue of this journal, but has not been fully edited. Content may change prior to final publication. Citation information: DOI 10.1109/TMI.2020.2981835, IEEE Transactions on Medical Imaging

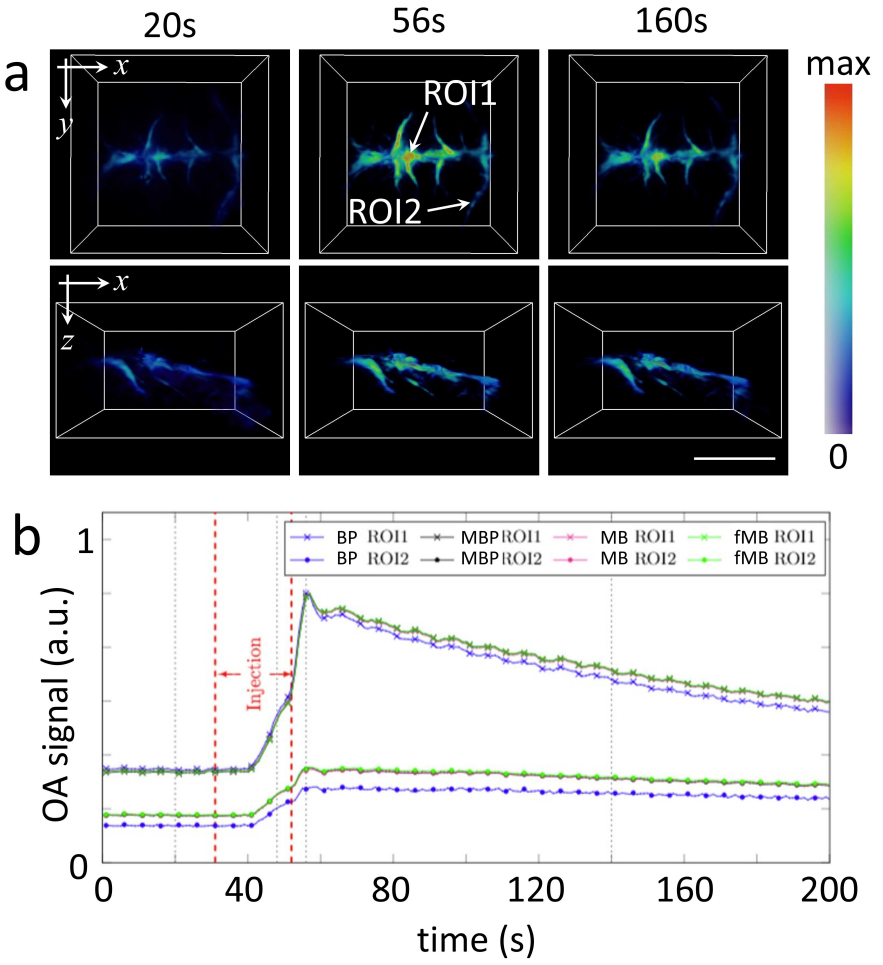

Fig. 5: ICG perfusion into the mouse brain. a) Top and lateral maximum intensity projections (MIPs) of the volumetric brain images reconstructed with the MBP method at four different time instants before and after injection. The white arrows point to two regions of interest (ROIs) in the superior sagittal sinus and the rostral rhinal vein, respectively. b) Temporal profiles of the optoacoustic signal intensity for the ROIs in a) as extracted from the images obtained with the BP, MBP, MB and fMB methods, respectively. Scalebar – 5mm.

with respect to a recently introduced approach based on a look-up table obtained using a trilinear interpolation kernel [48]. Herein, a Tikhonov regularization term was included in the inversion procedure, but other inversion algorithms based e.g. on L1-norm regularization can also be implemented by using the matrix-vector implementations suggested in this work. L1-norm regularization is used in compressed-sensing to recover images that are sparse in a specified domain, and has been used successfully in OA tomography [34], [35], [72]. In extremely large data-sets, where iterative methods are still impractical, it was shown that the non-iterative MBP approach yields more accurate results than the similarly complex BP method. The MBP approach further allowed accurately tracking relative changes in optical absorption. Indeed, it was demonstrated that it renders the same OA signal values as those obtained with the iterative method during the bolus appearance of a contrast agent. It is hence anticipated that the MBP method can also accurately track relative OA signal variations in hemoglobin, calcium indicators, photoswitchable agents, pH sensors and many other contrast agents generating dynamic changes in contrast [73]. On the other hand, accurate quantification of absolute absorption in OA imaging remains a challenging problem with many factors involved, such as the presence of optical and acoustic heterogeneities in biological tissues or the signal distortions induced by the ultrasound transducer(s) [74], [75], [76]. Model-based reconstruction potentially enables accounting for such effects. Considering that the suggested approach is practically applicable in large scale datasets, future developments are poised to enhance the quantitative performance in three-dimensional OA tomography.

In conclusion, the significant reduction of complexity in the discretization of the time-domain OA forward model introduced in this work is expected to greatly enhance the applicability of model-based reconstruction methods in three-dimensional OA reconstructions involving large amounts of data. Considering that model-based approaches offer an oth-

This article has been accepted for publication in a future issue of this journal, but has not been fully edited. Content may change prior to final publication. Citation information: DOI 10.1109/TMI.2020.2981835, IEEE Transactions on Medical Imaging

TABLE I: Reconstruction times per frame considering 10 iterations for the fMB and MB methods.

	MBP	fMB	MB
finger vessel scan ($M = 200 \times 200 \times 100$, $K = 1039$ and $Q = 512$)	0.18s	4.5s	32s
whole-mouse scan ($M = 300 \times 300 \times 500$, $K = 1317$ and $Q = 256 \times 735$)	430s	–	–
brain ICG perfusion ($M = 100 \times 100 \times 100$, $K = 1389$ and $Q = 512$)	0.03s	0.69s	7.9s

erwise unavailable flexibility to incorporate ultrasound propagation and transducer response effects, it is anticipated that future developments in the method introduced herein lead to important advances in the achievable resolution, quantitativeness and overall accuracy of many OA imaging systems.

APPENDIX A

Details on the calculation of $\mathbf{Sv}$ and $\mathbf{S}^T\mathbf{u}$ are given in Algorithms 1 and 2 respectively.

Algorithm 1 Calculation of $\mathbf{y} = \mathbf{Sv}$

for $i = 1, \ldots, M$ **do**
  for $q = 1, \ldots, Q$ **do**
    $d_{q,i} = \|\mathbf{r}_q - \mathbf{r}_i\|$
    $k_{q,i} = \left\lfloor \frac{d_{q,i}}{cT} - \frac{t_0}{T} \right\rceil$
    $[\mathbf{y}]_{K(q-1)+k_{q,i}} = [\mathbf{y}]_{K(q-1)+k_{q,i}} + [\mathbf{v}]_i \frac{c}{d_{q,i}}$
  end for
end for

Algorithm 2 Calculation of $\mathrm{x} = \mathrm{S}^T\mathrm{u}$

for $i = 1, \ldots, M$ **do**
  for $q = 1, \ldots, Q$ **do**
    $d_{q,i} = \|\mathbf{r}_q - \mathbf{r}_i\|$
    $k_{q,i} = \left\lfloor \frac{d_{q,i}}{cT} - \frac{t_0}{T} \right\rceil$
    $[\mathrm{x}]_i = [\mathrm{x}]_i + [\mathrm{u}]_{K(q-1)+k_{q,i}} \frac{c}{d_{q,i}}$
  end for
end for

ACKNOWLEDGMENT

Research leading to these results was partially supported by the European Research Council Grant ERC-2015-CoG-682379.

REFERENCES

[1] G. N. Hounsfield. "Computerized transverse axial scanning (tomography): Part 1. description of system," *The British journal of radiology*, vol. 46, no. 552, pp. 1016–1022, 1973.

[2] R. A. Brooks and G. Di Chiro. "Principles of computer assisted tomography (cat) in radiographic and radioisotopic imaging," *Physics in Medicine & Biology*, vol. 21, no. 5, pp. 689, 1976.

[3] M. Beister, D. Kolditz, and W. A. Kalender. "Iterative reconstruction methods in x-ray ct," *Physica medica*, vol. 28, no. 2, pp. 94–108, 2012.

[4] X. Pan, E. Sidky, and M. Vannier. "Why do commercial ct scanners still employ traditional, filtered back-projection for image reconstruction?," *Inverse problems*, vol. 25, no. 12, pp. 123009, 2009.

[5] G. Pratx and L. Xing. "Gpu computing in medical physics: A review," *Medical physics*, vol. 38, no. 5, pp. 2685–2697, 2011.

[6] L. L. Geyer *et al.,* "State of the art: iterative ct reconstruction techniques," *Radiology*, vol. 276, no. 2, pp. 339–357, 2015.

[7] G. Paltauf, J. A. Viator, S. A. Prahl, and S. L. Jacques. "Iterative reconstruction algorithm for optoacoustic imaging," *The Journal of the Acoustical Society of America*, vol. 112, no. 4, pp. 1536–1544, 2002.

[8] K. Wang, R. Su, A. A. Oraevsky, and M. A. Anastasio. "Investigation of iterative image reconstruction in three-dimensional optoacoustic tomography," *Physics in Medicine & Biology*, vol. 57, no. 17, pp. 5399, 2012.

[9] C. Lutzweiler, X. L. Deán-Ben, and Daniel Razansky. "Expediting model-based optoacoustic reconstructions with tomographic symmetries," *Medical physics*, vol. 41, no. 1, pp. 013302, 2014.

[10] P. Mohajerani, S. Kellnberger, and V. Ntziachristos. "Frequency domain optoacoustic tomography using amplitude and phase," *Photoacoustics*, vol. 2, no. 3, pp. 111–118, 2014.

[11] S. R. Arridge, M. M. Betcke, B. T. Cox, F. Lucka, and B. E. Treeby. "On the adjoint operator in photoacoustic tomography," *Inverse Problems*, vol. 32, no. 11, pp. 115012, 2016.

[12] A. Hauptmann *et al.,* "Model-based learning for accelerated, limited-view 3-d photoacoustic tomography," *IEEE transactions on medical imaging*, vol. 37, no. 6, pp. 1382–1393, 2018.

[13] R. Shang, R. Archibald, A. Gelb, and G. P. Luke. "Sparsity-based photoacoustic image reconstruction with a linear array transducer and direct measurement of the forward model," *Journal of biomedical optics*, vol. 24, no. 3, pp. 031015, 2018.

[14] L. V. Wang and J. Yao. "A practical guide to photoacoustic tomography in the life sciences," *Nature methods*, vol. 13, no. 8, pp. 627, 2016.

[15] A. Rosenthal, V. Ntziachristos, and D. Razansky. "Model-based optoacoustic inversion with arbitrary-shape detectors," *Medical physics*, vol. 38, no. 7, pp. 4285–4295, 2011.

[16] K. Mitsuhashi, K. Wang, and M. A. Anastasio. "Investigation of the far-field approximation for modeling a transducer's spatial impulse response in photoacoustic computed tomography," *Photoacoustics*, vol. 2, no. 1, pp. 21–32, 2014.

[17] D. Queirós, X. L. Déan-Ben, A. Buehler, D. Razansky, A. Rosenthal, and V. Ntziachristos. "Modeling the shape of cylindrically focused transducers in three-dimensional optoacoustic tomography," *Journal of biomedical optics*, vol. 18, no. 7, pp. 076014, 2013.

[18] D. Modgil, M. A. Anastasio, and P. J. La Rivière. "Image reconstruction in photoacoustic tomography with variable speed of sound using a higher-order geometrical acoustics approximation," *Journal of biomedical optics*, vol. 15, no. 2, pp. 021308, 2010.

[19] X. L. Deán-Ben, R. Ma, A. Rosenthal, V. Ntziachristos, and D. Razansky. "Weighted model-based optoacoustic reconstruction in acoustic scattering media," *Physics in Medicine & Biology*, vol. 58, no. 16, pp. 5555, 2013.

[20] C. Huang, K. Wang, L. Nie, L. V. Wang, and M. A. Anastasio. "Full-wave iterative image reconstruction in photoacoustic tomography with acoustically inhomogeneous media," *IEEE transactions on medical imaging*, vol. 32, no. 6, pp. 1097–1110, 2013.

[21] S. Mandal, X. L. Deán-Ben, and D. Razansky. "Visual quality enhancement in optoacoustic tomography using active contour segmentation priors," *IEEE transactions on medical imaging*, vol. 35, no. 10, pp. 2209–2217, 2016.

[22] M. Haltmeier and L. V. Nguyen. "Analysis of iterative methods in photoacoustic tomography with variable sound speed," *SIAM Journal on Imaging Sciences*, vol. 10, no. 2, pp. 751–781, 2017.

[23] T. P. Matthews and M. A. Anastasio. "Joint reconstruction of the initial pressure and speed of sound distributions from combined photoacoustic and ultrasound tomography measurements," *Inverse problems*, vol. 33, no. 12, pp. 124002, 2017.

[24] G. Zangerl, M. Haltmeier, L. V. Nguyen, and R. Nuster. "Full field inversion in photoacoustic tomography with variable sound speed," *Applied Sciences*, vol. 9, no. 8, pp. 1563, 2019.

[25] K. Mitsuhashi, J. Poudel, T. P. Matthews, A. Garcia-Uribe, L. V. Wang, and M. A. Anastasio. "A forward-adjoint operator pair based on the elastic wave equation for use in transcranial photoacoustic computed tomography," *SIAM journal on imaging sciences*, vol. 10, no. 4, pp. 2022–2048, 2017.

[26] Y. Hristova, P. Kuchment, and L. Nguyen. "Reconstruction and time reversal in thermoacoustic tomography in acoustically homogeneous and inhomogeneous media," *Inverse Problems*, vol. 24, no. 5, pp. 055006, 2008.

[27] H. Gruen, T. Berer, P. Burgholzer, R. Nuster, and G. Paltauf. "Three-dimensional photoacoustic imaging using fiber-based line detectors," *Journal of biomedical optics*, vol. 15, no. 2, pp. 021306, 2010.

[28] B. E. Treeby, E. Z. Zhang, and B. T. Cox. "Photoacoustic tomography in absorbing acoustic media using time reversal," *Inverse Problems*, vol. 26, no. 11, pp. 115003, 2010.

[29] Z. Belhachmi, T. Glatz, and O. Scherzer. "A direct method for photoacoustic tomography with inhomogeneous sound speed," *Inverse Problems*, vol. 32, no. 4, pp. 045005, 2016.

[30] Y. Xu and L. V. Wang. "Time reversal in photoacoustic or thermoacoustic tomography," in *Photoacoustic Imaging and Spectroscopy*, pp. 117–120. CRC Press, 2017.

[31] Y. Dong, T. Görner, and S. Kunis. "An algorithm for total variation regularized photoacoustic imaging," *Advances in Computational Mathematics*, vol. 41, no. 2, pp. 423–438, 2015.

[32] L. Ding, X. L. Deán-Ben, C. Lutzweiler, D. Razansky, and V. Ntziachristos. "Efficient non-negative constrained model-based inversion in optoacoustic tomography," *Physics in Medicine & Biology*, vol. 60, no. 17, pp. 6733, 2015.

[33] Q. Sheng *et al.,* "A constrained variable projection reconstruction method for photoacoustic computed tomography without accurate knowledge of transducer responses," *IEEE transactions on medical imaging*, vol. 34, no. 12, pp. 2443–2458, 2015.

[34] Y. Han, L. Ding, X. L. Deán Ben, D. Razansky, J. Prakash, and V. Ntziachristos. "Three-dimensional optoacoustic reconstruction using fast sparse representation," *Optics letters*, vol. 42, no. 5, pp. 979–982, 2017.

[35] D. M. Egolf, R. K. Chee, and R. J. Zemp. "Sparsity-based reconstruction for super-resolved limited-view photoacoustic computed tomography deep in a scattering medium," *Optics letters*, vol. 43, no. 10, pp. 2221–2224, 2018.

[36] T. Shan, J. Qi, M. Jiang, and H. Jiang. "Gpu-based acceleration and mesh optimization of finite-element-method-based quantitative photoacoustic tomography: a step towards clinical applications," *Applied optics*, vol. 56, no. 15, pp. 4426–4432, 2017.

[37] K. Peng, L. He, Z. Zhu, J. Tang, and J. Xiao. "Three-dimensional photoacoustic tomography based on graphics-processing-unit-accelerated finite element method," *Applied optics*, vol. 52, no. 34, pp. 8270–8279, 2013.

[38] K. Wang, R. W. Schoonover, R. Su, A. Oraevsky, and M. A. Anastasio. "Discrete imaging models for three-dimensional optoacoustic tomography using radially symmetric expansion functions," *IEEE transactions on medical imaging*, vol. 33, no. 5, pp. 1180–1193, 2014.

[39] L. Ding, X. L. Deán-Ben, and D. Razansky. "Real-time model-based inversion in cross-sectional optoacoustic tomography," *IEEE transactions on medical imaging*, vol. 35, no. 8, pp. 1883–1891, 2016.

[40] M. Roumeliotis *et al.,* "Analysis of a photoacoustic imaging system by the crosstalk matrix and singular value decomposition," *Optics express*, vol. 18, no. 11, pp. 11406–11417, 2010.

[41] A. Buehler, A. Rosenthal, T. Jetzfellner, A. Dima, D. Razansky, and V. Ntziachristos. "Model-based optoacoustic inversions with incomplete projection data," *Medical physics*, vol. 38, no. 3, pp. 1694–1704, 2011.

[42] D. Modgil, P. J. La Rivière, and B. E. Treeby. "Photoacoustic image reconstruction in an attenuating medium using singular-value decomposition," *Journal of biomedical optics*, vol. 17, no. 6, pp. 061204, 2012.

[43] A. Rosenthal, T. Jetzfellner, D. Razansky, and V. Ntziachristos. "Efficient framework for model-based tomographic image reconstruction using wavelet packets," *IEEE transactions on medical imaging*, vol. 31, no. 7, pp. 1346–1357, 2012.

[44] Y. Han, V. Ntziachristos, and A. Rosenthal. "Optoacoustic image reconstruction and system analysis for finite-aperture detectors under the wavelet-packet framework," *Journal of biomedical optics*, vol. 21, no. 1, pp. 016002, 2016.

[45] D. Allman, A. Reiter, and M. A. Bell. "Photoacoustic source detection and reflection artifact removal enabled by deep learning," *IEEE transactions on medical imaging*, vol. 37, no. 6, pp. 1464–1477, 2018.

[46] S. Antholzer, M. Haltmeier, and J. Schwab. "Deep learning for photoacoustic tomography from sparse data," *Inverse problems in science and engineering*, vol. 27, no. 7, pp. 987–1005, 2019.

[47] N. Davoudi, X. L. Deán-Ben, and D. Razansky. "Deep learning optoacoustic tomography with sparse data," *Nature Machine Intelligence*, vol. 1, no. 10, pp. 453–460, 2019.

[48] L. Ding, X. L. Deán-Ben, and D. Razansky. "Efficient 3-d model-based reconstruction scheme for arbitrary optoacoustic acquisition geometries," *IEEE transactions on medical imaging*, vol. 36, no. 9, pp. 1858–1867, 2017.

[49] H. P. Brecht, R. Su, M. P. Fronheiser, S. A. Ermilov, A. Conjusteau, and A. A. Oraevsky. "Whole-body three-dimensional optoacoustic tomography system for small animals," *Journal of biomedical optics*, vol. 14, no. 6, pp. 064007, 2009.

[50] R. A. Kruger, C. M. Kuzmiak, R. B. Lam, D. R. Reinecke, S. P. Del Rio, and D. Steed. "Dedicated 3d photoacoustic breast imaging," *Medical physics*, vol. 40, no. 11, pp. 113301, 2013.

[51] A. P. Jathoul *et al.,* "Deep in vivo photoacoustic imaging of mammalian tissues using a tyrosinase-based genetic reporter," *Nature Photonics*, vol. 9, no. 4, pp. 239, 2015.

[52] M. Heijblom *et al.,* "Visualizing breast cancer using the twente photoacoustic mammoscope: what do we learn from twelve new patient measurements?," *Optics express*, vol. 20, no. 11, pp. 11582–11597, 2012.

[53] J. Tang *et al.,* "Noninvasive high-speed photoacoustic tomography of cerebral hemodynamics in awake-moving rats," *Journal of Cerebral Blood Flow & Metabolism*, vol. 35, no. 8, pp. 224–1232, 2015.

[54] A. Özbek, X. L. Deán-Ben, and D. Razansky. "Optoacoustic imaging at kilohertz volumetric frame rates," *Optica*, vol. 5, no. 7, pp. 857–863, 2018.

[55] X. L. Deán-Ben, S. Gottschalk, G. Sela, S. Shoham, and D. Razansky. "Functional optoacoustic neuro-tomography of calcium fluxes in adult zebrafish brain in vivo," *Optics letters*, vol. 42, no. 5, pp. 959–962, 2017.

[56] X. L. Deán-Ben, T. F. Fehm, S. J. Ford, S. Gottschalk, and D. Razansky. Spiral volumetric optoacoustic tomography visualizes multi-scale dynamics in mice. *Light: Science & Applications*, vol. 6, no. 4, pp. e16247, 2017.

[57] C. C Paige and M. A. Saunders. "Lsqr: An algorithm for sparse linear equations and sparse least squares," *ACM Transactions on Mathematical Software (TOMS)*, vol. 8, no. 1, pp. 43–71, 1982.

[58] G. Turin. "An introduction to matched filters," *IRE transactions on Information theory*, vol. 6, no. 3, pp. 311–329, 1960.

[59] M. Xu and L. V. Wang. "Universal back-projection algorithm for photoacoustic computed tomography," *Physical Review E*, vol. 71, no. 1, pp. 016706, 2005.

[60] X. L. Deán-Ben *et al.,* "Functional optoacoustic neuro-tomography for scalable whole-brain monitoring of calcium indicators," *Light: Science & Applications*, vol. 5, no. 12, pp. e16201, 2016.

[61] X. L. Deán-Ben and D. Razansky. "Portable spherical array probe for volumetric real-time optoacoustic imaging at centimeter-scale depths," *Optics express*, vol. 21, no. 23, pp. 28062–28071, 2013.

[62] F. J. Landa, X. L. Deán-Ben, R Sroka, and D. Razansky. "Volumetric optoacoustic temperature mapping in photothermal therapy," *Scientific reports*, vol. 7, no. 1, pp. 9695, 2017.

[63] X. L. Deán-Ben and D. Razansky. "On the link between the speckle free nature of optoacoustics and visibility of structures in limited-view tomography," *Photoacoustics*, vol. 4, no. 4, pp. 133–140, 2016.

[64] X. L. Dean-Ben, A. Buehler, V. Ntziachristos, and D. Razansky. "Accurate model-based reconstruction algorithm for three-dimensional optoacoustic tomography," *IEEE Transactions on Medical Imaging*, vol. 31, no. 10, pp. 1922–1928, 2012.

[65] T. F. Fehm, X. L. Deán-Ben, S. J. Ford, and D. Razansky. "In vivo whole-body optoacoustic scanner with real-time volumetric imaging capacity," *Optica*, vol. 3, no. 11, pp. 1153–1159, 2016.

[66] S. Gottschalk, T. F. Fehm, X. L. Deán-Ben, V. Tsytsarev, and D. Razansky. "Correlation between volumetric oxygenation responses and electrophysiology identifies deep thalamocortical activity during epileptic seizures," *Neurophotonics*, vol. 4, no. 1, pp. 011007, 2016.

[67] B. Rao, R. Zhang, L. Li, J. Y. Shao, and L. V. Wang. "Photoacoustic imaging of voltage responses beyond the optical diffusion limit," *Scientific reports*, vol. 7, no. 1, pp. 2560, 2017.

[68] H. C. A. Lin *et al.,* "Characterization of cardiac dynamics in an acute myocardial infarction model by four-dimensional optoacoustic and magnetic resonance imaging," *Theranostics*, vol. 7, no. 18, pp. 4470, 2017.

[69] L. Li *et al.,* "Single-impulse panoramic photoacoustic computed tomography of small-animal whole-body dynamics at high spatiotemporal resolution," *Nature biomedical engineering*, vol. 1, no. 5, pp. 0071, 2017.

[70] S. Morscher, W. H. Driessen, J. Claussen, and N. C. Burton. "Semi-quantitative multispectral optoacoustic tomography (msot) for volumetric pk imaging of gastric emptying," *Photoacoustics*, vol. 2, no. 3, pp. 103–110, 2014.

[71] L. Scarfe *et al.,* "Measures of kidney function by minimally invasive techniques correlate with histological glomerular damage in scid mice with adriamycin-induced nephropathy," *Scientific reports*, vol. 5, pp. 13601, 2015.

[72] J. Poudel, Y. Lou, and M. A. Anastasio. "A survey of computational frameworks for solving the acoustic inverse problem in three-dimensional photoacoustic computed tomography," *Physics in Medicine & Biology*, vol. 64, no. 14, pp. 14TR01, 2019.

[73] X. L. Deán-Ben, S. Gottschalk, B. McLarney, S. Shoham, and D. Razansky. "Advanced optoacoustic methods for multiscale imaging of in vivo dynamics," *Chemical Society Reviews*, vol. 46, no. 8, pp. 2158–2198, 2017.

[74] A. Pulkkinen, B. T. Cox, S. R. Arridge, J. P. Kaipio, and T. Tarvainen. "Quantitative photoacoustic tomography using illuminations from a single direction," *Journal of biomedical optics*, vol. 20, no. 3, pp. 036015, 2015.

[75] M. A. Mastanduno and S. S. Gambhir. "Quantitative photoacoustic image reconstruction improves accuracy in deep tissue structures," *Biomedical optics express*, vol. 7, no. 10, pp. 3811–3825, 2016.

[76] C. Cai, K. Deng, C. Ma, and J. Luo. "End-to-end deep neural network for optical inversion in quantitative photoacoustic imaging," *Optics letters*, vol. 43, no. 12, pp. 2752–2755, 2018.

Appendix D

Three-dimensional Optoacoustic Reconstruction Using Fast Sparse Representation

Yiyong Han, **Lu Ding**, Xosé Luis Deán Ben, Daniel Razansky, Jaya Prakash, and Vasilis Ntziachristos. Three-dimensional optoacoustic reconstruction using fast sparse representation. *Optics Letters*, 42(5):979–982, 2017

Optics Letters

Three-dimensional optoacoustic reconstruction using fast sparse representation

Yiyong Han,[1,2] Lu Ding,[1,2] Xosé Luis Deán Ben,[1,2] Daniel Razansky,[1,2] Jaya Prakash,[1,2] and Vasilis Ntziachristos[1,2,*]

[1]Chair for Biological Imaging, Technical University of Munich, Ismaningerstraße 22, Munich 81675, Germany
[2]Institute for Biological and Medical Imaging, Helmholtz Center Munich, Ingolstadter Landstraße 1, Neuherberg 85764, Germany
*Corresponding author: v.ntziachristos@tum.de

Received 8 November 2016; revised 4 February 2017; accepted 6 February 2017; posted 7 February 2017 (Doc. ID 278984); published 28 February 2017

Optoacoustic tomography based on insufficient spatial sampling of ultrasound waves leads to loss of contrast and artifacts on the reconstructed images. Compared to reconstructions based on L2-norm regularization, sparsity-based reconstructions may improve contrast and reduce image artifacts but at a high computational cost, which has so far limited their use to 2D optoacoustic tomography. Here we propose a fast, sparsity-based reconstruction algorithm for 3D optoacoustic tomography, based on gradient descent with Barzilai–Borwein line search (L1-GDBB). Using simulations and experiments, we show that the L1-GDBB offers fourfold faster reconstruction than the previously reported L1-norm regularized reconstruction based on gradient descent with backtracking line search. Moreover, the new algorithm provides higher-quality images with fewer artifacts than the L2-norm regularized reconstruction and the back-projection reconstruction.

OCIS codes: (170.5120) Photoacoustic imaging; (170.3010) Image reconstruction techniques; (170.3880) Medical and biological imaging.

https://doi.org/10.1364/OL.42.000979

Tomographic reconstruction is often hampered by incomplete or insufficient data, and the selection of a reconstruction algorithm can make a substantial difference in the final image quality. In optoacoustic (photoacoustic) tomography, ultrasound waves are generated in a three-dimensional (3D) region and further propagate in all directions [1]. Therefore, the optoacoustic detector(s) should ideally collect sufficient pressure signals to accurately map the entire ultrasound wavefront surrounding the imaged sample [2]. However, spatial constraints in currently available optoacoustic systems usually limit the range of accessible projection angles, consequently, leading to artifacts and loss of resolution and contrast in the reconstructed images. For example, it has been shown that streak-type artifacts associated with sparse acquisition are clearly visible in the cross sections of the reconstructed 3D images when using back-projection (BP) algorithms or iterative inversion methods based on the L2-norm regularization [3,4].

Sparsity-based iterative image reconstructions are known to mitigate artifacts and, hence, enhance the contrast-to-noise ratio (CNR) of images [5]. In cross-sectional (2D) optoacoustic imaging, sparsity-based reconstruction generates better images with fewer artifacts [6,7] than reconstruction based on the LSQR algorithm with L2-norm regularization (L2-LSQR) [8,9]. One commonly used 2D sparsity-based reconstruction is based on gradient descent with backtracking line search (L1-GDBT) [6,8,9] in which the sparsity transformation is carried out using the Rice wavelet toolbox [6,8–10]. These approaches are inadequate for 3D optoacoustic imaging. The Rice wavelet toolbox restricts the reconstructed image in 2D with a size of $2^N \times 2^N$, where N is a positive integer. The backtracking line search involves several matrix-vector multiplications at each iteration, making the entire process computationally burdensome and, therefore, impractical for 3D imaging. An alternative is the Barzilai–Borwein line search, which allows fast step size calculation for various inversion methods. It has been applied to computed tomography [11], magnetic resonance imaging [12], and 2D optoacoustic imaging [10,13].

As optoacoustic systems collecting 3D information become available [14], it is necessary to develop fast and accurate sparsity-based algorithms for 3D optoacoustic reconstructions. Although we have achieved real-time BP reconstruction with GPU implementation [15], a more accurate 3D model-based iterative reconstruction is still needed for better visualization and subsequent multispectral analysis [16]. With the benefit of a multi-level wavelet decomposition (and reconstruction) for 2D and 3D images of any size, we develop a fast 3D sparsity-based optoacoustic reconstruction method based on gradient descent with Barzilai–Borwein line search and L1-norm regularization (L1-GDBB) [17,18]. We hypothesized that computing the gradient step size analytically at each iteration would make the L1-GDBB faster than the L1-GDBT [6,8,9]. Here we compare the performance of the BP [15], L2-LSQR, L1-GDBT, and L1-GDBB in simulations and

experiments, and we provide evidence of the advantages of theL1-GDBB over the other three methods.

In 3D model-based iterative reconstruction, the forward model leads to a discrete-to-discrete linear transformation from the reconstructed image u to the detected pressure signals p [3]:

$$p = \mathbf{M}u, \tag{1}$$

where $\mathbf{M}$ is the 3D forward model matrix. The reconstructed image can be obtained by solving the following minimization problem with the L2-LSQR method [19]:

$$\min\left\{\frac{1}{2}\|p - \mathbf{M}u\|_2^2 + \kappa\|u\|_2^2\right\}, \qquad u \geq 0, \tag{2}$$

where $\kappa \geq 0$ is the regularization parameter. An alternative approach to solve the inversion of Eq. (1) by sparse representation is [6,8,9]

$$\min\left\{\frac{1}{2}\|p - \mathbf{M}u\|_2^2 + \lambda\|\mathbf{\Phi}u\|_1\right\}, \qquad u \geq 0, \tag{3}$$

where $\lambda \geq 0$ is the regularization parameter and $\mathbf{\Phi}$ is the sparsity transform operator. If $v = \mathbf{\Phi}u$ represents the solution in a sparsity domain, then Eq. (3) can be rewritten as

$$\min f(v) = \min\left\{\frac{1}{2}\|p - \mathbf{H}v\|_2^2 + \lambda\|v\|_1\right\}, \qquad \mathbf{\Phi}^{-1}v \geq 0, \tag{4}$$

where $\mathbf{H} = \mathbf{M}\mathbf{\Phi}^{-1}$. Equation (4) can be solved efficiently using the L1-GDBB (Algorithm 1). In the present study, $\mathbf{\Phi}$ was defined to be the two-level Daubechies-4 wavelet transform.

Algorithm 1 *Sparsity-based Reconstruction using Gradient Descent with Backtracking Line Search*

Step 1: Initialize iteration variables $i = 1$, $v_1 = 0$, maximum iteration number max *Iter* and stopping criterion η.
Step 2: Calculate the gradient of the objective function $\nabla f(v_i)$ and update part of the solution $\Delta(v_i) = -\nabla f(v_i)$.
Step 3: If $i = 1$, set $t_1 = 1$. Otherwise choose step size t_i via Barzilai–Borwein line search: $t_i = \|v_i - v_{i-1}\|_2^2/((v_i - v_{i-1})^T(\Delta v_i - \Delta v_{i-1}))$.
Step 4: Update the solution with $v_{i+1} = \mathbf{\Phi}(\mathbf{max}(\mathbf{\Phi}^{-1}(v_i + t_i\Delta v_i), 0))$.
Step 5: Check the stopping criterion. If $((\|p - \mathbf{H}v_{i+1}\|_2 - \|p - \mathbf{H}v_i\|_2)/\|p\|_2) < \eta$ or $i >$ max *Iter*, go to next step; otherwise, $i = i + 1$ and go to Step 2.
Step 6: Transfer the final reconstruction back to image domain. $u = \mathbf{\Phi}^{-1}v$.

The L1-GDBT is similar to the L1-GDBB described in Algorithm 1 except that step 3 is replaced with the following:

Set $t_i = 1$,
while $(f(v_i + t_i\Delta v_i) > f(v_i) - \alpha t_i\Delta v_i^T\Delta v_i)$,
$t_i = \beta t_i$,
End,

where $\alpha \in (0, 0.5)$ and $\beta \in (0, 1)$ are the backtracking line search parameters [20]. In each L1-GDBT iteration, the backtracking line search stops only when the objective function decreases. As a result, the "$t_i = \beta t_i$" operation in the backtracking line search might execute several times at the cost of several time-consuming matrix-vector multiplications. In contrast, in the L1-GDBB, the step size is approximated by a formula reflecting the solutions from the previous and current iterations as well as the gradient of the objective function (Step 3 in Algorithm 1). Only two matrix-vector multiplications are needed for each L1-GDBB iteration or each L2-LSQR iteration, which should make them much faster than the L1-GDBT.

The numerical and experimental performance of the L1-GDBB was compared with the BP, L1-GDBT, and L2-LSQR on a CPU platform. Specifically, we considered the 3D optoacoustic geometry shown in Fig. 1(a), which corresponds to a recently developed 3D optoacoustic array [14]. The detecting array consists of a 256-element ultrasound transducer array (UTA) covering a 90° span of projection angles. The UTA has a central frequency of 4 MHz and −6 dB bandwidth of 100%. In the simulations, synthetic signals were analytically generated for five spherical absorbers with an absorption distribution given by a truncated parabolic function [21] in a region of interest (ROI) measuring 8 mm × 8 mm × 8 mm (81 × 81 × 81 voxels). The radius of the absorbers was set to 300 μm, and they were positioned at the following coordinates (in mm): (0, 0, 0); (0, −1, 0); (0, 1, 0); (0, 0, −1); and (0, 0, 1) [Fig. 1(b)]. The simulated pressure signals were sampled at 281 time points and supplemented with white Gaussian noise at a signal-to-noise ratio (SNR) of 0 dB. The simulated data were then reconstructed in Matlab on a 2× Intel Xeon DP X5650 (6× 2.67 GHz) workstation with 144 GB RAM. Regularization parameters were determined using the L-curve method [22], and a stopping criterion of $\eta = 1 \times 10^{-5}$ served as the criterion of convergence for the three iterative reconstruction methods. All reconstructions were normalized to the maximum value. Figure 1(c) shows the maximum intensity projection (MIP) of the original data as well as reconstructions using the BP, L2-LSQR, L1-GDBT, and L1-GDBB in the x–y plane (top view) and y–z plane (side view). Figure 1(c) clearly shows that the CNR of the images is enhanced with sparsity-based reconstruction methods. The root mean square deviations (RMSDs) between theoretical image and reconstructions were calculated as 0.0414, 0.0203, 0.0175, and 0.0174 for the BP, L2-LSQR, L1-GBDT, and L1-GDBB, respectively. Reconstruction times (in seconds) were 2.5, 27, 224,

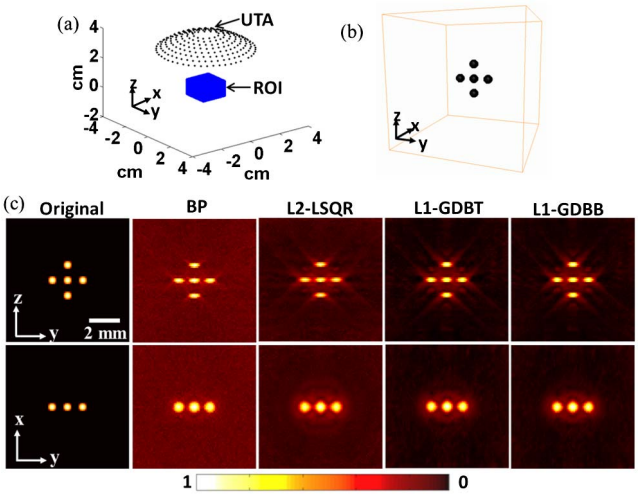

Fig. 1. (a) 3D optoacoustic tomography geometry tested in simulations and experiments. (b) Sketch of five spherical absorbers with truncated parabolic absorption. (c) MIP results from the original data and reconstructions using BP, L2-LSQR, L1-GDBT, or L1-GDBB. Reconstructions are shown in the x–y and y–z planes.

and 50 for the BP, L2-LSQR, L1-GBDT, and L1-GDBB, respectively.

Figure 2 illustrates the convergence performance of the L2-LSQR, L1-GDBT, and L1-GDBB in the simulation. Figures 2(a) and 2(b) show the variations in the RMSD and objective function $f(v)$ over 20 iterations, while Figs. 2(c) and 2(d) show the corresponding CPU times. The L2-LSQR converged in 4 iterations over 27 s. The non-monotonic behavior of RMSD in the case of the L2-LSQR illustrates the inability of this algorithm to deal with incomplete data. The L1-GDBB converged in 10 iterations over 50 s, while the L1-GDBT converged in 20 iterations over 224 s. As expected, the L1-GDBB converged much faster than the L1-GDBT.

Figure 3(a) shows two sets of slices (single plane) of the original data in planes of $z = 0$ (top row) and $y = 0$ (bottom row), as well as the corresponding reconstructions obtained using the BP, L2-LSQR, L1-GDBT, or L1-GDBB. The results of the L1-GDBT and the L1-GDBB in Fig. 3(a) show that sparsity-based reconstructions gave far fewer artifacts than the BP and the L2-LSQR. This corroborated the MIP results in Fig. 1(c). Figure 3(b) shows the line profiles of the original data and four reconstructions along Line 1 indicated in Fig. 3(a), which shows that the L1-GDBT and the L1-GDBB generated more accurate reconstructions than the BP and the L2-LSQR.

To verify and extend these simulations, we compared the performance of the BP, L2-LSQR, L1-GDBT, and L1-GDBB when the setup described above [14] was used to image the superficial palmar arch vessels of a healthy volunteer at a wavelength of 820 nm. The reconstruction region was 10 mm × 10 mm × 6.7 mm with a voxel mesh of 150 × 150 × 100. The acoustic signal was sampled at 251 time points for subsequent reconstructions. Figures 4(a) and 4(b) show MIP results from the side and top views; the regions enclosed by dashed lines in Fig. 4(b) are shown as zoomed-in views in Fig. 4(c). The comparison of the four reconstructions clearly indicates that both the L1-GDBT and the L1-GDBB generated fewer artifacts and a higher CNR than the BP and the L2-LSQR. To assess this quantitatively, we calculated the SNR and the CNR for the target region in dashed boxes labeled "T" and the respective background region in solid-line boxes labeled "B" in Figs. 4(a) and 4(b). SNR was calculated as the ratio of root mean square amplitude values of the target region and background region (in dB). The CNR was calculated as the mean value difference between the target region and background region divided by the standard deviation of the background region. The SNR values were 10.7, 20.8, 22.2, and 25.6 for the BP, L2-LSQR, L1-GBDT, and L1-GDBB, respectively. The CNR values were 3.2, 12.2, 16.7, and 20.9 for the BP, L2-LSQR, L1-GBDT, and

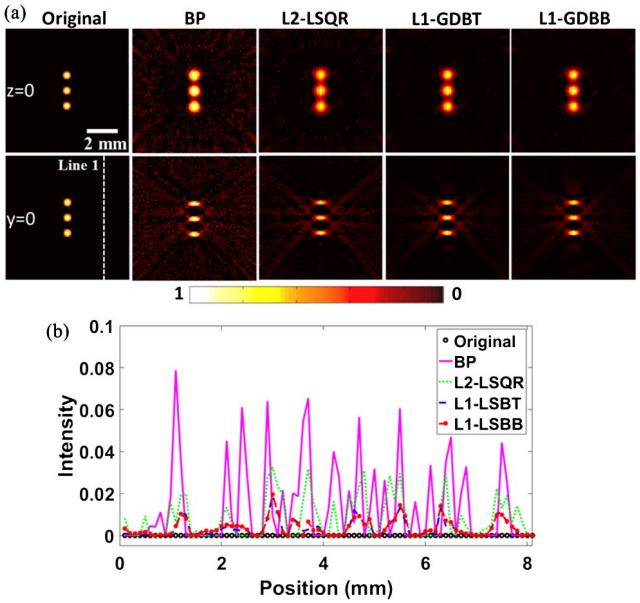

Fig. 3. (a) Single slices of original data and reconstructions generated using BP, L2-LSQR, L1-GDBT, or L1-GDBB in the $z = 0$ plane (top row) and $y = 0$ plane (bottom row). (b) Line profiles of the original data and four reconstructions along Line 1 in (a).

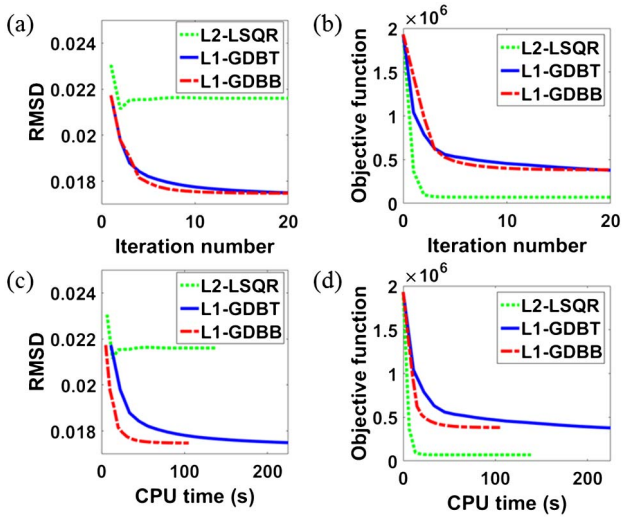

Fig. 2. Comparison of convergence performance of simulated reconstructions using L2-LSQR, L1-GDBT, or L1-GDBB. Variations in RMSD and objective function are depicted as a function of (a, b) iteration number and (c, d) CPU time.

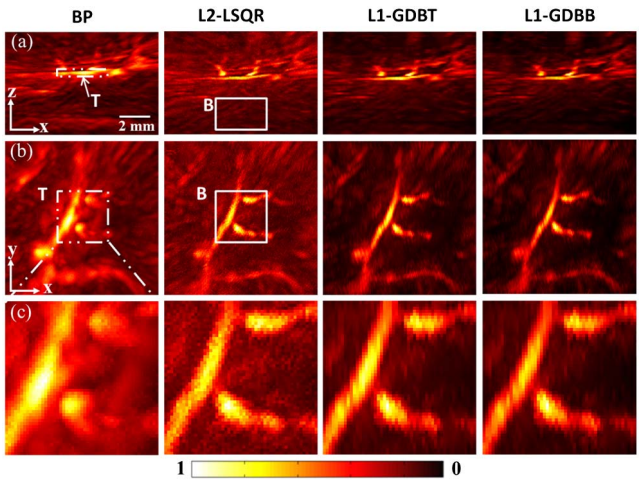

Fig. 4. (a, b) MIP results (side and top views) of reconstructions of experimental data using BP, L2-LSQR, L1-GDBT, and L1-GDBB. (c) Zoomed-in images of the top-view MIP region enclosed in the dot-dashed box in (b). The corresponding region for each reconstruction is shown, even though the box is drawn only for BP. The regions labeled "T" and "B" served as target and background regions, respectively, for calculating SNR and CNR.

L1-GDBB, respectively. These ratios confirm that sparsity-based reconstruction methods were superior to the BP or the L2-LSQR. The reconstruction times (in seconds) were 10, 158, 980, and 245 for the BP, L2-LSQR, L1-GBDT, and L1-GDBB, respectively.

The previous works have used the Barzilai–Borwein scheme in optoacoustic imaging, but were limited to 2D geometries [10,13]. In [10], the Barzilai–Borwein scheme was used along with the Augmented Lagrangian–type minimization and, in [13], the Barzilai–Borwein scheme was implemented to solve the block-sparse discrete cosine transform model-based reconstruction. In this paper, we perform the 3D sparsity-based reconstruction using a gradient descent with the Barzilai–Borwein approach. Importantly, the sparsity-based image reconstruction would perform better in 3D geometries compared to 2D geometries (owing to the fact that the compressibility of the reconstructed image would be higher in 3D). Also, advanced reconstruction approaches are necessary in 3D geometries (particularly for cardiovascular, neuroimaging applications), which could reduce the artifacts arising from insufficient data cases for precise biological analysis (as shown in Figs. 1, 3, and 4).

Taken together, our results indicate that the two sparsity-based methods perform well and generate far fewer artifacts and a higher CNR than the BP and the L2-LSQR. Also the L1-GDBB showed a fourfold faster computational time than the L1-GDBT. This substantial gain in reconstruction quality with the L1-GDBB with respect to the L2-LSQR comes with only a moderate 55% increase in CPU time. Short reconstruction time is essential in practical applications, particularly when processing large datasets, such as in biomedical research. Image reconstruction can be further accelerated through parallel implementations of the algorithms in a graphics processing unit (GPU). For example, efficient GPU implementation of the matrix-vector multiplications in iterative inversions can significantly accelerate the L2-LSQR–based reconstruction, even allowing real-time reconstruction with a 2D model [23]. Therefore, similar implementations for a 3D optoacoustic model combined with the L1-GDBB method described herein may lead to a highly practical and accurate approach in the future.

The L1-GDBB method may be particularly useful for dealing with the incompleteness of tomographic data. This incompleteness arises from the restricted accessibility to surrounding positions of the sample or technological constraints limiting the number of channels that can be acquired per laser pulse, such as in dynamic imaging applications. A particularly important example of insufficient data is the so-called limited-view acquisition, where signals are collected only along a limited angle. Limited-view acquisition is a challenge for translation of optoacoustics into the clinic, since hand-held and endoscopic probes cannot fully enclose the imaged tissue. In this case, proper regularization can also enhance the CNR of the images [4] and reduce sharp artifacts corresponding to the edges of the detection arc [24]. Limited-view acquisitions are further affected by lack of visibility of structures with certain orientations, which can be corrected with other approaches [25–27].

In conclusion, the reconstruction approach suggested herein can greatly impact the resolution, contrast, and overall quality of the optoacoustic images rendered with currently used 3D tomographic systems. The proposed method may become the method of choice in many practical cases.

Funding. European Research Council (ERC) (ERC-2010-StG-260991); National Institutes of Health (NIH) (R21-EY026382-01); Human Frontier Science Program (HFSP) (RGY0070/2016); Deutsche Forschungsgemeinschaft (DFG) (RA1848/5-1, Leibniz Prize 2013, NT 3/10-1).

Acknowledgment. The authors appreciate Dr. Chapin Rodriguez's help with editing the manuscript.

REFERENCES

1. P. Beard, Interface Focus **1**, 602 (2011).
2. A. Rosenthal, V. Ntziachristos, and D. Razansky, Curr. Med. Imaging Rev. **9**, 318 (2013).
3. X. L. Deán-Ben, A. Buehler, V. Ntziachristos, and D. Razansky, IEEE Trans. Med. Imaging **31**, 1922 (2012).
4. L. Yao and H. Jiang, Biomed. Opt. Express **2**, 2649 (2011).
5. M. Lustig, D. Donoho, and J. M. Pauly, Magn. Reson. Med. **58**, 1182 (2007).
6. J. Meng, L. H. V. Wang, L. L. Ying, D. Liang, and L. Song, Opt. Express **20**, 16510 (2012).
7. J. Provost and F. Lesage, IEEE Trans. Med. Imaging **28**, 585 (2009).
8. Z. Guo, C. Li, L. Song, and L. V. Wang, J. Biomed. Opt. **15**, 021311 (2010).
9. Y. Han, S. Tzoumas, A. Nunes, V. Ntziachristos, and A. Rosenthal, Med. Phys. **42**, 5444 (2015).
10. C. Zhang, Y. Zhang, and Y. Y. Wang, Biomed. Eng. **13** (2014).
11. J. C. Park, B. Y. Song, J. S. Kim, S. H. Park, H. K. Kim, Z. W. Liu, T. S. Suh, and W. Y. Song, Med. Phys. **39**, 1207 (2012).
12. X. Ye, Y. Chen, and F. Huang, IEEE Trans. Med. Imaging **30**, 1055 (2011).
13. C. Zhang, Y. Y. Wang, and J. Wang, Biomed. Signal Process. Control **26**, 11 (2016).
14. X. L. Deán-Ben and D. Razansky, Photoacoustics **1**, 68 (2013).
15. X. L. Deán-Ben, A. Ozbek, and D. Razansky, IEEE Trans. Med. Imaging **32**, 2050 (2013).
16. S. Tzoumas, A. Nunes, I. Olefir, S. Stangl, P. Symvoulidis, S. Glasl, C. Bayer, G. Multhoff, and V. Ntziachristos, Nat. Commun. **7**, 12121 (2016).
17. J. Barzilai and J. M. Borwein, IMA J. Numer. Anal. **8**, 141 (1988).
18. M. A. T. Figueiredo, R. D. Nowak, and S. J. Wright, IEEE J. Sel. Top. Signal Process. **1**, 586 (2007).
19. C. C. Paige and M. A. Saunders, ACM Trans. Math. Software **8**, 43 (1982).
20. S. Boyd and L. Vandenberghe, *Convex Optimization* (Cambridge University, 2004).
21. D. Queiros, X. L. Deán-Ben, A. Buehler, D. Razansky, A. Rosenthal, and V. Ntziachristos, J. Biomed. Opt. **18**, 076014 (2013).
22. P. C. Hansen and D. P. O'Leary, SIAM J. Sci. Comput. **14**, 1487 (1993).
23. L. Ding, X. L. Deán-Ben, and D. Razansky, IEEE Trans. Med. Imaging **35**, 1883 (2016).
24. J. Frikel and E. T. Quinto, SIAM J. Appl. Math. **75**, 703 (2015).
25. J. Gateau, T. Chaigne, O. Katz, S. Gigan, and E. Bossy, Opt. Lett. **38**, 5188 (2013).
26. L. Wang, G. Li, J. Xia, and L. V. Wang, Optica **2**, 307 (2015).
27. X. L. Deán-Ben, L. Ding, and D. Razansky, Opt. Lett. **42**, 827 (2017).

APPENDIX D. THREE-DIMENSIONAL OPTOACOUSTIC RECONSTRUCTION USING FAST SPARSE REPRESENTATION

Appendix E

Publication: Efficient Non-negative Constrained Model-based Inversion in Optoacoustic Tomography

Lu Ding, X Luís Deán-Ben, Christian Lutzweiler, Daniel Razansky, and Vasilis Ntziachristos. Efficient non-negative constrained model-based inversion in optoacoustic tomography. *Physics in medicine and biology*, 60(17):6733, 2015

IOP Publishing | Institute of Physics and Engineering in Medicine Physics in Medicine & Biology

Phys. Med. Biol. **60** (2015) 6733–6750 doi:10.1088/0031-9155/60/17/6733

Efficient non-negative constrained model-based inversion in optoacoustic tomography

Lu Ding, X Luís Deán-Ben, Christian Lutzweiler, Daniel Razansky and Vasilis Ntziachristos

Institute for Biological and Medical Imaging, Technical University of Munich and Helmholtz Center Munich, Ingolstädter Landstraße 1, 85764 Neuherberg, Germany

E-mail: v.ntziachristos@tum.de

Received 12 May 2015, revised 21 June 2015
Accepted for publication 6 July 2015
Published 21 August 2015

Abstract

The inversion accuracy in optoacoustic tomography depends on a number of parameters, including the number of detectors employed, discrete sampling issues or imperfectness of the forward model. These parameters result in ambiguities on the reconstructed image. A common ambiguity is the appearance of negative values, which have no physical meaning since optical absorption can only be higher or equal than zero. We investigate herein algorithms that impose non-negative constraints in model-based optoacoustic inversion. Several state-of-the-art non-negative constrained algorithms are analyzed. Furthermore, an algorithm based on the conjugate gradient method is introduced in this work. We are particularly interested in investigating whether positive restrictions lead to accurate solutions or drive the appearance of errors and artifacts. It is shown that the computational performance of non-negative constrained inversion is higher for the introduced algorithm than for the other algorithms, while yielding equivalent results. The experimental performance of this inversion procedure is then tested in phantoms and small animals, showing an improvement in image quality and quantitativeness with respect to the unconstrained approach. The study performed validates the use of non-negative constraints for improving image accuracy compared to unconstrained methods, while maintaining computational efficiency.

Keywords: optoacoustic tomography, photoacoustic tomography, model-based reconstruction, non-negative constrained least squares

(Some figures may appear in colour only in the online journal)

1. Introduction

Optoacoustic tomography offers high resolution optical imaging deep inside biological tissues (Beard 2011, Razansky *et al* 2011, Xia and Wang 2013). Using illumination at multiple wavelengths and spectral unmixing techniques, multi-spectral optoacoustic tomography (MSOT) in particular has shown potent visualization of functional and molecular tissue features obtained in real-time and in two or three dimensions (Herzog *et al* 2012, Cho *et al* 2013, Deán-Ben and Razansky 2013c, Yao *et al* 2013). There are two major approaches that enable optoacoustic imaging. The first approach employs raster scanning of focused light or focused detection of sound (Estrada *et al* 2014, Yao and Wang 2014) and pieces together signals from adjacent pixels to deliver an image. The second approach, tomography, collects sound emitted from the object imaged at different angles (projections). Image formation in this case relies on mathematical reconstruction algorithms that process the raw pressure signals acquired at several locations around the imaged object (Brecht *et al* 2009, Laufer *et al* 2009, Buehler *et al* 2012, Ma *et al* 2012, Nuster *et al* 2012, Xia *et al* 2012).

Most reconstruction algorithms developed for optoacoustic imaging fall into one of the following four catagories: back-projection algorithms, frequency-domain algorithms, time-reversal algorithms, and model-based algorithms. Among them, the back-projection approaches have been extensively utilized for tomographic imaging (Xu and Wang 2005). Requirements for improved image quality has also produced model-based optoacoustic inversion as a more accurate alternative to back-projection methods (Deán-Ben *et al* 2012b, Huang *et al* 2013, Deán-Ben *et al* 2013a, Queirós *et al* 2013, Mitsuhashi *et al* 2014). In model-based procedures, inversion is done by numerically minimizing the error between the measured signals and those theoretically predicted by an optoacoustic forward model (Paltauf *et al* 2002, Ephrat *et al* 2008, Deán-Ben *et al* 2012a). Model-based methods allow the incorporation of non-ideal parameters into the forward model, for example the effects of particular detector characteristics or acoustic heterogeneities in the object imaged (Rosenthal *et al* 2011a, Huang *et al* 2012, Deán-Ben *et al* 2012b, Huang *et al* 2013, Mitsuhashi *et al* 2014). Therefore, a forward model that better matches the real experimental situation than the idealized assumptions can be built; leading to more accurate inversions. However, even though such complex models generally improve the reconstruction accuracy over back-projection approaches, the forward model may not perfectly model the underlying experimental parameters. In addition, the tomographic information collected may be incomplete, i.e. the sound waves may only be collected in limited-view angles or only part of the ultrasound frequencies are detected. Finally, the optoacoustic inversion problem may be ill-posed (Hansen 1998), leading to inversion uncertainty. Such imperfections result in the appearance of negative values in the reconstructed images. These negative values have no physical meaning since the absorbed optical energy can only be higher or equal than zero, but are introduced during the inversion process as part of the minimization computation.

In principle, the better the forward model matches the underlying experimental parameters and the more complete the data set collected the less the number and intensity of the negative value artifacts. Regardless, the construction of a perfect forward model and a well-posed inverse problem is generally unattainable. Therefore the appearance of negative values in the reconstructed images is common. For instance, model-based reconstruction in cross-sectional tomographic imaging systems is typically done by assuming optoacoustic sources confined in a plane (Rosenthal *et al* 2010), which is an approximation considering the volumetric nature of optoacoustic signals and the imperfect rejection of out-of-plane signals seen in cylindrically focused ultrasound transducers. Some other imaging systems are constrained to detect

sound only at certain angular positions, which results in limited-view acquisition compromising the reconstruction performance (Buehler *et al* 2011). Additionally, the frequency response and the finite size of transducers also play an important role in the signal that is detected. All these inaccuracies in the model lead to negative value artifacts (Queirós *et al* 2013, Rosenthal *et al* 2011a, 2011b).

In most optoacoustics reconstruction procedures, these negative artifacts are either ignored or removed with simple approaches such as thresholding the images to zero. Non-negative constrained approaches have been suggested for model-based algorithms in a three-dimensional tomographic system to improve image smoothness (Wang *et al* 2012). However, the impact of adding non-negative constraints during reconstruction in terms of quantitativeness and computational complexity of the inversion procedure were not analyzed. Numerical inversion is computationally burdensome. Thereby, imposing this additional constraint further increases the inversion time for typical large scale problems in optoacoustic tomography. Fast non-negative constrained inversion approaches are then of critical importance.

Herein, we investigate whether non-negative constraints during the minimization process could improve the accuracy of the reconstructed optoacoustic images by eliminating the negative values without introduction of new artifacts. For this purpose, we introduce a non-negative inversion approach and compare its performance against six previously established non-negative inversion methods. The performance of the algorithms in optoacoustic cross-sectional model-based reconstruction was evaluated with experimental measurements from phantoms and animals *in vivo*, attaining realistic noise and overall experimental uncertainty conditions. We also show that non-negative constrained inversion leads to more meaningful quantitative results.

2. The non-negative inversion problem in optoacoustic tomography

The model-based inversion problem in optoacoustic tomography is briefly described herein for the two-dimensional (cross-sectional) imaging employed in analyzing the experimental measurements.

Optoacoustic excitation from short light pulses is assumed to fulfill the so-called stress and thermal confinement condition (Gusev and Karabutov 1991). Under this condition, the analytical expression for the generated optoacoustic pressure wave in a homogeneous non-attenuating medium is given by the Poisson-type integral as (Wang and Wu 2012)

$$p(\boldsymbol{r},t)=\frac{\Gamma}{4\pi c}\frac{\partial}{\partial t}\int_{S'(t)}\frac{H_r(\boldsymbol{r}')}{\|\boldsymbol{r}-\boldsymbol{r}'\|}\mathrm{d}S'(t), \tag{1}$$

where c is the speed of sound in the medium, Γ is the dimensionless Grueneisen parameter and H_r is the absorbed energy per unit volume. $S'(t)$ denotes a time-dependent spherical surface with radius $\|\boldsymbol{r}-\boldsymbol{r}'\|=ct$. In order to simplify the image acquisition, the setup is reduced into a two dimensional (cross-sectional) imaging geometry by means of cylindrically-focused transducers that provide maximum sensitivity in the imaged plane. If the optoacoustic sources are assumed to be confined in this plane, (1) can effectively be reduced to two dimensions, i.e.

$$p(\boldsymbol{r},t)=\frac{\partial}{\partial t}\int_{L'(t)}\frac{H_r(\boldsymbol{r}')}{\|\boldsymbol{r}-\boldsymbol{r}'\|}\mathrm{d}L'(t), \tag{2}$$

where $L'(t)$ denotes a circumference for which $\|\boldsymbol{r}-\boldsymbol{r}'\|=ct$. Note that the constants were removed from (1) for simplicity so that the pressure term is now expressed in arbitrary units. Discretization of (2) leads to a matrix equation in the form of (Rosenthal *et al* 2010)

$$\boldsymbol{p}=\boldsymbol{A}\boldsymbol{x}, \tag{3}$$

where $\boldsymbol{p}$ and $\boldsymbol{x}$ are two vectors corresponding to the optoacoustic pressure at the set of detector positions and instants and to the optical absorption distribution $H_r(\boldsymbol{r})$ in a two-dimensional Cartesian grid of points enclosing all optoacoustic sources. $\boldsymbol{A}$ is the model matrix representing the linear operator that maps the optical absorption to the resulting pressure wavefield. The model matrix is only dependent on the geometry of the experimental set-up and distribution of the speed of sound in the medium, not on the imaged object.

The distribution of optical absorption $\boldsymbol{x}$ is then reconstructed by minimizing the least squares (LS) difference between the measured pressure signals expressed in a vector form $\boldsymbol{b}$ and the pressure $\boldsymbol{p}$ predicted by the model at the same locations and instants, i.e.

$$\hat{\boldsymbol{x}} = \arg\min_{\boldsymbol{x}\geqslant\boldsymbol{0}} \|\boldsymbol{b} - \boldsymbol{A}\boldsymbol{x}\|^2, \tag{4}$$

which already contains a non-negative constraint in order to guarantee physical integrity of the solution. In contrast to unconstrained inversion, (4) cannot be solved analytically and only iterative methods are applicable.

In many cases, such as limited-view tomographic scenarios, regularization in the inversion procedure is essential. Thereby, the LS problem in (4) can be modified by adding a Tikhonov regularization term, i.e.

$$\hat{\boldsymbol{x}} = \arg\min_{\boldsymbol{x}\geqslant\boldsymbol{0}} \|\boldsymbol{b} - \boldsymbol{A}\boldsymbol{x}\|^2 + \lambda^2 \|\boldsymbol{L}\boldsymbol{x}\|^2, \tag{5}$$

where λ^2 is the regularization parameter and the matrix $\boldsymbol{L}$ can e.g. be selected as the identity matrix, which gives preference to solutions with a small norm, or a linear high-pass filtering operator leading to suppression of high-frequency noise (Deán-Ben *et al* 2012b). The regularized problem in (5) can be reformulated to the same form as (4)

$$\hat{\boldsymbol{x}} = \arg\min_{\boldsymbol{x}\geqslant\boldsymbol{0}} f(\boldsymbol{x}) = \arg\min_{\boldsymbol{x}\geqslant\boldsymbol{0}} \|\tilde{\boldsymbol{b}} - \tilde{\boldsymbol{A}}\boldsymbol{x}\|^2, \tag{6}$$

with

$$\tilde{\boldsymbol{b}} = \begin{pmatrix} \boldsymbol{b} \\ \boldsymbol{0} \end{pmatrix} \tag{7}$$

and

$$\tilde{\boldsymbol{A}} = \begin{pmatrix} \boldsymbol{A} \\ \lambda\boldsymbol{L} \end{pmatrix}. \tag{8}$$

Since (4) and (6) are equivalent for the inversion process, (4) is used as a general form in the following sections.

3. Non-negative least squares inversion (NNLS) methods

In this section, we present a short overview of non-negative least square (NNLS) methods that are experimentally evaluated in the context of optoacoustic tomography and introduce a new algorithm termed Accelerated Projected Conjugate Gradient (APCG). In section 4 we compare the relative performance of these methods.

3.1. Active set (AS)

The AS method was initially proposed by Lawson *et al* (1995) and was the first NNLS algorithm to be widely applied to inverse problems. For the NNLS problem in (4) with $\boldsymbol{x} \in \mathbb{R}^n$

we have n constraints, namely $x_i \geqslant 0$ for $i = 1, \ldots, n$. For a solution $\hat{\boldsymbol{x}}$ to (6), the term 'active constraints' refer to constraints that are active, meaning the corresponding elements $\hat{x}_i$ in $\hat{\boldsymbol{x}}$ are equal to 0 and the term 'passive constraints' refer to constraints that are passive, meaning the corresponding elements $\hat{x}_i$ in $\hat{\boldsymbol{x}}$ are greater than 0. If the set of active constraints (zero values) at the solution is known, the non-zero part of the solution or the sub-problem corresponding to the passive constraints can be solved as a non-constrained problem. The AS method is an iterative method. It assumes all constraints to be active at the beginning and in each iteration moves one constraint into the passive set until the true active set is found. The specific steps of the method are illustrated in the Appendix. The main disadvantage of the AS method is its computational inefficiency for large-scale problems since it can only handle one constraint per iteration. For our tests, we used the implementation available in the Matlab optimization toolbox (function lsqnonneg).

3.2. Fast non-negative least squares (FNNLS)

The FNNLS method (Bro and Jong 1997) was developed as an improvement of the original active-set method. The main differences over the AS method are (1) a pre-calculation of the quantities $\boldsymbol{A}^{\mathrm{T}}\boldsymbol{A}$ and $\boldsymbol{A}^{\mathrm{T}}\boldsymbol{b}$ and (2) an improved method to iterate through the possible active sets; the latter avoiding unnecessary computations. These differences make FNNLS more computationally efficient compared to the AS method. However, both the AS and the FNNLS methods require computation of the matrix product $\boldsymbol{A}^{\mathrm{T}}\boldsymbol{A}$ and the exact solution of a system of linear equations in each iteration, which is computationally expensive for large-scale problems. A Matlab implementation of this algorithm is available online (function fnnls).

3.3. Reflective newton (RN)

The RN method is applicable to minimization problems of a quadratic function with upper and lower bounds, NNLS inversion being a particular case. The RN method presents a good performance in large scale problems (Coleman and Li 1996). For our tests, we used the implementation available in the Matlab optimization toolbox (function lsqlin).

3.4. Projected gradient descent (PGD)

The PGD method is a constrained extension of the method of gradient descent, also termed steepest descent. The steepest descent is a first order optimization algorithm, which iteratively finds the local minimum of a function (Bertsekas 1976). The PGD method projects the updated solution obtained by taking steps along the negative gradient direction onto the constraint set after each iteration. Convergence is guaranteed as long as an appropriate step size control is employed. Contrary to the active-set methods, PGD is able to update more than one constraint in each iteration, leading to a significant acceleration in the computation time for large-scale problems. However, PGD may suffer from poor convergence rate, especially for ill-conditioned problems. The specific steps of the PGD algorithm are illustrated in the Appendix.

3.5. Projected quasi-newton (PQN)

The PQN method uses the well-established idea of separating the variables in each iteration into a set of free variables, for which improvement is possible, and a set of fixed variables,

which will stay constant for that iteration. More specifically, the method approximates the Newton step for the free variables in each iteration by considering a rank-one update of the inverse of the Hessian of the objective function. Convergence is ensured by the variable separation and projection of the updated solution in each iteration. PQN has a higher complexity per iteration than the PGD method. On the other hand, it presents better convergence behavior. The specific steps of the PQN method are illustrated in the Appendix. Two different variations of the PQN method based on two different approaches to approximate the inverse of the Hessian of the objective function have been introduced (Kim *et al* 2010), namely the Broyden–Fletcher–Goldfarb–Shanno (BFGS) method (Nocedal and Wright 2006) and the limited-memory Broyden–Fletcher–Goldfarb–Shanno (LBFGS) method (Byrd *et al* 1995). The LBFGS approach is particularly advantageous for large-scale problems. The corresponding two variations of the PQN method are then termed PQN-BFGS and PQN-LBFGS.

3.6. Projected conjugate gradient (PCG)

Similar to the PQN method, the PCG approach also splits the variables, i.e. the elements of vector $\boldsymbol{x}$, into free and fixed sets in each iteration. Then, instead of a quasi-Newton approach, the PCG method uses the conjugate gradient (CG) method to solve the unconstrained sub-problem given by

$$\hat{\boldsymbol{x}}_{\mathcal{I}} = \arg\min_{\boldsymbol{x}_{\mathcal{I}}} \|\boldsymbol{b} - \boldsymbol{A}_{\mathcal{I}}\boldsymbol{x}_{\mathcal{I}}\|^2, \tag{9}$$

where $\mathcal{I}$ denotes the set of indices corresponding to the free variables, $\boldsymbol{x}_{\mathcal{I}}$ contains components of $\boldsymbol{x}$ with indices in $\mathcal{I}$ and $\boldsymbol{A}_{\mathcal{I}}$ contains corresponding columns from $\boldsymbol{A}$. The updated solution, after each iteration, is projected to the non-negative region (Morigi *et al* 2007).

The CG method is an iterative method designed to solve positive definite systems of linear equations. It can be used to obtain the solution of unconstrained LS problems in the form $\boldsymbol{x} = \arg\min_{\boldsymbol{x}} \|\boldsymbol{b} - \boldsymbol{A}\boldsymbol{x}\|^2$ by solving the corresponding normal equations $\boldsymbol{A}^{\mathrm{T}}\boldsymbol{A}\boldsymbol{x} = \boldsymbol{A}^{\mathrm{T}}\boldsymbol{b}$. The search directions in the CG method are conjugate (A-orthogonal), where the initial search direction corresponds to the steepest descent direction of the LS problem. As all search directions are conjugate and have optimal step size, the search directions are not repeated in subsequent iterations (Fletcher and Reeves 1964). Thereby, the super-linear convergence of the CG method generally allows obtaining a good approximation of the optimal solution after a few iterations.

3.7. Accelerated projected conjugate gradient (APCG)

In the PCG method, the CG steps are restarted with the steepest descent direction in each iteration. In ill-conditioned problems, the steepest descent is often not a good choice and allows little progress. Therefore, the APCG is proposed in this work to improve the performance in ill-conditioned problems.

The APCG method shares the main structure of the PCG method. However, the CG procedure is initialized in each iteration by incorporating information from the previous iteration. In the first iteration, (9) is solved with the standard CG method. Then, considering that only a part of the set of free variable change for consecutive iterations, it is assumed that the search direction from a given iteration is a close guess for a conjugate direction in the LS sub-problem corresponding to the next iteration. That is, the steepest descent direction is not taken as initial search direction for the CG problem, but a correction term based on this last

search direction of the CG problem corresponding to the previous iteration is applied. With the suggested APCG method, the solution of the reduced LS problem in each iteration can be obtained with significantly smaller number of iterations of the CG method, and thus a higher computational efficiency is expected. Due to the different initialization employed, the orthogonality and conjugacy of the search directions and residuals is no longer guaranteed as in the standard CG method. Therefore, in the suggested approach, the correction of the conjugate directions is based on the Polak–Ribière formula known from nonlinear CG methods (Polak and Ribiere 1969). The optimal step sizes in each CG iteration of the sub-problem α_{cg} can still be calculated analytically. The step size of the outer iteration α can be determined with the Armijo-step-size rule (Bertsekas 1999). The specific steps of the algorithm are provided in the Appendix.

4. Methods

The performance of NNLS inversion was analyzed on experimental optoacoustic data as compared to unconstrained inversion, where the reconstructed image was thresholded to zero in order to avoid negative values with no physical meaning. The experiments were done with two cross-sectional optoacoustic tomography systems based on signal acquisition with an array of cylindrically-focused transducers (Razansky *et al* 2011). Specifically, the systems used were based on arrays of 64 elements with 172° angular coverage and 256 elements with 270° angular coverage respectively. The laser pulses are guided by ten fiber bundles forming an approximately homogeneous ring-shaped illumination profile on the surface of the imaging sample significantly wider than the focal width of the transducer. In a first step, the convergence rates of the different NNLS algorithms described in section 3 were tested in a phantom experiment. In a second experiment, phantoms with known optical properties were imaged in order to evaluate the quantitative improvement achieved with NNLS. Finally, *in vivo* mouse experiments were performed to provide a comparison of unconstrained and NNLS inversion as well as to evaluate the convergence behaviour in realistic scenarios. All NNLS algorithms were inplemented in Matlab and executed on a work computer with Intel Core i7-4820K CPU @ 3.7 GHz.

4.1. Phantom experiments

4.1.1. Phantom 1. A tissue-mimicking agar phantom (1.3% agar powder by weight) with a diameter of 16 mm was imaged in the first experiment with the 64-element cross-sectional optoacoustic tomography system. The agar matrix contained India ink and Intralipid to mimic, respectively, a background absorption coefficient $\mu_a = 0.2\ \mathrm{cm}^{-1}$ and a background reduced scattering coefficient $\mu_s' = 10\ \mathrm{cm}^{-1}$. Two straws containing different concentrations of ink corresponding to absorption coefficients of $\mu_a = 1\,\mathrm{cm}^{-1}$ and $\mu_a = 2\,\mathrm{cm}^{-1}$ were inserted in the cylindrical phantom. The laser wavelength was set to 760 nm corresponding to the maximum achievable energy per pulse. Prior to reconstruction, the acquired signals were band-pass filtered with cut-off frequencies 0.1 and 7 MHz.

4.1.2. Phantom 2. A different agar phantom with the same background optical properties as the one described above and a diameter of 20 mm was imaged in the 256-element cross-sectional system. A polyethylene tubing was inserted in the central region of the phantom. India ink with 5 different absorption coefficients ranging from $0.2\,\mathrm{cm}^{-1}$ to $4\,\mathrm{cm}^{-1}$ previously determined by spectrometer measurements was perfused into the tubing. The phantom was

imaged at a laser wavelength of 760 nm for all ink concentrations. The acquired signals were band-pass filtered between 0.1 and 8 MHz prior to reconstruction.

4.2. In vivo experiments

Several cross-sectional optoacoustic images of 6 weeks old CD1 mice were taken *in vivo* with the 256-element cross-sectional system. The *in vivo* experimentation was done according to approved institutional regulation regarding animal experiments. The fur of the mice was removed previous to the experiment with a shaving lotion. The mice were under isofluorane anesthesia during data acquisition at an optical wavelength of 800 nm. Prior to reconstruction, the signals acquired from all 256 projections were band-pass filtered with 0.1–8 MHz cut-off frequencies.

5. Results

5.1. Agar phantoms

The reconstructed images of phantom 1 are shown in figure 1. Figure 1(a) shows the result obtained with standard unconstrained LSQR inversion, which yields negative values for the reconstructed optical absorption maps and lack physical interpretation. In order to avoid presence of negative values, the image was thresholded by setting negative values to zero (figure 1(b)). Yet, most of the background absorption in the phantom cannot be perceived in the thresholded image. The reconstruction obtained with NNLS inversion (APCG) is displayed in figure 1(c). In this case, the background optical absorption in the phantom is positive except for a small region of zero values. Figures 1(d)–(f) show the profiles along the green dotted lines in (a)–(c) respectively. A major part of the profile in (d) is negative, which is set to zero in (e). On the other hand, the profile in (f) is positive throughout the phantom, which more faithfully represents the actual optical absorption distribution corresponding to a positive background absorption.

The convergence rates for the tested NNLS algorithms in the phantom experiment are also showcased in figure 1. Figure 1(g) displays the value of the objective function (least square error) as a function of the execution time for a typical region of interest consisting of 200×200 pixels^2 (180×180 mm^2). Each dot represents an iteration. For the inversion, 192 virtual projections were obtained by interpolating the actual data obtained with the 64 transducer elements and 1098 time samples were considered for each of these projections. This corresponds to a manageable matrix size of $250\,624 \times 40\,000$, including the regularization term in (8). Figure 1(h) shows a narrower time window in order to provide a comparison of the fastest algorithms. It is shown that the suggested APCG algorithm outperforms the other methods in terms of computational time. Methods 1–3 (AS, FNNLS and RN) have runtimes in the order of tens of minutes to hours, whereas the PCG and APCG methods converge after 23.8 and 10.8 s respectively. This convergence speed is confirmed with 25 datasets in the mice experiment in section 5.2. The stopping criterion used for the PQN-BFGS, PQN-LBFGS, PGD, PCG and APCG methods is explained in the Appendix. The PQN-LBFGS and PGD algorithms also present relatively fast convergence. It is also important to notice that during computation, the PCG, APCG, PQN-LBFGS and PGD algorithms only need to store a few vectors. They require significantly less memory as opposed to the other algorithms, which need to store the matrix $\boldsymbol{A}^{\mathrm{T}}\boldsymbol{A}$ (ca. 25 GB for 200×200 pixel reconstruction) or a matrix of similar size. Note that all NNLS algorithms yield the same reconstructed images since (6) is a

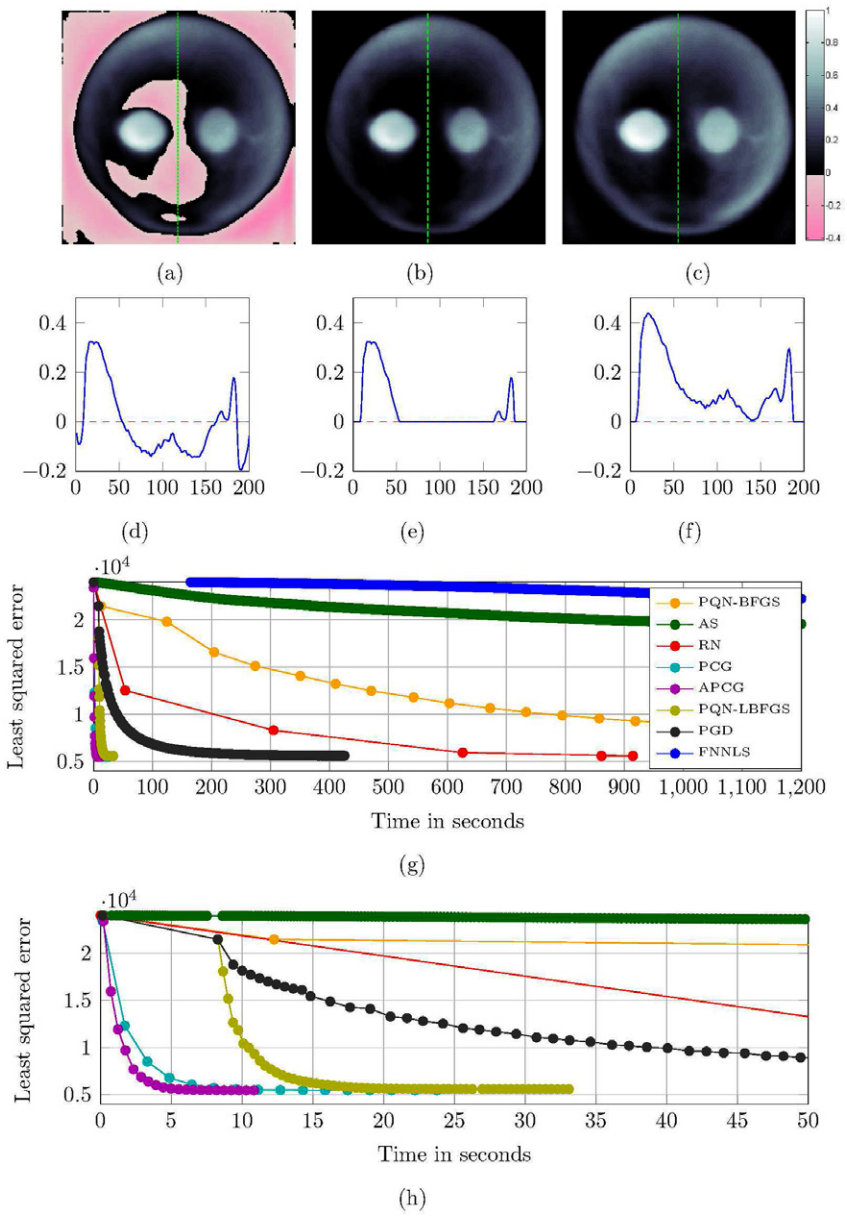

Figure 1. Performance of APCG compared to standard reconstructions. (a) Standard unconstrained inversion (LSQR algorithm) with negative values shown in pink. (b) Same inversion procedure as in (a) with negative values thresholded to zero. (c) Non-negative constrained inversion (APCG). (d)–(f) Profiles along the green dotted lines in (a)–(c) respectively. (g) Comparison of the value of the objective function (residual norm) in the phantom experiment as a function of time and number of iterations (dots) for the inversion algorithms listed in section 3. (h) the first 50 s in (g). In all cases, the reconstructed image consisted of 200×200 pixels.

convex optimization problem. Due to the strict convexity of the objective function, the optimal solution is the unique stationary point of the problem. Thus, all NNLS alogrithms converge towards the same solution, i.e. the same image.

The reconstructed images of phantom 2 are shown in figure 2. Each column represents a different optical absorption coefficient of the ink insertion, namely $0.276\,\mathrm{cm}^{-1}$, $0.874\,\mathrm{cm}^{-1}$, $1.84\,\mathrm{cm}^{-1}$, $3.75\,\mathrm{cm}^{-1}$ and $4.875\,\mathrm{cm}^{-1}$. The phantom images in the first row were reconstructed with standard unconstrained LSQR, where negative values are shown in pink. The images in the second row were obtained by thresholding negative values to zero and the images in the third row were reconstructed with the APCG algorithm. Some circles seem to appear around the sample in the APCG reconstructed images. These artifacts are presumably caused by the reflections as they appear in both constrained and unconstrained inversion approaches (Deán-Ben *et al* 2012c). Figure 2(b) shows the quantitative performance of the three inversion methods used in figure 2(a). The pixel values in the center of the insertion are plotted as a function of the actual optical absorption coefficient. The linear relationship between the actual absorption and the reconstructed value is lost when thresholding LSQR reconstructed images. On the other hand, the equivalent curve obtained with the APCG algorithm represents more reasonable results as it is almost linear while zero absorption is mapped to a zero value in the reconstructed images, i.e. the reconstructed signal intensity is proportional to the actual optical absorption. This shift observed in the LSQR curve is difficult to correct in realistic samples with heterogeneous optical properties as it is generally different for each sample and for each location of the absorber. On the other hand, the NNLS algorithms automatically corrects for this constant bias in a convenient way. Therefore, NNLS algorithms appear to deliver more meaningful quantitative absorption information of imaging samples.

5.2. In vivo mice

The 200×200 pixel cross-sectional images reconstructed in the mouse experiments are showcased in figure 3. Slices corresponding to the spleen region, the kidney region and the reproductive organs are shown in the rows from top to bottom. The LSQR reconstructed images with the entire value range (including the negative values) normalized between 0 and 1 are displayed in the left column. The LSQR reconstructed images with negative values thresholded to zero are displayed in the middle column. The equivalent images obtained with APCG reconstruction are showcased in the right column. For all 3 slices it can be observed that shifting the entire value range of the LSQR reconstructed images to above zero is not satisfactory. The images are distorted because shifting all of the negative values into the positive range gives a wrong impression of the absorption in some areas. The background, for example, should have zero absorption, but due to some negative outliers in the reconstruction, the corrected images appear to have absorption values of around 0.5 in the normalized scalebar in most of the background area. A similar observation can be made regarding the intensity of the inner structures. It is thus evident, that it is not possible to simply shift the values from the unconstrained reconstruction into the positive range to get a linear relation between absorption and concentration, i.e. quantitativeness is lost. The thresholding approach ensures the zero absorption in the background. However, many internal structures are lost since the internal absorption is weak and they are reconstructed as negative values with the LSQR inversion. Therefore, the APCG inversion procedure appears to represent the most accurate solution, where the internal details are distinguished while quantitativeness of the images is kept. This good performance of APCG motivates the use of NNLS reconstruction algorithms in actual biological samples.

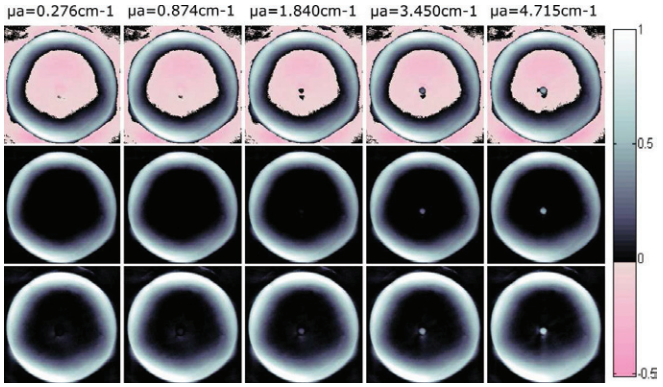

(a)

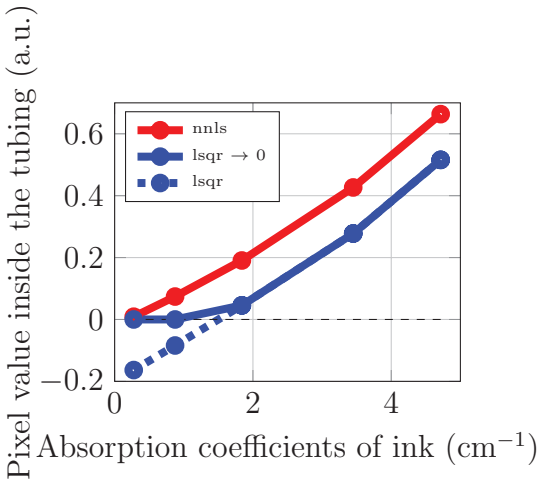

(b)

Figure 2. Quantification test of NNLS reconstruction. (a) Reconstructed phantom images with five different absorption coefficients of ink in the central insertion. First row: standard LSQR reconstructions. Second row: standard LSQR reconstructions with negative values thresholded to zero. Third row: APCG reconstructions. (b) Pixel value in the center of the insertion as a function of the optical absorption coefficient of ink determined from the spectrometer.

The convergence behavior of different NNLS algorithms tested with the mice data set is shown in table 1. The convergence rates and residuals are averaged over 25 mice slices. This result confirms the results obtained in phantom experiments, i.e. all algorithms converge to almost the same residual while the proposed APCG algorithm is the fastest inversion procedure.

6. Discussion

In this study we have showcased that non-negative constrained reconstruction represents a useful method for suppressing artefacts in the form of negative values typically appearing in

Table 1. The convergence behavior of different NNLS algorithms averaged over 25 mice slices.

Algorithms	PQN-BFGS	AS	RN	PCG	APCG	PQN-LBFGS	PGD	FNNLS
Convergence time	> 20 min	> 20 min	566.8 s	10.7 s	4.5 s	18.5 s	86.9 s	> 20 min
Residual	1.4425*e*5	2.2453*e*5	1.1927*e*5	1.1922*e*5	1.1926*e*5	1.1928*e*5	1.1940*e*5	2.4236*e*5

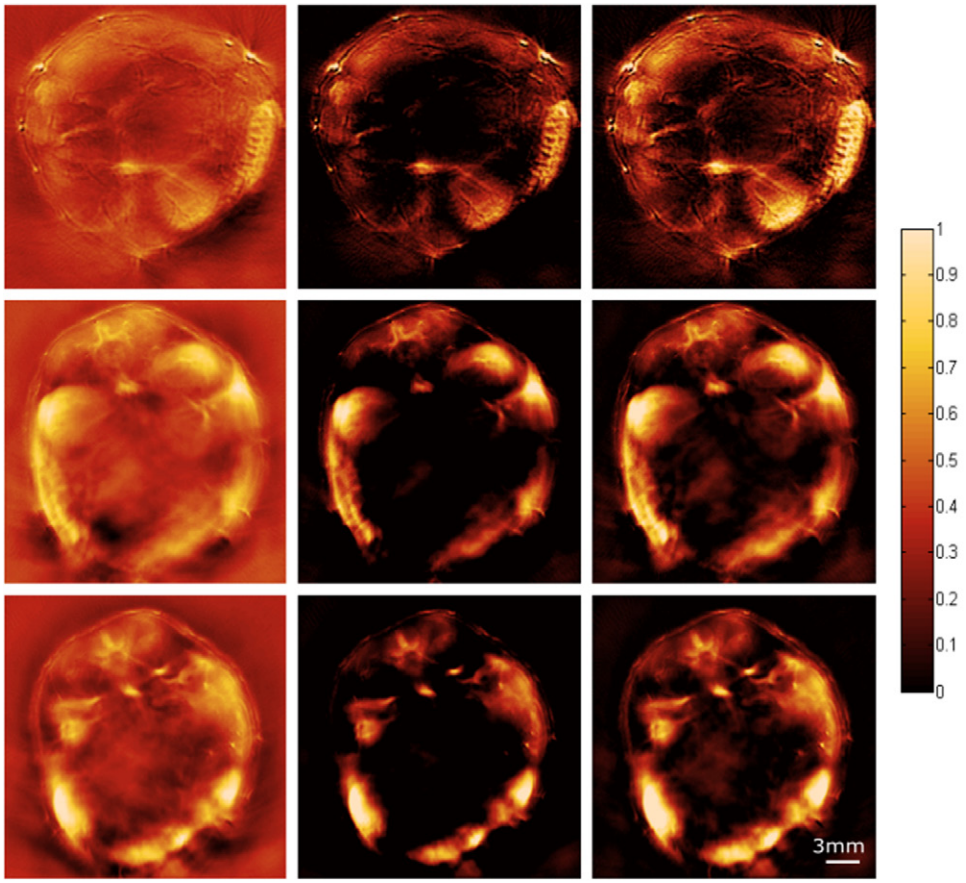

Figure 3. Tomographic reconstructions of 3 different mice regions with standard inversion (LSQR) normalized between 0 and 1 (left column), with standard inversion (LSQR) thresholded to zero (middle column) and with non-negative constrained inversion based on the APCG method (right column).

optoacoustic tomographic reconstructions. Performance of several non-negative constrained least squares algorithms for the inversion of a time-domain two-dimensional optoacoustic model has been analyzed in tissue-mimicking phantoms and small animals *in vivo*. In quantification tests with real phantoms, non-negative constrained reconstructions showed more quantitative and reasonable results while its computational efficiency could be maintained.

A new non-negative constrained minimization algorithm (termed APCG) based on the conjugate gradient method was introduced in this work and its reconstruction performance was

compared with state-of-the-art algorithms on real optoacoustic datasets. While the retrieved images are equivalent to those obtained with the other methods, the convergence speed of the introduced algorithm is significantly faster. The improvement of the proposed APCG method with respect to the fastest of the analyzed alternative approaches, the PCG method, is most significant for ill-conditioned systems. In these cases, the steepest descent is not an optimal search direction, therefore the frequent initialization of the CG method in the steepest descent direction slows down convergence. In order to guarantee convergence, an Armijo-based line search can be added. However, this line search procedure may not improve the performance of the algorithm and might even degrade performance due to the additional complexity. Thereby, based on the good performance with optoacoustic tomography, we anticipate the applicability of the suggested algorithm for model-based reconstruction in other biomedical imaging modalities.

Overall, the non-negative constraint ensures physical integrity and quantitative nature of the solution. For example, when the negative part of the solution obtained with unconstrained inversion is set to zero, large parts in the inner of the reconstructed object may become invisible but appear in the images when non-negative constrained inversion is employed instead. Also, the obtained solution is presumably closely representing the actual optical absorption distribution since additional a-priori information regarding positiveness of optical absorption, not used in the unconstrained optimizations, is included in the inversion procedure. It is important to highlight that the term quantitativeness is employed here to refer to proportionality of the reconstructed signal and the actual absorbed energy. If the objective is to provide a quantitative map of the optical absorption coefficient, other effects such as optical and acoustic attenuation as well as the transducer properties must be taken into account.

The current CPU implementation of the suggested non-negative least squares algorithm is more efficient in comparison to the other NNLS algorithms tested throughout this paper, but still not capable of rendering optoacoustic images in real time. However its simple structure potentially allows an efficient parallel inplementation on the graphics processing units (GPU) (Deán-Ben *et al* 2013b). Since the inversion procedures are identical for matrices corresponding to either two-dimensional or generally more accurate three-dimensional models, the APCG algorithm can be directly applied to three-dimensional image data.

In conclusion, the computationally efficient performance of the suggested non-negative constrained inversion anticipates the general applicability of this reconstruction approach in optoacoustic tomographic imaging systems with arbitrary detection geometries, allowing a more quantitative interpretation of the reconstructed images.

Acknowledgments

DR acknowledges support from the European Research Council under grant agreement ERC-2010-StG-260991. VN acknowledges support from the European Union project FAMOS (FP7 ICT, Contract 317744).

Appendix

A.1. Algorithms

We provide herein specific steps for the AS, PGD, PQN, PCG and the APCG methods. Given a set $\mathcal{I}$ of indices, we denote with $\boldsymbol{x}_{\mathcal{I}}$ the vector with the components of $\boldsymbol{x}$ corresponding to the indices in $\mathcal{I}$. Similarly, $\boldsymbol{A}_{\mathcal{I}}$ denotes the matrix with the columns from $\boldsymbol{A}$ corresponding to the indices in $\mathcal{I}$.

Algorithm 1. Active set method

Require: $\boldsymbol{A} \in \mathbb{R}^{m \times n},\ \boldsymbol{x} = \boldsymbol{0} \in \mathbb{R}^n,\ b \in \mathbb{R}^m,$ set $\mathcal{Z} = \{1, 2, \ldots, n\},\ \mathcal{P} = \varnothing$

Ensure: $\hat{\boldsymbol{x}} = \arg\min_{\boldsymbol{x}} \|\boldsymbol{A}\boldsymbol{x} - \boldsymbol{b}\|^2 \quad s.t. \quad \hat{\boldsymbol{x}} \geqslant \boldsymbol{0}$

while true **do**
  $\boldsymbol{w} \leftarrow \boldsymbol{A}^{\mathrm{T}}(\boldsymbol{b} - \boldsymbol{A}\boldsymbol{x})$ negative gradient
  if $\mathcal{Z} \neq \varnothing$ and $\max_{i \in \mathcal{Z}}(w_i) > 0$ **then**
    $j \leftarrow \arg\max_{i \in \mathcal{Z}}(w_i)$
    Move j from set $\mathcal{Z}$ to $\mathcal{P}$
    while: true **do**
    Solve the unconstrained subproblem $\boldsymbol{y}_{\mathcal{P}} \leftarrow \arg\min_{\boldsymbol{y}_{\mathcal{P}}} \|\boldsymbol{A}_{\mathcal{P}}\boldsymbol{y}_{\mathcal{P}} - \boldsymbol{b}\|^2$
      if $\min(y_i) \leqslant \boldsymbol{0}$ **then**
        $\alpha \leftarrow -\min_{i \in \mathcal{P}}\left(\dfrac{x_i}{x_i - y_i}\right)$
        $\boldsymbol{x} \leftarrow \boldsymbol{x} + \alpha(\boldsymbol{y} - \boldsymbol{x})$
        Move from $\mathcal{P}$ to $\mathcal{Z}$, all $i \in \mathcal{P}$ $s.t.$ $x_i = 0$
      else
        $\boldsymbol{x} \leftarrow \boldsymbol{y}$
        break
      end if
    end while
  else
    return $\boldsymbol{x}$
  end if
end while

Algorithm 2. Projected gradient descent

Require: $\boldsymbol{A} \in \mathbb{R}^{m \times n},\ \boldsymbol{x}_0 \geqslant \boldsymbol{0} \in \mathbb{R}^n,\ b \in \mathbb{R}^m$

Ensure: $\hat{\boldsymbol{x}} = \arg\min_{\boldsymbol{x}} \|\boldsymbol{A}\boldsymbol{x} - \boldsymbol{b}\|^2 \quad s.t. \quad \hat{\boldsymbol{x}} \geqslant \boldsymbol{0}$

repeat
  $\boldsymbol{r} \leftarrow \boldsymbol{b} - \boldsymbol{A}\boldsymbol{x}$
  $\boldsymbol{g} \leftarrow -\boldsymbol{A}^{\mathrm{T}}\boldsymbol{r}$ gradient
  $\mathcal{I} \leftarrow \{i | x_i > 0 \ \text{ or } \ -g_i > 0\}$ set of free variables
  Perform line search on the variables corresponding to $\mathcal{I}$ to find a proper step size α
  Update $\boldsymbol{x}$ by projecting the subset vector onto the non-negative region $\boldsymbol{x}_{\mathcal{I}} \leftarrow [\boldsymbol{x}_{\mathcal{I}} - \alpha \boldsymbol{g}_{\mathcal{I}}]_+$
until Convergence

Algorithm 3. Projected quasi-newton method

Require: $\boldsymbol{A} \in \mathbb{R}^{m\times n},\ \boldsymbol{x} \geqslant \boldsymbol{0} \in \mathbb{R}^n,\ b \in \mathbb{R}^m\ \boldsymbol{S} = \boldsymbol{I}$

Ensure: $\hat{\boldsymbol{x}} = \arg\min_{\boldsymbol{x}} \|\boldsymbol{A}\boldsymbol{x} - \boldsymbol{b}\|^2 \quad s.t. \quad \hat{\boldsymbol{x}} \geqslant \boldsymbol{0}$

1: **repeat**
2: $\boldsymbol{r} \leftarrow \boldsymbol{b} - \boldsymbol{A}\boldsymbol{x}$
3: $\boldsymbol{g} \leftarrow -\boldsymbol{A}^{\mathrm{T}}\boldsymbol{r}$ gradient
4: $\mathcal{I}_1 \leftarrow \{i | x_i > 0 \ \text{ or } \ -g_i > 0\}$ set of free variables
5: $\boldsymbol{d}_{\mathcal{I}_1} \leftarrow -\boldsymbol{S}_{\mathcal{I}_1}\boldsymbol{g}_{\mathcal{I}_1}$ search direction for free variables
6: $\mathcal{I}_2 \leftarrow \{j \in \mathcal{I}_1 | x_j > 0 \ \text{ or } \ d_j > 0\}$ reduced set of free variables
7: Perform line search along $\boldsymbol{d}_{\mathcal{I}_2}$ to find a proper step size α
8: Update $\boldsymbol{x}$ by projecting the subset vector onto the non-negative region
$\boldsymbol{x}_{\mathcal{I}_2} \leftarrow [\boldsymbol{x}_{\mathcal{I}_2} + \alpha \boldsymbol{d}_{\mathcal{I}_2}]_+$
9: Update the gradient scaling matrix $\boldsymbol{S}$
10: **until** Convergence

Algorithm 4. Projected conjugate gradient method

Require: $\boldsymbol{A} \in \mathbb{R}^{m\times n},\ \boldsymbol{x} \geqslant \boldsymbol{0} \in \mathbb{R}^n,\ b \in \mathbb{R}^m\ \boldsymbol{S} = \boldsymbol{I}$

Ensure: $\hat{\boldsymbol{x}} = \arg\min_{\boldsymbol{x}} \|\boldsymbol{A}\boldsymbol{x} - \boldsymbol{b}\|^2 \quad s.t. \quad \hat{\boldsymbol{x}} \geqslant \boldsymbol{0}$

1: **repeat**
2: $\boldsymbol{r} \leftarrow \boldsymbol{b} - \boldsymbol{A}\boldsymbol{x}$
3: $\boldsymbol{g} \leftarrow -\boldsymbol{A}^{\mathrm{T}}\boldsymbol{r}$ gradient
4: $\mathcal{I}_1 \leftarrow \{i | x_i > 0 \ \text{ or } \ -g_i > 0\}$ set of free variables
5: Solve the unconstrained subproblem with the standard conjugate gradient method
$\boldsymbol{x}_{\mathcal{I}_1} \leftarrow \arg\min_{\boldsymbol{x}_{\mathcal{I}_1}} \|\boldsymbol{A}_{\mathcal{I}_1}\boldsymbol{x}_{\mathcal{I}_1} - \boldsymbol{b}\|^2$
6: Update $\boldsymbol{x}$ by projecting the subset vector onto the non-negative region
$\boldsymbol{x}_{\mathcal{I}_1} \leftarrow [\boldsymbol{x}_{\mathcal{I}_1}]_+$
7: **until** Convergence

Algorithm 5. Accelerated projected conjugate gradient method

Require: $\boldsymbol{A} \in \mathbb{R}^{m\times n},\ \boldsymbol{x} \geqslant \boldsymbol{0} \in \mathbb{R}^n,\ b \in \mathbb{R}^m\ , \boldsymbol{g} = \boldsymbol{0} \in \mathbb{R}^n$

Ensure: $\hat{\boldsymbol{x}} = \arg\min_{\boldsymbol{x}} \|\boldsymbol{A}\boldsymbol{x} - \boldsymbol{b}\|^2 \quad s.t. \quad \hat{\boldsymbol{x}} \geqslant \boldsymbol{0}$

1: **repeat**
2: $\boldsymbol{r} \leftarrow \boldsymbol{b} - \boldsymbol{A}\boldsymbol{x}$
3: $\boldsymbol{g}_{\text{old}} \leftarrow \boldsymbol{g}$
4: $\boldsymbol{g} \leftarrow -\boldsymbol{A}^{\mathrm{T}}\boldsymbol{r}$ gradient
5: $\mathcal{I}_1 \leftarrow \{i | x_i > 0 \ \text{ or } \ -g_i > 0\}$ set of free variables
6: $\boldsymbol{d} \leftarrow \boldsymbol{0}$
7: **repeat**
8: Calculate the correction coefficient with the Polak–Ribière formula

(*Continued*)

Algorithm 5. (*Continued*)

$$\beta_{cg} \leftarrow \max\left(0, -\frac{\boldsymbol{g}_{\mathcal{I}_1}^{\mathrm{T}}(\boldsymbol{g}_{\mathcal{I}_1} - \boldsymbol{g}_{\mathrm{old},\mathcal{I}_1})}{\boldsymbol{g}_{\mathrm{old},\mathcal{I}_1}^{\mathrm{T}}\boldsymbol{g}_{\mathrm{old},\mathcal{I}_1}}\right)$$

Update the conjugate direction

$\boldsymbol{p}_{\mathcal{I}_1} \leftarrow -\boldsymbol{g}_{\mathcal{I}_1} + \beta_{cg}\boldsymbol{p}_{\mathcal{I}_1}$

$\boldsymbol{p}_{\mathcal{I}_1^c} \leftarrow \boldsymbol{0}$

$\boldsymbol{q} \leftarrow \boldsymbol{A}\boldsymbol{p}$

$\alpha_{cg} \leftarrow \dfrac{-\boldsymbol{g}^{\mathrm{T}}\boldsymbol{p}}{\boldsymbol{q}^{\mathrm{T}}\boldsymbol{q}}$ optimal step size

$\boldsymbol{d}_{\mathcal{I}_1} \leftarrow \boldsymbol{d}_{\mathcal{I}_1} + \alpha_{cg}\boldsymbol{p}_{\mathcal{I}_1}$

$\boldsymbol{r} \leftarrow \boldsymbol{r} - \alpha_{cg}\boldsymbol{q}$

$\boldsymbol{g}_{\mathrm{old}} \leftarrow \boldsymbol{g}$

$\boldsymbol{g} \leftarrow -\boldsymbol{A}^{\mathrm{T}}\boldsymbol{r}$

until Stop

$\mathcal{I}_2 \leftarrow \{j \in \mathcal{I}_1 | x_j > 0 \text{ or } d_j > 0\}$ reduced set of free variables

Perform line search along $\boldsymbol{d}_{\mathcal{I}_2}$ to find a proper step size α

Update $\boldsymbol{x}$ by projecting the subset vector onto the non-negative region

$\boldsymbol{x}_{\mathcal{I}_2} \leftarrow [\boldsymbol{x}_{\mathcal{I}_2} + \alpha\boldsymbol{d}_{\mathcal{I}_2}]_+$

until Convergence

A.2. Stopping criterion

We provide herein the stopping criterion employed for the PGD, PQN-BFGS, PQN-LBFGS, PCG and APCG methods. For the AS, FNNLS and RN methods, a maximum runtime of 20 min is applied.

The objective function $f(\boldsymbol{x})$ being minimized in the inversion procedure is given in (6). Since the projected gradient of the objective function converges to zero as the algorithm converges to the optimal solution, the relative infinity norm of the projected gradient was used to terminate the algorithm after n iterations, i.e.

$$\frac{\|\mathcal{P}_{\mathcal{T}_c}(\nabla f(\boldsymbol{x}_n))\|_\infty}{\|\mathcal{P}_{\mathcal{T}_c}(\nabla f(\boldsymbol{x}_0))\|_\infty} < \epsilon, \tag{A.1}$$

where ϵ is a small positive number and $\mathcal{P}_{\mathcal{T}_c}$ denotes the projection onto the tangent cone of the constraint set, i.e. setting the gradient elements corresponding to the fixed variables to zero.

References

Beard P 2011 Biomedical photoacoustic imaging *Interface Focus* **1** 602–31

Bertsekas D P 1976 On the goldstein-levitin-polyak gradient projection method *IEEE Trans. Autom. Control* **21** 174–84

Bertsekas D P 1999 *Nonlinear Programming* (*Athena Scientific Optimization and Computation Series*) (Belmont, MA: Athena Scientific)

Brecht H-P, Su R, Fronheiser M, Ermilov S A, Conjusteau A and Oraevsky A A 2009 Whole-body three-dimensional optoacoustic tomography system for small animals *J. Biomed. Opt.* **14** 064007

Bro R and Jong S D 1997 A fast non-negativity-constrained least squares algorithm *J. Chemometr.* **11** 393–401

Buehler A, Rosenthal A, Jetzfellner T, Dima A, Razansky D and Ntziachristos V 2011 Model-based optoacoustic inversions with incomplete projection data *Med. Phys.* **38** 1694–704
Buehler A, Deán-Ben X L, Claussen J, Ntziachristos V and Razansky D 2012 Three-dimensional optoacoustic tomography at video rate *Opt. Express* **20** 22712–9
Byrd R H, Lu P, Nocedal J and Zhu C 1995 A limited memory algorithm for bound constrained optimization *SIAM J. Sci. Comput.* **16** 1190–208
Cho E C, Zhang Y, Cai X, Moran C M, Wang L V and Xia Y 2013 Quantitative analysis of the fate of gold nanocages in vitro and *in vivo* after uptake by u87 mg tumor cells *Angew. Chem.* **125** 1190–3
Coleman T and Li Y 1996 A reflective newton method for minimizing a quadratic function subject to bounds on some of the variables *SIAM J. Optim.* **6** 1040–58
Deán-Ben X L, Buehler A, Ntziachristos V and Razansky D 2012a Accurate model-based reconstruction algorithm for three-dimensional optoacoustic tomography *IEEE Trans. Med. Imaging* **31** 1922–8
Deán-Ben X L, Ntziachristos V and Razansky D 2012b Acceleration of optoacoustic model-based reconstruction using angular image discretization *IEEE Transact/ Med. Imaging* **31** 1154–1162
Deán-Ben X L, Ntziachristos V and Razansky D 2012c Artefact reduction in optoacoustic tomographic imaging by estimating the distribution of acoustic scatterers *J. Biomed. Opt.* **17** 110504
Deán-Ben X L, Ma R, Rosenthal A, Ntziachristos V and Razansky D 2013a Weighted model-based optoacoustic reconstruction in acoustic scattering media *Phys. Med. Biol.* **58** 5555
Deán-Ben X L, Ozbek A and Razansky D 2013b Volumetric real-time tracking of peripheral human vasculature with GPU-accelerated three-dimensional optoacoustic tomography *IEEE Trans. Med. Imaging* **32** 2050–5
Deán-Ben X L and Razansky D 2013c Functional optoacoustic human angiography with handheld video rate three dimensional scanner *Photoacoustics* **1** 68–73
Ephrat P, Keenliside L, Prato F S, Carson J J L and Seabrook A 2008 Three-dimensional photoacoustic imaging by sparse-array detection and iterative image reconstruction *J. Biomed. Opt.* **13** 054052
Estrada H, Turner J, Kneipp M and Razansky D 2014 Real-time optoacoustic brain microscopy with hybrid optical and acoustic resolution *Laser Phys. Lett.* **11** 045601
Fletcher R and Reeves C M 1964 Function minimization by conjugate gradients *Comput. J.* **7** 149–54
Gusev V E and Karabutov A A 1991 Laser optoacoustics *NASA STI/Recon Technical Report A* vol 93 p 16842
Hansen P C 1998 *Rank-Deficient and Discrete Ill-Posed Problems* (Philadelphia: SIAM)
Herzog E, Taruttis A, Beziere N, Lutich A A, Razansky D and Ntziachristos V 2012 Optical imaging of cancer heterogeneity with multispectral optoacoustic tomography *Radiology* **263** 461–8
Huang C, Nie L, Schoonover R W, Wang L V and Anastasio M A 2012 Photoacoustic computed tomography correcting for heterogeneity and attenuation *J. Biomed. Opt.* **17** 0612111–5
Huang C, Wang K, Nie L, Wang L V and Anastasio M A 2013 Full-wave iterative image reconstruction in photoacoustic tomography with acoustically inhomogeneous media *IEEE Trans. Med. Imaging* **32** 1097–110
Kim D, Sra S and Dhillon I 2010 Tackling box-constrained optimization via a new projected quasi-newton approach *SIAM J. Sci. Comput.* **32** 3548–63
Laufer J, Zhang E, Raivich G and Beard P 2009 Three-dimensional noninvasive imaging of the vasculature in the mouse brain using a high resolution photoacoustic scanner *Appl. Optics* **48** D299–306
Lawson C L and Hanson R J 1995 *Solving Least Squares Problems. Classics in Applied Mathematics* (Philadelphia: SIAM)
Ma R, Distel M, Deán-Ben X L, Ntziachristos V and Razansky D 2012 Non-invasive whole-body imaging of adult zebrafish with optoacoustic tomography *Phys. Med. Biol.* **57** 7227–37
Mitsuhashi K, Wang K and Anastasio M A 2014 Investigation of the far-field approximation for modeling a transducer's spatial impulse response in photoacoustic computed tomography *Photoacoustics* **2** 21–32
Morigi S, Reichel L, Sgallari F and Zama F 2007 An iterative method for linear discrete ill-posed problems with box constraints *J. Comput. Appl. Math.* **198** 505–20
Nocedal J and Wright S 2006 *Numerical Optimization* (*Springer Series in Operations Research and Financial Engineering*) (Berlin: Springer)
Nuster R, Gratt S, Passler K, Meyer D and Paltauf G 2012 Photoacoustic section imaging using an elliptical acoustic mirror and optical detection *J. Biomed. Opt.* **17** 0305031–3
Paltauf G, Viator J A, Prahl S A and Jacques S L 2002 Iterative reconstruction algorithm for optoacoustic imaging *J. Acoust. Soc. Am.* **112** 1536–44

Polak E and Ribiere G 1969 Note sur la convergence de méthodes de directions conjuguées *Math. Modelling Numer. Anal.* **3** 35–43

Queirós D, Déan-Ben X L, Buehler A, Razansky D, Rosenthal A and Ntziachristos V 2013 Modeling the shape of cylindrically focused transducers in three-dimensional optoacoustic tomography *J. Biomed. Opt.* **18** 076014

Razansky D, Buehler A and Ntziachristos V 2011 Volumetric real-time multispectral optoacoustic tomography of biomarkers *Nat. Protocols* **6** 1121–9

Rosenthal A, Razansky D and Ntziachristos V 2010 Fast semi-analytical model-based acoustic inversion for quantitative optoacoustic tomography *IEEE Trans. Med. Imaging* **29** 1275–85

Rosenthal A, Ntziachristos V and Razansky D 2011 Model-based optoacoustic inversion with arbitrary-shape detectors *Med. Phys.* **38** 4285–95

Rosenthal A, Ntziachristos V and Razansky D 2011 Optoacoustic methods for frequency calibration of ultrasonic sensors *IEEE Trans. Ultrason. Ferroelectr. Freq. Control* **58** 316–26

Wang K, Su R, Oraevsky A A and Anastasio M A 2012 Investigation of iterative image reconstruction in three-dimensional optoacoustic tomography *Phys. Med. Biol.* **57** 5399

Wang L V and Wu H 2012 *Biomedical Optics: Principles and Imaging* (New York: Wiley)

Xia J, Chatni M R, Maslov K, Guo Z, Wang K, Anastasio M and Wang L V 2012 Whole-body ring-shaped confocal photoacoustic computed tomography of small animals *in vivo J. Biomed. Opt.* **17** 0505061–3

Xia J and Wang L 2013 Small-animal whole-body photoacoustic tomography: a review *IEEE Trans. Biomed. Eng.* **61** 1380–9

Xu M and Wang L V 2005 Universal back-projection algorithm for photoacoustic computed tomography *Phys. Rev.* E **71** 016706

Yao J, Xia J, Maslov K I, Nasiriavanaki M, Tsytsarev V, Demchenko A V and Wang L V 2013 Noninvasive photoacoustic computed tomography of mouse brain metabolism *in vivo Neuroimage* **64** 257–66

Yao J and Wang L V 2014 Sensitivity of photoacoustic microscopy *Photoacoustics* **2** 87–101

APPENDIX E. PUBLICATION: EFFICIENT NON-NEGATIVE CONSTRAINED MODEL-BASED INVERSION IN OPTOACOUSTIC TOMOGRAPHY

Appendix F

Publication: Constrained Inversion and Spectral Unmixing in Multispectral Optoacoustic Tomography

Constrained Inversion and Spectral Unmixing in Multispectral Optoacoustic Tomography

Lu Ding, Xosé Luís Deán-Ben, Neal C. Burton, Robert W. Sobol, Vasilis Ntziachristos, and Daniel Razansky*

***Abstract*— Accurate extraction of physical and biochemical parameters from optoacoustic images is often impeded due to the use of unrigorous inversion schemes, incomplete tomographic detection coverage, or other experimental factors that cannot be readily accounted for during the image acquisition and reconstruction process. For instance, inaccurate assumptions in the physical forward model may lead to negative optical absorption values in the reconstructed images. Any artifacts present in the single wavelength optoacoustic images can be significantly aggravated when performing a two-step reconstruction consisting in acoustic inversion and spectral unmixing aimed at rendering the distributions of spectrally distinct absorbers. We investigate a number of algorithmic strategies with non-negativity constraints imposed at the different phases of the reconstruction process. Performance is evaluated in cross-sectional multispectral optoacoustic tomography recordings from tissue-mimicking phantoms and *in vivo* mice embedded with varying concentrations of contrast agents. Additional *in vivo* validation is subsequently performed with molecular imaging data involving subcutaneous tumors labeled with genetically expressed iRFP proteins and organ perfusion by optical contrast agents. It is shown that constrained reconstruction is essential for reducing the critical image artifacts associated with inaccurate modeling assumptions. Furthermore, imposing the non-negativity constraint directly on the unmixed distribution of the probe of interest was found to maintain the most robust and accurate reconstruction performance in all experiments.**

***Index Terms*— Optoacoustic/photoacoustic tomography, multispectral imaging, spectral unmixing, non-negative constraint**

Manuscript received January 18, 2017; revised March 14, 2017; accepted March 19, 2017. Date of publication March 22, 2017; date of current version July 30, 2017. The work of D. Razansky was supported in part by the European Research Council under Consolidator Grant ERC-2015-CoG-682379 and in part by the Human Frontier Science Program under Grant RGY0070/2016. The work of V. Ntziachristos was supported by SFB1123. The work of R. W. Sobol was supported in part by NIH under Grant R01CA148629 and in part by the Abraham A. Mitchell Distinguished Investigator Fund. *Asterisk indicates corresponding author.*

L. Ding and V. Ntziachristos are with the Helmholtz Center Munich, Institute for Biological and Medical Imaging, Neuherberg 85769, Germany, and also with the Faculty of Medicine and the Faculty of Electrical Engineering, Technical University of Munich, Munich 80333, Germany.

X. L. Deán-Ben is with the Helmholtz Center Munich, Institute for Biological and Medical Imaging, Neuherberg 85769, Germany.

N. C. Burton is with iThera Medical GmbH, Munich 81379, Germany.

R. W. Sobol was with the Departments of Pharmacology & Chemical Biology and Human Genetics, University of Pittsburgh School of Medicine, Pittsburgh, PA 15261, USA. He is now with the Mitchell Cancer Institute, University of South Alabama, Mobile, AL 36604, USA.

*D. Razansky is with the Helmholtz Center Munich, Institute for Biological and Medical Imaging, Neuherberg, Germany, and also with the Faculty of Medicine and the Faculty of Electrical Engineering, Technical University of Munich, Munich 80333, Germany (e-mail: dr@tum.de).

Color versions of one or more of the figures in this paper are available online at http://ieeexplore.ieee.org.

Digital Object Identifier 10.1109/TMI.2017.2686006

I. Introduction

MULTISPECTRAL optoacoustic tomography (MSOT) is a hybrid light- and ultrasound-based imaging modality that can resolve the distribution of tissue chromophores and optical contrast agents deep inside highly scattering living organisms [1]–[5]. The basic operational principle consists in identification of absorption spectrum variations in a sequence of optoacoustic images acquired at multiple excitation wavelengths [6]–[8]. The large versatility of optical absorption contrast empowers MSOT with diverse functional and molecular imaging capabilities, often unique among the bio-imaging modalities [9]–[15].

MSOT images representing the distribution of spectrally-distinct chromophores are generally obtained with a two-step procedure. In a first step, optoacoustic tomographic images are reconstructed from the pressure signals generated by absorption of short laser pulses. The signals are recorded at several locations around the imaged object while various inverse algorithms based on back-projection [16], time-reversal [17] or model-based [18]–[21] can be employed for the reconstruction, each offering different trade-offs between the image reconstruction accuracy and computational cost [22]. In the second step, spectral unmixing algorithms are imposed on the images acquired at different excitation wavelengths in order to map the distribution of different absorbing substances present in the tissue. Several spectral processing algorithms based on spectral fitting [6] or blind unmixing [23] have been reported with performance greatly varying among the different approaches. The order of these two steps can be interchanged, i.e., the distribution of a specific substance can alternatively be rendered by multispectral unmixing of the acquired signals and subsequent image reconstruction.

Model-based inversion methods represent arguably the most accurate and versatile approach for both the image reconstruction and unmixing steps in MSOT. They can be adapted to account for the frequency response and geometrical shape of ultrasound sensors [24]–[26] as well as for acoustic mismatch and attenuation [27], [28] and hence significantly enhance image quality. However, applicability of the model-based approach is often limited by lack of exact knowledge of the underlying physical properties of the tissue as well as the illumination and detection geometry, which may lead to inaccurate reconstructions and image artifacts such as negative values with no physical meaning.

For instance, a non-linear spectral model incorporating wavelength-dependent light attenuation effects has been suggested to reduce cross-talk artifacts appearing in the

unmixed images obtained with standard linear unmixing [29]. Yet, accurate modeling of light propagation requires prior knowledge of background optical properties, which is very challenging to measure in highly heterogeneous living tissues [30]. Other factors leading to image artifacts are limited detection bandwidth of transducers, limited number of detectors and tomographic coverage, inaccurate modeling assumptions when reducing the problem into two dimensions, inability to accurately account for the spatial light distribution and spectral coloring effect.

To reduce the influence of modeling imperfections, the inversion procedure can be optimized by incorporating constraints or regularization terms, e.g. a non-negative constrained inversion has been shown to render images free of negative absorption values [31]. We have also recently demonstrated that non-negative constrained inversion of a linear two-dimensional optoacoustic tomographic model can further enhance quantitative performance by yielding reconstructed values proportional to the actual absorption coefficient [32].

In this work, we investigate on the impact of non-negative constrained inversion in both the reconstruction and unmixing steps of the MSOT. Linear inverse problems corresponding to reconstruction, unmixing and a combination of both are defined. Performance of the different approaches is subsequently evaluated based on the ability to accurately reconstruct contrast agent distribution in experimental data acquired from tissue-mimicking phantoms and living mice.

II. Theory

In this section, we describe the theoretical basis of MSOT and the simplifications introduced to derive the forward models for the reconstruction and unmixing steps. Based on these forward models, inverse problems where non-negative constraints can be incorporated are defined.

A. Model-Based Reconstruction

Time-domain model-based reconstruction algorithms are based on a discrete linear model of the propagation of pressure waves generated by a laser pulse. Assuming thermal and stress confinement conditions and approximating the short-pulsed laser illumination by a Dirac's delta in time, the optoacoustic wave equation for a homogeneous acoustic medium can be expressed as [33]

$$\frac{\partial^2 p(\boldsymbol{r},t)}{\partial t^2} - c^2\nabla^2 p(\boldsymbol{r},t) = \Gamma H(\boldsymbol{r})\frac{\partial \delta(t)}{\partial t}, \tag{1}$$

where Γ is the dimensionless Grüneisen parameter, c is the speed of sound in the medium and $H(\boldsymbol{r})$ is the amount of energy absorbed in the tissue per unit volume. The solution of (1) is given by the Poisson-type integral via [33]

$$p(\boldsymbol{r},t) = \frac{\Gamma}{4\pi c}\frac{\partial}{\partial t}\int_{S'(t)} \frac{H(\boldsymbol{r}')}{|\boldsymbol{r}-\boldsymbol{r}'|} dS'(t). \tag{2}$$

Integration is performed along a spherical surface $S'(t)$ for which $|\boldsymbol{r}-\boldsymbol{r}'| = ct$. A cross-sectional acquisition geometry is often assumed with the optoacoustic sources lying in a plane [21], in which case (2) is simplified to

$$p(\boldsymbol{r},t) \approx \frac{\Gamma}{4\pi c}\frac{\partial}{\partial t}\int_{L'(t)} \frac{H(\boldsymbol{r}')}{|\boldsymbol{r}-\boldsymbol{r}'|} dL'(t), \tag{3}$$

where $L'(t)$ is a circumference with radius of ct.

A discretization procedure of (2) or (3) leads to a linear forward model expressed as [21]

$$\boldsymbol{p} = \boldsymbol{A}\boldsymbol{h}, \tag{4}$$

where $\boldsymbol{p}$ is a vector representing pressure signals at all transducer positions, $\boldsymbol{A}$ is the model matrix with columns representing the time-resolved impulse response from each pixel of the reconstruction region of interest (ROI) to different transducer locations, and $\boldsymbol{h}$ is a vector containing the absorption at all pixel locations. In model-based reconstruction, the absorption vector is reconstructed from the measured pressure signals $\boldsymbol{p}_m$ by solving the following least squares problem

$$\hat{\boldsymbol{h}} = \arg\min_{\boldsymbol{h}} \|\boldsymbol{A}\boldsymbol{h} - \boldsymbol{p}_m\|_2^2. \tag{5}$$

A regularization term is sometimes incorporated into (5). However, regularization-free results are satisfactory in most cross-sectional optoacoustic tomography reconstructions, given that sufficient angular tomographic coverage is provided by the ultrasound transducers [34].

B. Linear Unmixing

In MSOT, multispectral unmixing is performed to distinguish absorbing substances based on their differential spectral absorption profiles. Assuming a homogeneous Grüneisen parameter in light absorbing regions (mainly vascular structures), the optical absorption h for a certain location $\boldsymbol{r}$ and a given wavelength λ_i can be expressed in arbitrary units as

$$\begin{aligned} h(\lambda_i,\boldsymbol{r}) &= \Phi(\lambda_i,\boldsymbol{r})\mu_a(\lambda_i,\boldsymbol{r}) \\ &= \Phi(\lambda_i,\boldsymbol{r})\sum_{j=1}^{S}\left(\boldsymbol{\varepsilon}_j(\lambda_i)\boldsymbol{c}_j(\boldsymbol{r})\right), \end{aligned} \tag{6}$$

where $\Phi(\lambda_i,\boldsymbol{r})$ is the wavelength dependent local light fluence for wavelength i, S is the total number of absorbing substances, $\boldsymbol{\varepsilon}_j(\lambda_i)$ is the molar extinction coefficient of the j-th substance at wavelength λ_i and $\boldsymbol{c}_j(\boldsymbol{r})$ is its concentration at location $\boldsymbol{r}$. The light fluence at different locations in living biological tissues is generally very difficult to measure or estimate without accurate knowledge of the distribution of absorption and scattering coefficients in the entire imaged region. Thereby, a common simplification consists in assuming that the spectral variations of $\Phi(\lambda)$ are negligible with respect to those of $\varepsilon_j(\lambda)$, i.e., $\Phi(\lambda_1,\boldsymbol{r}) = \Phi(\lambda_2,\boldsymbol{r}) = \cdots = \Phi(\lambda_W,\boldsymbol{r}) = \bar{\Phi}(\boldsymbol{r})$. Let $\bar{\boldsymbol{\Phi}}$ be the vector containing the light fluence at all pixel locations, $\boldsymbol{H} = [\boldsymbol{h}(\lambda_1)\ \boldsymbol{h}(\lambda_2)\ \cdots\ \boldsymbol{h}(\lambda_W)]$ the wavelength-dependent optical absorption, $\boldsymbol{C} = [\boldsymbol{c}_1 \odot \bar{\boldsymbol{\Phi}}\quad \boldsymbol{c}_2 \odot \bar{\boldsymbol{\Phi}}\quad \cdots\quad \boldsymbol{c}_S \odot \bar{\boldsymbol{\Phi}}]$ having each column being the Hadamard product of the concentration of an absorbing substance and the local light fluence at all pixels, and $\boldsymbol{E} = [\boldsymbol{\varepsilon}_1\ \boldsymbol{\varepsilon}_2\ \cdots\ \boldsymbol{\varepsilon}_S]^{\mathsf{T}}$ representing the molar extinction

coefficient of all the absorbing substances. Then, (6) can be expressed in the following simplified matrix relation

$$\boldsymbol{H} = \boldsymbol{C}\boldsymbol{E}. \tag{7}$$

Spectral unmixing of different absorbing substances is performed by solving the following least-square problem [29]

$$\hat{\boldsymbol{C}} = \arg\min_{\boldsymbol{C}} \|\boldsymbol{C}\boldsymbol{E} - \hat{\boldsymbol{H}}\|_2^2 \tag{8}$$

with the solution

$$\hat{\boldsymbol{C}} = \hat{\boldsymbol{H}}\boldsymbol{E}^+, \tag{9}$$

where $\hat{\boldsymbol{H}}$ is the reconstructed optical absorption at all wavelengths and $\boldsymbol{E}^+$ is the pseudoinverse of $\boldsymbol{E}$. Both the reconstruction and unmixing are linear problems that can be interchanged without affecting the final result. In particular, since $\hat{\boldsymbol{H}} = \boldsymbol{A}^+\boldsymbol{P}_m$, where $\boldsymbol{P}_m = [\boldsymbol{p}_m(\lambda_1)\ \boldsymbol{p}_m(\lambda_2)\ \cdots\ \boldsymbol{p}_m(\lambda_w)]$, one obtains

$$\hat{\boldsymbol{C}} = \boldsymbol{A}^+\boldsymbol{P}_m\boldsymbol{E}^+. \tag{10}$$

Thereby, the unmixed pressure signals

$$\hat{\boldsymbol{P}} = \boldsymbol{P}_m\boldsymbol{E}^+ \tag{11}$$

can be calculated first, while the images of the different absorbers

$$\hat{\boldsymbol{C}} = \boldsymbol{A}^+\hat{\boldsymbol{P}} \tag{12}$$

only reconstructed at the second step. Note that, since $\boldsymbol{E}$ is a wide matrix with a relatively small number of entries, a lower computational complexity is achieved by first unmixing the signals and subsequently reconstructing the images. Since (10) corresponds to a combined (reconstruction + unmixing) least squares problem expressed as

$$\hat{\boldsymbol{C}} = \arg\min_{\boldsymbol{C}} \|\boldsymbol{A}\boldsymbol{C}\boldsymbol{E} - \boldsymbol{P}_m\|_2^2, \tag{13}$$

solving the linear reconstruction and multispectral unmixing problems in a separate or in a combined manner would in principle yield equivalent results. However, performance is expected to significantly differ in the case of the non-negative constrained inversion, which introduces non-linearities in the reconstruction process, as described in the following section.

C. Non-Negative Constrained Approaches

Non-negative constraints are applicable in any of the inversion problems defined in the previous sections. The constrained least squares problem for tomographic reconstruction is formulated as

$$\hat{\boldsymbol{h}} = \arg\min_{\boldsymbol{h}\geqslant\boldsymbol{0}} \|\boldsymbol{A}\boldsymbol{h} - \boldsymbol{p}_m\|_2^2, \tag{14}$$

and the subsequent non-negative constrained unmixing problem is defined as

$$\hat{\boldsymbol{C}} = \arg\min_{\boldsymbol{C}\geqslant\boldsymbol{0}} \|\boldsymbol{C}\boldsymbol{E} - \hat{\boldsymbol{H}}\|_2^2. \tag{15}$$

On the other hand, the combined reconstruction and unmixing inversion procedure can also be formulated as a non-negative constrained inversion problem via

$$\hat{\boldsymbol{C}} = \arg\min_{\boldsymbol{C}\geqslant\boldsymbol{0}} \|\boldsymbol{A}\boldsymbol{C}\boldsymbol{E} - \boldsymbol{P}_m\|_2^2. \tag{16}$$

Note that the constraint $\boldsymbol{C} \geqslant \boldsymbol{0}$ also implies that $\boldsymbol{H} = \boldsymbol{C}\boldsymbol{E} \geqslant \boldsymbol{0}$ since the coefficients in $\boldsymbol{E}$ are non-negative. Note that the non-negative constraint is not applicable for the purpose of signal unmixing prior to reconstructions since the raw recorded optoacoustic signals may generally have physically meaningful negative values. Indeed, the optoacoustic pressure signals are bipolar. For example, the pressure response generated by a spherical object has a characteristic "N" shape with positive and negative pressure values [35]. On the other hand, non-negative constraints can be imposed solely on certain columns of $\boldsymbol{C}$ corresponding to the optical absorbers of interest for the inverse problems in (15) and (16).

As mentioned above, image reconstruction performed with (14) followed by the unmixing step defined in (15) does not generally lead to the same final result as the combined optimization problem in (16).

III. Methods

As discussed in the previous section, non-negativity constraints can be added to the reconstruction and/or unmixing steps. One may also change the order of the reconstruction and unmixing steps or calculate the desired concentrations in a combined manner. Herein, we investigate on the performance of all relevant combinations in terms of quantitativeness and cross-talk artifacts present in the unmixed images. Specifically, the following methods are considered:

- Constrained reconstruction followed by constrained unmixing (CR-CM)
- Constrained reconstruction followed by unconstrained unmixing (CR-UM)
- Unconstrained reconstruction followed by constrained unmixing (UR-CM)
- Unconstrained reconstruction followed by unconstrained unmixing (UR-UM)
- Unconstrained unmixing followed by constrained reconstruction (UM-CR)
- Combined and constrained reconstruction and unmixing (CB1)
- Combined reconstruction and unmixing with a non-negative constraint only imposed on the contrast agent of interest (CB2)

The unconstrained reconstruction problems (UR) defined in (5) were solved with the iterative method LSQR [36], while the unconstrained unmixing problems (UM) defined in (8) were solved directly with the pseudoinverse of $\boldsymbol{E}$, which can be easily calculated due to its small size. The constrained reconstruction (CR) and the constrained combined problems (CB1 and CB2) were solved using an efficient iterative non-negative least squares method introduced in [32]. On the other hand, the constrained unmixing problems (CM) defined in (15) were solved with the FNNLS method [37], which, due to the small dimensionality of this problem, is more efficient.

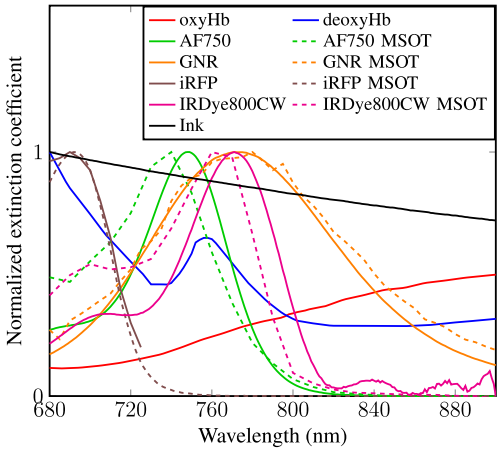

Fig. 1. Normalized extinction (absorption) spectra of the different intrinsic tissue chromophores and optical contrast agents considered in this study.

TABLE I
PEAK MOLAR EXTINCTION COEFFICIENT AND MOLECULAR WEIGHT OF THE INTRINSIC TISSUE CHROMOPHORES AND OPTICAL CONTRAST AGENTS

	Peak Molar Ext. ($M^{-1}cm^{-1}$)	Wavelength (nm)	Molecular Weight (g/mole)
oxyHb	1198	900	64500
deoxyHb	2407.92	680	64500
AF750	$2.9 \cdot 10^5$	749	~ 1300
GNR	$8.92 \cdot 10^8$	770	$\sim 3.1 \cdot 10^7$
iRFP	$8.5 \cdot 10^4$	692	35000
IRDye800CW	$2.4 \cdot 10^5$	774	1091.11

Reconstruction performance of all methods was experimentally validated by unmixing the distribution of various chromophores and contrast agents whose extinction (absorption) spectra are depicted in Fig. 1. The absorption spectra for AF750, gold-nanorods (GNR), iRFP [38] and IRDye800CW from spectrophotometer measurements are shown in solid lines and the spectra from MSOT measurements are shown in dashed lines. The MSOT spectra were obtained by imaging phantoms containing the isolated contrast agents at multiple wavelengths and averaging pixel values in the reconstructed optoacoustic images. The measured absorption values were further normalized by the wavelength-dependent energy of the laser source. The MSOT spectra of iRFP and GNR are almost identical to their spectrophotometer spectra while the MSOT spectra of IRDye800CW and AF750 are slightly shifted to the left and the MSOT spectra for AF750 is broadened. The corresponding peak molar extinction coefficients and molecular weight are further listed in TABLE I.

All imaging experiments were done with a commercial small animal multi-spectral optoacoustic tomography scanner (Model: MSOT256-TF, iThera Medical GmbH, Munich, Germany). The scanning system contains a wavelength-tunable (680-950nm) short-pulsed ($\leqslant$10ns) laser. The laser beam is guided through 10 fiber bundles onto the surface of the imaged sample to form a ring-shaped illumination on its surface. The generated optoacoustic responses are captured by a 256-element cylindrically-focused transducer array covering an angle of 270° around the imaged cross-section [39]. During all experiments, the temperature was stabilised at approximately 34°C.

A. Phantom Experiment

In the first experiment, a cylindrical 19 mm diameter agar phantom was imaged containing India ink and Intralipid for mimicking tissue background absorption ($\mu_a = 0.2$ cm^{-1} at 700nm) and scattering properties ($\mu_s' = 10$ cm^{-1}) [30]. The acoustic properties of agar are very similar to water. Two 1 mm diameter polyethylene tubings were inserted into the phantom at different depths. AlexaFluor 750 (InvitrogenTM) fluorescent dye at 6 different concentrations (optical densities 0.3, 0.5, 1.1, 1.5, 2.0 and 2.5 as measured with a spectrophotometer) was flushed into and out of the same tubings. Optoacoustic images were recorded with 20 averages at 9 vertical positions of the phantom and at 11 different wavelengths ranging from 700 to 800 nm with 10 nm steps.

B. iRFP-Expressing Tumor Cells

To facilitate the mouse tumor studies, we developed a lentiviral vector expressing the phytochrome-based near-infrared fluorescent protein, iRFP [40]. The iRFP [40] complementary DNA was PCR amplified and cloned into the pENTR/D-TOPO plasmid to create the pENTR-iRFP vector via a standard Topo-cloning methodology, as we have described [41]. Once sequence verified, the iRFP was transferred into a Gateway-modified pLVX-IRES-puro vector, as described [42], [43] by TOPO cloning, to generate pLVX-iRFP-IRES-puro. Positive clones were selected and plasmids were extracted with the QIAprep Spin Miniprep Kit (Qiagen). Lentiviral particles were generated by co-transfection of 4 plasmids (The iRFP expression vector pLVX-iRFP-IRES-puro together with pMD2.g (VSVG), pVSV-REV and pMDLg/pRRE) into 293-FT cells using *Trans*IT-X2® Dynamic Delivery System (Mirus Bio LLC). The breast cancer cell line MDA-MB-231 (a generous gift from Dr. Julie Eiseman, University of Pittsburgh) was cultured in RPMI 1640 media supplemented with heat-inactivated FBS (10%) and Gentamycin (10μg/ml) at 37°C in humidified chambers with 5% CO_2 and 20% O_2. The MDA-MB-231/iRFP expressing cells were established by overnight transduction of the MDA-MB-231cells with lentivirus expressing iRFP (pLVX-iRFP-IRES-puro). Transduced cells were then selected for 7-10 days in media supplemented with puromycin (1.5μg/ml). The collection and isolation of lentiviral particles and transduction of cells was performed as described previously [44].

C. In Vivo Mouse Experiments

In order to assess the accuracy and sensitivity of the different methods under realistic conditions (including conditions resembling typical molecular imaging studies), data from additional three *in vivo* mouse experiments was further analyzed. All procedures involving animal care and experimentation were conducted according to the guidelines of the

Helmholtz Center Munich and the government of Upper Bavaria and complied with German federal and international laws and regulations. All *in vivo* mouse experiments were terminal.

In the first *in vivo* experiment, a polyethylene tubing was inserted into the rectum of a mouse (mouse 1). Ultrasound gel was used as lubricant and for acoustic coupling. Different concentrations of AlexaFluor 750 (optical densities 0.2, 0.5, 1.0, 1.9 and 3.9) as well as GNR (Nanopartz D12-10-780, optical densities 0.3, 0.6, 1.5 and 1.9) were injected into the tubing. For each concentration of the contrast agents, cross-sectional images of the mouse were taken at 10 different positions, from the intestinal region to the legs. At each position, multi-spectral data was recorded with 10 averages at 22 different wavelengths ranging from 690 to 900 nm with 10 nm steps.

For unmixing, the known absorption spectra of oxygenated and deoxygenated hemoglobin were used whereas the spectra of AF750 and GNR were adopted from the results obtained with a blind unmixing procedure [45] in order to compensate for the spectral coloring effects at deep tissue locations [29]. In this scenario, accuracy of the retrieved spectra is ensured due to the local confinement of the imaging agents.

In the second experiment, an 8-week-old female Hsd:Athymic Nude-Foxn1nu/nu mouse was inoculated with 1 million of iRFP-expressing (MDA-MB-231-iRFP) tumor cells in the abdomen region (mouse 2). The tumor was allowed to grow over 10 days reaching an approximate size of 5 mm. No toxicity effects were observed due to the presence of iRFP. Cross-sectional MSOT images were acquired with 10 averages at 680, 690, 700, 715, 730, 760, 800 and 850 nm wavelengths.

In the third *in vivo* experiment, a healthy nude mouse was injected with 20 nmol of IRdye800CW optical contrast agent (LI-COR Biosciences, Lincoln, Nebraska USA) in 100 μl saline through its tail vein (mouse 3). MSOT images at 715, 730, 760, 780, 800 and 850 nm wavelengths were subsequently taken without averaging approximately 4 min post injection at the kidney region, where the probe accumulates during renal clearance [46].

IV. Results

Results from the phantom experiment are summarized in Fig. 2. Fig. 2a) shows the non-negative constrained reconstruction of the phantom imaged at 740 nm, corresponding to the peak absorption of AF750 in the blindly unmixed spectra. Figs. 2b) and c) display the unmixed distributions of India ink and AF750 for the CR-CM method, i.e., non-negative constrained reconstructions followed by non-negative constrained unmixing.

Clearly, the unmixed distribution of AF750 is confined within the tubings, whilst the amplitude of the deeper insertion is lower due to light fluence attenuation effects. On the other hand, ink is unmixed throughout the phantom as a background component, yet cross-talk artifacts appear inside the tubings. In order to evaluate the accuracy of the AF750 unmixing, the averaged pixel values inside the two tubings (unmixed concentration) obtained with the different methods

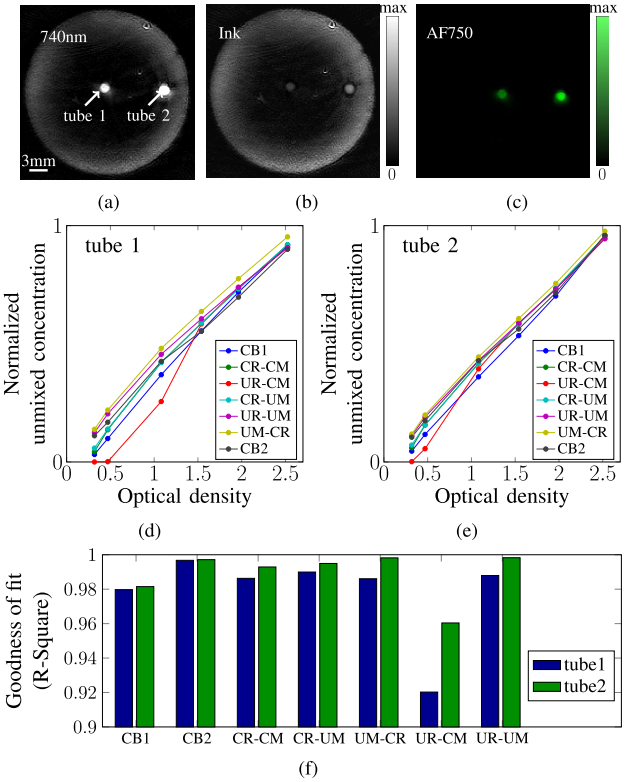

Fig. 2. Unmixing results for the phantom with background ink absorption and two insertions (tubes) containing AF750 dye. a) Optoacoustic image acquired at 740 nm with 2.5 OD of AF750 insertion. b) Unmixed image corresponding to the ink component obtained with the CR-CM method. c) Unmixed image corresponding to the AF750 component obtained with the CR-CM method. d)-e) Normalized unmixed concentration (pixel values of the unmixed image) within the tubes as a function of the optical density of AF750. f) The R^2 values, representing quality of the linear fit in d) and e).

are plotted in Figs. 2d) and e) as a function of the measured optical density values, which are proportional to the actual concentration. Ideally, the method employed for reconstruction and unmixing should yield unmixed values proportional to the actual concentration of the probe. It can be observed in Figs. 2d) and e) that all methods yield similar results except for UR-CM, for which the relationship between unmixed values and optical density is strongly non-linear for low concentrations of the probe. The data points in Figs. 2d) and e) were fitted to linear functions for each method. Quality of the linear fit is further shown in Fig. 2f). For this particular experiment, no significant differences were observed among the different approaches except for UR-CM, yet the CB2 method exhibits the best linearity.

Results of the *in vivo* mouse experiment (mouse 1) are shown in Fig. 3. Two representative examples for the unmixing of AF750 and GNR are displayed in Figs. 3a)-b) superimposed onto the single wavelength optoacoustic images taken at 800 nm. In particular, Fig. 3a) displays the distribution of AF750 (1.9 OD) in the intestinal region of the mouse unmixed by the CR-CM method while Fig. 3b) shows the distribution of GNR (1.5 OD) for the intestinal/leg area

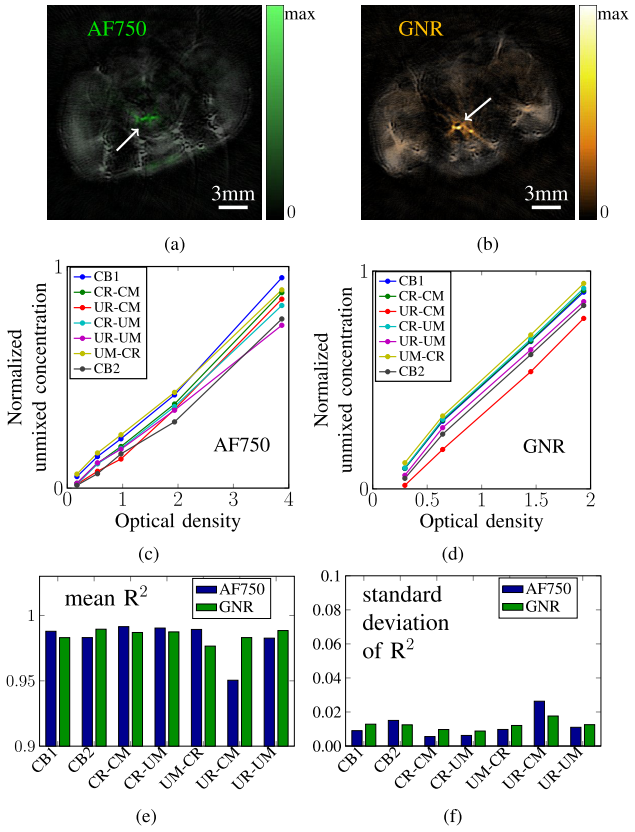

Fig. 3. Unmixing results for the *in vivo* (mouse 1) experiment. a) Unmixed distribution of AF750 obtained with the CR-CM method. b) Unmixed distribution of GNR obtained with the CR-CM method. c)-d) Unmixed optoacoustic signal within the tubes as a function of the optical density of AF750 and GNR, respectively, normalized to the maximum value for the corresponding slices. e)-f) Statistical analysis of the linear fit of the curves in c)-d). All 10 imaged cross-sections were taken into account.

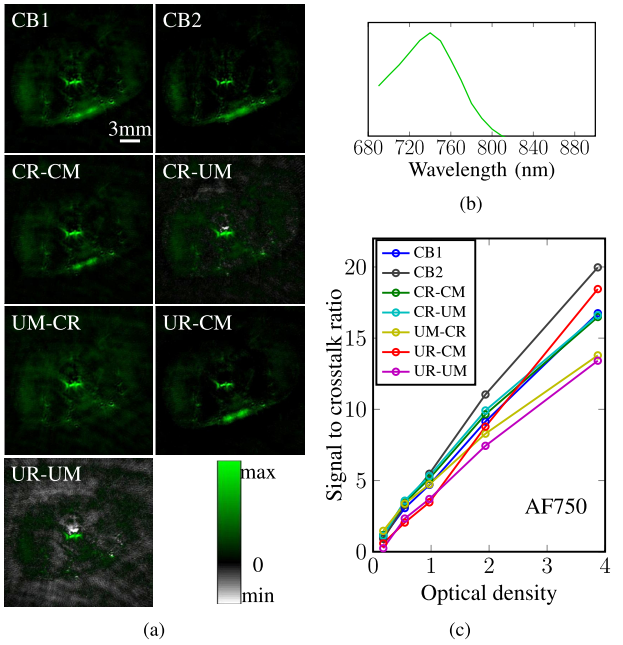

Fig. 4. Cross-talk artifacts evaluation for the AF750 probe unmixing in mouse 1. a) Unmixed distribution of AF750 (1.9 OD) for an intestinal region slice using the different reconstruction and unmixing methods. b) Blind spectrum of AF750 used for unmixing. c) Signal to cross-talk ratios as a function of the optical density of AF750 averaged over all 10 imaged cross-sections.

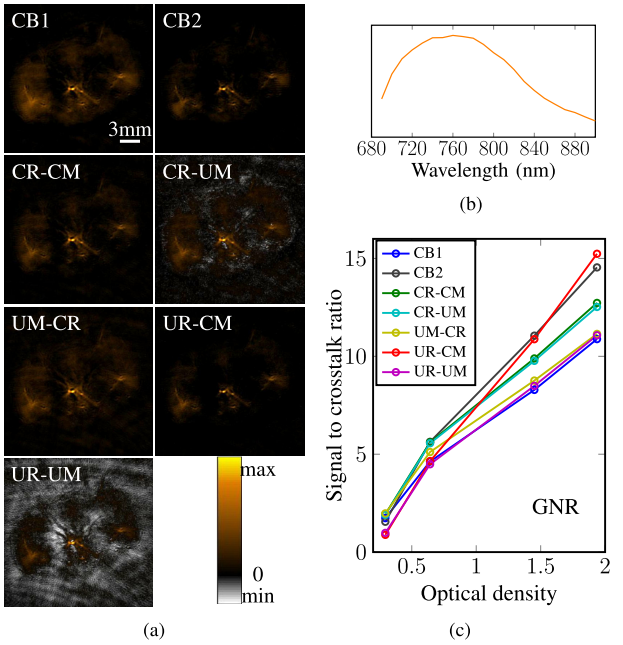

Fig. 5. Cross-talk artifacts evaluation for the GNR unmixing in mouse 1. a) Unmixed distribution of GNR (1.5 OD) for an intestinal/leg region. b) Blind spectrum of GNR used for unmixing. c) Signal to cross-talk ratios as a function of the optical density of GNR averaged over all 10 imaged cross-sections.

unmixed by the CR-CM method. For the particular slices shown, the probe concentrations inside the tubing obtained with the different methods are further plotted in Figs. 3c) (AF750) and d) (GNR) as a function of the measured optical density of the probes. Much like in the phantom experiments, all methods exhibited a similar performance. In this particular example, the relatively shallow depth of the tubing allows to distinguish relatively low concentrations of the contrast agents, which was not possible for other cross-sections. For a more comprehensive comparison, Figs. 3e)-f) depict the results of a statistical analysis considering 10 different cross-sections of the mouse. Figs. 3e) shows the mean R^2 values for all cross-sections in blue for AF750 and green for GNR and Figs. 3f) shows the standard deviation of the calculated R^2 values for the different methods. It can be seen that most methods again yield similar performance except for UR-CM, which results in a lower R^2 value and high variability of the unmixing performance.

Figs. 4 and 5 show the results of the cross-talk effects evaluation, for which the signal to cross-talk ratio (SCR) was defined as the ratio between the averaged pixel value within the tubings and standard deviation of the background (everywhere else except the tubings). Positive concentrations of AF750 and GNR are illustrated in green and gold respectively while negative values of both probes are illustrated in the color gray. It can be seen in Fig. 4a) that the images of

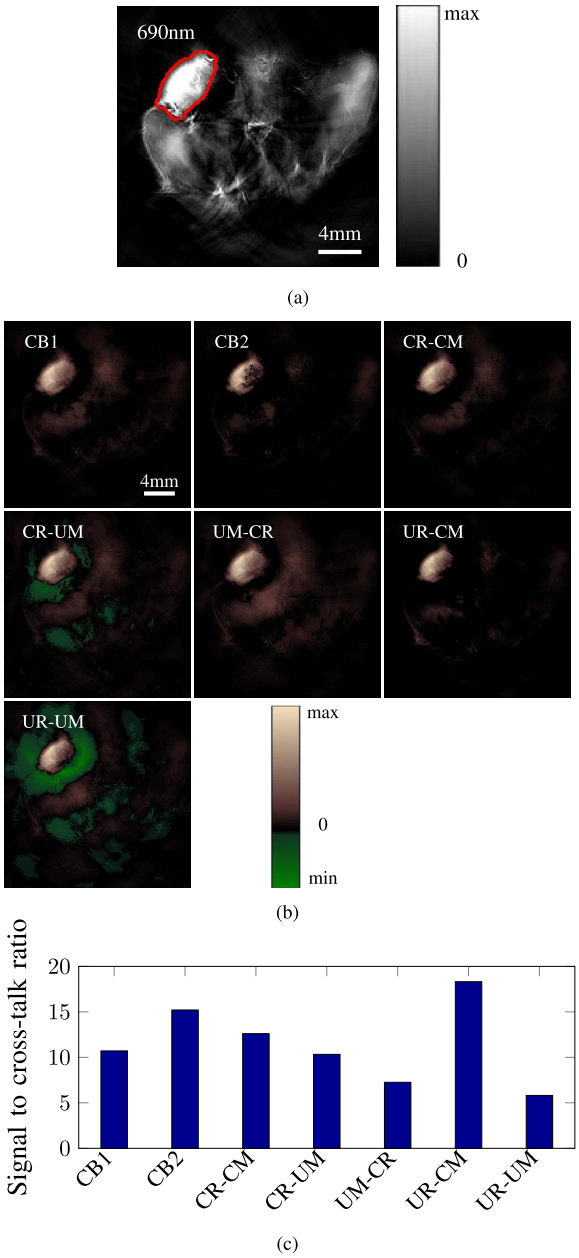

Fig. 6. Results of the *in vivo* iRFP unmixing experiment in mouse 2. a) Single wavelength optoacoustic image (gray scale) acquired at 690 nm. b) Unmixed distributions of iRFP obtained using different methods (brown-green scale). c) Cross-talk performance of different methods - the unmixed iRFP signal is assumed to be confined within the red region marked in a).

the unmixed AF750 distribution, which were obtained with the unconstrained methods (CR-UM and UR-UM), contain negative cross-talk artifacts. Fig. 4b) shows the blind spectrum of AF750 used for unmixing. Note that the shape is wider compared to the measured spectrum in Fig. 1 and the peak is slightly shifted to the left. Fig. 4c) shows the respective SCR as a function of the measured optical density of AF750 averaged over the 10 imaged cross-sections. As expected, the SCR is approximately linear with the optical density of the

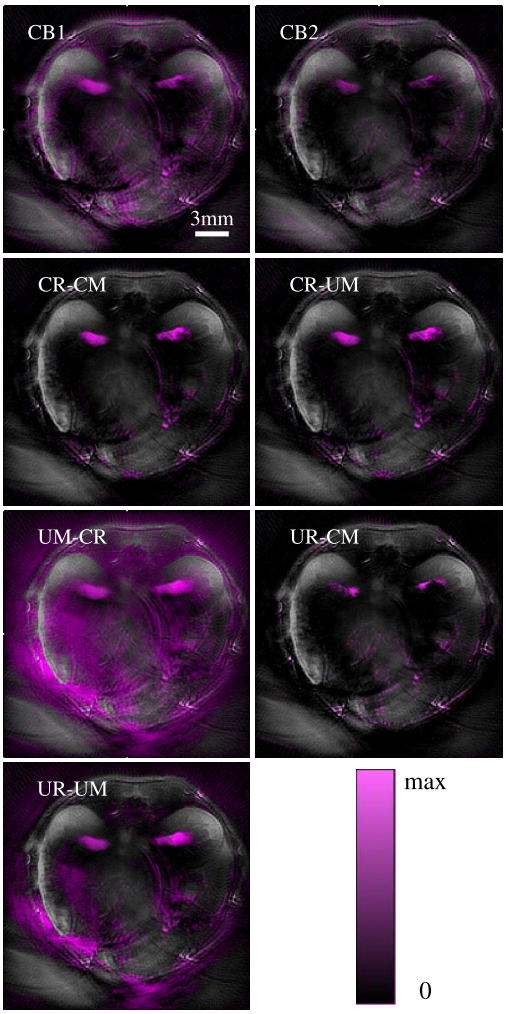

Fig. 7. Unmixed distributions of IRDye800CW obtained using the different non-negative constraints. The probe distribution (represented on a purple scale) is superimposed onto the single wavelength optoacoustic images acquired at 850 nm showing accumulation in the renal medulla while clearing through kidneys.

probe. In this particular experiment, the CB2 method yields the best cross-talk performance whereas the UM-CR and UR-UM methods render the strongest cross-talk artifacts. Fig. 5a) displays the unmixed GNR images in the intestinal/leg region rendered using the different methods. Negative cross-talk artifacts are again obtained using the CR-UM and UR-UM methods. Fig. 5b) shows the blind spectrum of GNR. The spectrum is very similar to the measured spectrum in Fig. 1. Fig. 5c) shows the result of the SCR analysis. UR-CM yields the best cross-talk performance while CB1, UM-CR and UR-UM render noisier images of the GNR distribution.

Fig. 6 presents the spectral unmixing results to render the iRFP distribution in mouse 2. Fig. 6a) shows the reconstructed optoacoustic image corresponding to 690 nm (absorption peak of iRFP). Fig. 6b) shows the unmixed iRFP images obtained using the different methods. Here positive concentrations of iRFP are displayed in brown and negative concentrations in green. The tumor can be clearly distinguished in both the

TABLE II
COMPUTATION TIME OF DIFFERENT METHODS FOR THE IN VIVO IRDye800CW EXPERIMENT

Method	Computation time
CB1	77s
CB2	120s
CR-CM	$42\text{s} + 4.6\text{s}$
CR-UM	$42\text{s} + 0.005\text{s}$
UM-CR	$0.01\text{s} + 22.5\text{s}$
UR-CM	$13.2\text{s} + 2.4\text{s}$
UR-UM	$13.2\text{s} + 0.005\text{s}$

single-wavelength and the unmixed images. Note however that the unconstrained methods, namely CR-UM and UR-UM, yield large areas with negative values. Fig. 6c) displays the cross-talk ratios of the unmixed images, calculated as the mean value of the unmixed image inside a region marked in red divided by the standard deviation outside this region. Segmentation of the marked region was done on the single wavelength image using an active contour method [47], [48]. It is readily observed that in this particular experiment the UR-CM method yields the lowest background while the UM-CR and UR-UM methods have the worst cross-talk performance.

Fig. 7 presents the unmixed images of the IRDye800CW dye distribution in the mouse 3 experiment. Here the unmixing results significantly differ among the different methods. Negative artifacts obtained with the CR-UM and UR-UM methods were set to zero for a more convenient representation. From the physiological perspective, the IRDye800CW is expected to clear through kidneys hence mostly accumulate in this area. However, part of the probe remains in the blood circulation, making it difficult to conclude which method renders the most accurate unmixing performance. It is yet clear that the unmixed images rendered with the UM-CR and UR-UM methods contain strong cross-talk artifacts present both inside and outside the mouse, which is consistent with the poor cross-talk performance rendered with these methods in the previous experiments. TABLE II shows the computation time of each method for this data set. Clearly, constrained image reconstruction increases the complexity. The combined methods (CB1 and CB2) are the most time consuming methods while UM-CR is the most efficient method.

V. DISCUSSION AND CONCLUSIONS

The accuracy of tomographic inversion and spectral unmixing in multispectral optoacoustic tomography (MSOT) depends on a number of experimental and theoretical factors, such as the number, shape and size of the detectors employed, forward modeling imperfections, and discrete sampling issues. This often results in ambiguous reconstructions and appearance of negative values in the images, which have no physical meaning since optical absorption can only be higher or equal than zero. Any artifacts present in the single wavelength optoacoustic images can be significantly aggravated when performing a two-step reconstruction consisting in acoustic inversion and spectral unmixing aimed at rendering the distributions of spectrally-distinct absorbers. In this work, performance of non-negative constrained inversion approaches in multispectral optoacoustic tomography (MSOT) has been evaluated by introducing the constraints at the different image reconstruction and/or probe unmixing steps.

It has been generally established that the constrained inversion is essential for reducing the critical image artifacts associated with inaccurate forward modeling assumptions. Yet, algorithmic sequence has a significant impact on the reconstruction and unmixing performance. Since the combined least squares problem defined in (16) is a convex optimization problem, its solution is the global minimum. Therefore, if we are looking for a solution satisfying $\hat{\boldsymbol{C}} \geqslant \mathbf{0}$, the combined problem yields the lowest possible least-squares residual of all approaches. The combined approach is then expected to outperform the other methods if the forward model is accurate. However, modeling imperfections present in practical imaging set-ups may have significant impact on the results, so that the lowest least squares residual may not necessarily guarantee the highest accuracy of the reconstructed images.

Indeed, in practice, imposing the non-negativity constraint directly on the unmixed distribution of the probe of interest (CB2) was found to have the most robust and accurate reconstruction performance in all experiments. Even though the method based on unconstrained reconstruction and subsequent non-negative constrained unmixing (UR-CM) has attained the best SCR in the iRFP experiment, this particular approach is generally not recommendable since it consistently showed an inferior quantitative performance exhibiting a prominent non-linear dependence between the pixel values in the unmixed image and the actual probe concentration, both in phantom and *in vivo* mouse experiments. On the other hand, more significant crosstalk artifacts were observed for all mouse experiments in the images rendered with the standard unconstrained method (UR-UM) and the method based on unconstrained unmixing followed by constrained reconstruction (UM-CR), which suggests that these approaches provide a lower sensitivity in detecting optical probes.

In view of both phantom and *in vivo* imaging results, the combined non-negative constrained method has arguably achieved the best results in terms of artifact-free spectral unmixing, also yielding the lowest least-squares residual during the inversion and unmixing process. The combined approach is further expected to provide an efficient platform for further improving the forward model accuracy by e.g. incorporating the wavelength-dependent light fluence distribution into the model. Estimation of light fluence variations is very challenging since the exact optical properties of heterogeneous living tissues cannot be easily estimated or measured [49]. Nevertheless, methods based on e.g. extraction of low spatial frequency components from the images [50], analyzing signal variations by means of photoswitchable probes [51] or multi-modal imaging approaches [52] have shown promise in delivering reasonably good estimates on the light fluence distribution. Note that the current work was aimed at unmixing the distribution of spatially-confined contrast agents, in which case the agent's contribution to the optical attenuation and spectral coloring is assumed to be insignificant. As a result, the utilized blind unmixing approach

can effectively account for the spectral coloring effects when the unmixed chromophore is assumed to be sparsely distributed in the sample. Yet, accurately accounting for the wavelength-dependent light fluence distribution may turn important when instead aiming at mapping the blood oxygen saturation levels. The absorption spectra of hemoglobin are distorted (colored) at deeper locations, resulting in errors in the estimated oxygen saturation if the theoretical spectra are considered for unmixing. In this regard, the proposed non-negative constrained framework can be potentially extended by incorporating more sophisticated methods accounting for the wavelength dependence attenuation in the light fluence model [53]. It is important to note that the results showcased in this work correspond to a cross-sectional acquisition geometry, for which a two-dimensional optoacoustic model was assumed. While being a practical imaging configuration widely employed in small-animal optoacoustic imaging studies, three-dimensional acquisition geometries are generally expected to provide more accurate estimates on the actual volumetric (three-dimensional) distribution of probes [5], [54]. In this case, a three-dimensional model-based reconstruction algorithm is required [20], [31], which can further be optimized by accounting for the exact three-dimensional shape of the individual ultrasound detectors [26]. A study on the influence of non-negative constraints in three-dimensional model-based reconstructions accounting for the actual shape of the sensors is aimed at in our future investigations.

In conclusion, the impact of non-negative constraints in inversion problems corresponding to reconstruction and unmixing in MSOT was investigated. The newly proposed combined reconstruction and unmixing method with a non-negative constraint imposed directly on the distribution of the probe (CB2) of interest appears to be an efficient approach with robust performance in all phantom and mouse experiments. The proposed method further establishes a convenient framework to account for a variety of additional factors affecting the final images.

Acknowledgment

The authors acknowledge assistance in cell culture and cell purification from T. C. P. Sardella.

References

[1] D. Razansky *et al.*, "Multispectral opto-acoustic tomography of deep-seated fluorescent proteins *in vivo*," *Nature Photon.*, vol. 3, no. 7, pp. 412–417, 2009.

[2] J. Yao and L. V. Wang, "Photoacoustic tomography: Fundamentals, advances and prospects," *Contrast Media Molecular Imag.*, vol. 6, no. 5, pp. 332–345, 2011.

[3] M. Jeon, J. Kim, and C. Kim, "Multiplane spectroscopic whole-body photoacoustic imaging of small animals *in vivo*," *Med. Biol. Eng. Comput.*, vol. 54, nos. 2–3, pp. 283–294, 2016.

[4] L. Nie and X. Chen, "Structural and functional photoacoustic molecular tomography aided by emerging contrast agents," *Chem. Soc. Rev.*, vol. 43, no. 20, pp. 7132–7170, 2014.

[5] X. L. Deán-Ben and D. Razansky, "Adding fifth dimension to optoacoustic imaging: Volumetric time-resolved spectrally enriched tomography," *Light, Sci. Appl.*, vol. 3, no. 1, p. e137, 2014.

[6] B. T. Cox, S. R. Arridge, and P. C. Beard, "Estimating chromophore distributions from multiwavelength photoacoustic images," *J. Opt. Soc. Amer. A, Opt. Image Sci.*, vol. 26, no. 2, pp. 443–455, 2009.

[7] G. P. Luke, S. Y. Nam, and S. Y. Emelianov, "Optical wavelength selection for improved spectroscopic photoacoustic imaging," *Photoacoustics*, vol. 1, no. 2, pp. 36–42, 2013.

[8] S. Tzoumas, N. Deliolanis, S. Morscher, and V. Ntziachristos, "Unmixing molecular agents from absorbing tissue in multispectral optoacoustic tomography," *IEEE Trans. Med. Imag.*, vol. 33, no. 1, pp. 48–60, Jan. 2014.

[9] J. Yao *et al.*, "Noninvasive photoacoustic computed tomography of mouse brain metabolism *in vivo*," *Neuroimage*, vol. 64, pp. 257–266, Jan. 2013.

[10] V. Ermolayev, X. L. Deán-Ben, S. Mandal, V. Ntziachristos, and D. Razansky, "Simultaneous visualization of tumour oxygenation, neovascularization and contrast agent perfusion by real-time three-dimensional optoacoustic tomography," *Eur. Radiol.*, vol. 26, no. 6, pp. 1843–1851, 2016.

[11] A. C. Stiel, X. L. Deán-Ben, Y. Jiang, V. Ntziachristos, D. Razansky, and G. G. Westmeyer, "High-contrast imaging of reversibly switchable fluorescent proteins via temporally unmixed multispectral optoacoustic tomography," *Opt. Lett.*, vol. 40, no. 3, pp. 367–370, 2015.

[12] S. E. Bohndiek, L. S. Sasportas, S. Machtaler, J. V. Jokerst, S. Hori, and S. S. Gambhir, "Photoacoustic tomography detects early vessel regression and normalization during ovarian tumor response to the antiangiogenic therapy trebananib," *J. Nucl. Med.*, vol. 56, no. 12, pp. 1942–1947, 2015.

[13] M. Schwarz, A. Buehler, J. Aguirre, and V. Ntziachristos, "Three-dimensional multispectral optoacoustic mesoscopy reveals melanin and blood oxygenation in human skin *in vivo*," *J. Biophoton.*, vol. 9, nos. 1–2, pp. 55–60, 2016.

[14] A. P. Jathoul *et al.*, "Deep *in vivo* photoacoustic imaging of mammalian tissues using a tyrosinase-based genetic reporter," *Nature Photon.*, vol. 9, pp. 239–246, Jan. 2015.

[15] S. Gottschalk, T. F. Fehm, X. L. Deán-Ben, and D. Razansky, "Noninvasive real-time visualization of multiple cerebral hemodynamic parameters in whole mouse brains using five-dimensional optoacoustic tomography," *J. Cerebral Blood Flow Metabolism*, vol. 35, no. 4, pp. 531–535, 2015.

[16] M. Xu and L. V. Wang, "Universal back-projection algorithm for photoacoustic computed tomography," *Phys. Rev. E, Stat. Phys. Plasmas Fluids Relat. Interdiscip. Top.*, vol. 71, no. 1, p. 016706, 2005.

[17] Y. Hristova, P. Kuchment, and L. Nguyen, "Reconstruction and time reversal in thermoacoustic tomography in acoustically homogeneous and inhomogeneous media," *Inverse Problems*, vol. 24, no. 5, p. 055006, 2008.

[18] G. Paltauf, J. A. Viator, S. A. Prahl, and S. L. Jacques, "Iterative reconstruction algorithm for optoacoustic imaging," *J. Acoust. Soc. Amer.*, vol. 112, no. 4, pp. 1536–1544, 2002.

[19] P. Ephrat, L. Keenliside, A. Seabrook, F. S. Prato, and J. J. Carson, "Three-dimensional photoacoustic imaging by sparse-array detection and iterative image reconstruction," *J. Biomed. Opt.*, vol. 13, no. 5, p. 054052, 2008.

[20] X. L. Dean-Ben, A. Buehler, V. Ntziachristos, and D. Razansky, "Accurate model-based reconstruction algorithm for three-dimensional optoacoustic tomography," *IEEE Trans. Med. Imag.*, vol. 31, no. 10, pp. 1922–1928, Oct. 2012.

[21] A. Rosenthal, D. Razansky, and V. Ntziachristos, "Fast semi-analytical model-based acoustic inversion for quantitative optoacoustic tomography," *IEEE Trans. Med. Imag.*, vol. 29, no. 6, pp. 1275–1285, Jun. 2010.

[22] A. Rosenthal, V. Ntziachristos, and D. Razansky, "Acoustic inversion in optoacoustic tomography: A review," *Current Med. Imag. Rev.*, vol. 9, no. 4, pp. 318–336, 2013.

[23] J. Glatz, N. C. Deliolanis, A. Buehler, D. Razansky, and V. Ntziachristos, "Blind source unmixing in multi-spectral optoacoustic tomography," *Opt. Exp.*, vol. 19, no. 4, pp. 3175–3184, 2011.

[24] A. Rosenthal, V. Ntziachristos, and D. Razansky, "Model-based optoacoustic inversion with arbitrary-shape detectors," *Med. Phys.*, vol. 38, no. 7, pp. 4285–4295, 2011.

[25] K. Mitsuhashi, K. Wang, and M. A. Anastasio, "Investigation of the far-field approximation for modeling a transducer's spatial impulse response in photoacoustic computed tomography," *Photoacoustics*, vol. 2, no. 1, pp. 21–32, 2014.

[26] D. Queirós, X. L. Deán-Ben, A. Buehler, D. Razansky, A. Rosenthal, and V. Ntziachristos, "Modeling the shape of cylindrically focused transducers in three-dimensional optoacoustic tomography," *J. Biomed. Opt.*, vol. 18, no. 7, p. 076014, 2013.

[27] X. L. Deán-Ben, R. Ma, A. Rosenthal, V. Ntziachristos, and D. Razansky, "Weighted model-based optoacoustic reconstruction in acoustic scattering media," *Phys. Med. Biol.*, vol. 58, no. 16, p. 5555, 2013.
[28] C. Huang, L. Nie, R. W. Schoonover, L. V. Wang, and M. A. Anastasio, "Photoacoustic computed tomography correcting for heterogeneity and attenuation," *J. Biomed. Opt.*, vol. 17, no. 6, p. 0612111, 2012.
[29] B. Cox, J. G. Laufer, S. R. Arridge, and P. C. Beard, "Quantitative spectroscopic photoacoustic imaging: A review," *J. Biomed. Opt.*, vol. 17, no. 6, p. 0612021, 2012.
[30] S. L. Jacques, "Optical properties of biological tissues: A review," *Phys. Med. Biol.*, vol. 58, no. 11, p. R37, 2013.
[31] K. Wang, R. Su, A. A. Oraevsky, and M. A. Anastasio, "Investigation of iterative image reconstruction in three-dimensional optoacoustic tomography," *Phys. Med. Biol.*, vol. 57, no. 17, p. 5399, 2012.
[32] L. Ding, X. L. Deán-Ben, C. Lutzweiler, D. Razansky, and V. Ntziachristos, "Efficient non-negative constrained model-based inversion in optoacoustic tomography," *Phys. Med. Biol.*, vol. 60, no. 17, p. 6733, 2015.
[33] B. Cox, S. Kara, S. R. Arridge, and P. C. Beard, "k-space propagation models for acoustically heterogeneous media: Application to biomedical photoacoustics," *J. Acoust. Soc. Amer.*, vol. 121, no. 6, pp. 3453–3464, 2007.
[34] A. Buehler, A. Rosenthal, T. Jetzfellner, A. Dima, D. Razansky, and V. Ntziachristos, "Model-based optoacoustic inversions with incomplete projection data," *Med. Phys.*, vol. 38, no. 3, pp. 1694–1704, 2011.
[35] L. V. Wang and H.-I. Wu, *Biomedical Optics: Principles and Imaging*. Hoboken, NJ, USA: Wiley, 2012.
[36] C. C. Paige and M. A. Saunders, "LSQR: An algorithm for sparse linear equations and sparse least squares," *ACM Trans. Math. Softw.*, vol. 8, no. 1, pp. 43–71, Mar. 1982.
[37] R. Bro and S. De Jong, "A fast non-negativity-constrained least squares algorithm," *J. Chemometrics*, vol. 11, no. 5, pp. 393–401, 1997.
[38] D. M. Shcherbakova and V. V. Verkhusha, "Near-infrared fluorescent proteins for multicolor *in vivo* imaging," *Nature Methods*, vol. 10, no. 8, pp. 751–754, 2013.
[39] D. Razansky, A. Buehler, and V. Ntziachristos, "Volumetric real-time multispectral optoacoustic tomography of biomarkers," *Nature Protocols*, vol. 6, no. 8, pp. 1121–1129, 2011.
[40] G. S. Filonov, K. D. Piatkevich, L.-M. Ting, J. Zhang, K. Kim, and V. V. Verkhusha, "Bright and stable near-infrared fluorescent protein for *in vivo* imaging," *Nature Biotechnol.*, vol. 29, no. 8, pp. 757–761, 2011.
[41] R. N. Trivedi, X.-H. Wang, E. Jelezcova, E. M. Goellner, J.-B. Tang, and R. W. Sobol, "Human methyl purine dna glycosylase and dna polymerase β expression collectively predict sensitivity to temozolomide," *Molecular Pharmacol.*, vol. 74, no. 2, pp. 505–516, 2008.
[42] Q. Fang *et al.*, "HSP90 regulates DNA repair via the interaction between XRCC1 and DNA polymerase β," *Nature Commun.*, vol. 5, Oct. 2014, Art. no. 5513.
[43] J.-B. Tang *et al.*, "Bioenergetic metabolites regulate base excision repair–dependent cell death in response to DNA damage," *Molecular Cancer Res.*, vol. 8, no. 1, pp. 67–79, 2010.
[44] E. Fouquerel *et al.*, "ARTD1/PARP1 negatively regulates glycolysis by inhibiting hexokinase 1 independent of NAD^+ depletion," *Cell Rep.*, vol. 8, no. 6, pp. 1819–1831, 2014.
[45] X. L. Deán-Ben, N. C. Deliolanis, V. Ntziachristos, and D. Razansky, "Fast unmixing of multispectral optoacoustic data with vertex component analysis," *Opt. Lasers Eng.*, vol. 58, pp. 119–125, Jul. 2014.
[46] L. Scarfe *et al.*, "Measures of kidney function by minimally invasive techniques correlate with histological glomerular damage in SCID mice with adriamycin-induced nephropathy," *Sci. Rep.*, vol. 5, Jul. 2015, Art. no. 13601.
[47] S. Mandal, X. L. Deán-Ben, and D. Razansky, "Visual quality enhancement in optoacoustic tomography using active contour segmentation priors," *IEEE Trans. Med. Imag.*, vol. 35, no. 10, pp. 2209–2217, 2016.
[48] T. F. Chan and L. A. Vese, "Active contours without edges," *IEEE Trans. Image Process.*, vol. 10, no. 2, pp. 266–277, Feb. 2001.
[49] C. Lutzweiler and D. Razansky, "Optoacoustic imaging and tomography: Reconstruction approaches and outstanding challenges in image performance and quantification," *Sensors*, vol. 13, no. 6, pp. 7345–7384, 2013.
[50] A. Rosenthal, D. Razansky, and V. Ntziachristos, "Quantitative optoacoustic signal extraction using sparse signal representation," *IEEE Trans. Med. Imag.*, vol. 28, no. 12, pp. 1997–2006, Dec. 2009.
[51] X. L. Deán-Ben *et al.*, "Light fluence normalization in turbid tissues via temporally unmixed multispectral optoacoustic tomography," *Opt. Lett.*, vol. 40, no. 20, pp. 4691–4694, 2015.
[52] A. Q. Bauer, R. E. Nothdurft, T. N. Erpelding, L. V. Wang, and J. P. Culver, "Quantitative photoacoustic imaging: Correcting for heterogeneous light fluence distributions using diffuse optical tomography," *J. Biomed. Opt.*, vol. 16, no. 9, p. 096016, 2011.
[53] S. Tzoumas *et al.*, "Eigenspectra optoacoustic tomography achieves quantitative blood oxygenation imaging deep in tissues," *Nature Commun.*, vol. 7, Jun. 2016, Art. no. 12121.
[54] X. L. Deán-Ben and D. Razansky, "Portable spherical array probe for volumetric real-time optoacoustic imaging at centimeter-scale depths," *Opt. Exp.*, vol. 21, no. 23, pp. 28062–28071, 2013.

APPENDIX F. PUBLICATION: CONSTRAINED INVERSION AND SPECTRAL UNMIXING IN MULTISPECTRAL OPTOACOUSTIC TOMOGRAPHY

Appendix G

Publication: Dynamic Particle Enhancement in Limited-view Optoacoustic Tomography

X Luís Deán-Ben, **Lu Ding**, and Daniel Razansky. Dynamic particle enhancement in limited-view optoacoustic tomography. *Optics Letters*, 42(4):827–830, 2017

Reprinted with permission.

Optics Letters

Dynamic particle enhancement in limited-view optoacoustic tomography

X. Luís Deán-Ben,[1] Lu Ding,[1] and Daniel Razansky[1,2,*]

[1]Institute for Biological and Medical Imaging (IBMI), Helmholtz Zentrum München, Neuherberg, Germany
[2]School of Medicine, Technische Universität München (TUM), Munich, Germany
*Corresponding author: dr@tum.de

Received 27 September 2016; revised 5 December 2016; accepted 6 December 2016; posted 17 January 2017 (Doc. ID 276271); published 13 February 2017

Limited-view artifacts are commonly present in optoacoustic tomography images, mainly due to practical geometrical and physical constraints imposed by the imaging systems. Herein, a new approach called dynamic particle-enhanced optoacoustic tomography (DPOT) is proposed for improving image contrast and visibility of optoacoustic images under limited-view scenarios. The method is based on a nonlinear combination of a temporal sequence of tomographic reconstructions representing sparsely distributed moving particles. We demonstrate experimental performance by dynamically imaging the flow of suspended microspheres in three dimensions, which shows promise for DPOT applicability in angiographic imaging in living organisms.

OCIS codes: (110.5120) Photoacoustic imaging; (110.5125) Photoacoustics; (110.6880) Three-dimensional image acquisition.

https://doi.org/10.1364/OL.42.000827

Due to its hybrid nature combining optical excitation with ultrasonic detection, optoacoustic imaging is capable of visualizing optical absorption contrast in deep tissues with diffraction-limited ultrasonic resolution. Optoacoustic images are not affected by speckle-grain artifacts present in backscattering-based coherent imaging techniques, such as pulse-echo ultrasonography or optical coherence tomography, which may hamper the ability to resolve small image features and thus deteriorate the overall image quality. For the latter techniques, the speckle pattern is associated with the superposition of partial waves corresponding to randomly distributed subresolution scatterers causing phase shifts in the incident wave ranging from 0 to 2π [1,2]. In contrast, bipolar optoacoustic waveforms mainly accentuate the boundaries of absorbers in A-mode signals, where prominent edges are built up by constructive interference [3]. The inner part of the objects appear then invisible when reconstructions are done by stacking the A-mode optoacoustic signals into B-scan images using, e.g., the so-called delay-and-sum algorithms [4–6]. Much like in other tomographic imaging modalities, such as x-ray-computed tomography, the imaged object must be fully enclosed by tomographic measurement locations in order to be accurately reconstructed [7,8]. The so-called limited-view effects would then naturally appear in optoacoustic B-scan images or any tomographic reconstructions lacking full (>180°) angular coverage [9]. These effects become particularly prominent when reconstructing images from objects having elongated structures (e.g., blood vessels), oriented such that they predominantly emit pressure waves in directions that are not covered by detection elements.

The generated optoacoustic waves for a high density of individual absorbers are approximately the same as those generated by a continuous absorption distribution. However, the contribution of individual absorbers to the optoacoustic wavefront can be detected for a relatively sparse distribution [6]. Based on this principle, the visibility of structures affected by limited-view artifacts can be potentially enhanced by artificially creating small optoacoustic sources within those structures. One approach has used a superposition of multiple images acquired with varying speckled illumination patterns for optoacoustic excitation, where the individual speckle grains represented individual sources [10]. Even though this approach has been experimentally demonstrated in phantoms having a controlled speckle-grain size, its applicability for imaging real biological tissues remains challenging due to the need to optoacoustically resolve submicron speckle grains of the order of the excitation optical wavelength. A different technique consists of locally heating well-confined spots in the imaged tissue using focused ultrasound, thus thermally encoding the optoacoustic sources via the corresponding local variations of the Grüneisen parameter [11]. The multiple images can then be obtained by scanning the focused ultrasound beam in two or three dimensions, which is generally a lengthy process that may further involve hard compromises with respect to the safety thresholds of focused ultrasound. In any case, it is important to notice that the appropriate image enhancement and improved visibility of structures may only be achieved if the images taken at different time instants are combined in a nonlinear manner. A linear superposition operation would merely reduce noise in the images without providing direct benefit in terms of reducing the limited-view artifacts. Indeed, a linear combination of reconstructed images is equivalent to the reconstructed image obtained with the combined signals, which would be equivalent to

the signals for a dense distribution of optoacoustic sources and hence affected by limited-view effects.

In this work, we developed a new approach called dynamic particle-enhanced optoacoustic tomography (DPOT) to improve the visibility in limited-view optoacoustic imaging scenarios. It is based on imaging the dynamic distribution of sparsely located microparticles, which emit optoacoustic waves omnidirectionally. The size and average distance between the particles is adapted according to the spatial resolution of the imaging system so that the signals from individual particles can be distinguished. The highest possible concentration of particles fulfilling the latter criterion would naturally result in the best image quality for a given number of combined frames, with the absorbing structures filled with a dense granular speckle-like pattern for each individual frame.

An illustrative example of the typical case under study is shown in Fig. 1(a). It corresponds to a two-dimensional optoacoustic imaging system where signals are collected by an arc-shaped detection array covering a finite angle around the imaged object. In this limited-view scenario, any absorbing object elongated along the central axis of the detection array would predominantly emit optoacoustic waves propagating in directions not covered by the detection aperture, leading to an inefficient tomographic collection of signals and invisibility of major portions of the object. Conversely, if small absorbing particles are present within the object, they will emit spherical waves measurable at any detection angle, resulting in better visibility under limited-view conditions. Figure 1(b) shows an example of 100 small particles randomly distributed along a mask mimicking a vascular structure. Superposition of 100 random distributions of the 100 particles leads to the image displayed in Fig. 1(c). It is shown that by superimposing multiple particle distributions, an almost continuous image is rendered, where the shape of all vessels is clearly distinguishable.

In practice, the combination of limited-view images should not be done by a simple superposition of the optoacoustic

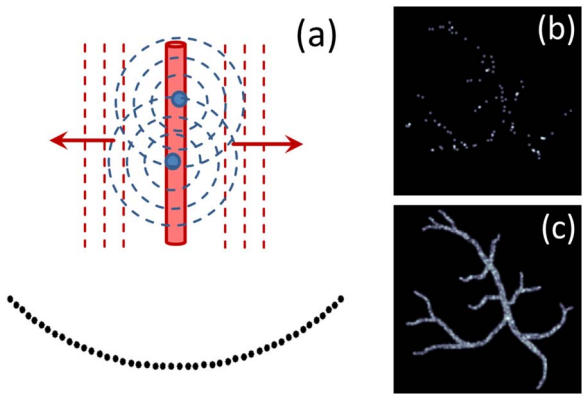

Fig. 1. (a) An example of the limited-view optoacoustic imaging scenario with an elongated absorbing object oriented along the central axis of an arc-shaped ultrasound detection array (labeled by black dots). The absorbing object would predominantly emit optoacoustic waves in the directions shown by the red dashed lines, leading to an inefficient tomographic collection of the generated responses. If small particles (large blue circles) are present within the object, they will emit waves in all directions. (b) An example of random distribution of 100 particles within a mask representing a vascular tree. (c) Superposition of 100 random distributions of 100 particles within the mask.

reconstructions obtained with a linear inversion algorithm. Even though all the particles may remain visible in the individual images, limited-view tomographic artifacts are usually manifested as negative shadows in the images, canceling out positive contributions in other images [6]. Thus, optimal visibility of structures can only be achieved with a proper nonlinear combination of images reconstructed from different random particle distributions. Here we achieved this by simply removing the negative absorption values from optoacoustic images using a nonnegative constrained model-based reconstruction algorithm [12]. Nonnegative constrained inversion is known to be a nonlinear procedure. In this way, the optical absorption in the region of interest for the ith particle distribution, expressed in a vector form $\mathbf{H}_i$, is estimated by solving the following least square problem:

$$\mathbf{H}_i = \text{argmin}_{\mathbf{H}\geq 0}\|\mathbf{p}_m - \mathbf{A}\mathbf{H}\|^2, \quad (1)$$

where $\mathbf{p}_m$ is a vector representing the measured signals, and $\mathbf{A}$ is the model matrix corresponding to the discretized linear optoacoustic forward model. The nonlinearity in the reconstruction is introduced with the nonnegative constraint $\mathbf{H} \geq 0$. The final image $\mathbf{H}$ of the object is then obtained by simple superposition of the nonnegative constrained images from multiple particle distributions, i.e.,

$$\mathbf{H} = \sum_i \mathbf{H}_i. \quad (2)$$

The performance of the suggested method was first tested in a numerical simulation corresponding to the acquisition geometry shown in Fig. 1(a). Specifically, 91 equally spaced measuring positions distributed along a 90° arc with a 40 mm radius were considered. The optical absorption coefficient distribution within the individual 150 μm radius particles was assumed to be parabolic, for which analytical signals can be analytically calculated [13]. Optoacoustic signals corresponding to 100 different random distributions of 100 particles were calculated. Prior to performing the reconstruction according to Eq. (1), the simulated signals were band-pass filtered between 0.25 and 5 MHz in order to further simulate the limited detection bandwidth of common ultrasound detectors. Figures 2(a)–2(c) show exemplary images reconstructed from three different random particle distributions. The center of the displayed images corresponds to the center of the arc array, which is located below. The image obtained by combining all the 100 reconstructions is shown in Fig. 2(d). For comparison, the same vascular mask was represented instead by a uniform optical absorption distribution. Image reconstruction was similarly performed with Eq. (1) after downsampling and filtering the signals obtained with the forward model represented by matrix $\mathbf{A}$. The resulting image is displayed in Fig. 2(e), showing reduced visibility of vertically oriented structures as compared to the image enhanced with DPOT.

The performance of DPOT was experimentally tested using our recently developed real-time three-dimensional optoacoustic imaging platform, which allows for three-dimensional image acquisition at 100 volumes per second rates [14]. The imaging system consists of a spherical array of piezocomposite elements covering an angle of 90° around the imaged object. The spherical detection aperture has a radius of 40 mm and contains 256 individual detection elements, which are simultaneously sampled at 40 megasamples per second by a custom-made digital acquisition system. While this three-dimensional tomographic configuration substantially improves optoacoustic

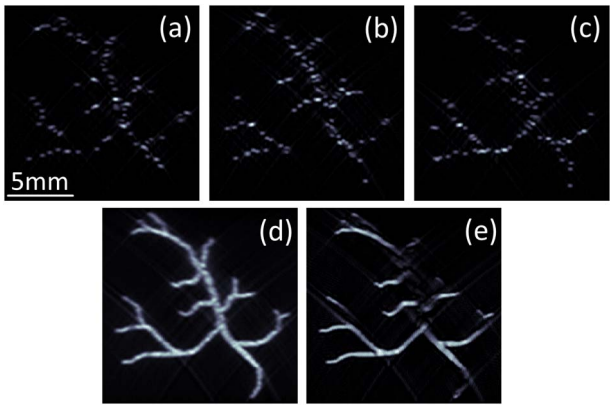

Fig. 2. Numerical simulation of model-based optoacoustic image reconstructions in a limited-view detection scenario. (a)–(c) Nonnegative constrained reconstructions obtained from three different random distributions of microparticle absorbers within a vascular structure. (d) Superposition of images of 100 different distributions of the particles rendered with nonnegative constrained reconstruction. (e) Nonnegative constrained reconstruction rendered for the same vascular mask represented by a uniform optical absorption distribution.

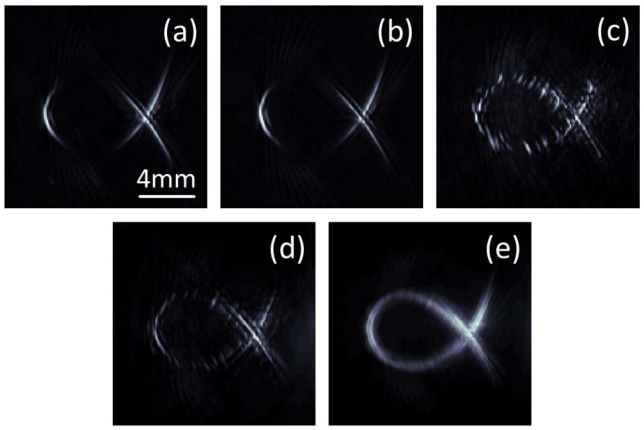

Fig. 3. Experimental validation of DPOT. The lateral maximum intensity projections of the three dimensional images are shown. (a) Unconstrained model-based reconstruction of the tubing filled with ink (optical density 20). (b) Unconstrained model-based reconstruction of the tubing filled with ink (optical density 2) with suspended 20 μm diameter polyethylene microspheres. (c) Unconstrained model-based reconstruction obtained with the same signals as (b) after substracting the reference signals. (d) Image obtained by superimposing 550 unconstrained reconstructions. (d) Image obtained by superimposing 550 nonnegative constrained reconstructions. Image formation results by superposition of an increasing number of frames obtained with constrained and unconstrained reconstruction are shown in Visualization 1. Three dimensional views of the images are shown in Visualization 2.

imaging performance with respect to systems making use of linear or planar arrays, limited-view effects still affect the images due to the 90° coverage of the spherical array geometry.

In our experiments, we relied on the powerful capacity of the imaging system for high-speed visualization of flowing particles in 3D. The experimental phantom consisted of a 20 μl Eppendorf microloader pipette tip (≈220 μm inner diameter) bent in a loop and placed in the field of view of the spherical detection array. A 10 mm diameter approximately Gaussian beam from a pulsed laser (Innolas Laser GmbH), tuned to a 720 nm wavelength and a 10 Hz pulse repetition frequency, was employed to illuminate the phantom. Figure 3(a) shows the lateral maximum intensity projection (MIP) of the reconstructed three-dimensional optoacoustic image acquired with the tubing filled with black India ink (Higgins, Chartpak, Inc., optical density 20). The array is located on the left-hand side of the displayed image. The reconstruction was done with the unconstrained model-based algorithm. As can be clearly seen, the lateral sides of the loop are invisible in this image in spite of the high light absorption of ink. Figure 3(b) displays the same MIP for the tubing filled with randomly distributed 20 μm diameter polyethylene microspheres (Cospheric BKPMS 20-27) suspended in ethanol. India ink was also added to mimic blood absorption in the near infrared (optical density 2). The lateral sides of the tubing remain invisible in this case. The suspended particles are also not distinguished in the image. However, the particles become clearly visible when applying the reconstruction algorithm to the difference of the acquired signals with respect to the reference signals corresponding to the average for all frames. The lateral MIP of the image reconstructed with unconstrained model-based inversion by considering the differential signals is shown in Fig. 3(c). The sparsely distributed particles lead to a granular (speckle-like) pattern in the image that allows one to infer the basic shape of the loop. The presence of background absorption does not represent a problem as long as (1) there is no motion of the sample and (2) the dynamic range for ultrasound detection is sufficient to cover both the strong background signals and the weak signals generated by individual particles. Figures 3(d) and 3(e) show the superposition of 550 different microsphere distributions being reconstructed with unconstrained and nonnegative constrained model-based inversion, respectively. Each frame was reconstructed from the difference of the acquired signals with respect to the reference signals. In the unconstrained case, the linear superposition of images results in reduced visibility of the same areas as in Fig. 3(a). Indeed, the superposition of images obtained with a linear reconstruction algorithm is equivalent to the reconstructed image for the superimposed signals, which ultimately would be equivalent to that of a continuous absorption distribution, i.e., it is affected by limited-view artifacts. In contrast, visibility of the loop is significantly enhanced by superimposing the images reconstructed with nonnegative constrained inversion [Fig. 3(e)]. The tubing volume is also more clearly defined than in the images obtained with the tubing filled with ink, where the boundaries are enhanced due to limited-view effects. The process of building up an image by superimposing the first 50 frames resconstructed with unconstrained or constrained model-based inversion is better illustrated in a movie available in the online version of the journal (Visualization 1). Three-dimensional rotating views of the resulting images along with the image for the tubing filled with ink are also provided in a second movie (Visualization 2).

The presented results open up new possibilities for optoacoustic imaging of areas not fully accessible with >180° tomographic angular coverage. This is of vast importance for clinical translation of optoacoustic imaging, where measurements can only be performed with very limited tomographic coverage of the imaged area [15,16]. *In vivo* imaging with full angular coverage is often hampered by additional practical factors, such as

the mechanical and geometrical constrains [17] or the need to immerse the living organism into a coupling medium [18]. Efficient performance of the suggested method in real *in vivo* imaging scenarios would imply the use of properly designed biocompatible particles providing a sufficient optoacoustic response to be detectable individually in the presence of strong background signals generated by optical absorption in hemoglobin and other endogenous chromophores. Such particles may serve additional purposes, e.g., provide an efficient optoacoustic feedback to control light intensity distribution through scattering samples [19]. The signals of individual absorbers can also be used to estimate the flow velocity with Doppler optoacoustic methods [20–22], which can also be done with the methodology described here when tracking individual particles in a sequence of time-lapse images. Furthermore, localization of individual particles may further enhance the resolution in optoacoustic tomographic imaging [23].

Future steps must be directed toward improving the spatiotemporal resolution of the optoacoustic imaging system used for DPOT. In principle, the spatial resolution is not modified with DPOT, although the images may be blurred due to motion between subsequent acquisitions. On the other hand, the effective temporal resolution of DPOT is reduced due to the need to acquire and combine multiple images. It has been shown that the combination of approximately 50 images is sufficient for a good performance (Visualization 1), and this number can be further reduced for a denser distribution of particles. Good spatial resolution is essential to efficiently image dense distributions of small particles. Thus, the development of a higher resolution imaging system is an important next step. The sensitivity of the optoacoustic system is also an important issue to consider along with the development of efficient particles for DPOT. Indeed, the number of acquisitions required for a good performance of the method is further determined by the signal-to-noise ratio of the individual images. The sensitivity can be potentially increased by unmixing spectrally distinct particles using multispectral image acquisitions [24] or photoswitchable substances generating specific temporal profiles [25], for which a very short delay between laser pulses would be necessary in order to avoid motion artifacts [26]. Ideally, a system with sufficient resolution and sensitivity to distinguish individual cells would be desirable, as it can potentially enable translating the DPOT method into a setting with only endogenous tissue contrast present.

In conclusion, DPOT allows one to improve the visibility of structures affected by limited-view tomographic acquisition artifacts. It thus holds promise for improving accuracy of deep-tissue angiographic imaging provided that the system has sufficient sensitivity to detect signals from individual particles. As limited-view effects are unavoidable in most realistic optoacoustic imaging scenarios, DPOT is expected to play an important role in improving the optoacoustic image quality.

Funding. European Research Council (ERC) (ERC-2010-StG-260991).

REFERENCES

1. J. W. Goodman, *Speckle Phenomena in Optics: Theory and Applications* (Roberts & Company, 2007).
2. T. L. Szabo, *Diagnostic Ultrasound Imaging: Inside Out* (Academic, 2004).
3. Z. Guo, L. Li, and L. V. Wang, Med. Phys. **36**, 4084 (2009).
4. M.-L. Li, H. F. Zhang, K. Maslov, G. Stoica, and L. V. Wang, Opt. Lett. **31**, 474 (2006).
5. J. Turner, H. Estrada, M. Kneipp, and D. Razansky, Opt. Lett. **39**, 3390 (2014).
6. X. L. Deán-Ben and D. Razansky, Photoacoustics **4**, 133 (2016).
7. Y. Xu, L. V. Wang, G. Ambartsoumian, and P. Kuchment, Med. Phys. **31**, 724 (2004).
8. G. Paltauf, R. Nuster, M. Haltmeier, and P. Burgholzer, Inverse Probl. **23**, S81 (2007).
9. A. Buehler, A. Rosenthal, T. Jetzfellner, A. Dima, D. Razansky, and V. Ntziachristos, Med. Phys. **38**, 1694 (2011).
10. J. Gateau, T. Chaigne, O. Katz, S. Gigan, and E. Bossy, Opt. Lett. **38**, 5188 (2013).
11. L. Wang, G. Li, J. Xia, and L. V. Wang, Optica **2**, 307 (2015).
12. L. Ding, X. L. Deán-Ben, C. Lutzweiler, D. Razansky, and V. Ntziachristos, Phys. Med. Biol. **60**, 6733 (2015).
13. A. Rosenthal, D. Razansky, and V. Ntziachristos, IEEE Trans. Med. Imaging **29**, 1275 (2010).
14. X. L. Deán-Ben, S. J. Ford, and D. Razansky, Sci. Rep. **5**, 10133 (2015).
15. G. A. Pang, E. Bay, X. L. Deán-Ben, and D. Razansky, J. Cardiovasc. Electrophysiol. **26**, 339 (2015).
16. T. F. Fehm, X. L. Deán-Ben, P. Schaur, R. Sroka, and D. Razansky, J. Biophoton. **9**, 934 (2015).
17. L. V. Wang and J. Yao, Nat. Methods **13**, 627 (2016).
18. X. L. Deán-Ben, G. A. Pang, F. M. de Espinosa, and D. Razansky, Appl. Phys. Lett. **107**, 051105 (2015).
19. X. L. Deán-Ben, A. C. Stiel, Y. Jiang, V. Ntziachristos, G. G. Westmeyer, and D. Razansky, Opt. Lett. **40**, 4691 (2015).
20. H. Fang, K. Maslov, and L. V. Wang, Phys. Rev. Lett. **99**, 184501 (2007).
21. J. Yao, K. I. Maslov, Y. Shi, L. A. Taber, and L. V. Wang, Opt. Lett. **35**, 1419 (2010).
22. J. Brunker and P. Beard, J. Acoust. Soc. Am. **132**, 1780 (2012).
23. C. Errico, J. Pierre, S. Pezet, Y. Desailly, Z. Lenkei, O. Couture, and M. Tanter, Nature **527**, 499 (2015).
24. S. Tzoumas, A. Nunes, N. C. Deliolanis, and V. Ntziachristos, J. Biophoton. **8**, 629 (2015).
25. A. C. Stiel, X. L. Deán-Ben, Y. Jiang, V. Ntziachristos, D. Razansky, and G. G. Westmeyer, Opt. Lett. **40**, 367 (2015).
26. X. L. Deán-Ben, E. Bay, and D. Razansky, Sci. Rep. **4**, 5878 (2014).

Appendix H

Publication: Noninvasive Anatomical and Functional Imaging of Orthotopic Glioblastoma Development and Therapy using Multispectral Optoacoustic Tomography

Ghayathri Balasundaram, **Lu Ding**, Xiuting Li, Amalina Binte Ebrahim Attia, Xose Luis Dean-Ben, Chris Jun Hui Ho, Prashant Chandrasekharan, Hui Chien Tay, Hann Qian Lim, Chee Bing Ong, Ralph P. Mason, Daniel Razansky, and Malini Olivo. Noninvasive anatomical and functional imaging of orthotopic glioblastoma development and therapy using multispectral optoacoustic tomography. *Translational Oncology*, 11(5):1251–1258, 2018 https://doi.org/10.1016/j.tranon.2018.07.001

Reprinted with permission.

Translational Oncology
www.transonc.com

Volume 11 Number 5 October 2018 pp. 1251–1258 1251

Noninvasive Anatomical and Functional Imaging of Orthotopic Glioblastoma Development and Therapy using Multispectral Optoacoustic Tomography

Ghayathri Balasundaram[*,1], Lu Ding[†,1], Xiuting Li[*,1], Amalina Binte Ebrahim Attia[*,1], Xose Luis Dean-Ben[†,1], Chris Jun Hui Ho[*], Prashant Chandrasekharan[*], Hui Chien Tay[*], Hann Qian Lim[*], Chee Bing Ong[‡], Ralph P. Mason[§], Daniel Razansky[†] and Malini Olivo[*]

[*]Laboratory of Bio-optical Imaging, Singapore Bioimaging Consortium, Agency for Science Technology and Research (A*STAR), 11 Biopolis Way, #02-02 Helios, Singapore 138667; [†]Institute for Biological and Medical Imaging, Technical University of Munich and Helmholtz Center Munich, Munich, Germany; [‡]Advanced Molecular Pathology Lab (AMPL), Institute of Molecular and Cell Biology (IMCB), Agency for Science, Technology and Research (A*STAR), 61 Biopolis Drive, Proteos building, Singapore 138673; [§]Department of Radiology, University of Texas Southwestern Medical Center, Dallas, TX 75390, USA

Abstract

PURPOSE: Here we demonstrate the potential of multispectral optoacoustic tomography (MSOT), a new non-invasive structural and functional imaging modality, to track the growth and changes in blood oxygen saturation (sO_2) in orthotopic glioblastoma (GBMs) and the surrounding brain tissues upon administration of a vascular disruptive agent (VDA). *METHODS:* Nude mice injected with U87MG tumor cells were longitudinally monitored for the development of orthotopic GBMs up to 15 days and observed for changes in sO_2 upon administration of combretastatin A4 phosphate (CA4P, 30 mg/kg), an FDA approved VDA for treating solid tumors. We employed a newly-developed non-negative constrained approach for combined MSOT image reconstruction and unmixing in order to quantitatively map sO_2 in whole mouse brains. *RESULTS:* Upon longitudinal monitoring, tumors could be detected in mouse brains using single-wavelength data as early as 6 days post tumor cell inoculation. Fifteen days post-inoculation, tumors had higher sO_2 of 63 ± 11% ($n = 5$, $P < .05$) against 48 ± 7% in the corresponding contralateral brain, indicating their hyperoxic status. In a different set of animals, 42 days post-inoculation, tumors had lower sO_2 of 42 ± 5% against 49 ± 4% ($n = 3$, $P < .05$) in the contralateral side, indicating their hypoxic status. Upon CA4P administration, sO_2 in 15 days post-inoculation tumors dropped from 61 ± 9% to 36 ± 1% ($n = 4$, $P < .01$) within one hour, then reverted to pre CA4P treatment values (63 ± 6%) and remained constant until the last observation time point of 6 hours. *CONCLUSION:* With the help of advanced post processing algorithms, MSOT was capable of monitoring the tumor growth and assessing hemodynamic changes upon administration of VDAs in orthotopic GBMs.

Translational Oncology (2018) 11, 1251–1258

Address all correspondence to: Daniel Razansky or Malini Olivo.
E-mail: dr@tum.de, malini_olivo@sbic.a-star.edu.sg
[1] Equal contributors.
Received 11 April 2018; Revised 26 June 2018; Accepted 2 July 2018

1936-5233/18
https://doi.org/10.1016/j.tranon.2018.07.001

Introduction

Optoacoustic tomography (OT) is emerging as an indispensable tool, both preclinically and clinically, to non-invasively visualize hemoglobin concentration and oxygenation. Its capacity to visualize anatomical structures and distinguish between different endogenous chromophores, including oxy and deoxy-hemoglobin, based on their distinct absorption spectra, with both high spatial and temporal resolution at centimeter-scale depths in living tissues [1,2], opens new avenues for studying many oxygenation-related pathologies [3–11]. In preclinical studies, OT has been chiefly employed for visualization of morphology and oxygenation status of tumor xenografts in order to unveil the link between poor oxygenation and therapeutic outcomes. Static OT readouts from subcutaneous tumors offered insights into the vessel developments in tumor [12,13], visualize the hemodynamic changes in response to vascular disrupting therapeutic agents [8,14] and predict therapeutic response [15] and recurrence [16]. In addition, dynamic OT readouts facilitated the acquisition of vascular information to understand spatial heterogeneity and evolution, which could ultimately serve for cancer diagnosis and staging [7]. However, subcutaneous tumor models are often not capable of simulating the cancer environment as good as their orthotopic counterparts [17–19], thus questioning their utility as essential systems in studying tumor biology or identifying therapeutic agents. Anatomical and functional OT imaging of orthotopic tumors may therefore help with better simulating human malignancies and understanding their microenvironment.

Previously, we have demonstrated the utility of Multispectral Optoacoustic Tomography (MSOT) to investigate orthotopic brain tumors using exogenous contrast agent [20]. Burton et al. [2] and Ni et al. [21] have investigated the utility MSOT for identifying hypoxic areas in mouse brain. In the current study, we investigated the performance of MSOT method in identifying tumors from the midst of brain tissues and understand their vascular dynamics upon administration of combretastatin A4 phosphate (CA4P), an FDA approved vascular disruptive agent for treating solid tumors. For this, an orthotopic U87MG glioma model was employed, which has been extensively used in preclinical studies to identify therapeutic agents [22,23] and whose molecular profile is known to simulate a subclass of human glioblastoma [24]. Additionally, in order to quantitatively map sO_2 in whole mouse brains, we employed a newly-developed non-negative constrained approach for combined MSOT image reconstruction and unmixing [25], the advantage of which compared to state-of-the-art back projection methods being reduced critical image artifacts, thus maximizing the available information. Specifically, the objectives of this study have been to investigate the MSOT performance in identifying orthotopic gliomas based on single wavelength information, evaluate their growth over time, visualize sO_2 in the tumor versus the rest of the brain and investigate hemodynamic changes upon administration of a vascular disruptive agent.

Materials and Methods

Animal Model and Procedures

All animals were housed in Biological Resource Centre, which is an Association for Assessment and Accreditation of Laboratory Animal Care (AAALAC)-accredited facility. All procedures performed on animal models were carried out under guidelines of Institutional Animal Care and Use Committee (IACUC) as approved in the protocol #140898 and #151085. The orthotopic tumor model was created by stereotaxic injection of U87MG cells into the brains of female NCr nude mice (age: 6–7 weeks old). In brief, $5–6 \times 10^6$ cells/mL were prepared in sterile 1× PBS. The animal was anesthetized under 2–3% isoflurane. The head was fixed to a digital stereotaxic system (Stoelting Co.) and a burr hole was made on the skull using a 23G sterile needle at 2 mm behind bregma, 1.5 mm to the right from the midline. A 10 µl NANOFIL syringe (World Precision Instruments, Inc.) pre-filled with cells was prepared and the needle was inserted 3 mm into the brain parenchyma through the burr whole. Five µl volume of cells was injected at a rate of 1 µl/min using an infusion pump (KD Scientific Inc.). After injection, the needle was removed, the burr hole was covered with bone wax, and the incision sutured with poly-lysine thread. The animals were given analgesics (Buprenorphine) and antibiotics (Enrofloxacin) over 5 days post-surgery. Tumor growth was monitored up to 15 days using MSOT. Vascular perturbation study was done by injecting 30 mg/kg of Fosbretabulin (CA4P, SelleckChem) intravenously.

Animal Preparation for Imaging

All animals were imaged under 2–3% isoflurane using medical air. For MSOT imaging of the brain, the animal was placed in supine position in a holder. Coupling gel was applied to the region of interest. The animal was wrapped in a thin polyethylene membrane and introduced into the water chamber (maintained at 34 °C) for imaging. Throughout the imaging session, all animals were maintained at a respiration rate of 70 to 90 breaths per minute by manually adjusting the isoflurane.

MSOT Imaging

MSOT imaging was performed using the inVision 512 small-animal MSOT system (iThera Medical GmbH, Munich, Germany). The system consists of a 512-element concave transducer array with a central frequency of 5 MHz spanning a circular arc of 270° to detect optoacoustic signals. Light excitation was provided with a tunable (700–900 nm) optical parametric oscillator (OPO) laser guided via a fiber bundle to the sample. The transducer array and fiber bundle output arms were submerged in a water bath maintained at 34°C. The animal was moved through the transducer array along its axis to acquire information as transverse image slices across the desired volume of interest (VOI). For data acquisition, a VOI of multiple transverse slices was set up with a step size of 0.5 mm and the acquired optoacoustic signals were averaged over 10 consecutive laser pulses for each recorded wavelength (715, 730, 760, 800, and 850 nm).

Image Processing and Data Analysis

In order to facilitate quantitative data analysis and avoid negative value artifacts commonly present in optoacoustic images reconstructed with back projection algorithms [26], we employed a combined model-based reconstruction and unmixing framework incorporating non-negative constrained inversion [25]. Basically, the method is based on the discretization of the optoacoustic forward model to build a linear set of equations, associated to a model-matrix, that represent the recorded pressure values at different locations and different wavelengths. The reconstruction-unmixing process is based on the least square minimization of the measured signals and those predicted by the model, where a non-negative constrain is imposed to avoid the appearance of negative values in the chromophore(s) of interest. Total hemoglobin (HbT) distribution was then calculated by adding the unmixed oxy- and deoxy-hemoglobin values and the sO_2 fraction was

calculated by dividing the unmixed oxy-hemoglobin values with HbT. For comparison, the images were also reconstructed using the default back projection based algorithm followed by spectral unmixing using linear regression algorithm [27,28], both available as a part of the data analysis software of the scanner.

In order to demonstrate the ability of MSOT to identify the anatomical location of tumors from the midst of normal brain tissue, difference in the reconstructed single wavelength images at 850 and 800 nm ($Diff_{850–800nm}$) was computed using Image J. Tumors appeared as hyperintense signals on the right cortex, the dimensions of which were measured manually on Image J at the largest cross section of the tumor. Tumor volume was estimated as 1/2(Length × $Width^2$).

MR Imaging and Data Analysis

Magnetic resonance imaging was carried out on a 7 Tesla MRI (ClinScan, Bruker Bio Spin GmbH) with a 72 mm volume transmit/receive coil along with a mouse brain array coil (Rx). After localizing the brain at the isocentre of the magnet, anatomy of the growing tumor was observed using a T2 weighted turbo-spin echo sequence. The MRI imaging was performed with TR/TE = 4050/33 ms. Refocusing pulse FA = 180°; in-plane resolution of 70×70 μm, 0.5 mm transverse slice thickness, 32 slices, 2 averages per slice. The tumor volume was manually segmented and measured from the hyper-intense lesion using ImageJ.

Histology

Brain tissues were harvested after euthanizing mice by cervical dislocation and fixed using 10% neutral buffered formalin (Sigma). Fixed tissues were embedded in paraffin blocks and sectioned into slices of 5 μm thickness. Consecutive sections of the brain were subjected to hematoxylin and eosin (H&E) staining for evaluation of tumor morphology and cellularity, and to bright field immunohistochemistry for markers of vascularity – CD34 (EP373Y, Abcam) and hypoxia - Carbonic anhydase IX (CAIX) enzyme (NB100–417, Novus Biologicals). After deparrafinizing and dehydrating, heat-induced epitope retrieval was performed using Bond™ Epitope Retrieval Solution (pH 9.6) for 40 min at 100°C. Slides were then incubated with the primary antibody followed by secondary antibody (goat anti-rat HRP, Invitrogen, Carlsbad, CA; 1:50) for 30 min. Bond™ Mixed DAB Refine was applied for 5 min, and rinsed with deionized water to stop the DAB reaction and counter stained with hematoxylin. Slides were finally dehydrated and mounted in synthetic mounting media. Bright field images of slides were taken using Nikon NiE: Ri2 microscope with DS-Ri2 camera using NIS elements 4.5 software. Tissue sections stained for H&E and CD34 were analyzed by board-certified pathologist. % areas of sections positively stained for CAIX were analyzed using Image J.

Statistical Analysis

Region of interest (ROI)-was drawn manually using ImageJ around the tumors versus healthy brain tissue from the contralateral side on the sO_2 fraction maps to derive the sO_2 fraction values. All data are reported as mean ± standard deviation (SD). Graphs were plotted using Graph Pad PRISM® 7.01. Paired t-test was used to assess the significance of difference in sO_2 fraction values obtained using MSOT between tumor and contralateral side across the animals. One way ANOVA test with Bonferroni's multiple comparison test was used to assess the significance of sO_2 changes upon CA4P administration across different time points for tumor and contralateral side. Unpaired t-test was used for assessing the significance of difference in CAIX (hypoxia marker) stained areas across different time points post CA4P administration. Data was considered significant with $P < 0.05$.

Results

Anatomical Imaging of Orthotopic Glioblastoma Using MSOT

Three nCr nude mice with orthotopic U87 glioblastoma on the right cortex were used to examine the performance of MSOT to track the tumor growth and development. Strong optoacoustic signals were seen clearly in major blood vessels, such as superior sagittal sinus (SSS, 1), middle cerebral artery (MCA, 2), superficial temporal arteries (TA, 3) and posterior communicating artery (PCA, 4) in the brain cross-sectional image at bregma +2 mm recorded at a wavelength of 800 nm (Figure 1*A*), the isosbestic point of hemoglobin absorption in the NIR region. Apart from the major blood vessels, strong optoacoustic signals could be seen from the cortex, in particular the right cortex and altered symmetry in right MCA (red arrow) suggesting the presence of tumor. The difference between the single-wavelength optoacoustic images acquired at 850 and 800 nm (($Diff_{850–800\ nm}$) clearly revealed the tumor location (Figure 1*B*). Interestingly, the shape of the hyperintense signals was similar to shape of the tumor observed on MRI anatomy scan (Figure 1*C*). Moreover, the tumor dimensions measured by MSOT across the largest cross section were similar to those measured by the T2-weighted MRI anatomical images (Figure S1). The same strategy was applied to images acquired pre and 3, 6 and 11 days post tumor cell inoculation (Figure S2) to track the tumor growth and calculate the increase in the tumor volume (Figure 1*D*).

Functional Imaging of Orthotopic Glioblastoma Using MSOT

As oxy- and deoxy-hemoglobin are characterized by unique absorption spectra in the NIR region, MSOT can distinguish between the different oxygenation states in blood, allowing for reconstructing the maps of sO_2 in the brain. However, it could be readily recognized that large areas of the brain are missing information when estimating the sO_2 values with the standard back-projection reconstruction method and setting negative image values to zero (Figure 2*B*). In contrary, the non-negative constrained reconstruction and unmixing method was able to render reasonable sO_2 values in the entire brain (Figure 2*C*). Maps of single wavelength optoacoustic image at 800 nm, oxy-, deoxy-hemoglobin and sO_2 obtained by non-negative constrained reconstruction and unmixing method for a representative animal are provided in Figure S3. The tumor mass (15 days post-inoculation, n = 5), was observed to have higher sO_2 of 63 ± 11% as compared with 48 ± 7% ($P < 0.05$, paired *t*-test) in the corresponding contralateral side (Figure 2*D*) indicating their hyperoxic status. In older tumors (42 days post-inoculation, n = 3), the sO_2 was 42 ± 5% against 49 ± 4% ($P < 0.05$, paired t-test) in the contralateral side, indicating their hypoxic status (Figure 2*H*).

In order to validate the sO_2 values of the tumors observed with MSOT, histological analysis was performed on tumors at two time points. The higher sO_2 in tumors 15 days post-inoculation could be attributed to the presence of rapidly dividing (indicated by increased number of mitotic cells, Figure 3*A*) poorly differentiated neoplastic cells forming neovasculature to draw sufficient nutrients and oxygen to support their growth. This is further corroborated by the higher

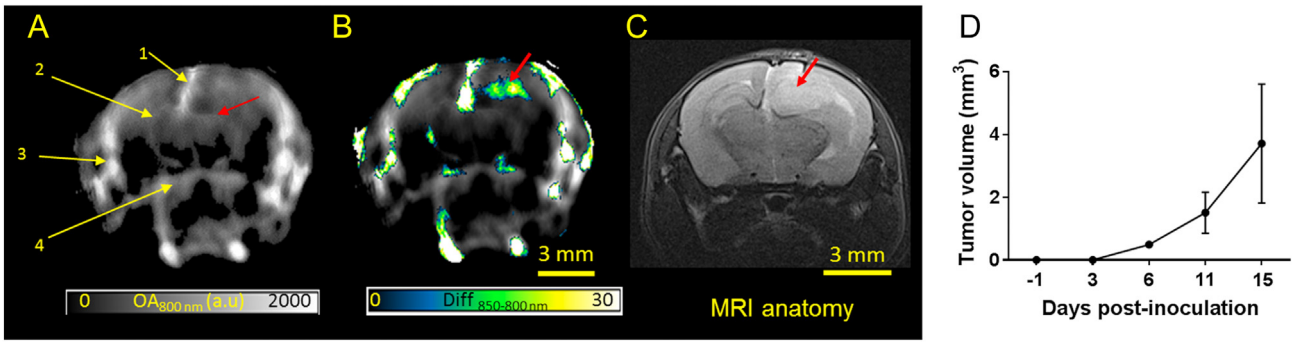

Figure 1. Anatomical imaging of orthotopic glioblastoma in mice using MSOT. (A) In vivo single wavelength (800 nm) optoacoustic image depicting the anatomy of an intact mouse brain with U87MG glioblastoma. The slice is at bregma +2 mm. Brain structures such as superior sagittal sinus (SSS, 1), middle cerebral artery (MCA, 2), superficial temporal arteries (TA, 3) and posterior communicating artery (PCA, 4) and altered symmetry at the right MCA (red arrow) are visible. (B) Difference of the optoacoustic images acquired at 850 and 800 nm, highlighting the tumor location and shape (red arrow). (C) T2 weighted MRI anatomy image of the corresponding brain slice with the hyperintense lesion (red arrow) representing the tumor. (D) Graph showing increase in tumor volume across different days post tumor inoculation calculated using the difference in OA signals at 850 and 800 nm (n = 3).

degree of vascularity (measured by the number of blood vessels per unit field of view), as indicated by CD34 stain (Figure 3, *B* and *G*), and smaller fraction of the tumor positively stained for CAIX (Figure 3, *C* and *H*). The lower sO_2 in tumors 42 days post inoculation could be attributed to well differentiated neoplastic cells with fewer mitotic cells indicating a slack in their growth and spread (Figure 3*D*). Lesser degree of vascularity as indicated by CD34 staining (Figure 3, *E* and *G*) compared to tumors that were 15 day post inoculation and increased fraction of CAIX stained tumor areas (Figure 3, *F* and *H*) corroborate the values observed using MSOT.

MSOT Tracks Hemodynamic Changes in Tumor Upon Administration of Therapeutic Agent

To investigate the utility of MSOT for tracking hemodynamic changes as a part of treatment monitoring, we administered 30 mg/kg of combretastatin A4 phosphate (CA4P), a vascular disruptive agent into 4 animals with tumors that were 15 days post-inoculation. CA4P binds to tubulin and affects the cytoskeleton and morphology of endothelial cells resulting in increased vascular permeability to macromolecules resulting in increased interstitial pressure and thus, shutdown of blood flow [29,30]. Dynamic changes in sO_2 post CA4P

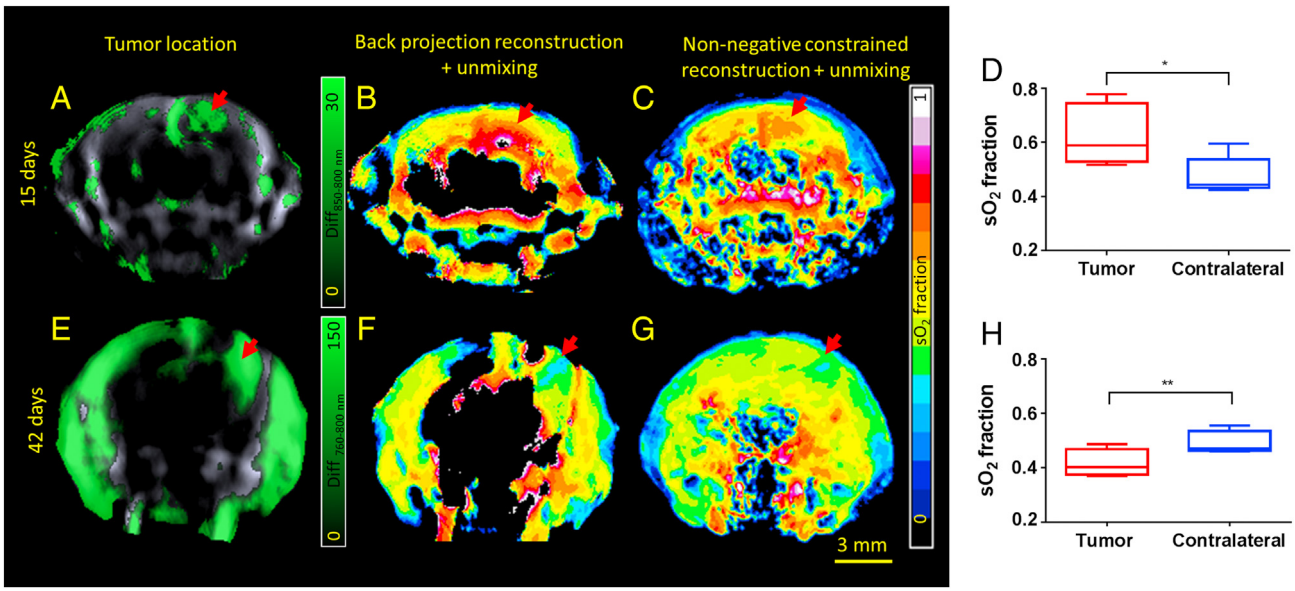

Figure 2. Functional Imaging of Orthotopic Glioblastoma. Panels A & E show the location of the tumor in a representative animal 15 and 42 days post inoculation respectively. Panels B & F show the sO_2 fraction map after reconstruction using back-projection and unmixing using linear regression of the corresponding animals. Panels C and G denote the sO_2 fraction map after combined non-negative constrained reconstruction and unmixing in the corresponding animals. Panels D and H show the sO_2 values in the tumor and the contralateral side of the brain in animals 15 (n = 5) and 42 (n = 3) day post inoculation. sO_2 values between the tumor and contralateral side were found to be statistically significantly different using paired t-test. * - $P < 0.05$; ** - $P < 0.01$.

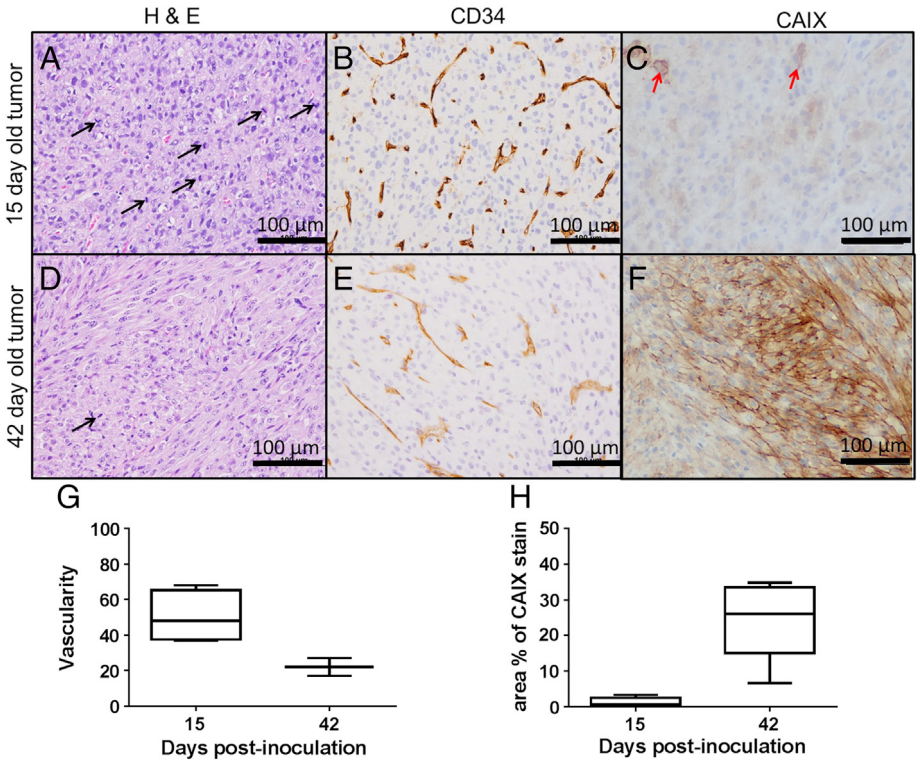

Figure 3. Histological validation of sO_2 values observed on MSOT. Panels A & D show mitotic cells (black arrow) in the histological sections of H&E stained tumors 15 and 42 days post inoculation. Panels B & E show corresponding tissue sections of tumors stained for CD34, a marker for neovasculature and panels C and F, areas stained for CAIX (a marker for hypoxia). Panels G and H shows the quantification of CD34 and CAIX stains respectively in tumors 15 and 42 days post inoculation. Red arrow indicates hypoxic cells.

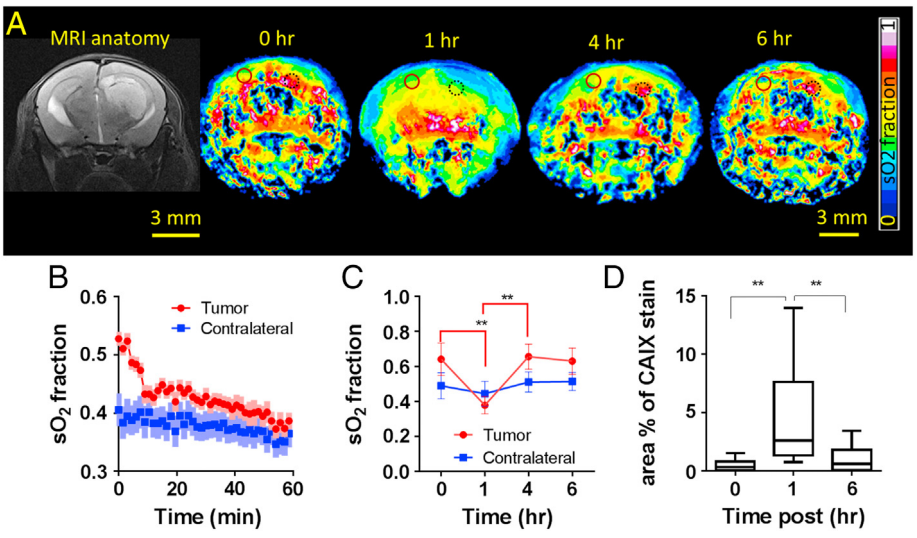

Figure 4. Real-time hemodynamic changes in the tumor upon administration of CA4P. Panel A shows the MRI anatomical reference of the tumor, followed by sO_2 maps of a slice of brain showing the largest cross section of the tumor at time points 0, 1, 4 and 6 h. post CA4P administration. Panel B shows the real-time sO_2 changes in the tumor and contralateral brain occurring immediately post CA4P administration over 1 hour in a representative animal. SD is represented by lighter shades on the graph. Panel C shows the real-time sO_2 changes in the tumor and contralateral brain occurring immediately post CA4P administration (n = 4). Panel D shows the quantification of hypoxia in tumors using CAIX as a marker at times 0 (n = 3), 1 (n = 4) and 6 h. (n = 3) post CA4P administration. Unpaired t-test showed statistically significant difference in CAIX staining at 1 hour post CA4P administration compared to 0 and 6 hours. ** - $P > 0.01$. Black dotted circle and Red full circle denote the ROIs drawn at the tumor and contralateral brain respectively to compute the sO_2.

administration is demonstrated in Figure 4*A*. Immediately after CA4P administration, the sO_2 dropped sharply from 61 ± 9% within the first ten minutes and gradually after that to reach 36 ± 1% ($P < .01$) at the end of 1 hour (4B and 4C). This drop was attributed by rapid decrease in oxy-hemoglobin levels and increase in deoxy-hemoglobin levels in the tumor (Figure S4), indicative of a disruption to the blood flow leading to fast depletion of the available oxygen and onset of transient hypoxia. Also, a sharp decrease in total hemoglobin was observed within 10 minutes and a 20% decrease over 1 hour (Figure S4). As CA4P is known to have a disruptive effect mainly on the irregularly formed neovasculatures, no significant changes in total hemoglobin or sO_2 were observed on the contralateral side (Figure 4*B*). Four hours post CA4P administration, sO_2 in the tumors reverted to pre CA4P treatment values (63 ± 6%) and remained the same until the last observation time of 6 hours (Figure 4*C*). This suggested the recovery of blood vessels post treatment. In order to validate the changes in sO_2 of the tumors observed using MSOT, histological analysis were performed on tumors at 0, 1 and 6 hours. There was a significant increase in CAIX stained areas at 1 hour compared to 0 and 6 hours post CA4P administration (Figure 4*D*).

Discussion

Optoacoustic imaging has been emerging as a powerful tool in revealing sO_2 with high spatial resolution and sensitivity. While previously published works have shown sO_2 measurement in the superficial cortical vasculature of brain [31], imaging sO_2 in deeper regions is severely hampered by the strong light attenuation in brain tissue and its wavelength dependent nature, resulting in the so-called spectral coloring effects that can significantly affect the unmixing results. Advanced reconstruction and unmixing approaches that can accurately account for the complex underlying physical phenomena behind optoacoustic signal generation are therefore essential for accurate estimation of sO_2 values. Herein, we experimentally showed that a combined model-based reconstruction and unmixing method incorporating non-negative constrains can render reasonable sO_2 values across the entire mouse brain. Furthermore, upon analyzing the images showing difference in single wavelength images acquired at 715, 730, 760, 800 and 850 nm, hyperintense signals found on $Diff_{850–800\ nm}$ images were useful in locating the tumors while the others were not very useful for identifying hyperoxic tumors. The higher absorption of oxygenated hemoglobin at 850 nm as compared to other wavelengths and its abundance in hyperoxic tumors could have resulted in hyperintense signal in $Diff_{850–800\ nm}$ images at the tumor region. Similarly, the higher absorption of deoxyhemoglobin at 760 nm as compared to other wavelengths and its abundance in the hyperoxic tumors could have resulted in hyperintense signal in $Diff_{760–800\ nm}$ images at the tumor region.

For the first time to our knowledge, we were able to provide a direct comparison of the sO_2 in orthotopic glioblastoma against the healthy contralateral side in whole-brain cross sections. The brain area covered with MSOT is thus comparable to that of small animal CT or MR imaging, but it can additionally provide enhanced functional information. The spatial resolution of MSOT in the range of 150 μm only allows for distinguishing major blood vessels, yet sO_2 could still be estimated reliably across the entire brain by relying on spatially averaged signals. This is evinced by the ability of MSOT to pick up sO_2 in hyperoxic (15 days post tumor inoculation) and hypoxic tumors (42 days post tumor inoculation) against the normoxic contralateral brain and the validation by histological studies.

The real-time imaging capabilities of MSOT represent yet another significant advantage of the technique to evaluate the kinetics and course of action of vascular targeting drugs on orthotopic glioblastoma. Upon CA4P administration, as expected, tumors showed a significant decrease in sO_2 up to 1 hour due to the shutdown of tumor vasculature and recovered almost completely after 4 hours. This is not surprising as a low dose (30 mg/kg) of CA4P is known to result in partial or complete recovery sooner or later after instantaneous reduction in blood flow as demonstrated by us [32] and others [33,34]. While different techniques like MRI, bioluminescence imaging (BLI) and fluorescence imaging (FLI) have been used previously to understand the mechanism of action or to evaluate the performance of vascular targeting drugs on tumors [12,35], they have only offered an indirect estimation of the vasculature damage by evaluating the consequences of vascular shutdown. Contrast-enhanced ultrasound does offer a direct estimation of the damage to the vasculature resulting from the treatment [36], however with the help of exogenous contrast agents. On the other hand, high resolution intravital microscopy [37] and photoacoustic microscopy [12], which can provide a direct measure of the vascular growth and shut down upon administration of vascular disruptive agents (VDA), are not capable of deep tissue penetration attained by MSOT. Rich et al. [8] and Bar-Zion et al. [9] have used optoacoustic imaging to investigate the hemodynamics following administration of vascular disruptive agents in superficial xenograft tumors. In the current study, we were able to measure directly the drug-evoked rapid hemodynamic changes in the entire tumor as well as the normal contralateral brain at a reasonable (mesoscopic-scale) spatial resolution of 150 μm. This performance makes MSOT highly appealing for preclinical evaluation of the drug where it is important to understand the effects of the drug on the normal tissue as well in order to evaluate its toxicity on healthy tissues.

There were several limitations to our study. Firstly, the concept of using differences in single wavelength optoacoustic images to perform anatomical imaging of orthotopic glioblastoma was tested on fewer animals (n = 3 each for hyperoxic and hypoxic tumors) with cortical tumors. The sample size should be increased to further validate the hypothesis in tumors located in different regions of the brain and thus to be eventually useful in tumor volume calculation. Moreover, in tumors with mixed hyperoxic and hypoxic areas, this strategy may indicate only parts of the tumor and not the entire tumor, thus restricting the method to tracking of early tumor growth. Secondly, though the combined non-negative constrained reconstruction and unmixing method helped in extracting sO_2 values from most parts of the brain, it could not be of much help in regions below thalamus consistently across all animals. This can be attributed to the strong light attenuation in the brain. A number of efforts are being made to minimize these limitations, including improving the instrumentation, data acquisition and post-processing [7,38–40]. Thirdly, we have used CA4P as a vascular perturbation agent looking at its short term effect rather than its long term effect as a therapeutic agent. Investigating long term treatment outcomes may help to establish the potential of MSOT imaging to predict the therapeutic responses. Finally, as no gold standard exists for validating the in vivo deep-tissue sO_2 measurements, the closest validation we provided was histological evidences at cellular scale to support the hemodynamic changes.

Conclusion

In summary, for the first time, we have demonstrated the capacity of MSOT to visualize the location and anatomy of the early tumors and sO_2 in the whole mouse brain in the presence of a glioblastoma. The

study emphasizes the importance of post processing algorithms to improve the image quality as well as maximize the information available from this novel imaging modality. The study also establishes MSOT as a treatment monitoring modality by being able to image the hemodynamic changes occurring upon administration of vascular disruptive agent.

The following are the supplementary data related to this article.

Acknowledgements

The authors acknowledge the Advanced Molecular Pathology Lab (AMPL), Institute of Molecular and Cell Biology (IMCB), A*STAR, Singapore for their help with the tissue preparation and IHC staining.

Funding

This study was funded in part by the European Research Council Consolidator grant ERC-2015-CoG-682379 (D.R.) and A*STAR (Agency for Science, Technology and Research, Singapore) Biomedical Research Council intramural funds and research collaborative agreement (RCA) with iThera Medical GmbH (M.O.).

Conflict of Interest

The authors declare that they have no conflict of interest.

Appendix A. Supplementary Data

Supplementary data to this article can be found online at https://doi.org/10.1016/j.tranon.2018.07.001.

References

[1] Deán-Ben XL, López-Schier H, and Razansky D (2017). Optoacoustic micro-tomography at 100 volumes per second. *Sci Rep* **7**, 6850.

[2] Burton NC, Patel M, Morscher S, Driessen WH, Claussen J, Beziere N, Jetzfellner T, Taruttis A, Razansky D, and Bednar B (2013). Multispectral opto-acoustic tomography (MSOT) of the brain and glioblastoma characterization. *Neuroimage* **65**, 522–528.

[3] McNally LR, Mezera M, Morgan DE, Frederick PJ, Yang ES, Eltoum I-E, and Grizzle WE (2016). Current and Emerging Clinical Applications of Multispectral Optoacoustic Tomography (MSOT) in Oncology. *Clin Cancer Res* **22**(14), 3432–3439.

[4] Reber J, Willershäuser M, Karlas A, Paul-Yuan K, Diot G, Franz D, Fromme T, Ovsepian SV, Bézière N, and Dubikovskaya E, et al (2018). Non-invasive measurement of brown fat metabolism based on optoacoustic imaging of hemoglobin gradients. *Cell Metab* **27**(3), 689–701.e4.

[5] Esenaliev RO (2017). Optoacoustic Monitoring of Physiologic Variables. *Front Physiol* **8**, 1030.

[6] Attia ABE, Chuah SY, Razansky D, Ho CJH, Malempati P, Dinish U, Bi R, Fu CY, Ford SJ, and Lee JS-S (2017). Noninvasive real-time characterization of non-melanoma skin cancers with handheld optoacoustic probes. *Photoacoustics* **7**, 20–26.

[7] Tomaszewski MR, Gonzalez IQ, O'Connor JP, Abeyakoon O, Parker GJ, Williams KJ, Gilbert FJ, and Bohndiek SE (2017). Oxygen enhanced optoacoustic tomography (OE-OT) reveals vascular dynamics in murine models of prostate cancer. *Theranostics* **7**(11), 2900–2913.

[8] Rich LJ and Seshadri M (2015). Photoacoustic Imaging of Vascular Hemodynamics: Validation with Blood Oxygenation Level–Dependent MR Imaging. *Radiology* **275**(1), 110–118.

[9] Bar-Zion A, Yin M, Adam D, and Foster FS (2016). Functional Flow Patterns and Static Blood Pooling in Tumors Revealed by Combined Contrast-Enhanced Ultrasound and Photoacoustic Imaging. *Cancer Res* **76**(15), 4320–4331.

[10] Menezes GLG, Pijnappel RM, Meeuwis C, Bisschops R, Veltman J, Lavin PT, Vijver MJvd, and Mann RM (2018). Downgrading of breast masses suspicious for cancer by using optoacoustic breast imaging. *Radiology* **0**(0), 170500.

[11] Aguirre J, Schwarz M, Garzorz N, Omar M, Buehler A, Eyerich K, and Ntziachristos V (2017). Precision assessment of label-free psoriasis biomarkers with ultra-broadband optoacoustic mesoscopy. *Nat Biomed Eng* **1** 68.

[12] Laufer J, Johnson P, Zhang E, Treeby B, Cox B, Pedley B, and Beard P (2012). In vivo preclinical photoacoustic imaging of tumor vasculature development and therapy. *J Biomed Opt* **17**(5), 0560161–0560168.

[13] Gerling M, Zhao Y, Nania S, Norberg KJ, Verbeke CS, Englert B, Kuiper RV, Bergstrom A, Hassan M, and Neesse A, et al (2014). Real-time assessment of tissue hypoxia in vivo with combined photoacoustics and high-frequency ultrasound. *Theranostics* **4**(6), 604–613.

[14] Dey S, Kumari S, Kalainayakan SP, Campbell J, Ghosh P, Zhou H, FitzGerald KE, Li M, Mason RP, and Zhang L, et al (2018). The vascular disrupting agent combretastatin A-4 phosphate causes prolonged elevation of proteins involved in heme flux and function in resistant tumor cells. *Oncotarget* **9**(3), 4090–4101.

[15] Rich LJ and Seshadri M (2016). Photoacoustic monitoring of tumor and normal tissue response to radiation. *Sci Rep* **6**, 21237.

[16] Mallidi S, Watanabe K, Timerman D, Schoenfeld D, and Hasan T (2015). Prediction of tumor recurrence and therapy monitoring using ultrasound-guided photoacoustic imaging. *Theranostics* **5**(3), 289–301.

[17] Du Q, Jiang L, Wang XQ, Pan W, She FF, and Chen YL (2014). Establishment of and comparison between orthotopic xenograft and subcutaneous xenograft models of gallbladder carcinoma. *Asian Pac J Cancer Prev* **15**(8), 3747–3752.

[18] Zhao X, Li L, Starr TK, and Subramanian S (2017). Tumor location impacts immune response in mouse models of colon cancer. *Oncotarget* **8**(33), 54775–54787.

[19] Zhang Y, Toneri M, Ma H, Yang Z, Bouvet M, Goto Y, Seki N, and Hoffman RM (2016). Real-Time GFP Intravital Imaging of the Differences in Cellular and Angiogenic Behavior of Subcutaneous and Orthotopic Nude-Mouse Models of Human PC-3 Prostate Cancer. *J Cell Biochem* **117**(11), 2546–2551.

[20] Attia AB, Ho CJ, Chandrasekharan P, Balasundaram G, Tay HC, Burton NC, Chuang KH, Ntziachristos V, and Olivo M (2016). Multispectral optoacoustic and MRI coregistration for molecular imaging of orthotopic model of human glioblastoma. *J Biophotonics* **9**(7), 701–708.

[21] Ni R, Vaas M, Ren W, and Klohs J (2018). Noninvasive detection of acute cerebral hypoxia and subsequent matrix-metalloproteinase activity in a mouse model of cerebral ischemia using multispectral-optoacoustic-tomography. *Neurophotonics* **5**(1), 015005.

[22] Hanihara M, Kawataki T, Oh-Oka K, Mitsuka K, Nakao A, and Kinouchi H (2016). Synergistic antitumor effect with indoleamine 2,3-dioxygenase inhibition and temozolomide in a murine glioma model. *J Neurosurg* **124**(6), 1594–1601.

[23] Szabo E, Phillips DJ, Droste M, Marti A, Kretzschmar T, Shamshiev A, and Weller M (2018). Anti-tumor activity of DLX1008, an anti-VEGFA antibody fragment with low picomolar affinity, in human glioma models. *J Pharmacol Exp Ther* **365**, 422–429.

[24] Shankavaram UT, Bredel M, Burgan WE, Carter D, Tofilon P, and Camphausen K (2012). Molecular profiling indicates orthotopic xenograft of glioma cell lines simulate a subclass of human glioblastoma. *J Cell Mol Med* **16**(3), 545–554.

[25] Ding L, Ben XLD, Burton NC, Sobol RW, Ntziachristos V, and Razansky D (2017). Constrained Inversion and Spectral Unmixing in Multispectral Optoacoustic Tomography. *IEEE Trans Med Imaging* **36**, 1676–1685.

[26] Ding L, Deán-Ben XL, Lutzweiler C, Razansky D, and Ntziachristos V (2015). Efficient non-negative constrained model-based inversion in optoacoustic tomography. *Phys Med Biol* **60**(17), 6733–6750.

[27] Xu M and Wang LV (2005). Universal back-projection algorithm for photoacoustic computed tomography. *Phys Rev E Stat Nonlin Soft Matter Phys* **71**(1 Pt 2), 016706.

[28] Razansky D (2012). Multispectral Optoacoustic Tomography - Volumetric Color Hearing in Real Time. *IEEE J Sel Top Quantum Electron* **18**(3), 1234–1243.

[29] West CM and Price P (2004). Combretastatin A4 phosphate. *Anticancer Drugs* **15**(3), 179–187.

[30] Tozer GM, Kanthou C, Parkins CS, and Hill SA (2002). The biology of the combretastatins as tumour vascular targeting agents. *Int J Exp Pathol* **83**(1), 21–38.

[31] Yao J, Wang L, Yang J-M, Maslov KI, Wong TT, Li L, Huang C-H, Zou J, and Wang LV (2015). High-speed label-free functional photoacoustic microscopy of mouse brain in action. *Nat Methods* **12**(5), 407–410.

[32] Bi R, Balasundaram G, Jeon S, Tay HC, Pu Y, Li X, Moothanchery M, Kim C, and Olivo M (2018). Photoacoustic microscopy for evaluating combretastatin A4 phosphate induced vascular disruption in orthotopic glioma. *J Biophotonics* p. [e201700327-n/a].

[33] Murata R, Overgaard J, and Horsman MR (2001). Comparative effects of combretastatin A-4 disodium phosphate and 5, 6-dimethylxanthenone-4-acetic

acid on blood perfusion in a murine tumour and normal tissues. *Int J Radiat Biol* **77**(2), 195–204.

[34] Rustin G, Price P, Stratford M, Galbraith S, Anderson H, Folkes L, Robbins A, and Senna L (2001). Phase I study of weekly intravenous combretastatin A4 phosphate (CA4P): pharmacokinetics and toxicity. *Proc Am Soc Clin Oncol* 20012099a (abstract 392).

[35] Liu L, Mason RP, and Gimi B (2015). Dynamic bioluminescence and fluorescence imaging of the effects of the antivascular agent Combretastatin-A4P (CA4P) on brain tumor xenografts. *Cancer Lett* **356**(2), 462–469.

[36] Sorace AG, Saini R, Mahoney M, and Hoyt K (2012). Molecular Ultrasound Imaging Using a Targeted Contrast Agent for Assessing Early Tumor Response to Antiangiogenic Therapy. *J Ultrasound Med* **31**(10), 1543–1550.

[37] Tozer GM, Prise VE, Wilson J, Cemazar M, Shan S, Dewhirst MW, Barber PR, Vojnovic B, and Chaplin DJ (2001). Mechanisms associated with tumor vascular shut-down induced by combretastatin A-4 phosphate: intravital microscopy and measurement of vascular permeability. *Cancer Res* **61**(17), 6413–6422.

[38] Nie L, Cai X, Maslov K, Garcia-Uribe A, Anastasio MA, and Wang LV (2012). Photoacoustic tomography through a whole adult human skull with a photon recycler. *J Biomed Opt* **17**(11), 110506.

[39] Huang C, Nie L, Schoonover RW, Guo Z, Schirra CO, Anastasio MA, and Wang LV (2012). Aberration correction for transcranial photoacoustic tomography of primates employing adjunct image data. *J Biomed Opt* **17**(6), 0660161–0660168.

[40] Estrada H, Rebling J, Turner J, and Razansky D (2016). Broadband acoustic properties of a murine skull. *Phys Med Biol* **61**(5), 1932–1946.